



University of
Sheffield

Insights into laminarisation and turbulence dynamics in spatially accelerating flows

Matthew Falcone

A thesis submitted in partial fulfilment of the requirements for the degree of
Doctor of Philosophy

The University of Sheffield
Faculty of Engineering
Department of Mechanical Engineering

Submission Date

Autumn 2023

This thesis is dedicated to my parents
for the love and support you have given me
over all these years

Acknowledgements

First and foremost, I am indebted to my supervisor, Prof. Shuisheng He. Not only for his guidance and encouragement throughout my Master's and PhD research, for which he was indispensable, but also for his pastoral support.

I want to thank the UK Turbulence Consortium for the computational resources on ARCHER2, without which this project would not have been possible. Also, thanks to the developers of Incompact3D, who always gave me prompt assistance when required, and Dr. Wei Wang for her technical help using CHAPSim. I also want to thank my examiners, Professor Pierre Ricco and Professor Sylvain Laizet, for the thought-provoking discussions that significantly improved this work.

To my colleagues in the Heat, Flow, and Turbulence research group and The Farm, thank you for the support, encouragement, and conversations that have always been stimulating. I would especially like to thank Dr. Kenneth Chinembiri for all his support and assistance since my days as an undergraduate summer researcher.

Last but not least, I would like to thank my friends, family, and particularly my parents and brother for the encouragement and support you have given me over the last few years,

Abstract

Spatially accelerating turbulent flows occur in many applications and contain intriguing flow phenomena, most notably laminarisation, which causes rapid changes in flow characteristics in strong accelerations. This study uses numerical simulations to provide new insights into the turbulence dynamics that lead to the emergence of laminarisation in these flows. This study has used the open-source solvers CHAPSim and Incompact3D, implementing and validating a method for simulating spatially accelerating turbulent boundary layers (TBLs). It is shown that the turbulence response in spatially accelerating flows is dominated by a three-stage transition-like process in the near-wall region similar to that which occurs in a temporally accelerating flow (He & Seddighi, *J. Fluid Mech.* 715:60-102, 2013), noting that spatially accelerating flows are more complex due to influence of flow contraction and spatial development.

The study comprises three investigations. First, a direct numerical simulation (DNS) of an idealised spatial acceleration is examined, where longitudinally accelerating moving walls are used to create a relative spatial acceleration, removing the influence of flow contraction. This flow has been found to be described by a three-stage process akin to the bypass transition of a laminar boundary layer. During pre-transition, a new boundary layer forms due to the viscous resistance to the acceleration provided by the wall. This thin layer of enhanced mean shear amplifies the near-wall streaks through the lift-up effect without significantly affecting the transverse motions. At the onset of the transition stage, these streaks break down, forming turbulent spots which grow in the spanwise direction until the wall is covered in newly generated turbulence. Finally, this turbulence spreads into the core in the fully turbulent stage. This flow exhibits many similarities with more typical spatial accelerating flows, such as the amplification of the streaks and the changes in their spanwise scale.

In the second investigation, spatially accelerating TBLs are studied, which incorporates the effect of the flow contraction. Four simulations were conducted over a range of acceleration rates, including laminarising accelerations and weaker cases that did not show signs of laminarisation. All cases are characterised by a transition process that resulted from the development of a new boundary layer similar to the moving wall acceleration. However, flow contraction also results in a flattening of the mean velocity profile away from the wall. Differences emerged between the stronger and weaker accelerations during the pre-transition stage, with the laminarising cases exhibiting an absolute attenuation of the transverse stresses in the inner layer, whereas in the weaker accelerations, the transverse stresses remain largely unchanged close to the wall. The differences between the weak and strong acceleration can be traced to distinct behaviours in the intercomponent energy transfer close to the wall, particularly for the wall-normal component.

Finally, spatially accelerating TBLs are compared with a carefully established equivalent temporally accelerating channel flow to improve the understanding of the similarities and differences between these two types of acceleration. Previous studies have often highlighted the apparent similarities between the accelerations, but no direct comparison has been done previously. To facilitate the comparison, the acceleration parameter, $K = (\nu^*/U_\infty^*)d_x U_\infty^*$ and freestream/centreline velocities were matched throughout the accelerations. The mean flow parameters exhibit generally similar variations in both accelerations, but the excursions in the skin friction coefficient and shape factor are significantly greater in the spatial acceleration cases, primarily due to the influence of flow contraction. During the pre-transition region, the turbulence response shared some similarities, with the near-wall peak of the streamwise Reynolds stress nearly collapsing between the spatial and temporal accelerations. However, the strong reductions in streamwise turbulence away from the wall and the transverse components everywhere are observed in strong spatial accelerations but not in temporal cases.

Contents

Abstract	iii
Contents	v
List of Figures	x
List of Tables	xix
Publications	xxi
1 Introduction	1
1.1 Structure of the thesis	4
2 Background theory	5
2.1 Governing equations	5
2.2 Statistical description of turbulence	6
2.2.1 Reynolds-averaged Navier-Stokes equations	7
2.2.2 Reynolds stress transport equations	8
2.2.3 Two-point correlations and spectra	8
2.3 Vorticity and vortex identification	9
2.4 Wall-bounded turbulent flows	10
2.4.1 Mean velocity profile	13
2.4.2 Quadrant analysis, ejection and sweep events	15
2.4.3 Near-wall turbulence structures and turbulence regeneration cycle	16
3 Literature Review	19
3.1 Spatially accelerating flows	19
3.1.1 Mean flow and turbulent statistics	22
3.1.2 Turbulence structures	24

3.1.3	Mechanisms of laminarisation	27
3.2	Bypass transition of laminar boundary layers	28
3.3	Temporal acceleration	33
4	Numerical methods and validation	38
4.1	Incompact3D	39
4.1.1	Time advancement and discretisation	39
4.1.2	Spatial discretisation	41
4.1.3	Large eddy simulation	43
4.2	CHAPSim	45
4.2.1	Time advancement	45
4.2.2	Spatial discretisation	46
4.3	Important considerations for DNS	48
4.3.1	Grid resolution, domain size and time step	48
4.3.2	High-performance computing strategy	49
4.4	Channel flow and temporal acceleration	52
4.4.1	Initial and boundary conditions	52
4.5	Simulation of turbulent boundary layers	53
4.5.1	Implementation details	54
4.5.1.1	Recycling-rescaling method	54
4.5.1.2	Computational domain and boundary conditions	57
4.5.1.3	Initialisation and flow development	59
4.5.2	Specific considerations for the simulation of TBLs	62
4.6	Computation of statistics	64
4.6.1	Statistic computation for different flow configurations	64
4.7	Validation and assessment of numerical tools	66
4.7.1	Turbulent channel flow	66
4.7.2	Temporally accelerating channel flow	67
4.7.3	Zero pressure gradient TBLs	68
4.7.4	Favourable pressure gradient TBLs	71
4.7.4.1	Applicability of iSVV method	72
4.7.4.2	Validation	75

5	A spatially accelerating flow with longitudinally contracting walls	79
5.1	Moving wall acceleration	79
5.2	Mean flow	81
5.3	Instantaneous flow	84
5.4	Turbulence statistics	87
5.4.1	Reynolds stresses	87
5.4.2	Reynolds stress budgets	91
5.4.3	Quadrant analysis	93
5.4.4	Correlations	96
5.4.5	Flow structures	98
5.5	Summary and conclusion	101
5.5.1	Summary of flow development	102
5.5.2	Similarities and differences with conventional spatial acceleration	102
6	Transition in spatially accelerating turbulent boundary layers	104
6.1	Case setup	104
6.2	Case characterisation	106
6.3	The transition process	109
6.4	Reynolds stresses and higher-order statistics	115
6.4.1	Normal Reynolds stresses	115
6.4.2	Reynolds shear stress and eddy viscosity	120
6.4.3	Kurtosis	122
6.4.4	Reynolds stress budgets	124
6.4.5	Quadrant analysis	126
6.5	Energy spectra	128
6.5.1	Streak generation	130
6.6	Transverse stresses	132
6.6.1	Pressure strain	133
6.6.2	Spectral analysis of Reynolds stress budget	135
6.6.3	Rapid pressure	139
6.7	Summary and Conclusion	141
6.7.1	Summary of near-wall transition process	142
6.7.2	Comparison of spatial accelerations with different K	143
6.7.3	Laminarisation: where are we?	144

7	A comparison of spatially and temporally accelerating flows	146
7.1	Comparison approach	146
7.1.1	Initial flow	146
7.1.2	Matched accelerations	149
7.2	Simulation setup	152
7.3	Mean flow response	154
7.4	Momentum balance	160
7.5	Turbulence response	163
7.6	Discussion	169
7.6.1	Influence of the initial flow	169
7.6.2	Assessment of the comparison approach	169
7.7	Summary and Conclusions	170
8	Conclusions and future work	172
8.1	Conclusions	172
8.1.1	Moving wall acceleration	173
8.1.2	Spatially accelerating turbulent boundary layers	173
8.1.3	Comparison of spatially and temporally accelerating flows . .	174
8.2	Proposed future work	175
	Appendices	177
A	Moving wall acceleration	177
A.1	Details of the turbulence generator	177
A.2	Moving-wall acceleration with a smooth and gradual flow increase . .	178
A.3	Algorithm for quadrant events	179
B	Transition in spatially accelerating TBLs	181
B.1	Conditions upstream of acceleration	181
B.2	Spot detection algorithm	181
B.3	Derivation of $\widehat{\mathcal{G}}$	182
B.4	Derivation of terms in the spectral Reynolds stress transport equation	184
C	Comparison of spatially and temporally accelerating flows	186
C.1	Stokes first problem	186
C.1.1	Different reference heights	187
C.1.2	Different boundary layer thickness definitions	189
C.1.3	Different reference planes	189

C.1.4	Different freestream velocities	189
	Bibliography	193

List of Figures

1.1	Schematic of laminarisation occurring on a leading edge slat during landing. ① Freestream disturbances, which can originate from the TBL developing over the fuselage, induce the boundary layer developing over the wing to transition shortly after the attachment line. ② During landing, the leading edge slat is deployed, leading to significant streamline contraction and strong streamwise acceleration with acceleration parameter, $K > 1 \times 10^{-5}$ [1]. ③ Acceleration induces the laminarisation of the transitioned boundary layer.	2
2.1	Schematics of a turbulent channel flow (a) and a turbulent boundary layer (b).	11
2.2	The inner-scaled mean velocity profile of turbulent wall-bounded flows. (a) shows \bar{u}^+ vs y^+ for turbulent channel flow [2] and TBLs [3] at $Re_\tau = 2000$ $\bar{u}^+ = y^+$ and the logarithmic law, where $\kappa = 0.4$ and $B = 5$, are indicated.. (b) shows the diagnostic function, Ξ for channels flows up to $Re_\tau = 5200$ [4, 5].	13
2.3	Quadrant analysis. (a) joint PDF of u' and v' of a channel flow at $Re_\tau = 180$ at $y^+ = 9$ with quadrant events labelled. The contours are at 0.08(0.08)0.64. (b) burst pattern of a TBL at $y^+ = 15$ showing ejection and sweep events reproduced from Blackwelder and Kaplan [6].	15
2.4	Schematic of the layout of a meandering streamwise streak and staggered opposing quasi-streamwise vortices (QSV) from Jeong et al. [7]. (a) top-down view, (b) sideways view. SN and SP indicates QSVs with negative and positive ω'_x , respectively.	16
2.5	Classical regeneration cycle, reproduced from Kim [8].	17
3.1	Schematic of a typical wind tunnel experiment for a spatially accelerating flow, where a liner has been used to create the reduction of flow area.	19

3.2	Schematic of stages proposed by Narasimha and Sreenivasan [9]: Fully turbulent (I), reverse transition (II), quasi-laminar (III), retransition (IV). The freestream velocity, U_∞ and boundary layer thickness, δ are also indicated.	22
3.3	Isosurfaces of the Q criterion, where $Q = -\partial_j u_i \partial_i u_j / 2$ from Piomelli and Yuan [10] coloured by $\omega'_x / \omega'_{rms}$. The reduction in the density of vortices can be observed.	26
3.4	The velocity fluctuations from Nagarajan et al. [11] showing the typical progression of a boundary layer undergoing bypass transition. (a) u' ; (b) v' ; (c) w'	29
3.5	$z - t$ surface plots of the streamwise and wall-normal velocity fluctuations for transient channel flow at $y^{+0} = 15$ from Mathur et al. [12]. The two vertical planes indicate the onset of acceleration and transition, respectively. (a) u' ; (b) v'	34
4.1	Partial staggered grid: the computation of derivatives for equations (4.1c) and (4.1d) is indicated with the blue and red arrows representing the computation of $\partial_x \tilde{p}$ and $\partial_x u^{**}$ respectively. ① indicates differentiation using equation (4.9) and ② indicates interpolation using equation (4.10). Used in Incompact3D.	42
4.2	(a) shows the modified wavenumber for equation (4.7) and the iSVV model for various values of ν_0 . (b) shows the resulting spectral viscosity, ν_s / ν_0 for different values of ν_0 compared with the SVV kernel [13].	44
4.3	Diagram showing the turbulence generator and inlet-outlet domain of CHAPSim	47
4.4	Fully staggered grid. Used in CHAPSim	47
4.5	Domain partitioning strategies. (a) Pencil decomposition showing from left-to-right the X pencil, Y pencil and Z pencil. (b) Slab decomposition showing from left-to-right the XZ slab and the XY slab.	50
4.6	Strong scaling for a spatially accelerating TBL turbulent boundary layer with 1.4 billion points (case 3 from chapter 6).	51
4.7	Schematic of the recycling-rescaling method showing the computational domain, inlet, and recycling planes in relation to the boundary layer leading edge.	55
4.8	Schematic of the computational domain used for a typical spatially accelerating TBL compared with a typical experimental setup	58

4.9	U_∞ compared with U_∞^{des} and the wall-normal mean velocity, \bar{v} showing substantial inflow as a result of the flow contraction induced by equation (4.38).	59
4.10	Initialisation of the streamwise mean velocity. (a) initialised \bar{u}^+ at $Re_\theta = 1000, 2000, 4060$ (lines) compared with Schlatter and Örlü [14] (markers). (b) computed Re_θ compared with target value.	61
4.11	Tripping method: u and v early in the simulation showing the periodic arrays of tripping locations and the resulting turbulent structures. (a) u' $x - z$ plane, (b) v' $x - z$ plane. (c) u' $x - y$ plane	62
4.12	Spatiotemporal autocorrelation of the streamwise velocity showing spurious periodicities in the recycling method and several mitigation approaches. (a) Normal Recycling method. (b) Shifting the inlet plane by $L_z/2$ in the z direction. (c) Reflecting the inlet plane about $z = L_z/2$	64
4.13	Monitoring fully developed channel flow at $Re_\tau = 180$: Instantaneous, u and spanwise averaged streamwise velocity, \bar{u} (y axis right), and skin friction coefficient C_f (y axis left).	65
4.14	Channel flow validation: (a) \bar{u}^+ vs y^+ at $Re_\tau = 180$; (b) Normal Reynolds stresses at $Re_\tau = 180$; (c) \bar{u}^+ vs y^+ at $Re_\tau = 395$; (d) Normal Reynolds stresses at $Re_\tau = 395$	67
4.15	$\overline{u'u'}$ budget at $Re_\tau = 180$	68
4.16	Temporal acceleration validation against He and Seddighi [15]: (a) C_f ; (b) \bar{u}^+ vs y^+ . In (b) lines indicate present results and markers indicate those from He and Seddighi [15]	69
4.17	Comparison of mean flow parameters with validating data [14, 16, 17, 18]. (a) C_f compared with correlation [19]. (b) Re_θ vs Re_τ compared with correlation [14]. (c) H compared with Chauhan et al. [20] relation. (d) $\tau_{w,rms}^+$ compared with relation from Schlatter and Örlü [14].	70
4.18	Comparison of mean velocity and normal Reynolds stresses with Schlatter and Örlü [14]. Present: solid lines. Schlatter and Örlü [14]: dashed lines with markers.	71
4.19	Comparison of $\overline{u'u'}$ budget with Schlatter and Örlü [14]: (a) $Re_\theta = 1000$; (b) $Re_\theta = 1410$. Solid lines indicate the present results; the dashed lines with markers indicate those of Schlatter and Örlü [14].	72
4.20	Wall-normal velocity fluctuations, v' for DNS, LES (WALE) and LES (iSVV). (a) DNS, (b) WALE, (c) iSVV.	74

4.21	Comparison of mean flow parameters between DNS and the iSVV model for case 1 with $\nu_0 \in \{20, 30, 50\}$. (a) C_f , (b) Re_θ , and (c) H	74
4.22	Inner-scaled mean velocity and Reynolds shear stress for DNS (lines) and iSVV models (markers). (a) \bar{u}^+ vs y^+ , (b) $-\overline{u'v'}^+$ vs y^+	75
4.23	Comparison of mean flow parameter with Piomelli and Yuan [10]. (a) U_∞ , (b) K , (c) C_f , (d) Re_θ	76
4.24	Comparison of inner-scaled mean velocity profile. (a) \bar{u}^+ , where lines represent the present results; the markers are from Piomelli and Yuan [10]. (b) shows the variation of the logarithmic law constants, κB vs. B and $\kappa B = 1.6[\exp(0.1663B) - 1]$. (c) shows the consistency of the computed logarithmic law constants with the inner scaled mean velocity. (d) shows the diagnostic function, Ξ during laminarisation for case P, with the symbols having the same meaning as (c).	77
4.25	Comparison of the inner-scaled Reynolds shear stress with Piomelli and Yuan [10]. Lines and symbols are the same as figure 4.24(a).	78
5.1	Flow acceleration caused using the moving-wall approach. (a) the absolute streamwise velocity profile at different streamwise locations. (b) the channel and its streamwise boundary condition are shown with the arrows representing the wall velocity. The shaded yellow region is the region where the acceleration is applied. (c) A plot showing the variation of the absolute velocity (dashed), wall velocity (dotted), and relative velocity (solid).	80
5.2	Streamwise mean velocity profile. (a): Absolute mean velocity, \bar{u}_a ; (b): Mean velocity relative to the wall, \bar{u} ; (c) inner-scaled relative mean velocity profile in the pre-transition stage ($x \leq 5$); and (d) post onset of transition ($x > 5$) including $x = 0, 5$. In figures 5.2(c) and 5.2(d), the red line is $\bar{u}^+ = y^+$	82
5.3	(a) shows the skin friction coefficient, C_f and wall shear stress, $\tau_w = 1/Re_0 \cdot \partial\bar{u}/\partial y$. (b) shows the shape factor, H ; and the acceleration parameter, K . As stated in section 5.1, these quantities have been calculated relative to the wall. The vertical lines indicate the onset and completion of transition using the definitions described in section 5.3.	83

5.4	A $x - z$ plane of the streamwise (u'/U_{b0}) and wall-normal (v'/U_{b0}) fluctuating velocities at single instance in time at $y^{+0} = 4.9$. The relative bulk velocity, U_b , is shown in (a) for reference. The first black line indicates the start of the acceleration, while the final black line is the end of the acceleration. The red line indicates the approximate location of the onset of transition as indicated by the minimum in C_f .	85
5.5	Streamwise distribution of the peak normal Reynolds stresses normalised by U_{b0}^2 . $\overline{u'u'}$ is shown on the left axis with $\overline{v'v'}$ and $\overline{w'w'}$ on the right axis. The vertical line indicates the onset of transition as indicated by the minimum in C_f .	87
5.6	The wall-normal distribution of the normal Reynolds stresses normalised by U_{b0}^2 . The figures on the left ((a), (c), and (e)), are of x locations prior to transition and those on the right ((b), (d), and (f)) are of locations after the onset of transition. The legend in (a) is used in (c) and (e) while the legend in (b) is used in (d) and (f).	88
5.7	Reynolds shear stress, $-\overline{u'v'}$ ((a) and (b)) normalised by U_{b0}^2 and eddy viscosity, ν_t/ν ((c) and (d)).	90
5.8	Streamwise Reynolds stress budget scaled with initial wall units, $u_{\tau,0}^{*4}/\nu^*$.	92
5.9	The wall-normal integral of production, pressure strain and dissipation terms of the $\overline{u'u'}$ budget normalised by $u_{\tau,0}^{*4}h^*/\nu^*$. The meaning of the vertical line is the same as figure 5.5.	93
5.10	$\overline{u'v'_Q}/\overline{u'v'}$ calculated using the method of Willmarth and Lu [21]. The values of the threshold h are given in the legend. The black dashed line indicates the onset of transition.	94
5.11	Number of distinct events using the method of Willmarth and Lu [21]. The black dashed line indicates the onset of transition.	95
5.12	The ratio of the mean duration of quadrant events and the interval between quadrant events. The black dashed line indicates the onset of transition.	96
5.13	Streamwise velocity autocorrelation in the spanwise (a) and streamwise (b) directions at various streamwise locations. The blue lines are from locations after the onset of transition.	97
5.14	A $\Delta z - y$ contour of the spanwise autocorrelation of the streamwise velocity at streamwise locations indicated in the top right of each figure. Only the values where the autocorrelation is negative are shown for clarity.	98

5.15	Wall-normal distribution of $\omega'_{x,rms}$ at different streamwise locations. (a) during pre-transition. (b) after the onset of transition.	99
5.16	$z - y$ contours of the streamwise vorticity ω'_x at different streamwise locations.	100
5.17	A top-down view of u' and ω'_x isosurfaces at $t^* \in \{70.5, 71.5, 72.5, 73.5, 74.5, 75.5\}$. u' surfaces: -0.31 (blue); 0.31 (green). ω'_x isosurfaces: -8 (red); 8 (black).101	
6.1	The freestream velocity, U_∞ and the acceleration parameter, K . (a): case 1. (b): case 2. (c): case 3. (d): Case 4.	106
6.2	Skin friction coefficient, C_f and the wall shear stress, τ_w . (a): case 1. (b): case 2. (c): case 3. (d): Case 4. All y axis limits are fixed to highlight the influence of the acceleration in the different cases. . . .	107
6.3	Shape factor, H . (a): case 1. (b): case 2. (c): case 3. (d): Case 4. All y axis limits are fixed to highlight the influence of the acceleration in the different cases.	107
6.4	Boundary layer thickness, δ and the momentum thickness Reynolds number, Re_θ . (a): case 1. (b): case 2. (c): case 3. (d): Case 4.	108
6.5	Mean flow development for case 1. (a): \bar{u} vs y , (b): \bar{u}^+ vs y^+ . τ/τ_{w0} vs y^{+0} : before transition (c); after transition (d).	110
6.6	Mean flow development for case 3. (a): \bar{u} vs y , (b): \bar{u}^+ vs y^+ . τ/τ_{w0} vs y^{+0} : before transition (c); after transition (d).	111
6.7	$x - z$ plane of the velocity fluctuations at $y^{+0} = 15$ for case 1. (a) U_∞ , (b) u' , (c) v' , (d) w'	112
6.8	$x - z$ plane of the velocity fluctuations at $y^{+0} = 15$ for case 3. (a) U_∞ , (b) u' , (c) v' , (d) w'	113
6.9	Isosurfaces of λ_2 for cases 1 and 3. (a) case 1 for $200 < x < 350$ at $\lambda_2 = -0.1$. (b) case 3 for $300 < x < 450$ at $\lambda_2 = -0.16$. The isosurfaces are coloured by the mean velocity at $x = 0$	114
6.10	Development of $\overline{u'u'}^{+0}$ vs y^{+0} in cases 1 to 4. Blue lines indicate locations before the onset of transition, and red lines indicate those after.	116
6.11	Development of $\overline{v'v'}^{+0}$ vs y^{+0} in cases 1 to 4. Blue lines indicate loca- tions before the onset of transition, and red lines indicate those after.	117
6.12	Development of peak normal Reynolds stress with x in cases 1 to 4 with the boundaries of each region from table 6.3 indicated with vertical lines. (a) case 1, (b) case 2, (c) case 3, (d) case 4.	119

6.13	Development of $\overline{u'v'}^{+0}$ vs y^{+0} in cases 1 to 4. Blue lines indicate locations before the onset of transition, and red lines indicate those after. (a) case 1, (b) case 2, (c) case 3, (d) case 4.	121
6.14	Development of ν_t vs y^{+0} in cases 1 to 4. Blue lines indicate locations before the onset of transition, and red lines indicate those after. . . .	122
6.15	Kurtosis, $F = \overline{v'^4}/\overline{v'^2}^2$ at $y^{+0} = 15$ with a vertical line indicating the onset of transition from table 6.3. (a) case 1, (b) case 2, (c) case 3, (d) case 4.	123
6.16	Isosurfaces of $ v' = 3.5v'_{rms}$ (blue colourmap) and $ w' = 3.5w'_{rms}$ (red colourmap) for case 1. The isosurfaces are shaded by the mean streamwise velocity at $x = 0$	124
6.17	Streamwise Reynolds stress budget. Case 1 is presented on the left, and case 3 is presented on the right.	125
6.18	Reynolds shear stress contributions for case 1 using the hyperbolic hole method [21] with threshold, $h \in \{0, 1, 3\}$. (a) $-\overline{u'v'}_{Q1}$, (b) $-\overline{u'v'}_{Q2}$, (c) $-\overline{u'v'}_{Q3}$, (d) $-\overline{u'v'}_{Q4}$	126
6.19	Reynolds shear stress contributions for case 3 using the hyperbolic hole method [21] with threshold, $h \in \{0, 1, 3\}$. (a) $-\overline{u'v'}_{Q1}$, (b) $-\overline{u'v'}_{Q2}$, (c) $-\overline{u'v'}_{Q3}$, (d) $-\overline{u'v'}_{Q4}$	127
6.20	Pre-multiplied spanwise spectrum of the streamwise velocity, $k_z \Phi_{11}^{+0}(x, y, k_z)$ against referenced inner-scaled spanwise wavelength, λ_z^{+0} for cases 1 ((a), (c), (e), (g), (i)) and 3 ((b), (d), (f), (h), (j)).	129
6.21	Pre-multiplied spanwise ‘lift-up’ spectrum, $k_z \widehat{\mathcal{G}}^{+0}$ against referenced inner-scaled spanwise wavelength, λ_z^{+0} for cases 1 ((a) and (b)) and 3 ((c) and (d)). Locations during pre-transition are on the left at $y^{+0} = 13$, and locations after the onset of transition are on the right at $y^{+0} = 8$	131
6.22	$\overline{v'v'}^{+0}$ and $\overline{w'w'}^{+0}$ against streamfunction ψ for cases 1 (left) and 3 (right).	132
6.23	Pressure strain components, Π_{ii}^s and wall-normal dilational production, \mathcal{P}_{22} for cases 1 (left) and 3 (right).	134
6.24	Pre-multiplied pressure-strain spectra for case 1. Wall-normal component, $\widehat{\Pi}_{22}^{s+0}$ (left) and spanwise component, $\widehat{\Pi}_{33}^{s+0}$ (right).	136
6.25	Pre-multiplied wall-normal dilational production, $\widehat{\mathcal{P}}_{22}^{+0}$ spectra for case 1.	137

6.26	$z - y$ plane of instantaneous velocity vectors for case 1 superimposed with contours of $p'\partial_y v' < 0$ (blue lines). Filled contours represent $u'v'$ corresponding Q4 events. The thick black lines indicates where $u = 0.92U_\infty$	138
6.27	Isosurfaces of the source of the rapid pressure, $f_r = 0.03$ for cases 1 and 3 for streamwise locations upstream of the onset of transition. The isosurfaces are coloured by the mean streamwise velocity at $x = 0$. . .	140
7.1	Variation of first and second-order statistics for the low Reynolds number channel and TBLs: (a) \bar{u}^+ vs y^+ ; (b) $\overline{u'u'^+}$ vs y^+ ; (c) $\overline{v'v'^+}$ vs y^+ ; (d) $\overline{w'w'^+}$ vs y^+	148
7.2	Higher order statistics: (a): skewness of u' , $S(u')$; (b): kurtosis of u' , $F(u')$	149
7.3	Freestream/centreline velocity and acceleration parameter. (a) U_∞ and U_c for cases 1 and 1T. (b) U_∞ and U_c for cases 2 and 2T. The bulk velocity, U_b for the channel flows is also presented, shifted upwards so that it initially overlaps with U_c . (c) K for cases 1 and 1T. (d) K for cases 2 and 2T. The legend in (a) applies to (c) and the legend in (b) applies to (d).	153
7.4	Comparison of other acceleration parameters. Λ [9] (a), (b). Δ_p [22] (c), (d). Cases 1 and 1T: (a) (c). Cases 2 and 2T: (b) (d).	154
7.5	Comparison of mean flow parameters. Skin friction coefficient C_f (c) (d). Shape factor H (e) (f). Cases 1 and 1T: (c) (e). Cases 2 and 2T: (d) (f)	155
7.6	Comparison of mean velocity: (a) \bar{u} case 1; (b) \bar{u} case 1T; (c) \bar{u}^+ case 1; (d) \bar{u}^+ case 1T.	157
7.7	Development of integral thicknesses in cases 1 (a) and 1T (b).	158
7.8	Comparison of integral thickness integrands pre-multiplied by y . $1 - \bar{u}/U_\infty$ (a) (b). $(\bar{u}/U_\infty)(1 - \bar{u}/U_\infty)$ (c) (d). Case 1: (a) (c). Case 1T: (b) (d)	159
7.9	Momentum balance during pre-transition. Cases 1 and 1T are presented on the left and right, respectively. Streamwise locations: $X_c = 0$ (a) and (b); $X_c = 16$ (c) and (d); $X_c = 23$ (e) and (f).	161
7.10	Maxima of RMS velocity fluctuations for cases 1 and 1T (left), and cases 2 and 2T (right). u'_{rms}^{+0} (a) (b); v'_{rms}^{+0} (c) (d); w'_{rms}^{+0} (e) (f).	163

7.11	Wall normal distributions of $\overline{v'v'^{+0}}$ ((c)(d)) and $\overline{w'w'^{+0}}$ ((e)(f)) for cases 1 (left) and 1T (right.)	164
7.12	Comparison of the velocity fluctuations for cases 1 and 1T at an $x - z$ plane close to the wall and at various $z - y$ planes. (a) u' case 1, (b) u' case 1T, (c) v' case 1, (d) v' case 1T. The colourmap for u' is presented in the top left, the colourmap for v' is shown in the bottom right. . .	166
7.13	$\Delta x - y$ streamwise velocity autocorrelation, $R_{11}(\Delta x, y, y_0; t)$ for case 1T at $y^{+0} = 11$ (a) and $y^{+0} = 97$ (b) for $X_c \in -5, 18, 23, 33$ with subsequent stations shifted by 3 to the right. Inclination computed using the method of Volino et al. [23] is given to the left of R_{11} . At ($y^{+0} = 11, X_c = -5$), the points used to compute the inclination angle are marked with red dots.	167
A.1	Streamwise autocorrelation for turbulence generator at $y^+ \in \{5, 15, 50, 150\}$. (a) spanwise direction. (b) streamwise direction.	177
A.2	Smooth case compared with the case presented in the paper. (a) Relative bulk velocity. (b) Acceleration parameter.	178
A.3	Smooth case compared with the case presented in the paper. (a) Skin friction coefficient. (b) Shape factor.	179
B.1	Comparison of the reference plane of cases 1 to 4 with ZPG case from chapter 4	182
C.1	Validation of the laminar model for pre-transition region. (a) Case 1. (b) Case 2.	187
C.2	Comparison of extended Stokes' solution for different reference heights.	188
C.3	Comparison of case 1 with laminar models using different definitions of the boundary layer thickness. (a) 99% thickness. (b) 99.5% thickness.	189
C.4	Comparison of case 1 with different reference plane locations. (a) $x/\theta_0 = 300$, (b) $x/\theta_0 = 350$, (c) $x/\theta_0 = 400$, (d) $x/\theta_0 = 450$	190
C.5	Pressure gradient at two locations during pre-transition showing the terms of equation (C.8). (a) $X_c = 16$, (b) $X_c = 23$	191
C.6	Comparison of case 1 with different definitions of U_∞ computed using the extended Stokes' solution.	192

List of Tables

2.1	Regions of the mean velocity profile	14
4.1	Case setup for the channel flow validation at $Re_\tau = 180$ and $Re_\tau = 395$.	66
4.2	Simulations configuration for temporal acceleration validation.	68
4.3	Simulation configuration for ZPG turbulent boundary layer validation. The grid resolutions indicate their worst in the domain.	69
4.4	Case characteristics for the iSVV tests, noting that the resolutions are the worst in the domain. Coarse case is at $\nu_0 = 20$	72
4.5	Simulation configuration of spatially accelerating turbulent boundary layer validation.	75
5.1	Details of the inlet-outlet domain presented in this study. Note that the resolutions indicate the worst resolutions in the domain.	81
6.1	Case setup for the spatially accelerating TBLs. The acceleration pa- rameter, K , is multiplied by 10^6 . Here, the lengths, L , are normalised with the maximum boundary layer thickness in the domain, showing that the height of the domain, $L_y \gtrsim 3$. The mesh resolutions represent their worst value in the domain with Δy_δ^+ , indicating the wall-normal mesh resolution at $y = \delta$	105
6.2	Maximum pressure gradient parameters from Narasimha and Sreeni- vasan [9] and Patel [22] for each case.	105
6.3	Limits of regions, where $\alpha = 0.07$, which ensures that $\overline{u'u'}$ and $\overline{v'v'}$ are on unambiguously increasing trajectories. The limits using the definitions from the moving wall acceleration are shown in brackets for cases 1 to 3.	119
7.1	Characteristics of channel flow cases at low Reynolds number to be compared with ZPGTBL from chapter 4.	147

7.2 Details of the temporally accelerating simulations. ΔT is the time from the start of the acceleration to where it has reached 90% of its final value. K is multiplied by 10^6 . Resolutions represent their worst values during the simulations. 152

Publications

Journal papers

1. M. Falcone and S. He. A spatially accelerating turbulent flow with longitudinally contracting walls. *Journal of Fluid Mechanics*, 945:A23, 8 2022
2. M Falcone and S. He. The evolution of turbulence in spatially accelerating turbulent boundary layers. *To be submitted*, 2024
3. M. Falcone and S. He. A comparison of spatially and temporally accelerating flows. *To be submitted*, 2024

Conferences

1. Matthew Falcone and Shuisheng He. A Spatially Accelerating Turbulent Flow with Longitudinally Moving Walls. In *Progress in Turbulence IX*, pages 109–114. Springer, 2021
2. A comparison of the development of spatially and temporally accelerating flows, UK Fluids Conference 2021, Southampton (Online), 8-10 September 2021.
3. Application of CHAPSim in the study of accelerating turbulent flows, UK Special Interest Group on Nuclear Thermal Hydraulics Annual Technical Meeting 2022, 27-28 June 2022.
4. Matthew A Falcone and Shuisheng He. A comparison of spatial and temporal acceleration in turbulent channel flows. *12th International Symposium on Turbulence and Shear Flow Phenomena (TSFP12)*, pages 1–6, 2022
5. The evolution of turbulence in spatially accelerating turbulent boundary layers, UK Fluids Conference 2022, Sheffield, 6-8 September 2022

6. Turbulence in spatially accelerating turbulent boundary layers, UK Turbulence Consortium annual meeting at Imperial College London 2023, 27-28 March 2023.
7. Using the recycling-rescaling method to investigate spatially accelerating turbulent boundary layers, Xcompact3D Showcase 2023, Imperial College London, 27-28 April 2023.
8. Turbulence in spatially accelerating turbulent boundary layers, iTi 2023 Conference on Turbulence, Bertinoro, Italy, 24-26 July 2023.
9. A comparison of spatially and temporally accelerating flows, European Turbulence Conference 2023, Valencia, Spain, 4-6 September 2023.

Chapter 1

Introduction

For subsonic flows, spatial acceleration occurs when the effective flow area is reduced, resulting in an increased flow velocity due to mass conservation and a favourable pressure gradient (FPG). These flows contain interesting phenomena that can be significantly different from those observed in canonical boundary layers. One of the most important phenomena is laminarisation*, which occurs in strong spatial accelerations, where key mean flow parameters, such as the skin friction coefficient and shape factor, shift towards values more typical of a laminar flow. This can have implications for many applications, including heat transfer, where the diffusive nature of turbulence is often beneficial. Laminarisation is observed in a range of engineering applications. Studies have reported that laminarisation can occur on the wings during important stages of flight. In-flight and wind tunnel measurements showed that substantial acceleration rates and laminarisation could be observed on the leading edge slats of modern passenger aircraft during landing, which can reduce the lift loss resulting from attachment line transition [29, 1, 30, 31]. A schematic of laminarisation on a leading edge slat in the presence of freestream disturbances is presented in figure 1.1 with a detailed description in the caption. Laminarisation can also occur at high angles of attack and on the leading edges of swept wings [32, 33]. Laminarisation has also been observed in turbomachinery, occurring on the pressure and suction sides of turbine blades, affecting their aerodynamic efficiency [34, 35, 36]. Laminarisation was noted to be detrimental to the effectiveness of the film cooling of turbine blades located after the gas turbine combustor [37]. Given the frequent occurrence of these flows in engineering applications, accurate prediction is essential but currently lacking [38].

While prevalent in many engineering applications, laminarisation in spatially accelerating flows remains not well-understood and requires further study. Of particular

*sometimes called relaminarisation or reverse transition, but in this study, laminarisation will be used when describing the overall process.

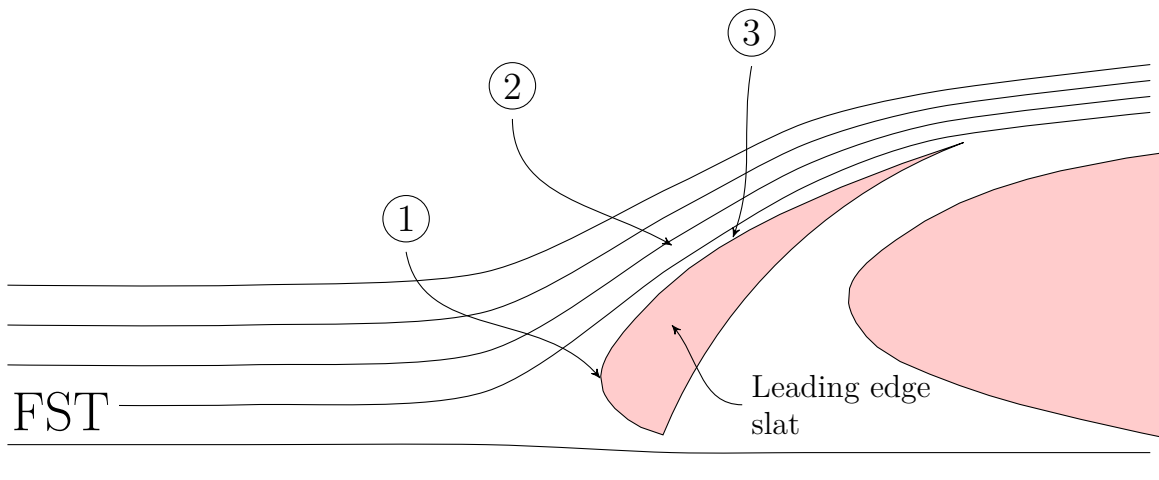


Figure 1.1: Schematic of laminarisation occurring on a leading edge slat during landing. (1) Freestream disturbances, which can originate from the TBL developing over the fuselage, induce the boundary layer developing over the wing to transition shortly after the attachment line. (2) During landing, the leading edge slat is deployed, leading to significant streamline contraction and strong streamwise acceleration with acceleration parameter, $K > 1 \times 10^{-5}$ [1]. (3) Acceleration induces the laminarisation of the transitioned boundary layer.

interest is the gradual emergence of laminarisation, the onset of which is not clearly defined by parametric criteria [39]. The processes that cause it also differ from those that cause laminarisation in buoyant flows or diverging pipes [40, 41]. Furthermore, improvements in the understanding of these complex flows can help provide further insight into the physics of non-equilibrium wall turbulence more generally.

Alongside spatial acceleration, flows can be accelerated temporally, which is typically achieved by merely increasing the flow rate, such as by opening a valve. Temporal accelerations are widely found in engineering applications and natural flows, such as during pump start-up and blood flowing around the body [42]. Temporally accelerating flows have been studied extensively in the Heat, Flow and Turbulence research group at the University of Sheffield, with substantial progress being made in understanding these flows. He and Seddighi [43] proposed that the flow and turbulence response to temporal acceleration is characterised by a process of transition resembling that which occurs in laminar-to-turbulent bypass transition. This process results from the development of a new time-developing boundary layer in response to the rapid increase in flow rate. Subsequent studies in the research group and beyond have observed this process over a range of acceleration rates, Reynolds numbers, and

acceleration profiles [44, 15, 12, 45]. Previous studies have long noted the overarching similarities between spatial and temporal acceleration, particularly the slow evolution of the Reynolds stresses in much of the early stages of both accelerations [46, 47]. Similar concepts have also been used to explain the turbulence response in both accelerations [48, 49]. There are also some important differences between these accelerations, such as the influence of flow contraction in spatial accelerations, which is not present in temporal accelerations.

The central premise of this study is to assess whether the recently developed understanding of temporally accelerating flows can help to explain the mechanisms underlying the response of turbulent flows to spatial acceleration, including processes such as laminarisation. We also note that despite the reported similarities between temporal and spatial accelerations, there have not yet been any direct detailed comparisons between spatial and temporal acceleration to understand the extent of the similarities. This thesis has four main elements:

1. The development and validation of numerical tools to investigate spatially accelerating turbulent boundary layers in an open-source numerical solver capable of investigating flows at Reynolds numbers larger than previous numerical studies and over a wide range of acceleration rates.
2. An investigation of a relative spatial acceleration incorporating accelerating moving walls. This element aims to understand whether a simplified spatial acceleration, where the influence of flow contraction is removed, can be characterised by a transition process similar to temporal acceleration.
3. A study of spatially accelerating turbulent boundary layers, including accelerations where the process of laminarisation occurs and those where it does not. The primary objective is to evaluate whether spatial accelerations involving flow contraction can be characterised by a transition process and gain insights into how the phenomena associated with laminarisation emerge as the acceleration rate increases. These simulations represent the widest range of acceleration rates in a single numerical study of laminarising spatial accelerating TBLs to date (to the author's knowledge).
4. A comparison of spatially accelerating turbulent boundary layers and temporally accelerating channel flows to assess the similarities and differences in the response of key mean flow parameters and turbulence, identifying the primary factors contributing to their differences.

As a result of this study, a new understanding of the overarching processes in spatially accelerating flows over a wide range of acceleration rates is developed based on the concepts from temporally accelerating flows.

1.1 Structure of the thesis

The structure of this thesis is given below:

- **Chapter 2:** This chapter gives an overview of the background turbulence theory that is used throughout the study focussing on wall-bounded turbulent flows.
- **Chapter 3:** Provides a literature review covering spatially accelerating flows, the bypass transition of laminar boundary layers, and temporally accelerating flows.
- **Chapter 4:** This chapter details the numerical methods used in the study. This chapter also details the implementation of the recycling-rescaling method for turbulent inflow generation into Incompact3D to enable simulations of accelerating TBLs. The validation of all numerical tools is also described here.
- **Chapter 5:** The results are presented of a relative spatial acceleration in which accelerating moving walls are used to create a spatial acceleration without wall-ward contraction.
- **Chapter 6:** Simulations of four spatially accelerating TBLs are presented, covering a wide range of acceleration rates.
- **Chapter 7:** Comparisons of the two strongest spatially accelerating turbulent boundary layers from chapter 6 are compared with temporally accelerating channel flow with matched acceleration parameter.
- **Chapter 8:** Overall conclusions are presented alongside some recommendations for future work.

Chapter 2

Background theory

Turbulence is a key feature in many engineering and natural flows, and its investigation dates back to Leonardo da Vinci's renowned illustrations in the 16th century. Turbulence is famous for its complexity and has been described as 'the last great unsolved problem of classical physics' [50]. The characteristics of turbulence include being random in time and space, having a large range of space and time scales, and being highly diffusive of momentum and scalars.

In this chapter, we introduce some of the key turbulence concepts used throughout this study including the governing equations (section 2.1), turbulence statistics (section 2.2), and the fundamentals of wall-bounded turbulent flows (section 2.4).

2.1 Governing equations

Fluid flow problems that satisfy the continuum hypothesis [51] can be described using the Navier-Stokes equations that describe the conservation of mass and momentum in a fluid. For incompressible, isothermal flows, these are the continuity and momentum equations, given in dimensional form by

$$\frac{\partial u_i^*}{\partial x_i^*} = 0, \quad (2.1a)$$

$$\frac{\partial u_i^*}{\partial t^*} + \frac{\partial u_i^* u_j^*}{\partial x_j^*} = -\frac{1}{\rho^*} \frac{\partial p^*}{\partial x_i^*} + \nu^* \frac{\partial^2 u_i^*}{\partial x_j^* \partial x_j^*}, \quad (2.1b)$$

where u_i^* represents the dimensional velocity vector, p^* is the modified pressure, and $\nu^* = \mu^*/\rho^*$ is the kinematic viscosity. Hereafter, unless otherwise stated, the superscript * indicates dimensional quantities. Being highly nonlinear, these equations pose well-known mathematical challenges and cannot generally be solved analytically. Nonetheless, these equations remain at the heart of almost all analyses of turbulent

flows. In this study, we will exclusively consider equation (2.1) in non-dimensional form by normalising the state variables, (u_i^*, p^*) . The non-dimensional variables are given by

$$u_i = \frac{u_i^*}{\mathcal{U}^*} \quad x_i = \frac{x_i^*}{\mathcal{L}^*} \quad t = \frac{t^* \mathcal{U}^*}{\mathcal{L}^*} \quad p = \frac{p^*}{\rho^* \mathcal{U}^{*2}} \quad (2.2)$$

where \mathcal{U}^* and \mathcal{L}^* are characteristic reference velocity and length scales. Substituting these into equation (2.1) yields

$$\frac{\partial u_i}{\partial x_i} = 0, \quad (2.3a)$$

$$\frac{\partial u_i}{\partial t} + \frac{\partial u_i u_j}{\partial x_j} = -\frac{\partial p}{\partial x_i} + \frac{1}{Re} \frac{\partial^2 u_i}{\partial x_j \partial x_j}. \quad (2.3b)$$

In non-dimensional form, the Navier-Stokes equations are dependent on a single parameter, the Reynolds number Re . The values of \mathcal{U}^* and \mathcal{L}^* depend on the flow and the physics being investigated.

2.2 Statistical description of turbulence

Due to the chaotic nature of turbulence, the velocity signal is not predictable as two flows with very slight differences in initial conditions will lead, after a short time, to flows that appear substantially different. Nonetheless, its statistical properties are reproducible [?]. The mean of a random variable, ϕ is given by

$$\bar{\phi} = \int_{-\infty}^{\infty} \phi f(\phi) d\phi, \quad (2.4)$$

where f is the probability density function (PDF) in which the probability, P of ϕ being between the values a and b , where $a \leq b$ is

$$P\{a \leq \phi \leq b\} = \int_a^b f(\phi) d\phi. \quad (2.5)$$

In this study, $(\bar{\quad})$ will usually be used to indicate averaging, although sometimes $\langle \quad \rangle$ will be used for clarity. If the PDF of the state variables do not vary in time, the flow is statistically stationary. If it does not vary in a particular direction, the flow is statistically homogeneous in that direction.

One of the most important statistical properties of turbulent flows is that they have been found (but not proved) to be ergodic in time and space, meaning that

if a flow is statistically stationary, the ensemble average over many realisations is equivalent to the time average

$$\bar{\phi} = \lim_{N \rightarrow \infty} \frac{1}{N} \sum_N \phi_n = \lim_{T \rightarrow \infty} \frac{1}{T} \int_0^T \phi(\tau) d\tau, \quad (2.6)$$

when T is sufficiently large. If a flow is statistically homogeneous in a given direction, then the ensemble average over many realisations is equivalent to the spatial average in that direction:

$$\bar{\phi} = \lim_{N \rightarrow \infty} \frac{1}{N} \sum_N \phi_n = \lim_{L \rightarrow \infty} \frac{1}{L} \int_0^L \phi(x) dx, \quad (2.7)$$

when L is sufficiently large. This makes the computation of statistics far simpler. Fluctuations in the state variables are given by $\phi' = \phi - \bar{\phi}$, from which the m^{th} central moments can be defined,

$$\overline{\phi'^m} = \lim_{N \rightarrow \infty} \frac{1}{N} \sum_N \phi_n'^m. \quad (2.8)$$

Statistics of particular relevance in this study are the velocity variance, $\overline{u_i'^2}$, the root mean square (RMS) of the velocity fluctuations, $u_{i,rms}' = \sqrt{\overline{u_i'^2}}$, the skewness, $\overline{u_i'^3} / (\overline{u_i'^2})^{3/2}$, and the kurtosis, $\overline{u_i'^4} / (\overline{u_i'^2})^2$.

2.2.1 Reynolds-averaged Navier-Stokes equations

The statistical approach above can be combined with the Navier-Stokes equations to derive transport equations for statistical quantities. The transport equations for the mean velocity are derived by applying the Reynolds decomposition, $\phi = \bar{\phi} + \phi'$ to the state variables and averaging leads to the Reynolds-averaged Navier-Stokes (RANS) equations

$$\frac{\partial \bar{u}_i}{\partial x_i} = 0, \quad (2.9a)$$

$$\frac{\partial \bar{u}_i}{\partial t} + \frac{\partial \bar{u}_i \bar{u}_j}{\partial x_j} = -\frac{\partial \bar{p}}{\partial x_i} + \frac{\partial}{\partial x_j} \left[\frac{1}{Re} \frac{\partial \bar{u}_i}{\partial x_j} - \overline{u_i' u_j'} \right]. \quad (2.9b)$$

In appearance, the RANS equations are the same as equation (2.1), except for the Reynolds stress tensor (blue), which is an apparent stress arising from turbulent fluctuations and represents the additional mean momentum transport by turbulence. The diagonal terms, $\overline{u_i' u_i'}$ are called the normal Reynolds stresses, and the off-diagonal terms are the Reynolds shear stresses. The normal stresses are also the velocity variance and the turbulence energy per unit mass in each direction.

2.2.2 Reynolds stress transport equations

The Reynolds stresses can be further analysed using the Reynolds stress transport equation, the evolution equation for the Reynolds stress tensor. These are given by

$$\frac{\partial \overline{u'_i u'_j}}{\partial t} = \mathcal{A}_{ij} + \mathcal{P}_{ij} + \mathcal{T}_{ij} + \Pi_{ij}^d + \Pi_{ij}^s + \mathcal{D}_{ij} - \epsilon_{ij}. \quad (2.10)$$

The terms on the right-hand side (RHS) are from left to right: advection, production, turbulent diffusion, pressure diffusion, pressure strain, viscous diffusion, and dissipation. Their definitions are given below:

$$\begin{aligned} \mathcal{A}_{ij} &= -\bar{u}_k \frac{\partial \overline{u'_i u'_j}}{\partial x_k} & \Pi_{ij}^s &= \left\langle p' \left(\frac{\partial u'_i}{\partial x_j} + \frac{\partial u'_j}{\partial x_i} \right) \right\rangle \\ \mathcal{P}_{ij} &= -\overline{u'_i u'_k} \frac{\partial \bar{u}_j}{\partial x_k} - \overline{u'_j u'_k} \frac{\partial \bar{u}_i}{\partial x_k} & \mathcal{D}_{ij} &= \frac{1}{Re} \frac{\partial \overline{u'_i u'_j}}{\partial x_k \partial x_k} \\ \mathcal{T}_{ij} &= -\frac{\partial \overline{u'_i u'_j u'_k}}{\partial x_k} & -\epsilon_{ij} &= -\frac{2}{Re} \left\langle \frac{\partial u'_i}{\partial x_k} \frac{\partial u'_j}{\partial x_k} \right\rangle \\ \Pi_{ij}^d &= -\frac{\partial \overline{u'_i p'}}{\partial x_j} - \frac{\partial \overline{u'_j p'}}{\partial x_i} \end{aligned} \quad (2.11)$$

Of particular importance are the production term, \mathcal{P}_{ij} , which represents the energy being extracted from the mean flow; the pressure strain term Π_{ij}^s , which is traceless and hence represents the intercomponent energy transfer between the normal stresses; and the dissipation, ϵ , which represents the action of viscosity to destroy the Reynolds stresses and dissipate them as heat.

2.2.3 Two-point correlations and spectra

The structure of turbulence in space can be investigated using two-point statistics. The two-point correlation tensor is given by

$$\tilde{R}_{ij}(\mathbf{x}^{(1)}, \mathbf{x}^{(2)}; t) = \langle u'_i(\mathbf{x}^{(1)}; t) u'_j(\mathbf{x}^{(2)}; t) \rangle. \quad (2.12)$$

For homogeneous directions, the two-point correlation is independent of the starting location and is just a function of separation, \mathbf{r}

$$\tilde{R}_{ij}(\mathbf{r}; t) = \langle u'_i(\mathbf{x}; t) u'_j(\mathbf{x} + \mathbf{r}; t) \rangle \quad (2.13)$$

The two-point correlation is often normalised by its value at $r = 0$, where $\tilde{R}_{ij}(\mathbf{0}; t) = \langle u'_i u'_j \rangle$

$$R_{ij}(\mathbf{x}, \mathbf{r}; t) = \frac{\tilde{R}_{ij}}{\langle u'_i u'_j \rangle}, \quad (2.14)$$

The scale-by-scale energy distribution, the velocity spectra can be used, defined as

$$\Phi_{ij}(k) = \langle \widehat{u}_i^* \widehat{u}_j \rangle, \quad (2.15)$$

where $(\widehat{})$ indicates the Fourier transform, and $(^*)$ is the complex conjugate, and k is the wavenumber. $\Phi_{uu}(k)$ can be related to the Reynolds stresses through

$$\overline{u'_i u'_j} = \int_{-\infty}^{\infty} \Phi_{ij}(k) dk. \quad (2.16)$$

For homogeneous directions, the two-point correlation can be related to the velocity spectrum by taking the inverse Fourier transform

$$R_{ij} = \int_{-\infty}^{\infty} \Phi_{ij}(k) e^{ikx} dk. \quad (2.17)$$

Equation (2.17) enables the efficient computation of the two-point correlations in homogeneous directions by first computing $\Phi_{ij}(k)$ and then applying the inverse transform. In this study, all autocorrelations in homogenous directions are computed in this manner.

2.3 Vorticity and vortex identification

A feature of turbulent flows is that they are inherently rotational, meaning they have non-zero vorticity, ω_i , which for a flow with coordinates (x, y, z) , and velocity field (u, v, w) is defined as

$$\omega_x = \frac{\partial w}{\partial y} - \frac{\partial v}{\partial z} \quad \omega_y = \frac{\partial u}{\partial z} - \frac{\partial w}{\partial x} \quad \omega_z = \frac{\partial v}{\partial x} - \frac{\partial u}{\partial y} \quad (2.18)$$

Turbulent flows are frequently considered from the perspective of coherent structures, which Panton [52] defined simply as fluid motion that has coherence over a spatial region and lasts for a reasonable period of time. Vortices represent one form of coherent structures, which Robinson [53] roughly defined as a region where the streamlines mapped onto a plane normal to the vortex core exhibit an approximately circular pattern when viewed from a reference frame moving with the vortex core.

Several identification criteria for vortex cores have been developed to understand the evolution of vortical structures in turbulent flows. This study uses the λ_2 criterion developed by Jeong and Hussain [54]. This method originates from a prior criterion that identified vortex cores with the local minimum of pressure in a plane normal to the vortex axis, which can be identified by regions where the pressure Hessian, $H(p) =$

$\partial_{ij}p^*$, has two positive eigenvalues. Jeong and Hussain [54] noted that vortex cores tend to deviate from the local pressure minimum in the case of unsteady straining, which leads to a pressure minimum without vortical motion, and viscous effects, which can eliminate the pressure minimum associated with vortical motion. The contributions to the pressure Hessian can be considered by taking the gradient of the momentum equation and considering its symmetric part,

$$\frac{DS_{ij}}{Dt} - \frac{1}{Re} \frac{\partial^2 S_{ij}}{\partial_k \partial_k} + S_{ik}S_{kj} + \Omega_{ik}\Omega_{kj} = -H(p), \quad (2.19)$$

where $S_{ij} = (\partial_j u_i + \partial_i u_j)/2$ is the strain rate tensor and $\Omega_{ij} = (\partial_j u_i - \partial_i u_j)/2$ is the rotation rate tensor. The influence of unsteady stretching and viscosity can consequently be removed by considering just the matrix, $S_{ik}S_{kj} + \Omega_{ik}\Omega_{kj}$, with $H(p)$ having two positive eigenvalues when $S_{ik}S_{kj} + \Omega_{ik}\Omega_{kj}$ has two negative eigenvalues: where its second largest eigenvalue, $\lambda_2 < 0$. Other criteria, such as the Q criterion [55] and swirling strength criterion [56], were also considered but did not lead to visibly different results.

2.4 Wall-bounded turbulent flows

This study focuses on wall-bounded turbulent flows: turbulent channel flow and turbulent boundary layers (TBLs). A schematic of these flows is shown in figure 2.1. We take the convention that the streamwise, wall-normal, and spanwise directions are given by (x^*, y^*, z^*) , and velocities by (u^*, v^*, w^*) . In wall-bounded flows, the mean velocity and turbulence intensity are concentrated in the streamwise component, and the flow develops much more rapidly in the wall-normal direction, such that typically $\partial_y \gg \partial_x$.

Channel flows are flows that exist between two parallel flat plates, which are separated by a distance of $2h^*$, where h^* is the half-channel height. The most commonly studied channel flow is the fully developed channel flow, which is homogeneous in both the streamwise and spanwise directions. The flow rate of the channel is maintained by a pressure gradient. This flow represents the start and end conditions of the accelerating channel flows in chapters 5 and 7. TBLs are bounded by a single flat plate and extend infinitely (in principle) in the wall-normal direction. These flows are inherently inhomogeneous in the streamwise direction with a (dimensional) boundary layer

*Hereafter, for compactness, when first derivatives are used inline $\partial_x f$ refers to $\frac{\partial f}{\partial x}$ and $\partial_i f = \frac{\partial f}{\partial x_i}$. For second derivatives, $\partial_{xx} f$ refers to $\frac{\partial^2 f}{\partial x \partial x}$ and $\partial_{ij} f$ refers to $\frac{\partial^2 f}{\partial x_i \partial x_j}$.

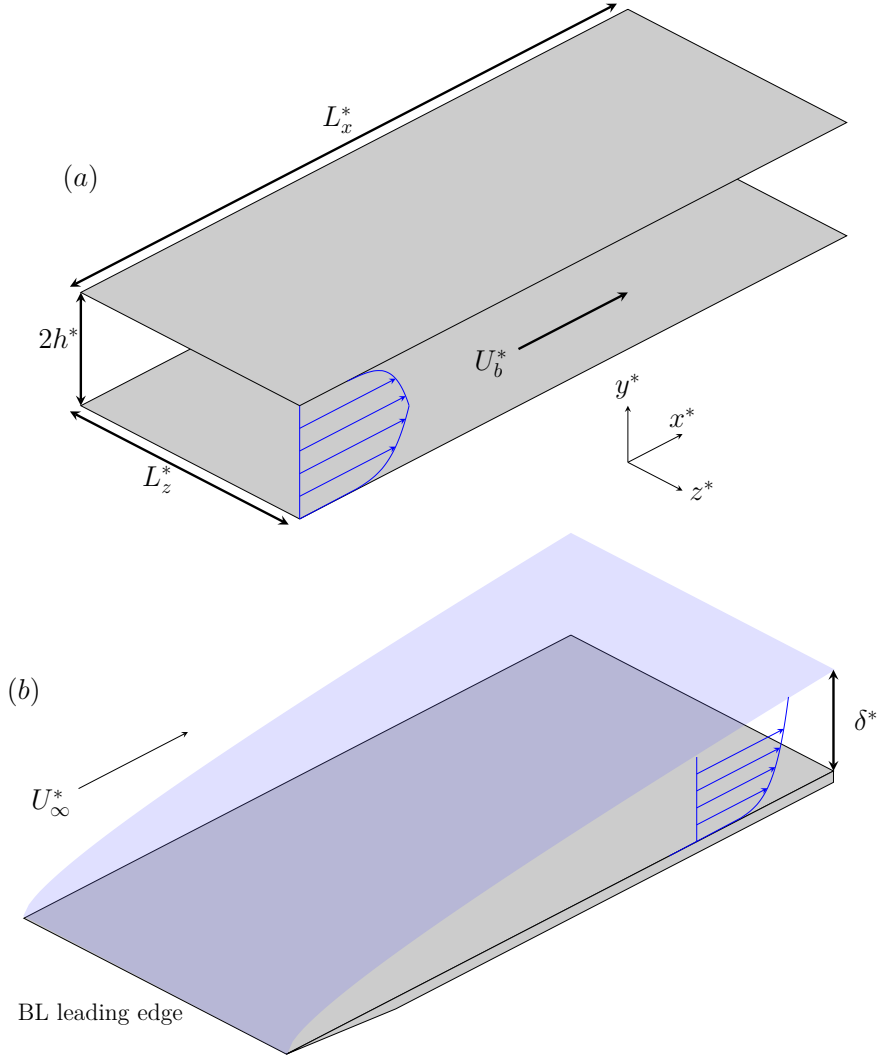


Figure 2.1: Schematics of a turbulent channel flow (a) and a turbulent boundary layer (b).

thickness, δ^* that grows downstream (as depicted in figure 2.1(b)), with a freestream velocity, U_∞^* , above the boundary layer. In this study, the boundary layer thickness is determined using the 99% thickness, δ_{99}^* , the wall-normal distance where the mean velocity reaches 99% of the freestream velocity. Unlike channels, non-accelerating TBLs have zero pressure gradient (ZPG) while spatially accelerating flows have a favourable pressure gradient (FPG) $\partial_x \bar{p} < 0$.

We now introduce important quantities that are used throughout the study. A useful quantity in all wall-bounded flows is the wall-shear stress, τ_w^* , which is defined as

$$\tau_w^* = \mu \left. \frac{\partial \bar{u}^*}{\partial y^*} \right|_{y^*=0} \Rightarrow \tau_w = \frac{1}{Re} \left. \frac{\partial \bar{u}}{\partial y} \right|_{y=0}, \quad (2.20)$$

representing the mean stress imparted by the flow on the wall. It is often normalised using the dynamic pressure, resulting in the skin friction coefficient

$$C_f = \frac{2\tau_w^*}{\rho^* \mathcal{U}^{*2}}. \quad (2.21)$$

In channel flows, \mathcal{U}^* is usually the cross-section $z - y$ average (or bulk) velocity, U_b^* , although in chapter 7 we use the centreline velocity, U_c^* . In TBLs, the freestream velocity U_∞^* is used. τ_w^* can be used to define the viscous scales or the wall units: the friction velocity, u_τ^* and the viscous length scale δ_v^*

$$u_\tau^* = \sqrt{\frac{\tau_w^*}{\rho^*}} \quad \delta_v^* = \frac{\nu}{u_\tau^*}. \quad (2.22)$$

Normalising flow variables using the viscous scales (or inner scaling) is indicated using $^+$, such that the inner-scaled mean velocity is $\bar{u}^+ = \bar{u}/u_\tau^*$ and the inner-scaled wall-normal distance is $y^+ = y/\delta_v^*$. Other important lengthscales are the integral thicknesses: the displacement thickness, δ_u^* and momentum thickness, θ^* . In boundary layers, these are given by

$$\delta_u^* = \int_0^{\delta^*} \left(1 - \frac{\bar{u}^*}{U_\infty^*}\right) dy^* \quad \theta^* = \int_0^{\delta^*} \frac{\bar{u}^*}{U_\infty^*} \left(1 - \frac{\bar{u}^*}{U_\infty^*}\right) dy^*. \quad (2.23)$$

For channel flow, the upper limit of integration is h^* , and U_c^* is used rather than U_∞^* . The ratio of these thicknesses is called the shape factor, $H = \delta_u/\theta$, and is useful in accelerating flows as it has different values in laminar and turbulent flows and consequently has been used to assess the degree of laminarisation. These velocity and length scales can be used to define Reynolds numbers that are commonly used in channels and boundary layers. The Reynolds numbers used for channel flows in this study are the bulk Reynolds number, Re_b ; the centreline velocity Reynolds number Re_c ; and the friction Reynolds number, Re_τ , which represents the ratio of the largest to the smallest scales:

$$Re_b = \frac{U_b^* h^*}{\nu^*} \quad Re_c = \frac{U_c^* h^*}{\nu^*} \quad Re_\tau = \frac{u_\tau^* h^*}{\nu^*} = \frac{h^*}{\delta_v^*} \quad (2.24)$$

In TBLs, some important examples are the momentum thickness Reynolds number, boundary layer thickness Reynolds number, and the friction Reynolds number

$$Re_\theta = \frac{U_\infty^* \theta^*}{\nu^*} \quad Re_\delta = \frac{U_\infty^* \delta^*}{\nu^*} \quad Re_\tau = \frac{u_\tau^* \delta^*}{\nu^*} = \frac{\delta^*}{\delta_v^*} \quad (2.25)$$

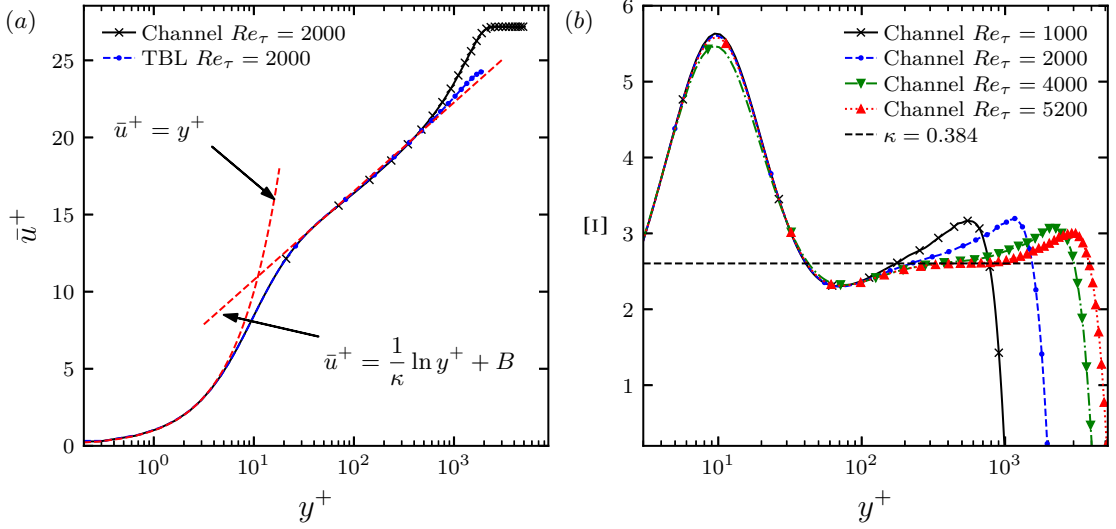


Figure 2.2: The inner-scaled mean velocity profile of turbulent wall-bounded flows. (a) shows \bar{u}^+ vs y^+ for turbulent channel flow [2] and TBLs [3] at $Re_\tau = 2000$ $\bar{u}^+ = y^+$ and the logarithmic law, where $\kappa = 0.4$ and $B = 5$, are indicated.. (b) shows the diagnostic function, Ξ for channels flows up to $Re_\tau = 5200$ [4, 5].

2.4.1 Mean velocity profile

The inner-scaled mean velocity profile in ZPGTBL and channel flows is presented in figure 2.2(a) for $Re_\tau = 2000$ [2, 3] and shows that both flows have a similar general form. Dimensional analysis has shown that the mean velocity profile depends on two length scales: $\eta = y/\delta$ and y^+ . In the inner region ($\eta \ll 1$), the mean velocity becomes independent of δ and depends only on the viscous scales leading to the law of the wall

$$\bar{u}^+ = F_1(y^+). \quad (2.26)$$

In the outer region ($y^+ \gg 0$), the mean velocity profile depends only on the outer scale, resulting in the velocity defect law

$$\frac{U_0 - \bar{u}}{u_\tau} = F_2(\eta), \quad (2.27)$$

where U_0 is either U_∞ or U_c depend on flow configuration. At asymptotically high Reynolds number ($Re_\tau \rightarrow \infty$), there is an ‘overlap’ region where ($\eta \ll 1$) and ($y^+ \gg 0$) and both laws should overlap smoothly. Millikan [57] showed that this leads to the logarithmic law of the wall:

$$\bar{u}^+ = \frac{1}{\kappa} \ln(y^+) + B, \quad (2.28)$$

Table 2.1: Regions of the mean velocity profile

Region	Location
Viscous sublayer	$y^+ \leq 5$
Buffer layer	$5 < y^+ \leq 30$
Logarithmic region	$y^+ > 30, y/\delta \lesssim 0.15$
Velocity defect region	$y/\delta \gtrsim 0.15$

where κ and B are the von Kármán and additive constants, respectively. The value of the κ is usually determined using the diagnostic function, Ξ defined as

$$\Xi = y^+ \frac{d\bar{u}^+}{dy^+}. \quad (2.29)$$

with Ξ a constant, $1/\kappa$ in the logarithmic region and hence κ can be extracted from mean flow data with B curve-fitted to this region. Panton [58] noted that high Reynolds numbers are required to observe a well-developed logarithmic region, with figure 2.2(b) showing that for channel flows, an extended region with approximately constant Ξ is only observed for $Re_\tau = 5200$. At lower Reynolds numbers, Ξ exhibits a roughly linear trend, which is consistent with the finite Reynolds number refinements of the overlap Region discussed in Jiménez and Moser [59] and Bernardini et al. [5]. The mean velocity in this region may still appear approximately logarithmic even at lower Reynolds numbers, with figure 2.2(a) showing that \bar{u}^+ approximately follows the logarithmic law for $30 < y^+ < 400$. Historically, κ and B have been regarded as universal, although it has now been shown that they take slightly different values in channels and ZPGTBLs [60].

Empirically, the mean velocity profile is usually further subdivided as indicated in table 2.1. Other notable regions include the viscous sublayer where $\bar{u}^+ = y^+$ (also indicated in figure 2.2(a)) and the buffer layer which lies between the viscous sublayer and the logarithmic layer. The buffer layer is associated with the maximum in the turbulence kinetic energy (TKE), $k = \frac{1}{2}\overline{u'_i u'_i}$ and TKE production, $\mathcal{P} = \frac{1}{2}\mathcal{P}_{ii}$. The structures and dynamics of this region are briefly reviewed in section 2.4.3. The inner part of channels and TBLs ($y/\delta < 0.1$) is usually regarded as being essentially the same [61].

The mean velocity profile deviates from the logarithmic law in the outer part of flows. This deviation is much larger in TBLs than in channels. The velocity defect in TBLs is usually described through the additional law of the wake [62], leading to a velocity profile of the form

$$\bar{u}^+ = \frac{1}{\kappa} \ln(y^+) + B + \frac{\Pi}{\kappa} w(y/\delta), \quad (2.30)$$

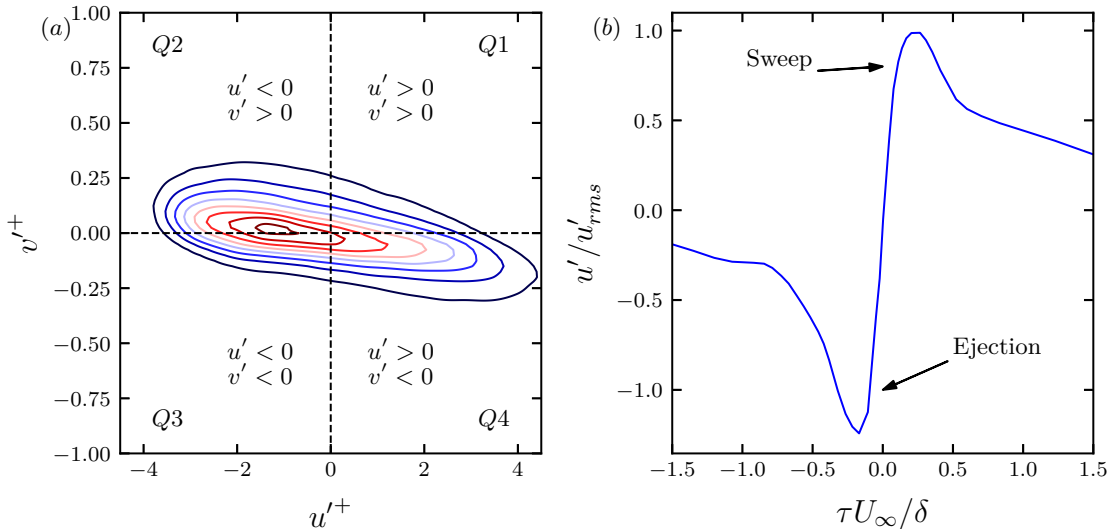


Figure 2.3: Quadrant analysis. (a) joint PDF of u' and v' of a channel flow at $Re_\tau = 180$ at $y^+ = 9$ with quadrant events labelled. The contours are at 0.08(0.08)0.64. (b) burst pattern of a TBL at $y^+ = 15$ showing ejection and sweep events reproduced from Blackwelder and Kaplan [6].

where w is the assumed universal ‘wake’ function and Π is the wake strength parameter [61].

2.4.2 Quadrant analysis, ejection and sweep events

In wall-bounded turbulent flows, the most dynamically significant Reynolds stress is the Reynolds shear stress, $\overline{u'v'}$, which is the dominant component in the turbulent transport term in the mean momentum equation, $-\partial_y \overline{u'v'}$ and for the TKE production, $\mathcal{P} \approx -\overline{u'v'} \partial_y \bar{u}$. Events that contribute to positive \mathcal{P} in a shear flow have $u'v' < 0$ and events, which lead to negative \mathcal{P} have $u'v' > 0$. These events are frequently analysed using quadrant analysis which categorises events based on the sign of u' and v' . A joint probability density function of u' and v' in a channel flow at $Re_\tau = 180$ is presented in figure 2.3(a) with the quadrants, $Q1$ to $Q4$ and their definitions labelled. The events that contribute to positive \mathcal{P} and shear stress are $Q2$ and $Q4$ events, and those that contribute to negative \mathcal{P} and shear stress are $Q1$ and $Q3$ events. Figure 2.3(a) shows that $Q2$ and $Q4$ events tend to dominate the joint PDF.

Among the most dynamically significant events are ejections and sweeps, which often occur in pairs. Ejections are the result of low-speed fluid ($u' < 0$) being ejected ($v' > 0$) from the near-wall region, with sweeps resulting from high-speed fluid ($u' >$

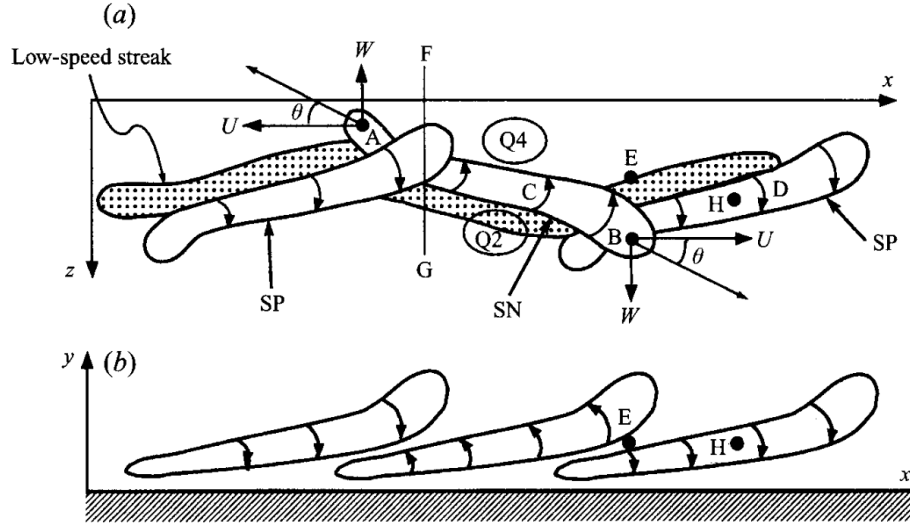


Figure 2.4: Schematic of the layout of a meandering streamwise streak and staggered opposing quasi-streamwise vortices (QSV) from Jeong et al. [7]. (a) top-down view, (b) sideways view. SN and SP indicates QSVs with negative and positive ω'_x , respectively.

0) further from wall rushing wall-wards ($v' < 0$) to replace the ejected fluid [61]. Consequently, these motions contribute to $Q2$ and $Q4$ events, respectively. These bursting events have been analysed using the variable-interval time-averaging (VITA) technique, where a signal, such as velocity, from a stationary probe is conditionally averaged around a burst. A typical burst signal from Blackwelder and Kaplan [6] is shown in figure 2.3(b), where $u' < 0$ corresponds to the ejection part of the burst, with the sweep part occurring where $u' > 0$. A review of quadrant analysis can be found in Wallace [63].

2.4.3 Near-wall turbulence structures and turbulence regeneration cycle

In this study, we are most concerned with the dynamics of the near-wall region, which, as stated previously, is associated with maximum turbulence intensity and production. Even at very high Reynolds numbers where its height is a tiny fraction of the flow thickness, it contributes to a large proportion of total energy dissipation [64]. The presence of coherent structures in the near-wall region of turbulent flows was first observed in Kline et al. [65], where elongated streaky structures were observed close to the wall. These streaks have alternating high-low streamwise velocity with lengths of approximately 1000 wall units and widths of approximately 80 wall units [66]. Blackwelder and Eckelmann [67] indicated that pairs of counter-rotating streamwise

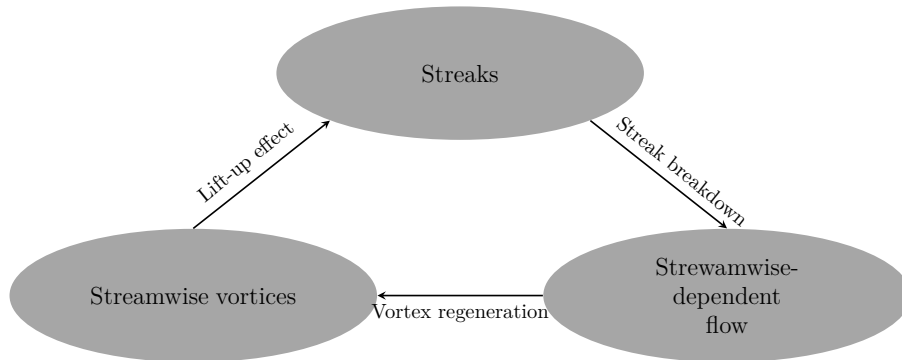


Figure 2.5: Classical regeneration cycle, reproduced from Kim [8].

vortices frequently occur in the near-wall region of turbulent flows, with Jeong et al. [7] finding that quasi-streamwise vortices of opposing vorticity were typically observed in a staggered arrangement on the flanks of low-speed streaks. This arrangement can be observed in figure 2.4. Robinson [53] highlighted that these quasi-streamwise vortices were strongly associated with ejection and sweep events and highlighted that these quasi-streamwise vortices are long-lived in the buffer layer.

The interactions between the streaks and quasi-streamwise and their role in the sustenance of near-wall turbulence have been investigated extensively in recent decades, with the overall process referred to as the turbulence regeneration cycle. Waleffe [68] noted that this cycle is conjectured to be generic for wall-bounded shear flows. Waleffe [68] also emphasised how the streaks and vortices depend on each other for their regeneration and sustenance against viscous decay. The cycle is often summarised as a three-leg process, which is depicted in figure 2.5

In the first leg, the streaks are created via the lift-up effect, where quasi-streamwise vortices lift low-speed fluid from close to the wall and push down high-speed fluid further from the wall. The tendency of shear flows to generate long streamwise disturbances is frequently understood using transient growth theory, which originated from Ellingsen and Palm [69] and Landahl [70], who studied inviscid shear flows with cross-stream disturbances, finding that streamwise disturbance energy grows at least linearly in time. The extension of these concepts to viscous flows has focussed on the non-normality of the Orr-Sommerfeld/Squires equations [71], the system of equations that describes the linear evolution of perturbations in parallel flows. This non-normality leads to certain ‘dangerous’ initial conditions growing substantially for a short duration even if all the modes decay [72]. Butler and Farrell [73] found that the initial perturbations that lead to the largest transient growth corresponded with quasi-streamwise vortices, with the resulting disturbances consistent with long

streamwise streaks, a process that is consistent with the lift-up effect. Pujals et al. [74] and del Álamo and Jiménez [75] found that the spanwise scale of the optimal streaks was consistent with experimental and numerical observations of streaks in the buffer and outer layers.

The second and third legs of the cycle link how the streaks, generated by the lift-up effect, result in the regeneration of the streamwise vortices and the restart of the cycle. The breakdown of the streaks has often been associated with the sinuous (spanwise anti-symmetric) instability of low-speed streaks with both normal mode and transient growth mechanism being proposed [76, 77]. Understanding these processes is still an area of active research, with recent work even casting doubt on the role of long streaks in sustaining near-wall turbulence [78]. The near-wall turbulence regeneration cycle is autonomous in the sense that it can be maintained without input from the outer flow and can be maintained even if all fluctuations above $y^+ \gtrsim 60$ or structures wider than 100 wall units are damped [79, 80]. Review of the turbulence regeneration cycle can be found in Kim [8] and Panton [52].

Chapter 3

Literature Review

3.1 Spatially accelerating flows

Spatially accelerating flows have been widely studied for more than six decades, with the first observations of laminarisation occurring even earlier [81, 82]. Figure 3.1 shows a schematic of a typical spatial acceleration experiment, where the flow area is reduced using a liner placed onto the wall of a wind tunnel, with measurements taken of the boundary layer developing on the opposing flat wall. Many of the themes and terminology regarding spatially accelerating flows were established in the 1960s and 1970s. Launder [83, 84, 85] was the first to study laminarisation specifically and introduced the acceleration parameter

$$K = \frac{\nu^*}{U_\infty^{*2}} \frac{dU_\infty^*}{dx^*}, \quad (3.1)$$

to characterise the rate of acceleration imposed on the boundary layer. Investigating the flow in a two-dimensional nozzle, Launder found that after initially following

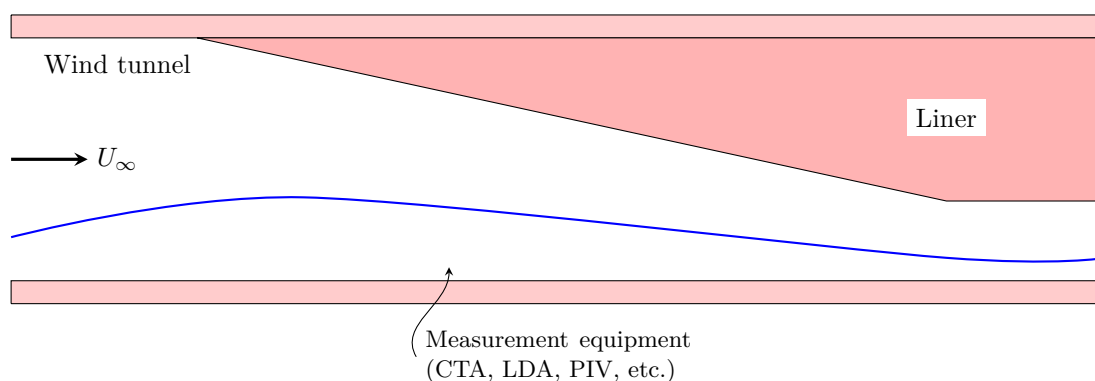


Figure 3.1: Schematic of a typical wind tunnel experiment for a spatially accelerating flow, where a liner has been used to create the reduction of flow area.

turbulent predictions, when $K \gtrsim 3.5 \times 10^{-6}$, significant changes to the mean velocity profile were observed with the skin friction coefficient, C_f decreasing, and shape factor, H increasing. By the end of the nozzle, these parameters approach values consistent with laminar boundary layers. Schraub and Kline [86] surmised that at low acceleration rates, $K < 10^{-6}$, the mean velocity profile was little impacted by the acceleration, while where $10^{-6} < K < 3.5 \times 10^{-6}$, the flow was considered ‘laminarescent’, with the flow affected by the acceleration but not yet exhibiting clear signs of reverting to the laminar state. Other parametric criteria have been developed for the onset of laminarisation, such as the pressure gradient parameter, $\Delta_p = (\nu^*/\rho^*u_\tau^{*3})d_x p^* < -0.02$ introduced by Patel [22] and Schraub and Kline [86]. It should be highlighted that laminarisation is a gradual process with few clear physical onset markers, which, as Sreenivasan [39] noted, meant that parametric criteria can only be considered approximate markers for laminarisation onset. Furthermore, in strong accelerations, K often increases substantially over short streamwise distances, meaning that determining the critical values of parameters such as K or Δ_p can be challenging. For the critical acceleration parameter, K_{crit} , values in the range of 2.8×10^{-6} to 3.5×10^{-6} have been reported with 3×10^{-6} , the most widely accepted value [87].

The early studies also noted changes in near-wall turbulence structures due to the laminarisation process. The seminal work of Kline et al. [65] investigated turbulent boundary layers with adverse, zero, and favourable pressure gradients and found that in strong favourable pressure gradients, the inner-scaled bursting frequency near the wall was found to reduce for $K > 10^{-6}$ with a cessation of bursting observed when $K > 3.5 \times 10^{-6}$. Retransition, where the laminarised boundary layer becomes turbulent again, was found to occur once the acceleration had relaxed with ($K < 10^{-6}$) [86]. Early studies assumed this process was similar to natural transition [85].

Many of the studies of spatial acceleration, including the present one, are not in equilibrium and develop spatially. However, equilibrium sink flows are an important category of spatially accelerating flows that have been studied extensively. Sink flows develop between two converging planes in which the streamlines converge to a point (the sink). Many of the studies discussing weaker spatial accelerations belong to this category and are therefore important for understanding how the phenomena associated with laminarisation emerge. If set up appropriately, sink flows can become self-preserving, and complete similarity can be attained, representing the only class of turbulent flow with varying freestream velocity where this is possible [39]. In these flows, parameters such as K , C_f , H , and Re all become constant, with the mean velocity profile and Reynolds stresses exhibiting similarity at downstream stations

in inner and outer scaling (among others). At small values of K , turbulent sink flows develop with little change to the logarithmic law parameters, albeit with the near-complete absence of the wake [88]. At larger values of K , a departure from the logarithmic law is observed with a progressive shift towards the laminar Falkner-Skan solution for sink flows [89, 90, 91].

The cornerstone of the present understanding of spatial acceleration is Narasimha and Sreenivasan [9]. Its key development was the introduction of a quasi-laminar model, which was used to make accurate predictions of the flow in the region of strong acceleration. This quasi-laminar model was a two-layer formulation in which the inner layer was modelled as laminar, and the outer layer was considered inviscid and rotational. This model accurately predicted mean flow behaviours in the region with strong favourable pressure gradients. While this model was successful in the region of strong acceleration, there was a small region between the region of strong acceleration and the upstream zero-pressure gradient region, in which neither the quasi-laminar model nor turbulent predictions were valid. Sreenivasan [39] later described this region as the ‘island of ignorance’. The model’s success in the strong acceleration region was not related to the absolute decrease of the turbulent stresses, which tended to approximately freeze along streamlines, but due to their relative domination by the significant increases in pressure gradient in strong spatial acceleration. In a sense, the turbulent stresses were rendered negligible, so they did not contribute to the mean flow dynamics. The process was subsequently referred to as a ‘soft’ laminarisation or a quasi-laminarisation in contrast to the ‘hard’ laminarisation processes that occur in buoyant flows or diverging pipes [41, 40]. The study suggested a pressure gradient parameter to mark where the turbulence stresses should be rendered negligible

$$\Lambda = -\frac{\delta^*}{\tau_{w0}^*} \frac{dp^*}{dx^*} \gtrsim 50, \quad (3.2)$$

which represents the approximate ratio of the pressure gradient to the turbulent stresses. The quasi-laminar model also led to laminarisation being characterised into four stages which will be used herein: fully turbulent (I), where after the onset of the acceleration, the flow retains its turbulent characteristics; reverse transition (II), where the flow becomes increasingly laminar-like, but neither turbulent nor quasi-laminar predictions are valid; quasi-laminar (III), where the flow statistics follow the quasi laminar model; and retransition (IV), where the flow begins to return to the turbulent state. A schematic of these stages is shown in figure 3.2, based on a figure in Narasimha and Sreenivasan [9].

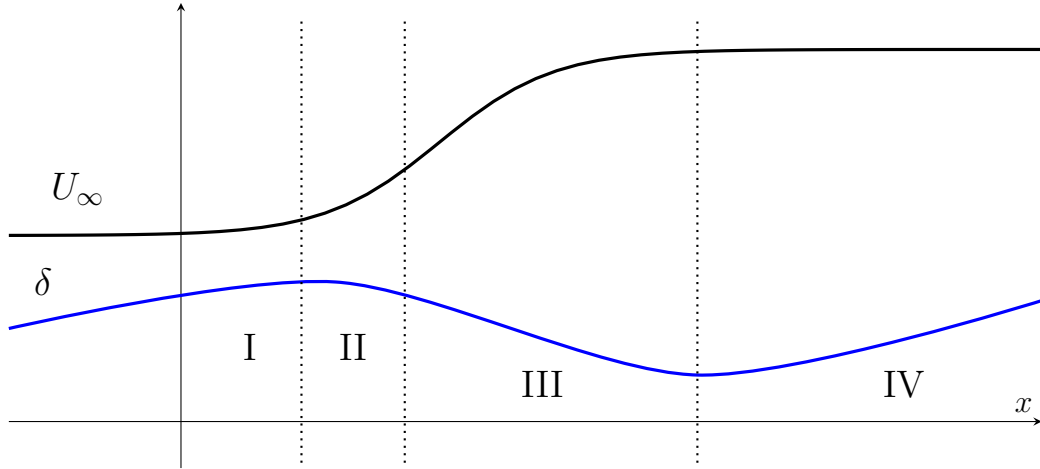


Figure 3.2: Schematic of stages proposed by Narasimha and Sreenivasan [9]: Fully turbulent (I), reverse transition (II), quasi-laminar (III), retransition (IV). The freestream velocity, U_∞ and boundary layer thickness, δ are also indicated.

With some of the core concepts and terminology described, the characteristics of the response of flow statistics and turbulent structures to acceleration will be discussed to provide a broad overview of the current understanding of spatial acceleration. The characterisation and mechanisms of laminarisation proposed by previous studies will also be reviewed.

3.1.1 Mean flow and turbulent statistics

As discussed above, mean flow parameters such as C_f and H can indicate whether a boundary layer has started to revert to the laminar state. As described in Narasimha and Sreenivasan [9], C_f typically increases during the initial stages of the acceleration. For flows that undergo laminarisation, C_f typically reach a maximum before reducing towards values typical of laminar flows [92, 93, 94]. The shape factor, H is found to initially reduce during the acceleration before rising significantly after the onset of laminarisation. Several studies have noted that for sufficiently sustained accelerations, H can approach or overshoot values typically observed in laminar flows [94, 92]. With the onset of retransition, C_f is observed to increase with H reducing, consistent with a return to the turbulent state. Consequently, the minimum of C_f and the maximum of H are regarded as approximate onset markers for retransition [9]. Consistent with a reduction of turbulent diffusion during laminarisation, Moretti and Kays [95] and Back et al. [96] found that the heat transfer coefficient reduced, taking values similar to laminar flows during strong laminarising accelerations.

Changes to the mean velocity profile are typical of spatial acceleration with an uplift of the mean velocity profile from the law of the wall and an increase in the thickness of the viscous sublayer [97, 98, 92]. Talamelli et al. [94] studied a strong and sustained spatial acceleration where the mean velocity eventually tended to the laminar Falkner-Skan solution [99]. Departures from the logarithmic law occur even in relatively weak accelerations with Fernholz and Warnack [93] observing uplift in a laminarescent case where $K_{max} = 1.5 \times 10^{-6}$. This indicated that while strong departures from the standard logarithmic law are observed in laminarising spatial acceleration, a breakdown of the law of the wall does not necessarily imply laminarisation [39]. Dixit and Ramesh [100] studied sink flows using experiment and asymptotic analysis over a range of K . It noted that while there was a departure from the standard logarithmic law, the mean velocity profile remained logarithmic, albeit with a slope that is dependent on the pressure gradient. Bourassa and Thomas [87], investigating a very strong non-equilibrium spatial acceleration at a high Reynolds number, also found that the mean velocity remained logarithmic with the von Kármán and Additive constants, κ and B , following the correlation from Nagib and Chauhan [60] developed for canonical flows (TBLs, channels and pipes), significantly extending its range of validity. Similar results have also been found in the numerical studies of Piomelli and Yuan [10] and the rough wall study of Yuan and Piomelli [49], where B was modified to account for roughness.

The response of the turbulent normal and shear stresses during laminarisation has been a major focus of research on these flows. Usually, these quantities are presented in a local scaling, which is useful for highlighting the ‘soft’ nature of laminarisation as some of these quantities may increase but do not keep up with local scalings [101, 102]. The streamwise Reynolds stress has been most commonly reported in previous studies. Badri Narayanan and Ramjee [92], who studied both strong and weak accelerations experimentally, found that in strong acceleration, u'_{rms}/U_∞ tended to decay throughout the region of high acceleration across the boundary layer. In contrast, for weaker accelerations, u'_{rms}/U_∞ increased initially before reducing. The development of the streamwise Reynolds stress has also been reported in absolute terms, with many studies showing that it increases close to the wall throughout the acceleration for both weak and strong accelerations [103, 102, 93, 10]. Piomelli and Yuan [10] noted that during laminarisation, the transverse stresses near the wall tend to reduce in absolute terms, with these stresses becoming negligible when presented in local scalings [101]. In the outer region, the turbulent stresses are found to reduce in local scalings even in the weakly accelerating flows of Harun et al. [104]

($K \approx 0.08 \times 10^{-6}$), although it has been noted that along streamlines the turbulent stresses remain relatively constant even in strong spatial accelerations [97, 9]. The Reynolds shear stress is found to decrease when scaled locally in both weaker and stronger accelerations throughout the flow [93, 102], while close to the wall, the Reynolds shear stress typically increases in absolute terms [105, 102].

The turbulent energy transfer mechanisms have also been explored in previous studies through the budgets of turbulence kinetic energy and Reynolds stress transport equations. Studies typically have mainly focussed on the budgets of the streamwise Reynolds stress or the TKE equations. Unlike other forms of laminarisation, production tends to remain significant throughout the acceleration and is everywhere larger than dissipation, even in the outer flow [9, 106]. Nonetheless, in the typical inner scaling, production was found to reduce substantially [107]. These large reductions occurred despite substantial absolute increases in the production close to the wall [87]. Fernholz and Warnack [93] noted that for a weaker case with $K_{max} = 2 \times 10^{-6}$, the production still increased substantially, noting that this was responsible for the large absolute increases in streamwise Reynolds stress close to the wall. In the outer region, Bourassa and Thomas [87] found that the shear production of TKE, $-\overline{u'v'}\partial_y\bar{u}$ tends to decrease away from the wall while the dilational production, $-(\overline{u'^2} - \overline{v'^2})\partial_x\bar{u}$, which tends to transfer energy back to the mean flow in accelerating flows, becomes substantially larger to the extent that the shear and dilational productions become comparable but opposing. Piomelli and Yuan [10], looking to understand the causes behind the absolute reductions in transverse stresses discussed above, examined the budget of the $\overline{v'v'}$ equation. The study noted that laminarisation appeared to be strongly related to the reduction in the inner-scaled pressure strain term, $\Pi_{22}^s = 2\overline{p'\partial_y v'}$, which is the primary source of the $\overline{v'^2}$ equation and represents intercomponent energy transfer. With the onset of retransition, the pressure strain was noted to increase substantially. Overall, the response of the turbulence in spatially accelerating flows has been described as a ‘dual-layer’ structure [87] with distinctly different responses from the near-wall and outer regions.

3.1.2 Turbulence structures

Much of the early interest in turbulent structures of spatial acceleration focused on the buffer layer structures. As discussed above, Schraub and Kline [86] highlighted the reduction of scaled near-wall bursting and the shallower trajectories of remaining bursts. These changes are important given the importance of near-wall bursting to

the generation of Reynold shear stress [6] and turbulence production [108]. Such observations have also been found in sink flows, with the numerical study of Spalart [109] noting the emergence of quiescent patches near the wall at $K = 3 \times 10^{-6}$, although the study noted the continued presence of near-wall streaks. Piomelli et al. [110] noted that for strong accelerations, the streaks become elongated and tend to meander less in the spanwise direction. However, for weaker accelerations ($K_{max} \approx 2.5 \times 10^{-6}$), there is little visual distinction in streaks during the acceleration. However, the elongation of the streamwise structures in both strong and weak acceleration can be observed using the integral length scale with larger changes observed in laminarising accelerations [102]. The spanwise scale of the streaks has also been investigated, with most authors indicating significant increases in the inner scaled streak spacing [111, 107], although Talamelli et al. [94] noted that this was mostly due to the changes in viscous length scale, ν/u_τ with the absolute spanwise spacing reducing. Consistent with streak strengthening in strong accelerations, the streamwise energy spectra have been noted to strengthen at low wavenumbers consistent with a strengthening of the larger scale structures [90, 102].

The overall reduction in turbulence activity in strong spatial accelerations has been widely observed with intermittency, typically present in the outer layer of the boundary layer, being observed all the way to the wall [97, 112, 103]. This has been extensively visualised both in simulation [110] and experiment using smoke [113], with a visible reduction in the number of vortices, although the remaining vortices become more intense due to stretching caused by the acceleration. The reduction in the number of vortices during laminarisation can be observed in figure 3.3, which shows the isosurfaces of the Q vortex identification criterion becoming sparser with downstream distance.

A number of studies have also examined how acceleration affects shear stress-producing events - ejections (Q2) and sweeps (Q4). Earlier experimental studies tended to use the VITA technique around near-wall bursts. Ichimiya et al. [112] found that in strong accelerations, the ejection part of the bursts away from the wall was largely unaffected by the acceleration, while the sweep events typically weakened. Closer to the wall, the reverse was found, with the ejection part weakening and the sweep part strengthening. Bourassa and Thomas [87] used the hyperbolic hole method [21] and found that, compared to the local eddy turnover time, δ/u_τ , there were reductions in both ejection and sweep events with the latter being particularly affected. However, it was noted that the remaining events were stronger. The study also noted the apparent aliasing of Q4 events into shear stress-destroying Q3

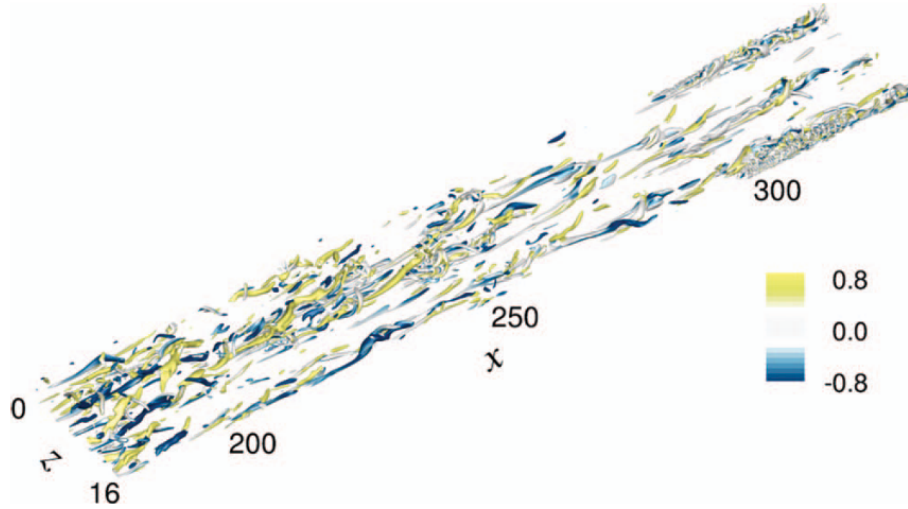


Figure 3.3: Isosurfaces of the Q criterion, where $Q = -\partial_j u_i \partial_i u_j / 2$ from Piomelli and Yuan [10] coloured by $\omega'_x / \omega'_{rms}$. The reduction in the density of vortices can be observed.

events. Piomelli and Yuan [10] found generally similar results away from the wall ($y^+ > 40$) but noted that for $y^+ < 10$, there was a substantial increase in Q4 events as irrotational fluid outside the boundary layer is redirected towards the wall and decelerated there. This may be consistent with the changes in burst pattern observed in Ichimiya et al. [112]. Joshi et al. [105], examining weaker accelerations, noted that the behaviour of Q2 and Q4 events changed significantly in an accelerating case compared with ZPG flows. Q4 events are associated with incursions of outer layer fluid into the inner part of the boundary layer, and in an FPG flow, they transport the lower-intensity turbulence located in the outer layer into the inner layer, contributing to the reduction of intermittency. McEligot and co-workers [114, 115, 116, 117] studied an innovative laterally-converging duct that enabled an investigation of spatial acceleration without the effect of a wall-ward contraction. They found that the shape of the burst pattern did not significantly change, which appears to contrast with the observations in the conventional accelerations of Ichimiya et al. [112].

Changes in flow structure have also been noted in the outer flow, with the main observation being a reduction in the inclination angle of outer layer hairpin vortices compared with ZPG flows, which was first reported in Dixit and Ramesh [118] using two-point correlations for sink flows over a wide range of K . Joshi et al. [105] also observed these reductions in weaker acceleration and explained them heuristically by considering the self-induced velocity of typical hairpin vortices in the presence of

streamwise acceleration and mean shear. In the rough-wall sink flow study of Yuan and Piomelli [119], the roughness is found to resist this reduction of inclination angle.

With the onset of retransition, there is a significant change in the turbulence structures. Blackwelder and Kovaszny [97] identified the presence of turbulent spots forming in the buffer layer. In the early stage of retransition, Ichimiya et al. [112] noted that violent fluctuations appear initially to be intermittent before becoming continuous further downstream. While early studies suggested that retransition resembled natural transition [84, 9], more recent studies have typically considered the process more complex due to the residual turbulence in the boundary layer and more akin to bypass transition [103, 10]. de Prisco et al. [120] and Piomelli and Yuan [10] highlighted a prominent role for the residual turbulence in the freestream during retransition with these motions disturbing the near-wall region, which until that point had been stabilised by the acceleration. Bader et al. [121] showed in detail how retransition initiated in the near-wall region with newly generated turbulence gradually spreading into the outer part of the boundary layer as it is convected downstream.

3.1.3 Mechanisms of laminarisation

While Narasimha and Sreenivasan [9] explained many important aspects of the mean flow and turbulence during strong spatial accelerations, questions remain, particularly relating to the island of ignorance. The most important question is what processes progressively lead to the flow attaining a quasi-laminar state under sustained acceleration. Some early studies believed the observations were related to turbulence decaying due to dissipation exceeding production [96, 86] or the Reynolds number reducing below some critical threshold [122, 92]. These mechanisms were challenged by results indicating that production remains significant and exceeds dissipation even in strong accelerations [106, 9] and that laminarisation can begin and may even be more susceptible to laminarisation at high Reynolds numbers [40]. Despite their flaws, these mechanisms are often the basis for some of the parametric criteria still used today, such as Δ_p .

Some of the more recent studies have built on the improved understanding of the structures and processes of near-wall turbulence, with several studies suggesting that laminarisation results from the interruption of the near-wall turbulence regeneration cycle. This cycle is discussed in more detail in chapter 4. Bourassa and Thomas [87] suggested that strong spatial accelerations inhibit the sinuous normal mode streak instability mechanism by reducing the inclination angle of lifted low-speed streaks, which Schoppa and Hussain [76] had found to be unstable only if this angle exceeded

a certain threshold. Piomelli and Yuan [10] proposed that the cause of the reduction in v' and w' was related to the decrease of the source of the rapid pressure Poisson equation leading to a reduction of pressure fluctuations and, consequently, a reduction of pressure strain. The decrease in w' would then inhibit the streak transient growth mechanism, also proposed in Schoppa and Hussain [76], thus inhibiting the regeneration cycle.

Yuan and Piomelli [49] suggested that the reduction of turbulence near the wall in smooth wall accelerations could be associated with rapid distortion due to shear, which for initially homogeneous isotropic turbulence results in an accumulation of energy in the streamwise component similar to that observed in spatial acceleration [61, 123]. In rough walls, where laminarisation can often be avoided, it was noted that the shear parameter was reduced compared with a smooth wall case with the same acceleration rate. Dixit and Ramesh [118] proposed a mechanism to explain the success of the quasi-laminar model of Narasimha and Sreenivasan [9]. This was based on the observed reduction of structure inclination angle and a structural argument relating this reduction to the elimination of turbulent transport, leading to a laminar-like inner layer. Some of these mechanisms are plausible but generally difficult to test and are usually based on a limited number of simulations or experiments, meaning that their ability to explain the emergence of laminarisation is largely untested. As a result, a large range of K is used in this study.

3.2 Bypass transition of laminar boundary layers

Early studies of transition in laminar boundary layers tended to focus on natural transition via the generation and propagation of two-dimensional Tollmein-Schlichting (TS) waves [124], which lead to three-dimensional secondary instabilities leading to turbulent spot generation and transition. These disturbances grow slowly on viscous time scales and only attain the required amplitude for the development of secondary instabilities when $Re_x = U_\infty^* x^* / \nu^* = O(10^6)$ [125], where x is the distance from the leading edge of a flat plate. Early studies of transition, such as Dryden [126] and Taylor [127], found that at elevated freestream turbulence (FST) intensities, $Tu = u'_{rms}/U_\infty \gtrsim 1\%$, the onset of transition occurred much further upstream ($Re_x = O(10^5)$), with the presence of low-frequency streamwise velocity fluctuations in the boundary layer. At these intensities, modal growth mechanisms, such as the TS wave mechanism, may be bypassed [128].

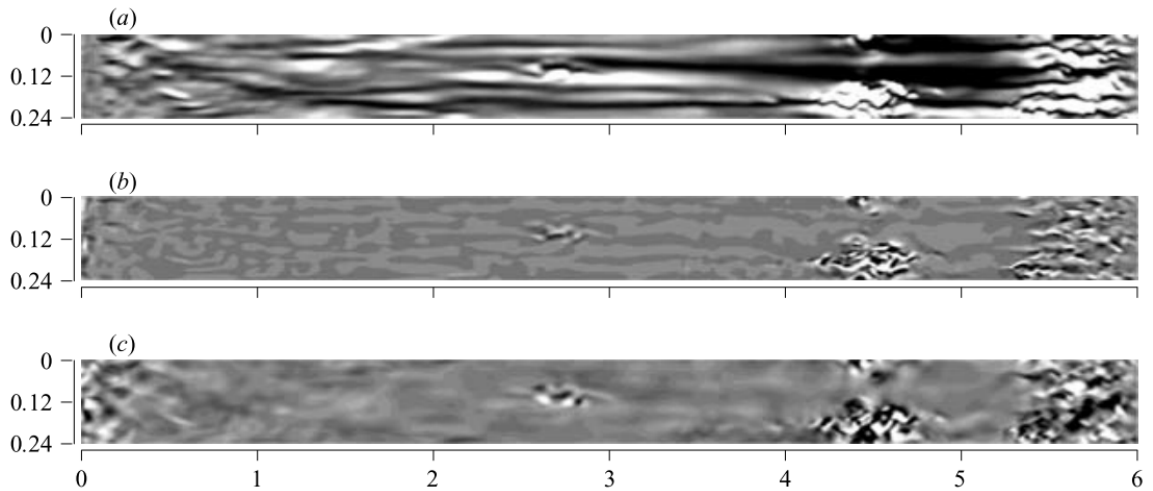


Figure 3.4: The velocity fluctuations from Nagarajan et al. [11] showing the typical progression of a boundary layer undergoing bypass transition. (a) u' ; (b) v' ; (c) w' .

One of the most consequential observations of what is now known as bypass transition is Klebanoff [129], who noted the presence of long streaks of alternating high and low streamwise velocity that grow from near the leading edge of the flat plate. These streaks reach amplitudes far larger than those typical of TS waves and have subsequently been referred to as ‘Klebanoff’ modes [130]. Jacobs and Durbin [131] characterised the overall bypass transition process in three stages: the buffeted laminar boundary layer, the intermittent region, and the fully turbulent boundary layer. The first region is largely characterised by the development and amplification of the Klebanoff modes, which eventually results in secondary instabilities developing on specific streaks, leading to their breakdown and the formation of turbulent spots. The Klebanoff modes can be observed in figure 3.4(a), which shows the elongated u' fluctuations from Nagarajan et al. [11] with turbulent spots being observed somewhat further downstream. In the second region, these spots grow in the spanwise direction, co-existing with the streaks until the spots merge, covering the spanwise extent of the wall, culminating in the final fully turbulent region, which can be observed at the downstream end of figure 3.4. The remainder of this review focuses on the key themes of bypass transition research that are particularly relevant to this study, such as the amplification of near-wall streaks and their eventual breakdown mechanisms.

The formation of these streaks is linked to the internalisation of freestream disturbances into the boundary layer in a process known as receptivity. The boundary layer shear acts like a low-pass filter where smaller scale disturbances are filtered out while larger scale disturbances are amplified [132, 133, 134]. The basic mechanism for

the growth of streaks within the boundary layer is the lift-up effect [135, 136], which is also responsible for the growth of streaks in turbulent flows (section 2.4.3). Westin et al. [137] also noted the importance of the wall-normal component in penetrating, highlighting the spanwise gradients of v' in particular. The growth of the streaks within the boundary layer has been an important focus of research on bypass transition. Kendall [130] found that the streamwise disturbance energy, $\overline{u'u'}$ associated with these streaks has been found to grow linearly with downstream distance, which was subsequently found by other authors, including Westin et al. [138] and Matsubara and Alfredsson [139]. Westin et al. [138] also noted that the streamwise scale of the structures inside the boundary layer was much larger than for the freestream turbulence, with Matsubara and Alfredsson [139] showing that the energy growth is concentrated at low streamwise wavenumbers initially, with growth occurring at higher wavenumbers only with the breakdown of the streaks.

Several theoretical approaches to modelling the development of streaks in laminar boundary layers have been proposed. First, optimal growth theory which was developed by Andersson et al. [140] and Luchini [141]. This approach looked for the initial velocity profile that maximised the transient energy growth in the boundary layer. The wall-normal profile of resulting streamwise disturbances was found to be similar to experimental studies [138], with the transient growth exhibiting a linear profile similar to experiments [138, 130, 139]. Ricco et al. [142] reviewed this approach, highlighting that it does not model the freestream disturbances that lead to bypass transition, with the initial conditions instead being an output of the method. Therefore, the development of the laminar streaks cannot be linked with the characteristics of the freestream vortical disturbances that cause them. Leib et al. [143] developed another theoretical approach that does include the influence of the FST by deriving initial and freestream conditions that describe the conditions close to the leading edge and the interaction between the outer part of the boundary layer and freestream using matched asymptotic expansions. Using the same approach, Ricco et al. [142] found good agreement with the DNS of Wu and Moin [144] throughout the pre-transitional boundary layer. The importance of modelling the freestream is also highlighted by Lengani et al. [145], which studied bypass transition on low-pressure turbine blades. These results highlighted the strong correlation of the most amplified spanwise wavelengths with the FST in the blade passage, while the spanwise wavelengths associated with optimal growth were less amplified.

The eventual formation of turbulent spots in bypass transition depends on many factors, including FST intensity, integral length scale, and leading edge geometry

[11, 146]. The most relevant literature for the current study is the transition that occurs with $0.5\% < Tu < 2\%$ [147]. In these cases, the spots are caused by the instabilities developing on low-speed streaks. These come in two principle types: a varicose (spanwise symmetric) instability and a sinuous (spanwise anti-symmetric) instability.

Jacobs and Durbin [131] studied bypass transition using DNS without explicitly modelling the leading edge by using the continuous spectrum of the Orr-Sommerfeld/Squire equations to model the FST. This approach has also been frequently used by other studies such as Brandt et al. [148], Brandt and de Lange [149] and Schlatter et al. [150]. Dong and Wu [151] and Ricco et al. [142] showed that this approach leads to non-physical spurious entanglements between freestream modes, which are related to the parallel flow assumption in the Orr-Sommerfeld equations. Ricco et al. [142] also notes that using the Orr-Sommerfeld equation implies that the presence of the FST is dependent on the presence of the boundary layer, whereas the freestream disturbances clearly should exist independently of the presence of the flat plate. Nonetheless, the results of studies using this approach have significantly influenced the understanding of the breakdown of laminar streaks, with qualitative similarities with subsequent experiments. Jacobs and Durbin [131] identified a varicose Kelvin-Helmholtz-like instability that develops on specific lifted low-speed streaks or ‘backward jets’ due to their interaction with the elevated high-frequency FST at the boundary layer edge. These then subsequently develop into patches of irregular motion or turbulent spots. Asai et al. [152] experimentally investigated both mechanisms on a single streak through acoustic excitement. The varicose mode was found to be a Kelvin-Helmholtz instability resembling Jacobs and Durbin [131] with an inflectional wall-normal velocity profile, whose growth rate reduces as a streak’s spanwise scale increases. The sinuous instability was found to cause streak meandering and could propagate further downstream. As a result, the sinuous instability was found to occur more frequently. Mans et al. [153], studying a full flat plate boundary layer, found that the propagation velocity of the spots from both mechanisms could be linked to low-speed streaks and that the critical amplitudes related to the varicose mode were larger than for the sinuous modes, consistent with the sinuous mode occurring more frequently. The greater prevalence of sinuous instabilities has also been observed in DNS [150] and theoretical investigations on streak instability [154, 155, 156, 157].

Several studies have also considered the time evolution of these mechanisms using DNS. Brandt et al. [148] found that varicose breakdowns could be the result of interactions of lifted low-speed streaks with freestream disturbances as discussed in Jacobs

and Durbin [131] or streak interactions with the head of a high-speed streak reaching the tail of a low-speed streak. Sinuous breakdowns were caused by a higher-speed streak passing on one side of a low-speed streak, causing an inflectional spanwise velocity profile. Brandt and de Lange [149] further studied the role of streak collision with the varicose instabilities initiating the development of Λ or hairpin vortices, while sinuous instabilities lead to quasi-streamwise vortices on the flank of the low-speed streak flank. The role of streak collisions in sinuous and varicose breakdowns have also been observed in experiments such as Mans et al. [158], Nolan and Walsh [134] and Balamurugan and Mandal [159].

Beyond the breakdown mechanism, the statistical characteristics of the formation of turbulent spots have also been examined. Hernon et al. [160], using experiment, showed that as the boundary layer approaches transition, the streamwise velocity has a strong negative skewness in the upper part of the boundary layer, consistent with the presence of strong low-speed streaks there, which can subsequently interact with the FST. Nolan et al. [161] used quadrant analysis to examine the breakdown of the streaks with the formation of spots associated with short but strong ejection events in regions associated with low-speed streaks, although the mechanism of breakdown could not be discerned. Voke and Yang [162], using large eddy simulation, noted that the break up of the streaks at the onset of transition was marked by a significant increase in the pressure strain, indicating energy transfer from the streamwise component to the transverse motions. It is interesting to note that transition onset is typically delayed in laminar boundary layers subject to strong spatial acceleration [163, 164].

The development of these nascent spots in the intermittent region has also been investigated. Nolan and Zaki [165] used conditional averaging in which the statistics of the quiescent and turbulent patches within the intermittent region were computed separately, with the mean velocity profile of the turbulent patches consistent with a fully turbulent flow throughout this region, although the velocity perturbations were observed to be elevated compared to turbulent flows near the formation of the turbulent spots. Marxen and Zaki [166] extended this analysis, and it was found that the velocity perturbation in the core of sufficiently large spots was consistent with ZPGTBL flows.

3.3 Temporal acceleration

The development of turbulence in temporally accelerating internal flows has been studied extensively, particularly in recent years. Much of the interest in temporal acceleration is because when accelerated strongly they laminarise, with the mean flow parameters undershooting quasi-steady predictions during the transient. This leads to challenges in predicting mean flow quantities such as heat transfer and skin friction coefficients that are vitally important in engineering applications [167, 168, 169]. Studies have consequently been focussed on predicting the transient development of these flows and understanding their turbulence dynamics.

Among the first studies to investigate temporal acceleration was Maruyama et al. [170], which highlighted some of the key aspects of the turbulence response in these flows, notably the generation of ‘new’ turbulence, which begins at the wall and propagates into the core with time. With advances in experimental methods, greater insights into the transient turbulence development were obtained. He and Jackson [171] investigating ramp-up accelerations made substantial progress in understanding the mean flow and turbulence response. The study noted the tendency of the flow to accelerate in an essentially uniform manner for much of the acceleration, except for a thin region near the wall. The response of the turbulence is marked by an increase in the streamwise Reynolds stress component from shortly after the beginning, with the transverse components at any wall-normal location increasing only after a more significant delay. Their eventual response was strongly linked to a delayed increase in the pressure strain. This new turbulence subsequently propagated away from the wall. The frozen nature of the turbulence in the core of the flow was also noted by Greenblatt and Moss [47], who studied higher Reynolds numbers and noted the changes in the outer region with the weakening of the wake part of the velocity profile during the acceleration, which was not restored until the delayed increase of turbulence there.

The current understanding of temporal acceleration largely derives from He and Seddighi [43], which investigated a step-change temporal acceleration at low Reynolds number using DNS. The transient turbulence response to the acceleration was characterised as a three-stage transition process: pre-transition, transition, and fully turbulent, mirroring the stages of boundary layer bypass transition from Jacobs and Durbin [131]. At the beginning of the acceleration, due to the influence of viscosity and the wall, a thin region of high strain rate forms at the wall, representing a new time-developing boundary layer that modulates the near-wall turbulence structures.

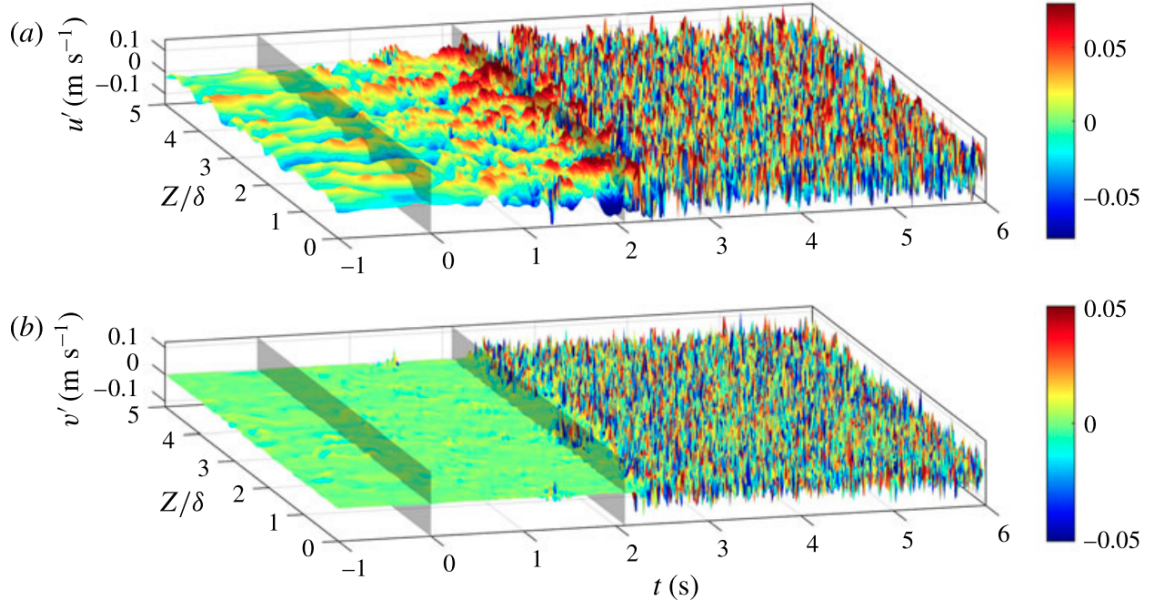


Figure 3.5: $z-t$ surface plots of the streamwise and wall-normal velocity fluctuations for transient channel flow at $y^{+0} = 15$ from Mathur et al. [12]. The two vertical planes indicate the onset of acceleration and transition, respectively. (a) u' ; (b) v' .

The result is that during pre-transition, there is significant amplification of the near-wall streaks, resulting in a linear increase in the streamwise energy disturbance near the wall [139], similar to bypass transition. During this region, the transverse stresses were observed to freeze across the channel. This region is associated with the delay between the streamwise and transverse stresses in He and Jackson [171]. This region was terminated by the formation of localised turbulent spots, which was linked to the breakdown of the strengthened streaks in an apparent varicose instability mechanism resembling the ‘backward jets’ in Jacobs and Durbin [131]. Throughout the transition region, these spots grow in the spanwise and streamwise direction with time until the wall is covered in the newly generated turbulence. The final region is associated with the diffusion of turbulence into the core, as found in prior studies [171, 47, 170]. The overall near-wall turbulence development can be observed in figure 3.5, which shows the spanwise and temporal development of u' and v' with the initial growth of u' being observed from $t = 0$ s and the delayed increase of v' only being observed at $t \approx 2$ s. He and Seddighi [43] highlighted that unlike the bypass transition of a laminar boundary layer, the pre-existing flow is already a turbulent wall shear flow and consequently has a different structure to the homogeneous isotropic turbulence that characterises the FST in bypass transition. In this sense, the transition-like process here may be

described as a turbulent-to-turbulent transition.

Following He and Seddighi [43], studies extended this understanding to a much greater range of temporal accelerations. Seddighi et al. [44] investigated a ramp-up temporal acceleration using DNS and found significant similarities to the step change case. However, it noted that the transition was delayed compared to step change due to the continuous strong FPG associated with gradual acceleration. He and Seddighi [15] investigated step-change accelerations with a range of velocity ratios, U_{b1}/U_{b0} from 1.1 to 4.5 alongside variations of initial Reynolds number. All cases exhibited signs of the transition process in the turbulence statistics, although for the instantaneous results, the processes became less prominent in weaker accelerations, with the streaks only strengthening slightly during pretransition. The results of Jung and Kim [45] indicated that the transition process could not be detected in sufficiently long and weak accelerations. The accelerations with a clear transition process exhibited a sinuous instability similar to those in Schlatter et al. [150]. Similar mechanisms were also observed by Mathur et al. [12] and Mathur et al. [172] in which some of the strongest accelerations to date were performed ($U_{b1}/U_{b0} < 19.3$) using both simulations and experiments. In these strong accelerations ($U_{b1}/U_{b0} > 6.5$), absolute reductions in the transverse stresses could be observed close to the wall. Sundstrom and Cervantes [173] examined the response of the turbulent stresses around the onset of transition, noting significant increases in TKE production, and hypothesised the role of the rapid pressure in the initial increases of the pressure strain, although this could not be tested in their experiments.

More recently, Guerrero et al. [174] investigated unsteady pipe flow focusing on the changes to momentum balance and skin friction using Fukagata, Iwamoto, and Kasagi (FIK) identity [175], which indicated the presence of an inertia-dominated region at the beginning of the acceleration, which results in significant increases of viscous stresses near the wall while the turbulent transport remains frozen. In the fully turbulent region, the FIK identity indicated that redevelopment of the core region was a slow process that lasted substantially longer than the comparatively steady C_f suggested.

Much research on temporal acceleration investigated predictions of the mean flow evolution, particularly during pre-transition. He and Seddighi [43] decomposed the mean flow by defining a differential or perturbation mean velocity defined as $\bar{u}^\wedge = \bar{u}(y; t) - \bar{u}(y; t = 0)$, with \bar{u}^\wedge encapsulating the new time-developing boundary layer. \bar{u}^\wedge and associated mean flow parameters were found to follow the Blasius solution during pre-transition. He and Seddighi [15] over the large range of Re and

U_{b1}/U_{b0} found that during pre-transition, \bar{u}^{\wedge} followed the laminar similarity solution to Stokes' First Problem. The laminar similarities in temporal acceleration were explored in more detail by Sundstrom and Cervantes [176], who derived them from the mean momentum equation with the assumption of a negligible change to the turbulent transport, which is valid during pretransition. A similar approach was used in the predictions of the wall shear stress in He et al. [177] and He and Ariyaratne [178]. Mathur et al. [12] used an 'extended' Stokes first problem to predict the perturbation mean flow in arbitrary changes of bulk velocity in which the acceleration is considered as a convolution of small acceleration increments. Good predictions using this approach were found in Oluwadare [179] over a wide range of Reynolds numbers and acceleration rates. Alternative approaches explaining the mean flow development have also been proposed by García García and Alvarino [180].

From the above discussion, it is clear that there are many similarities between the turbulence development in temporal and spatial acceleration. These similarities include the response of the streamwise Reynolds stress, which increases from near the start of the acceleration in both cases [93, 102, 43]. The delayed response of the transverse stresses has been widely observed in temporal acceleration [171] and well-documented particularly in strong spatial accelerations [10]. Furthermore, in both accelerations, the eventual increases of the transverse stresses has been associated with increases in pressure strain [10, 171, 173]. Several authors have previously discussed the similarities between spatial and temporal acceleration. Greenblatt and Moss [46, 47] found that the development of mean flow parameters exhibited similar trends to their spatial counterparts, even if the excursions in these parameters were smaller and did not reach values typical of a laminar flow. Recently, Mangavelli et al. [181] and Mangavelli and Yuan [48] showed that the role of roughness in temporal acceleration is similar to that in spatial acceleration [49], indicating that the near-wall mean shear may play a similar role in the laminarisation in temporal accelerations. These similarities suggest that there are likely to be common, fundamental processes at work in both accelerations, which are of value for further study.

It is also useful to highlight the conceptual differences between the existing understanding of spatial and temporal acceleration. Spatial acceleration is usually considered from the perspective of the gradual reversion of the boundary layer to the laminar state, followed by its recovery during retransition. Temporally accelerating flows are considered from the perspective of the time-developing boundary layer resulting from the resistance to the acceleration provided by the wall. The interactions

of the new boundary layer with the existing turbulence dominate the turbulence response leading initially to the amplification of the near-wall streaks and eventually their breakdown resulting in transition. These will concepts will be developed and explored further throughout the remainder of the study.

Chapter 4

Numerical methods and validation

Due in large part to the complexity of turbulence, computational fluid dynamics (CFD) has become a cornerstone of fluids research both in industry and in the study of fundamental turbulent flows. In this study, we primarily use direct numerical simulation (DNS), which resolves all spatio-temporal turbulence scales by directly solving the Navier-Stokes equations. We also make limited use of large eddy simulation (LES) in which only the larger scales are resolved, with the dissipative effects of the small scales being modelled, meaning more computationally demanding cases can be simulated due to the relaxation of grid and time resolution requirements. Direct numerical simulations were first used to study homogeneous isotropic turbulence on small grids with periodicity in all three directions [182]. Full DNS of turbulent plane channel flow was not performed until Kim et al. [183], while the simulation of turbulent boundary layers [17] tended to lag further behind mainly due to the issues of dealing with streamwise inhomogeneity. Much of the early work using DNS employed spectral methods, which enabled sufficient spatial resolution at an economical computational cost [184]. As the power of computers has increased, other solution methods have become popular. This includes finite difference (FD) methods, which have a greater ability to handle complex geometries and reduced aliasing errors compared with spectral methods [185]. Other developments in FD schemes include the development of high-order compact finite difference schemes, which allow quasi-spectral accuracy while using small FD stencils [186].

The finite difference solvers Incompact3D and CHAPSim have been used in this study. These solvers are overviewed in sections 4.1 and 4.2. The main software contributions of this study are:

1. The development of a method for simulating spatially accelerating TBLs in Incompact3D, which included the implementation of the recycling-rescaling

method for inflow generation and freestream boundary conditions to create streamwise acceleration. This contribution is described in section 4.5.

2. The implementation of temporal acceleration into Incompact3D, including modifications to reduce the development time for turbulent channel flow enabling shorter duration simulations. This is described in section 4.4.
3. Implementation of novel moving wall acceleration into CHAPSim, which is described in more detail in chapter 5.
4. The addition of on-the-fly statistics processing for a large number of useful quantities including one-point statistics, energy spectra and quadrant analysis for both stationary and transient simulations. These are described in section 4.6.

The assessment and validation of all numerical tools used in this study are presented in section 4.7.

4.1 Incompact3D

Incompact3D is an open-source DNS/LES solver based on the finite difference method to solve incompressible and compressible flows in the low-Mach number limit [187, 188]. Incompact3D numerically solves the non-dimensional Navier-Stokes Equations (equation (2.3)) with characteristic velocity and length scales determined by flow configuration (sections 4.4 and 4.5). Incompact3D is written in Fortran 90 using the Message Passing Interface (MPI) for distributed memory parallelisation. A two-dimensional pencil decomposition is used to partition the mesh using the library 2DECOMP&FFT, which will be discussed in more detail in section 4.3.2. The key elements of the solver will now be reviewed.

4.1.1 Time advancement and discretisation

An important difficulty in numerically solving the Navier-Stokes equations is that there is no independent equation for pressure, with the velocity and pressure being coupled through the incompressibility constraint. To resolve this issue, Incompact3D uses the fractional step method for time advancement of the simulations while ensuring the momentum and continuity equations are satisfied at each time step [189, 190]. The fractional step method is a projection method where the momentum equation is solved first without considering the continuity equation, then this intermediate solution is projected onto the space of divergence-free solutions. A hybrid approach is

used for the temporal discretisation with the third-order explicit multi-step Adams-Bashforth scheme used for the convective terms and the diffusive terms in the streamwise and spanwise directions, while the second-order implicit Crank-Nicolson scheme is used for the diffusive terms in the wall-normal direction.

The time advancement in Incompact3D, accounting for both the fractional step method and the temporal discretisation, is

$$\frac{u_i^* - u_i^n}{\Delta t} = aF_i^n + bF_i^{n-1} + cF_i^{n-2} - \frac{\partial \tilde{p}^n}{\partial x_i} + \frac{1}{2Re}[L_{yy}u_i^* + L_{yy}u_i^n], \quad (4.1a)$$

$$\frac{u_i^{**} - u_i^*}{\Delta t} = \frac{\partial \tilde{p}^n}{\partial x_i}, \quad (4.1b)$$

$$DG\tilde{p}^{n+1} = \frac{1}{\Delta t}Du_i^{**}, \quad (4.1c)$$

$$\frac{u_i^{n+1} - u_i^{**}}{\Delta t} = -\frac{\partial \tilde{p}^{n+1}}{\partial x_i} \quad (4.1d)$$

where the coefficients of the Adams-Bashforth time scheme are $a = 23/12$, $b = -16/12$, $c = 5/12$. $L_{\alpha\alpha}$ represents the second derivative with respect to α , with D and G representing the vector divergence and gradient operations respectively. Note that, in this case, $*$ and $**$ represent intermediate velocity fields rather dimensional quantities. The Crank-Nicolson component can be observed on the right of equation (4.1a). The projection variable, \tilde{p} represents an approximation of the physical pressure with Temam [191] highlighting that equation (4.1c) is different from the Poisson equation for the exact pressure and has different boundary conditions. For the fractional step method of Kim and Moin [190], \tilde{p} represents the time-averaged pressure over the interval Δt [192, 187], and is related to the physical pressure, $p^{n+1} = \tilde{p}^{n+1} + O(\Delta t)$ [190]. F_i^n is the explicit part of the right-hand side at time step n , defined as

$$F_i^n = -\frac{1}{2} \left[\frac{\partial u_i^n u_j^n}{\partial x_j} - u_j^n \frac{\partial u_i^n}{\partial x_j} \right] + \frac{1}{Re} [L_{xx}u_i^n + L_{zz}u_i^n]. \quad (4.2)$$

Note the skew-symmetric form of the convection terms, which ensures their conservation while reducing aliasing errors [185, 187].

Due to the implicit Crank-Nicolson terms and the use of the sixth-order compact scheme (equation (4.7)), equation (4.1a) is solved by inverting $N_x \times N_z$ (up to) non-diagonal matrices using LU decomposition, this is presented in detail for a stretched mesh in the appendix of Mahfoze and Laizet [193]. In equation (4.1b), the pressure gradient from the previous time step is removed from the predicted velocity, u_i^* , ensuring that the tangential velocity boundary conditions imposed after equation (4.1a) are accurate to $O(\Delta t^2)$ after the correction step (equation (4.1d)) [190, 194]. Equation (4.1c) is solved using a fully spectral approach. This takes advantage of the

equivalence between differentiation in physical space and multiplication by wavenumber in spectral space alongside the efficient Fast Fourier Transform (FFT) algorithm. The general form of the 3D discrete Fourier transform, \mathcal{F} is given by

$$\hat{f}_{lmn} = \frac{1}{N_x N_y N_z} \sum_i \sum_j \sum_k f_{ijk} W_x(-k_x x_i) W_y(-k_y y_j) W_z(-k_z z_k), \quad (4.3)$$

and its inverse

$$f_{ijk} = \sum_l \sum_m \sum_n \hat{f}_{lmn} W_x(k_x x_i) W_y(k_y y_j) W_z(k_z z_k). \quad (4.4)$$

Applying equation (4.3) to equation (4.1c) leads to

$$-k'^2 \hat{p}^{n+1} = \mathcal{F} \left(\frac{1}{\Delta t} D u_i^{**} \right) \quad (4.5)$$

where \mathcal{F} indicates the Fourier transform and $k'^2 = k_x'^2 + k_y'^2 + k_z'^2$ is the modified wavenumbers associated with the spatial discretisation and interpolations schemes used (section 4.1.2). These ensure the equivalence of differentiation in physical and spectral space that is required by the correction step [195]. The particular basis functions for W in equations (4.3) and (4.4) depend on the pressure boundary conditions. For periodic boundary conditions, the FFT is used in that direction, while for homogeneous Neumann BCs, such as those used on no-slip walls, a discrete cosine transform is used. The FFTW backend of 2DECOMP&FFT is used in this study to provide FFTs. Note that these transforms are shifted in space due to the partially staggered grid. \hat{p}^{n+1} is recovered from equation (4.5) by dividing by $-k'^2$ and performing the inverse transform. The correction step is subsequently performed with the computed \hat{p}^{n+1} (equation (4.1d)).

4.1.2 Spatial discretisation

Incompact3D has a single computational domain and uses a cartesian grid with uniform grid spacing in the streamwise and spanwise directions. A non-uniform grid is used in the wall-normal direction, which allows the grid to be refined close to the walls, allowing the smaller turbulence scales located there to be resolved economically. The mesh stretching function [196, 187] can be expressed in a small number of Fourier modes, allowing the pressure field to be solved fully in spectral space at a moderate cost (a pentadiagonal matrix is inverted for each (k_x, k_z)). The mesh is partially staggered with the pressure mesh offset in each direction by half a cell with the velocity components collocated (figure 4.1). The staggering of the mesh prevents

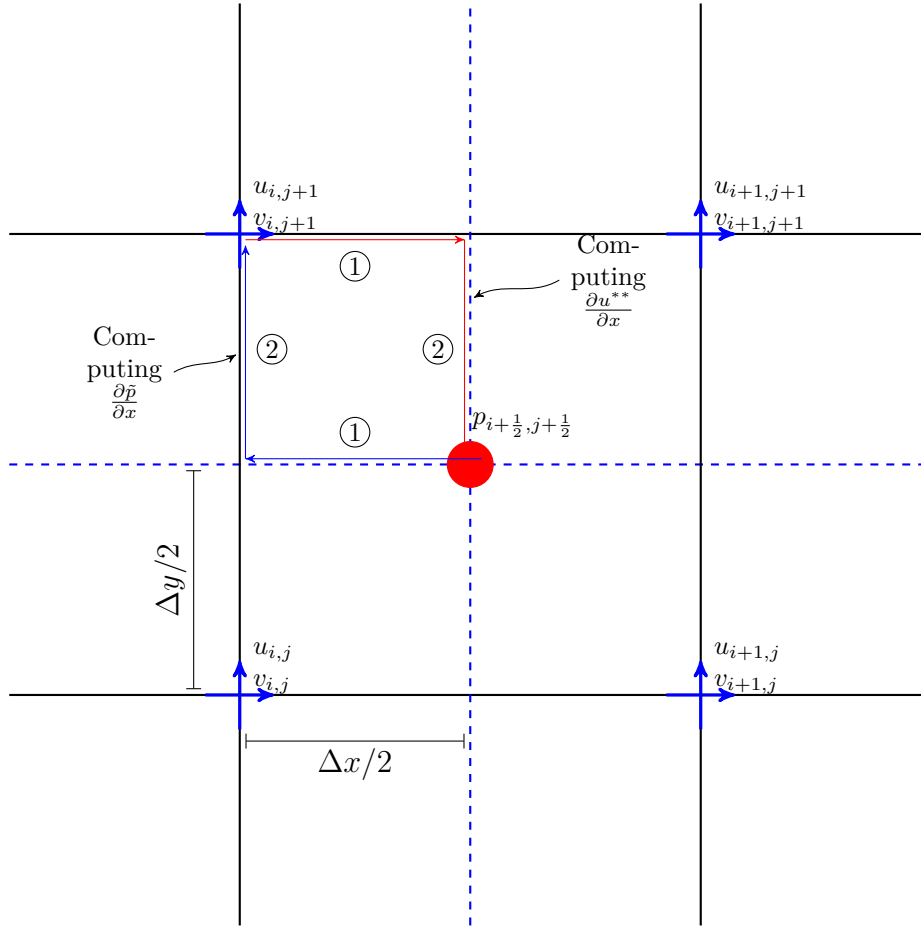


Figure 4.1: Partial staggered grid: the computation of derivatives for equations (4.1c) and (4.1d) is indicated with the blue and red arrows representing the computation of $\partial_x \tilde{p}$ and $\partial_x u^{**}$ respectively. ① indicates differentiation using equation (4.9) and ② indicates interpolation using equation (4.10). Used in Incompact3D.

unphysical oscillations in the pressure and velocity fields, which can be associated with fully collocated grids [197].

Incompact3D uses the sixth-order compact finite difference scheme for the spatial derivatives. For gradients computed on the velocity mesh, the first derivative [186] is given by

$$\alpha f'_{i-1} + f'_i + \alpha f'_{i+1} = a \frac{f_{i+1} - f_{i-1}}{2\Delta x} + b \frac{f_{i+2} - f_{i-2}}{4\Delta x}, \quad (4.6)$$

with $\alpha = 1/3$, $a = 14/9$ and $b = 1/9$. The second derivative [186] is given by

$$\begin{aligned} \alpha f''_{i-1} + f''_i + \alpha f''_{i+1} = & a \frac{f_{i+1} - 2f_i + f_{i-1}}{\Delta x^2} + b \frac{f_{i+2} - 2f_i + f_{i-2}}{4\Delta x^2} \\ & + c \frac{f_{i+3} - 2f_i + f_{i-3}}{9\Delta x^2} + d \frac{f_{i+4} - 2f_i + f_{i-4}}{16\Delta x^2}, \end{aligned} \quad (4.7)$$

with $\alpha = 2/11$, $a = 12/11$, $b = 3/11$, $c = 0$, and $d = 0$. Equations (4.6) and (4.7) can-

not be used close to solid boundaries. Consequently, a third-order one-sided compact difference scheme is used at the boundary cell, while a fourth-order Padé scheme is used for the adjacent point. Ghost nodes are used for symmetric and periodic boundary conditions. This implicit formulation of spatial derivatives results in a tridiagonal system (cyclic tridiagonal for periodic boundary conditions)

$$\mathbf{A}_1 f' = \mathbf{B}_1 f, \quad \mathbf{A}_2 f'' = \mathbf{B}_2 f, \quad (4.8)$$

which is solved using the Tridiagonal Matrix Algorithm (TDMA). Due to the partially staggered grid, the divergence on the right-hand side of the Poisson equation (equation (4.1c)) requires the computation of velocity derivatives on the pressure mesh. Conversely, the correction step requires the pressure gradient to be located on the velocity mesh. This is achieved using a staggered sixth-order first-derivative scheme

$$\alpha f'_{i-1/2} + f'_{i+1/2} + \alpha f'_{i+3/2} = a \frac{f_{i+1} - f_i}{\Delta x} + b \frac{f_{i+2} - f_{i-1}}{3\Delta x}, \quad (4.9)$$

where $\alpha = 9/62$, $a = 63/62$, and $b = 17/62$, and a sixth-order mid-point interpolation scheme,

$$\alpha f^I_{i-1/2} + f^I_{i+1/2} + \alpha f^I_{i+3/2} = a \frac{f_{i+1} + f_i}{2} + b \frac{f_{i+2} + f_{i-1}}{2}, \quad (4.10)$$

with $\alpha = 3/10$, $a = 3/4$, and $b = 1/20$. The successive differentiation and interpolation for the gradient computations of $\partial_x u^{**}$ and $\partial_x \tilde{p}$ is shown in figure 4.1.

4.1.3 Large eddy simulation

While DNS requires all spatio-temporal scales to be resolved, LES is only interested in the large anisotropic scales of the turbulent flow. LES is predominantly based on the filtered Navier-Stokes equations, with the resulting subgrid terms representing the influence of the unresolved small-scale motions on the filtered variables. Subgrid-scale (SGS) viscosity models use the Boussinesq hypothesis to relate the subgrid terms to the filtered velocity gradient through a subgrid-scale viscosity [61]. While these SGS models are popular in many applications, they struggle when used with high-order compact finite difference schemes because the second derivative (equation (4.7)) is sub-dissipative meaning that it underpredicts the exact derivative at high wavenumbers. This can lead to spurious ‘wiggles’ when the mesh is coarse as the system is insufficiently damped. Using Incompact3D, Dairay et al. [198] showed that to prevent wiggles using the Smagorinsky [199] and Dynamic Smagorinsky [200] SGS viscosity models required substantial mesh resolution such that the benefits of using LES were negated.

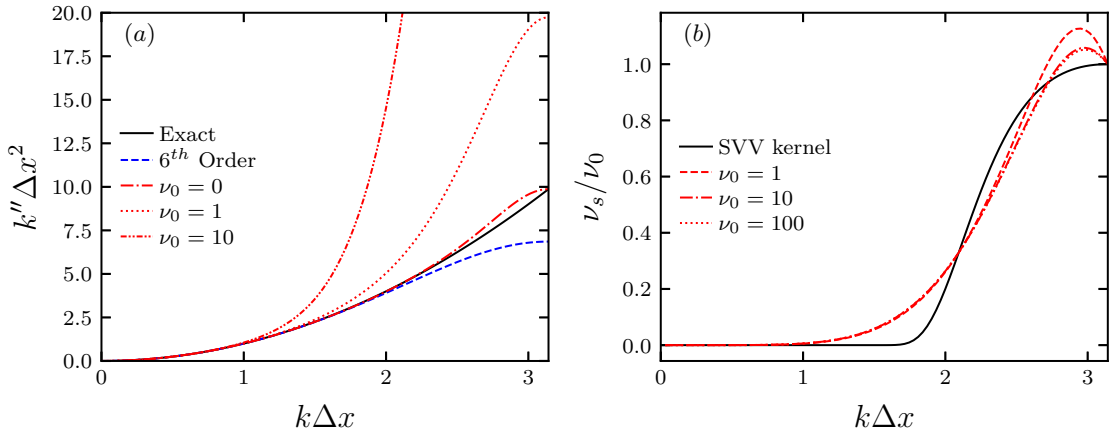


Figure 4.2: (a) shows the modified wavenumber for equation (4.7) and the iSVV model for various values of ν_0 . (b) shows the resulting spectral viscosity, ν_s/ν_0 for different values of ν_0 compared with the SVV kernel [13].

Another approach is the Spectral Vanishing Viscosity method developed for LES by Karamanos and Karniadakis [13], where the premise is to add additional dissipation at high wavenumbers that can damp wiggles and can mimic the dissipative effects of the subgrid scales, leading to its use in LES. In Incompact3D, a method imitating this approach is implemented efficiently by modifying the coefficients of the second derivative scheme (equation (4.7)) to provide additional dissipation at high wavenumbers at no additional computation cost per time step. The modified wavenumber for the scheme in equation (4.7) is [193]

$$k''\Delta x^2 = \frac{2a[1 - \cos(k\Delta x)] + \frac{b}{2}[1 - \cos(2k\Delta x)] + \frac{2c}{9}[1 - \cos(3k\Delta x)] + \frac{d}{8}[1 - \cos(4k\Delta x)]}{1 + 2\alpha \cos(k\Delta x)}. \quad (4.11)$$

$k''\Delta x^2$ is shown in figure 4.2(a) alongside the exact derivative (k^2) and can be observed to underpredict the exact derivative at high wavenumbers leading to the sub-dissipative behaviour described above. The premise of the method in Incompact3D is to modify the coefficients of equation (4.7) such that k'' is changed, giving a different dissipative behaviour than the coefficients in section 4.1.2 while maintaining high-order accuracy. This results in a spectral viscosity, ν_s , which is defined by comparing the discrete second derivative operator with the exact derivative in spectral space

$$\nu k'' = (\nu + \nu_s(k))k^2 \Rightarrow \frac{\nu_s(k)}{\nu} = \frac{k'' - k^2}{k^2} \quad (4.12)$$

Details of how the coefficients are determined are given in Mahfoze and Laizet [193] but results in two parameters that need to be determined: ν_0 a parameter that controls

the spectral viscosity, ν_s at the cut-off wavenumber, k_c and c_ν , which is the ratio of the ν_s between $2/3k_c$ and k_c .

Following Mahfoze and Laizet [193], c_ν is determined such that ν_s matches the SVV kernel at the $2/3k_c$ yielding $c_\nu \approx 0.33$. A drawback of this method is that ν_0 is generally case dependent, although strategies can be employed to make it dependent on the local strain rate, mesh size, or Reynolds number [193]. Figure 4.2(a) shows the modified wavenumber with different values of ν_0 and figure 4.2(b) shows the resulting spectral viscosity ν_s/ν_0 compared with the original SVV kernel of Karamanos and Karniadakis [13]. This shows that ν_s is similar to the original SVV kernel and is self-similar over large values of ν_0 . This implicit SVV (iSVV) approach has been used sparingly in this study with one computationally expensive validation case and one case in chapter 6, which is minor but very computationally demanding if full DNS was used. The iSVV method is evaluated for spatially accelerating TBLs in section 4.7.4.1.

4.2 CHAPSim

CHAPSim is a pipe and channel flow DNS solver developed at Sheffield [201, 202]. It has been used previously in the study of temporally accelerating channel flow [43, 15, 12], mixed convection of supercritical CO₂ in vertically heated pipes [203] and body forced influenced flows [204]. CHAPSim is also written in Fortran 90 and uses the Message Passing Interface (MPI) to provide multi-process parallelisation. For parallel computing, the mesh is partitioned in the y direction, resulting in a ‘slab’ decomposition that will be discussed in more detail in section 4.3.2.

4.2.1 Time advancement

CHAPSim follows a modified form of the fractional step method detailed in Orlandi [205], which uses a different projection variable to Incompact3D, ϕ , which represents an incremental pressure correction with the physical pressure, $p^{n+1} = p^n + \phi + O(\Delta t)$. Equation (4.13) shows the fractional step method alongside the three-stage, low-storage Runge-Kutta scheme [206], where the superscript k represents each stage of the scheme with $f^3 = f^{n+1}$. The Crank-Nicolson scheme is used for the linear terms

in all three directions.

$$\frac{u_i^* - u_i^{k-1}}{\Delta t} = \gamma_k H_i^{k-1} + \zeta_k H_i^{k-2} - \alpha_k \frac{\partial p^{k-1}}{\partial x_i} + \frac{\alpha_k}{2Re_0} [L_{jj}(u_i^*) + L_{jj}(u_i^{k-1})] \quad (4.13a)$$

$$DG(\phi^k) = \frac{1}{\alpha_k \Delta t} D(u_i^*) \quad (4.13b)$$

$$\frac{u_i^k - u_i^*}{\Delta t} = \alpha_k \frac{\partial \phi^k}{\partial x_i} \quad (4.13c)$$

$$p^k = p^{k-1} + \phi^k - \frac{\alpha_k \Delta t}{2Re_0} L_{jj}(\phi^k) \quad (4.13d)$$

where H_i is the convection term. The numerical scheme coefficients γ , ζ , and α are defined as:

$$\begin{aligned} \gamma_1 &= 8/15 & \zeta_1 &= 0 & \alpha_1 &= \gamma_1 + \zeta_1 = 8/15 \\ \gamma_2 &= 5/12 & \zeta_2 &= -17/60 & \alpha_2 &= \gamma_2 + \zeta_2 = 2/15 \\ \gamma_3 &= 3/4 & \zeta_3 &= -5/12 & \alpha_3 &= \gamma_3 + \zeta_3 = 1/3 \end{aligned}$$

Similar to Incompact3D, the Crank-Nicolson scheme means that u_i^* cannot be determined directly from known quantities. Here, u_i^* is computed using an approximate matrix factorisation which leads to a splitting error $O(\Delta t^2)$ [201].

$$\left[I - \frac{\alpha_k \Delta t}{Re_0} L_{i1} \right] \left[I - \frac{\alpha_k \Delta t}{Re_0} L_{i2} \right] \left[I - \frac{\alpha_k \Delta t}{Re_0} L_{i3} \right] \Delta u_i = RHS_i \quad (4.14)$$

where $\Delta u_i = u_i^* - u_i^n$. The three matrices on the LHS are successively inverted using the TDMA. The Poisson equation (equation (4.13b)) is solved using a combined FFT-TDMA solver where the streamwise and spanwise directions are solved spectrally. This leads to a tri-diagonal system

$$\left(-k_x'^2 - k_z'^2 + \frac{\partial^2}{\partial y^2} \right) \widehat{\phi}^k(k_x, k_z, y) = \mathcal{F} \left(\frac{1}{\alpha_k \Delta t} D(u_i^*) \right), \quad (4.15)$$

which is solved using the TDMA with ϕ being recovered by performing the inverse FFT in the streamwise and spanwise directions.

4.2.2 Spatial discretisation

CHAPSim includes two computational domains: a streamwise periodic turbulence generator, which is used to provide fully developed turbulent inflow conditions for an inlet-outlet solver. A schematic of this configuration is presented in figure 4.3. The mesh is fully staggered with the pressure stored at the cell centre, with each velocity component shifted by half a cell in the direction it is normal to. A schematic of a fully

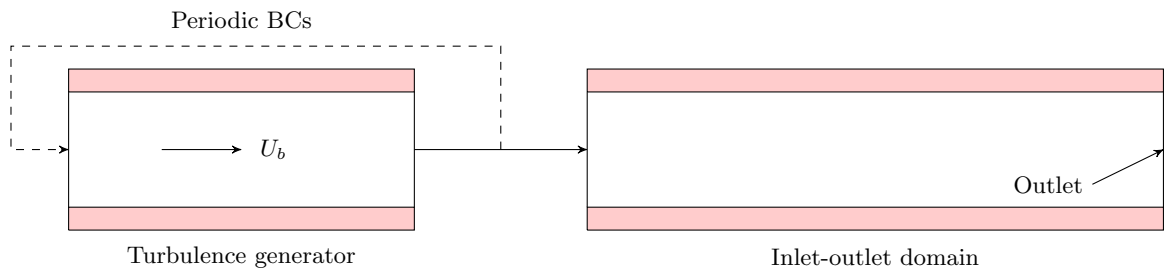


Figure 4.3: Diagram showing the turbulence generator and inlet-outlet domain of CHAPSim

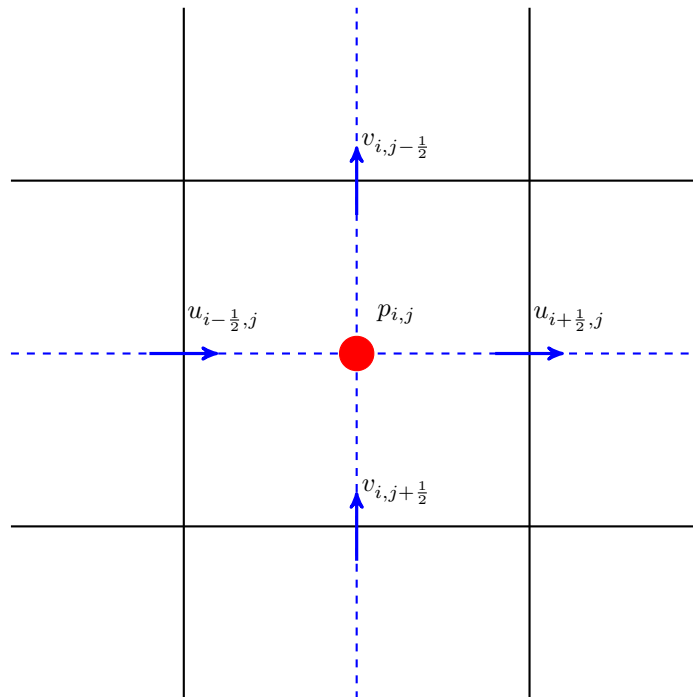


Figure 4.4: Fully staggered grid. Used in CHAPSim

staggered grid is shown in figure 4.4. A fully staggered grid helps to eliminate pressure chequering, although this requires extensive mid-point interpolation, particularly in the computation of the convection terms. Unlike Incompact3D, no interpolation is required to compute the velocity divergence or pressure gradient. CHAPSim uses the second-order central difference scheme for all derivatives. This scheme less accurately represents the exact derivative compared with the sixth-order scheme of Incompact3D.

4.3 Important considerations for DNS

4.3.1 Grid resolution, domain size and time step

Alongside the numerical methods, the simulations must be set up correctly to capture the turbulence physics accurately. For homogeneous directions where periodic boundary conditions are imposed, the domain size must be large enough such that the two-point correlations of the flow variables decay to zero within half the domain [184]. This guideline is satisfied for all cases in this study, ensuring that the domain size should not affect the statistics in those directions. However, this criterion does not necessarily mean that all energy-containing motions are captured, with superstructures and very-large-scale motions (VLSMs) present in the outer layer at high Reynolds numbers that can extend for $20 h^*$ in the streamwise direction [207, 208, 209].

The grid resolution must ensure that all relevant turbulence scales are captured. It follows that DNS must resolve down to the Kolmogorov length scale, $\eta = (\nu^3/\epsilon)^{1/4}$, the length scale associated with the dissipation of the smallest turbulent eddies. Moin and Mahesh [184] noted that this condition is likely too stringent and that the requirement is $O(\eta)$, highlighting that most of the dissipation occurs at scales greater than 15η . For wall-bounded flows, Coleman and Sandberg [210] noted that the streamwise and spanwise grid spacing should be $\Delta x^+ < 15$ and $\Delta z^+ < 8$, respectively, for spectral methods. For finite difference methods, the resolution requirements are finer due to their high-wavenumber behaviour, although this is mitigated somewhat by the high-order compact scheme used in Incompact3D. The wall-normal resolution at the wall should be $\Delta y^+ < 1$ to resolve the viscous length, δ_v^* scale with the first ten points within $y^+ < 10$ [210].

Also significant is the time step duration required to capture the flow physics and ensure a stable numerical solution. Regarding flow physics, Choi and Moin [194] performed simulations with a fully implicit time scheme, allowing consideration of the physical aspects alone. Their results indicated that turbulence could not be sustained if Δt was larger than the Kolmogorov time scale, $\tau_\eta = (\nu/\epsilon)^{1/2}$ with second-order statistics converging for $\Delta t^+ < 0.4$ corresponding to $\Delta t U_b/h = 0.05$. Another important consideration for choosing the time step is numerical stability. Given that the momentum equation is an advection-diffusion problem, the stability of simulations is indicated by two dimensionless numbers. The Courant-Friedrich-Lewy criterion comes from the advection term

$$C = \frac{U\Delta t}{\Delta x} \leq C_{max}, \quad (4.16)$$

where C is the Courant number. The second number is the diffusion number, which leads to the condition

$$D = \frac{\nu \Delta t}{\Delta x^2} \leq D_{max}. \quad (4.17)$$

The specific values of C_{max} and D_{max} depend on the temporal and spatial discretisation schemes used. For explicit schemes, typically $C_{max} \leq 1$. In the study of wall-bounded turbulence, equation (4.17) is often a more stringent condition, particularly in the y direction due to its dependence on Δy^2 , which is small close to the wall. This has been mitigated in this study by using the implicit Crank-Nicolson scheme for the y diffusion term, which relaxes this condition. C also has a physical meaning: it is the ratio of the distance traveled by a particle of speed U in time Δt to the grid spacing. The implication is that if $C > 1$, information is lost as a particle would travel more than one grid spacing per time step. As a result, it is desirable for $C < 1$ regardless of numerical stability considerations. Typically, in DNS studies of wall-bounded turbulence, equations (4.16) and (4.17) are a more stringent constraint on Δt than flow physics with Δt an order of magnitude below the values suggested in Choi and Moin [194]. The total simulation duration must ensure that the flow statistics are sufficiently converged.

4.3.2 High-performance computing strategy

All simulations in this study are conducted on supercomputers. Described simply, supercomputers comprise many computational cores grouped into a ‘node’ with many nodes connected via high-speed interconnects. This architecture allows a large CFD problem to be broken down into smaller chunks, which are solved by individual cores in parallel. The result is that computationally expensive CFD problems can be solved rapidly. Supercomputing is considered a subset of high-performance computing (HPC), which encompasses the hardware and software technologies that enable the solution of large-scale computational problems. Most simulations have been run on ARCHER2, the UK national supercomputer, which contains more than 750,000 cores.

Both Incompact3D and CHAPSim are specifically designed to take advantage of the massively parallel architectures of supercomputers. The main strategy of these codes is to partition the computational mesh into smaller subdomains, which are solved by separate processes on individual cores, with information being communicated between cores using the Message Passing Interface (MPI). Consequently, as the number of cores increases, the number of points being solved by each core reduces,

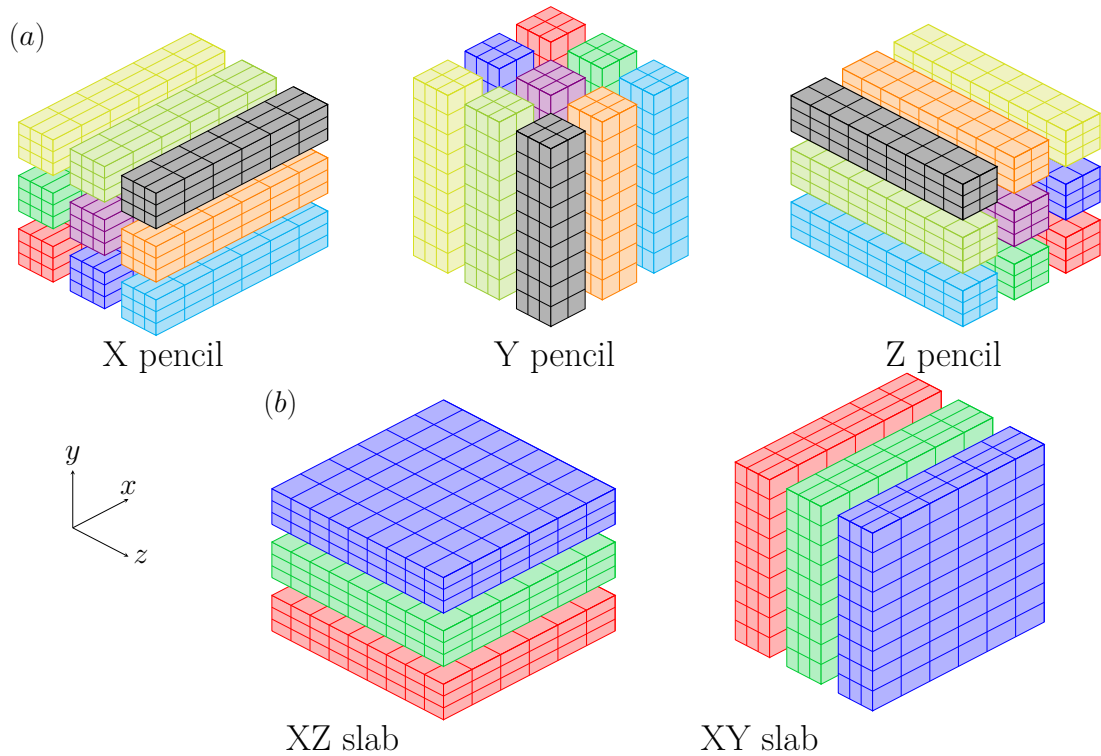


Figure 4.5: Domain partitioning strategies. (a) Pencil decomposition showing from left-to-right the X pencil, Y pencil and Z pencil. (b) Slab decomposition showing from left-to-right the XZ slab and the XY slab.

typically reducing the overall duration of the simulation. The parallel efficiency of a program is also determined by the amount of data that needs to be communicated between the processes. The ability of a code to effectively use an increasing number of cores determines the parallel efficiency and this depends on the partitioning and communication strategies.

As discussed above, Incompact3D uses 2DECOMP&FFT to provide a ‘pencil’ decomposition, which is shown in figure 4.5(a). The computation of derivatives (section 4.1.2) and FFTs in a particular direction requires the pencil to be aligned in that direction. This requires the domain decomposition to be transposed, as indicated by the different orientations of the pencils in figure 4.5(a). The 2DECOMP&FFT library provides subroutines for transposition based on the `MPI_Alltoallv` subroutine. For cases run using Incompact3D, the strong scaling of the problem, where the same problem is tested on an increasing number of CPUs, is investigated. Ideally, as the number of cores increases, the wall time per time step should reduce proportionally, leading to a ‘linear’ speed-up. In the present study, the simulations are run

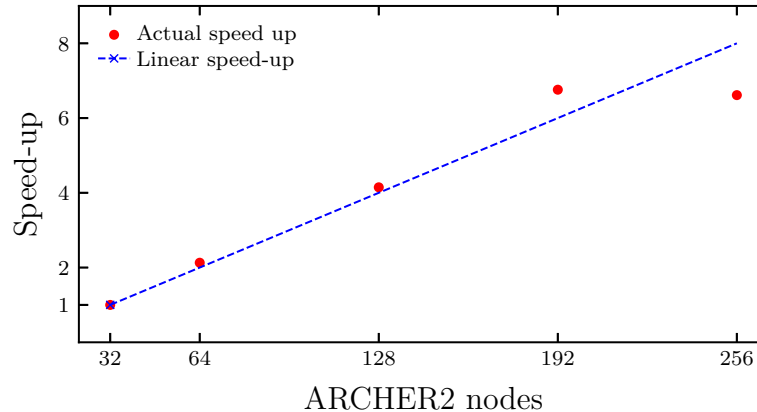


Figure 4.6: Strong scaling for a spatially accelerating TBL turbulent boundary layer with 1.4 billion points (case 3 from chapter 6).

on the maximum number of cores where at least linear speed-up is observed. Figure 4.6 shows the strong scaling for a turbulent boundary layer simulation with 1.4 billion mesh points on ARCHER2 and shows that for up to 192 nodes (24576 cores), Incompact3D exhibits super-linear scaling with the speed-up falling below linear for 256 nodes.

CHAPSim uses a slab decomposition, with most computations being performed on the XZ slab and most inter-process communication performed using a classic halo exchange, in which only the boundary information of each slab is communicated. Where TDMAs are performed in the y direction, the domain is transposed into the XY slab (figure 4.5(b)) using `MPI_Sendrecv` calls. The use of slab decomposition is less parallel efficient because the amount of data communicated during the halo exchange per process does not decrease as the number of cores increases. The maximum number of cores is also limited by the number of cells in the y or z direction. For CHAPSim, the number of cores used was determined such that there should be a core for each 1 or 2 cells in the y direction. While this is not parallel efficient, it ensures the simulations are completed in a reasonable time.

It is also important to consider file input-output (I/O) and data management. Significant amounts of data may be produced for large simulations such as the TBL case above. As a result, the amount of data written to disk must be minimised, particularly for the turbulent statistics. This is achieved by performing averaging in the homogeneous directions on the fly and thus reducing the total amount of data being written to disk. MPI-IO is used for all large data writes, allowing the different processes to write collectively to disk. Striping is used on the ‘Lustre’ parallel file

system on ARCHER2, meaning that multiple processes can write to the same file simultaneously, which significantly increases the speed of file I/O for large files.

4.4 Channel flow and temporal acceleration

For the channel flows in this study, the non-dimensional Navier-Stokes equations are solved with the initial bulk velocity, U_{b0}^* as the characteristic velocity scale and the half-channel height, h^* as the characteristic length scale both in Incompact3D and CHAPSim. This results in the non-dimensional variables: $u = u^*/U_{b0}^*$, $x = x^*/h^*$, $t = t^*U_{b0}^*/h^*$, and $p = p^*/\rho_0^*U_{b0}^{*2}$. The domain extents are consequently $(0, L_x)$, $(0, 2)$, $(0, L_z)$ in the streamwise, wall-normal, and spanwise directions, respectively. Consistent with previous numerical studies of streamwise homogeneous channel flow, the mean flow and turbulence are developed in time during the initial phase of the simulation. This contrasts with experiments where the flow develops in space and time before the test section.

4.4.1 Initial and boundary conditions

The velocity field in Incompact3D and CHAPSim is initialised with

$$u_i(x, y, z; t = 0) = \bar{u}_p(y)\delta_{i1} + u'_i(x, y, z) \quad (4.18)$$

where $\bar{u}_p(y)$ is the laminar Poiseuille profile, δ_{i1} is the Kronecker delta, and $u'_i(x, y, z)$ is an additional random perturbation. For Incompact3D, $u'_i(x, y, z)$ has been modified compared to the base source code to promote a more rapid development of the turbulent channel flow. This is particularly important for temporal acceleration cases, where the duration of the transient arising from the acceleration is usually short compared with the time required for the flow to fully develop after initialisation. In this case, the $u'_i(x, y, z)$ distribution is given by

$$u'_i(x, y, z) = A(x, y, z)[\exp(-\ln(y/0.1)^2) + \exp(-\ln((2-y)/0.1)^2)], \quad (4.19)$$

where $A(x, y, z)$ is an array of random numbers in the range $[-b, b]$ generated by a pseudo-random number generator (Fortran intrinsic function `random_number`) where b is an amplitude specified in the input file. The random number generator is seeded with a number based on the system clock (time since 1st January 1970). This means that the $u'_i(x, y, z)$ will be different each time the simulation is run, allowing for repeated independent runs for temporally accelerating flows where time averaging is

not permitted. The log-normal form of equation (4.19) results in strong fluctuations close to the wall with peaks at $y = 0.1$ and $y = 1.9$, which was found to trigger turbulence in the channel rapidly. The code is also modified to use a higher Reynolds number in the initial stage of the flow, which further promotes transition.

Periodic boundary conditions are used in the streamwise and spanwise directions. In the wall-normal direction, a no-slip condition is applied for the velocity field, and homogeneous Neumann boundary conditions are used for pressure. For channel flows, a uniform streamwise pressure gradient is applied at each time step to maintain mass flow with

$$S = \frac{U_b^{des} - U_b}{\Delta t}. \quad (4.20)$$

For steady channel flows, the desired bulk velocity, $U_b^{des} = 1$, while for temporally accelerating cases, U_b^{des} varies with time. In practice, this is implemented by adding a uniform velocity, $U_b^{des} - U_b$ to the velocity field at the start of each time step. For a given time-step the $U_b^{des} - U_b$ is $< 10^{-5}$. For temporally accelerating channel flow, it is necessary to ensure that the flow is fully developed and the statistics are stationary before beginning the acceleration.

4.5 Simulation of turbulent boundary layers

The simulation of turbulent boundary layers has some additional challenges compared with turbulent channel flow. This includes the presence of streamwise inhomogeneity, which invalidates the use of periodic boundary conditions in the streamwise direction, and the need to generate reliable inflow conditions. Two main approaches to generating inflow data are available in the literature. In the first, a laminar inflow is used in conjunction with a numerical ‘trip’ to trigger transition. Prominent studies that have used this approach include Schlatter et al. [211] and Wu and Moin [144]. The second approach, developed in Lund et al. [212], uses a turbulent inflow condition with the velocity components on the inlet plane determined by recycling and rescaling a plane from the flow interior. This method eliminates the need to simulate transition, meaning smaller domains, and hence reduces computational cost. Other studies using the ‘recycling-rescaling’ method include Sillero et al. [3] and Simens et al. [16].

In this study, the recycling-rescaling method has been implemented in Incompact3D and is used in order to reduce computational cost. For spatially accelerating flows, this is particularly important because of the fine mesh required to adequately resolve the onset of retransition. It is also anticipated that in the future, simulations of spatially accelerating flows at much higher Reynolds numbers than the current

study will be required to bridge the gap between recent experiments and simulations. The current implementation is capable of achieving substantially higher Reynolds numbers efficiently. It should be noted that Schlatter and Örlü [14] highlighted that both approaches could be used effectively in the simulation of turbulent boundary layers. The recycling-rescaling method has also been widely used in the study of spatially accelerating TBLs [110, 120, 10, 213, 214, 215]. In this implementation in Incompact3D, the method of Lund et al. [212] has been used with some improvements to mean flow initialisation and a simplified freestream condition to impose the acceleration.

4.5.1 Implementation details

For turbulent boundary layer cases, the non-dimensional Navier-Stokes equations are solved with the inlet freestream velocity, $U_{\infty,0}^*$ as the characteristic velocity scale and the target inlet momentum thickness θ_0^* as the characteristic length scale. This leads to the non-dimensional flow variables: $u = u^*/U_{\infty,0}^*$, $x = x^*/\theta_0^*$, $t = t^*U_{\infty,0}^*/\theta_0^*$, and $p = p^*/\rho_0^*U_{\infty,0}^{*2}$ and a scaling momentum thickness Reynolds number, $Re_0 = Re_{\theta,0} = U_{\infty,0}^*\theta_0^*/\nu$, a quantity often given in studies of turbulent boundary layers. The momentum thickness is an output from the simulation, and hence, the target value of $Re_{\theta,0}$ can be approached by iteratively adjusting the conditions. Therefore, the inlet conditions must approach the desired conditions after the start of the simulations such that the conditions in the domain are predictable *a priori*.

4.5.1.1 Recycling-rescaling method

The basic approach of Lund et al. [212] is used in the present study. Lund et al. [212] uses scaling arguments to rescale the mean flow and turbulent fluctuations from the recycling plane to the inlet plane. This has been found to be capable of locking onto the statistics expected of zero-pressure gradient TBLs within a short distance of the inlet. Other rescaling approaches have also been suggested [216, 217], based on the scalings derived from George and Castillo [218]. A schematic of the recycling-rescaling method is shown in figure 4.7. In the following sections, the following conventions will be used: subscripts *inlt* and *recy* represent quantities at the inlet and recycling planes, respectively and the superscript *des* indicates a desired quantity. The superscripts *inner* and *outer* indicate where in the boundary layer, a quantity is used. For the mean streamwise velocity, the law of the wall and velocity defect law are used,

$$\frac{\bar{u}}{u_\tau} = F_1(y^+) \quad \frac{U_\infty - \bar{u}}{u_\tau} = F_2(\eta), \quad (4.21)$$

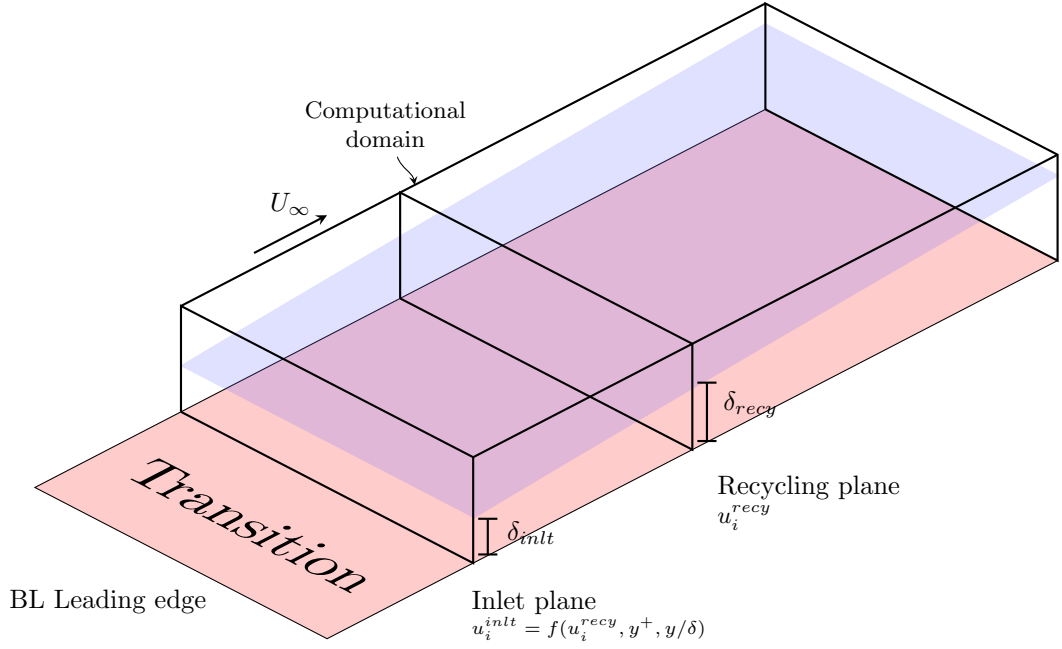


Figure 4.7: Schematic of the recycling-rescaling method showing the computational domain, inlet, and recycling planes in relation to the boundary layer leading edge.

where F_1 is the law of the wall and F_2 is the velocity defect law.

The following relations can be derived relating the recycling and inlet planes in the inner and outer parts of the boundary layer.

$$\bar{u}_{inlt}^{inner}(y_{inlt}^+) = \gamma \bar{u}_{recy}(y_{recy}^+) \quad (4.22)$$

$$\bar{u}_{inlt}^{outer} = \gamma \bar{u}_{recy}(\eta_{inlt}) + (1 - \gamma)U_\infty, \quad (4.23)$$

where $\gamma = u_\tau^{inlt}/u_\tau^{recy}$. For the wall-normal mean velocity, it was assumed that in the inner and outer regions, respectively

$$\bar{v}/U_\infty = F_3(y^+) \quad \bar{v}/U_\infty = F_4(\eta). \quad (4.24)$$

While this is not strictly true, Lund et al. [212] indicated that it was an adequate assumption due to the small value of the wall-normal mean velocity. The inlet mean wall-normal velocity is consequently given by

$$\bar{v}_{inlt}^{inner}(y_{inlt}^+) = \bar{v}_{recy}(y_{recy}^+) \quad (4.25)$$

$$\bar{v}_{inlt}^{inner}(\eta_{inlt}) = \bar{v}_{recy}(\eta_{recy}). \quad (4.26)$$

The spanwise mean velocity, $\bar{w} = 0$. The velocity fluctuations at the inlet are based on the similarity of the normal Reynolds stresses in the inner and outer layer

$$\overline{u_i'^2}^+ = F_5(y^+) \quad \overline{u_i'^2}^+ = F_6(\eta), \quad (4.27)$$

While these scalings do not hold over a large Reynolds number range [219], the Reynolds number dependence is weak. These scalings lead to

$$(u'_i)_{inner}(y_{inlt}^+) = \gamma u_i(y_{recy}^+), \quad (4.28)$$

$$(u'_i)_{outer}(\eta_{inlt}) = \gamma u_i(\eta_{recy}). \quad (4.29)$$

The mean and fluctuating components are combined into a composite profile using a weighting function

$$(u_i)_{inlt} = [(\bar{u}_i)_{inlt}^{inner} + (u'_i)_{inlt}^{inner}][1 - W(\eta_{inlt})] + [(\bar{u}_i)_{inlt}^{outer} + (u'_i)_{inlt}^{outer}]W(\eta_{inlt}), \quad (4.30)$$

With the weighting function $W(\eta_{inlet})$ defined as:

$$W(\eta) = \frac{1}{2} \left[1 + \tanh \left(\frac{\alpha(\eta - b)}{(1 - 2b)\eta + b} \right) / \tanh(\alpha) \right]. \quad (4.31)$$

If $\alpha = 4$ and $\beta = 0.2$, $W(\eta) = 0.5$ at $\eta = 0.2$, the traditional boundary between the inner and outer layers. While it is interesting to note that equation (4.30) assumes scale separation between the inner and outer regions of the boundary layer, which is unlikely to be fully the case for any DNS studies using this method*. For stability reasons, equation (4.30) is imposed before equation (4.1c) which is equivalent to imposition before equation (4.1b) (when the other boundary conditions are imposed) with

$$v^* = v_{inlt} - \Delta t \frac{\partial \tilde{p}^n}{\partial y} \quad w^* = w_{inlt} - \Delta t \frac{\partial \tilde{p}^n}{\partial z}. \quad (4.32)$$

This modification of equation (4.30) does not have an adverse effect on flow development, and the flow developing from the inflow after a short distance attains statistics consistent with ZPGTBL. This will be shown in section 4.7.

The recycling-rescaling method requires the computation of the mean flow. The mean velocity at time-step $n + 1$ is determined using a similar approach to Lund et al. [212].

$$\bar{u}_i^{n+1} = \frac{\Delta t}{T} \langle u_i \rangle_z^n + \left(1 - \frac{\Delta t}{T} \right) \bar{u}_i^n, \quad (4.33)$$

where $\langle u_i \rangle_z^n$ indicates the spanwise averaging only, and T is a reference time period. Initially, T is fixed so that the contributions of older averages become less significant with time. Eventually, the weighting is changed such that the contributions of all subsequent times are equally weighted. From equation (4.33), $u_{\tau,recy}$, δ_{recy} and θ_{recy}

*Scale separation typically requires $Re_\tau \geq 2000$

are computed with δ being the 99% thickness. The fluctuating velocities are defined by

$$u_i^{n+1} = u_i^n - \langle u_i \rangle_z^n, \quad (4.34)$$

ensuring that the fluctuation has zero mean. $u_{\tau, inlt}$ and δ_{inlt} are determined such that the desired conditions at the inlet are approached. $u_{\tau, inlt}$ is specified by relating the flow at the inlet to that at the recycling plane using the relation [212, 19]

$$u_{\tau} \propto Re_{\theta}^{-1/8} \implies u_{\tau, inlt} = u_{\tau, recy} \frac{\theta_{recy}^{-1/8}}{\theta_{inlt}^{des}}, \quad (4.35)$$

with the desired inlet momentum thickness $\theta_{inlt}^{des} = 1$. The boundary layer thickness at the inlet is determined such that measured inlet momentum thickness, θ_{inlt} approaches 1. A relaxation-based scheme is used

$$\delta_{inlt}^{n+1} = \delta_{inlt}^n + \alpha(1 - \theta_{inlt})\delta_{inlt}^n, \quad (4.36)$$

where α is a relaxation factor. Therefore, if $\theta_{inlt} < 1$, δ_{inlt}^{n+1} increases and vice versa. Given that equation (4.33) will not immediately respond to such changes, a limit to the value of δ_{inlt}^{n+1} is imposed to prevent δ_{inlt}^{n+1} quickly reaching extreme values

$$|\delta_{inlt}^{n+1} - \delta_{inlt}| < 1, \quad (4.37)$$

where δ_{inlt} is the measured inlet boundary layer thickness. This approach was found to be effective at reaching the desired inlet Reynolds number with the computed $Re_{\theta,0}$ always within 1% of its desired value.

4.5.1.2 Computational domain and boundary conditions

Similarly to other numerical studies of spatially accelerating TBLs [110, 10], the acceleration is performed on a Cartesian mesh without explicitly contracting the flow domain by applying freestream boundary conditions that mimic the effect of the contraction on the wall-normal and streamwise velocities. This approach considers the flow development on a plane wall where it is assumed that the opposite contracting wall is sufficiently far away that the boundary layer developing on that wall does not affect the plane wall except for causing the desired flow contraction and streamwise flow acceleration. The resulting computational domain and its relationship to a typical experimental setup are depicted in figure 4.8.

The acceleration is imposed by specifying the freestream wall-normal boundary condition such that a desired freestream streamwise velocity, U_{∞}^{des} , is approached. The boundary conditions at L_y are

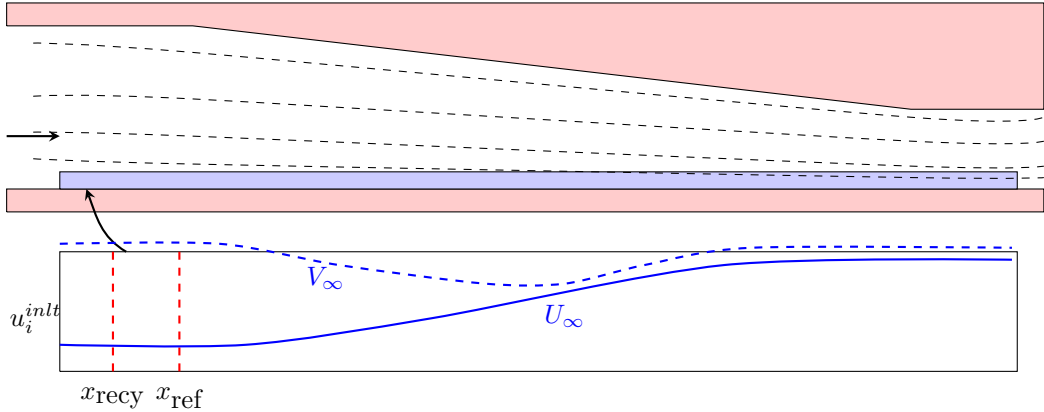


Figure 4.8: Schematic of the computational domain used for a typical spatially accelerating TBL compared with a typical experimental setup

$$\frac{\partial u}{\partial y} = 0 \quad \frac{\partial v}{\partial y} = -\frac{dU_\infty^{des}}{dx} \quad \frac{\partial w}{\partial y} = 0, \quad (4.38)$$

where the boundary condition for v is a statement of mass continuity at the freestream. After the correction step (equation (4.1d)), $\partial_y v = -d_x U_\infty^{des}$ will not apply exactly. Nonetheless, figure 4.9(a) shows that U_∞^{des} is recovered accurately. The wall-normal mean velocity is shown in figure 4.9(b) and shows large wall-ward velocities originating from the freestream consistent with the effect of flow contraction, noting that there is a mild suction at the freestream upstream of acceleration consistent with a slowly growing boundary layer there. The approach used here differs from that used in Piomelli et al. [110] which uses the integrated continuity equation where $V_\infty = U_\infty^{des} d_x \delta_u + (\delta_u - h) d_x U_\infty^{des}$. However, equation (4.38) was found to tend to the desired freestream velocity more rapidly as it does not depend on a local computation of δ_u . Testing indicated that both approaches produced essentially the same results. Acceleration could also be imposed using the immersed boundary method to explicitly contract the flow, although the current approach is more straightforward to implement and less computationally demanding.

Similar to many studies of pressure gradient turbulent boundary layers [10, 215, 220], a single computational domain is used for all cases in this study. As the method of Lund et al. [212] is developed for ZPG flows, it is necessary to ensure that the acceleration has a minimal effect on the recycling plane. This was ensured by checking that the statistics upstream of the FPG region are consistent with ZPG turbulent boundary layers *a posteriori*, which indicated that only small deviations were observed.

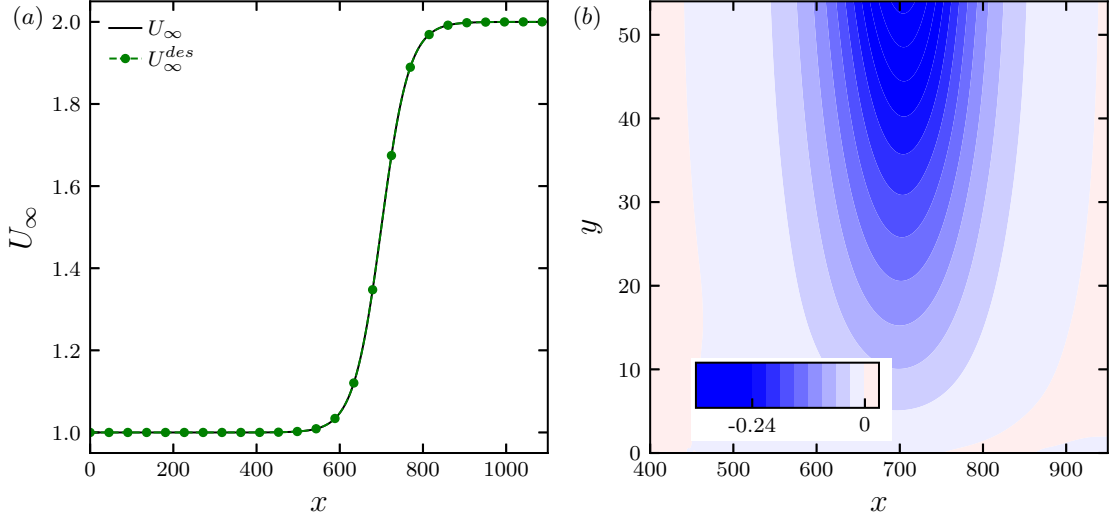


Figure 4.9: U_∞ compared with U_∞^{des} and the wall-normal mean velocity, \bar{v} showing substantial inflow as a result of the flow contraction induced by equation (4.38).

A no-slip/impermeability condition is applied at $y = 0$, and the spanwise direction is periodic. A convective outlet boundary condition, based on the one-dimensional advection equation, is applied at $x = L_x$,

$$\frac{\partial u_i}{\partial t} + U_c \frac{\partial u_i}{\partial x} = 0, \quad (4.39)$$

where U_c is the local streamwise velocity at the outflow plane. Homogeneous Neumann boundary conditions are used for the pressure at the inlet, outlet, freestream, and wall, with a periodic boundary condition used for the spanwise direction. The Poisson equation is singular with these boundary conditions, with the pressure only determined up to an additive constant. As a result, the right-hand-side of the Poisson equation must satisfy the compatibility condition [16]

$$\int_{\mathcal{V}} DG\tilde{p}^{n+1} d\mathcal{V} = \int_{\mathcal{S}} \frac{\partial \tilde{p}^{n+1}}{\partial n} d\mathcal{S} = 0 = \int_{\mathcal{V}} Du^{**} d\mathcal{V} = \int_{\mathcal{S}} u^{**} \cdot \mathbf{n} d\mathcal{S}, \quad (4.40)$$

which is a statement of global mass conservation on the predicted velocity field. As a result, a small uniform velocity ($< 10^{-5}$) is added to u at the outlet plane such that equation (4.40) is satisfied.

4.5.1.3 Initialisation and flow development

The flow is initialised for TBL simulations such that the duration of the initial transient is minimised. For the mean streamwise velocity, it is desired that $\delta(x, t = 0)$,

$\theta(x, t = 0)$, and $u_\tau(x, t = 0)$ are consistent with ZPG turbulent boundary layers to aid the initial development of the recycling method. It is also desired that the θ_{int} is initialised close to θ_{int}^{des} . The composite profile proposed by Nickels [221] is used to determine \bar{u}^+ with correlations, effective at low Reynolds number, used to determine the streamwise development of u_τ and δ . Nickels' profile has several advantages, such as its relative simplicity, ability to capture the wake accurately even at low Reynolds numbers [14], and its asymptotic behaviour as $y \rightarrow \infty$. This approach represents an improvement over previous studies such as Lund et al. [212] and Lee and Sung [222], which used Spalding's law of the wall [223], which does not asymptote as $y^+ \rightarrow \infty$, does not account for the wake, and requires root-finding. Luchini [224] also showed that Spalding [223] exhibited worse agreement with numerical data than alternatives. The composite profile developed by Luchini [224] is a possible alternative to the current approach. The Nickels profile is given by

$$\bar{u}^+ = \bar{u}_s^+ + \bar{u}_o^+ + \bar{u}_w^+, \quad (4.41)$$

where \bar{u}_s describes the viscous sublayer, \bar{u}_o describes the overlap region and \bar{u}_w describes the wake region. These components are defined as

$$\bar{u}_s^+ = y_c^+ \left[1 - \left(1 + 2(y^+/y_c^+) + \frac{3}{2}(y^+/y_c^+)^2 \right) e^{-3y^+/y_c^+} \right], \quad (4.42a)$$

$$\bar{u}_o^+ = \frac{1}{6\kappa} \ln \left(\frac{1 + (0.6(y^+/y_c^+))^6}{1 + \eta^6} \right), \quad (4.42b)$$

$$\bar{u}_w^+ = b \left[1 - \exp \left(-\frac{5(\eta^4 + \eta^8)}{1 + 5\eta^3} \right) \right]. \quad (4.42c)$$

where κ is von Kármán constant and b represents the wake strength which is determined by taking equation (4.41) with $y^+ \rightarrow \infty$

$$b = U_\infty^+ - y_c^+ - \frac{1}{6\kappa} \ln \left(\frac{0.6^6 \delta^{+6}}{y_c^{+6}} \right), \quad (4.43)$$

where $U_\infty^+ = \sqrt{2/C_f}$, $y_c^+ = 12$. δ^+ and C_f are determined from correlations [19, 14]

$$C_f = 0.024 Re_\theta^{-1/4}, \quad (4.44)$$

$$\delta^+ = Re_\tau = \chi 1.13 Re_\theta^{0.843}. \quad (4.45)$$

where $\chi = 0.86$ is a correction factor that accounts for the difference between the definition of δ originating from Nickels' composite profile and the 99% thickness which equation (4.45) is based on. Re_θ is computed at each streamwise location, x , from a

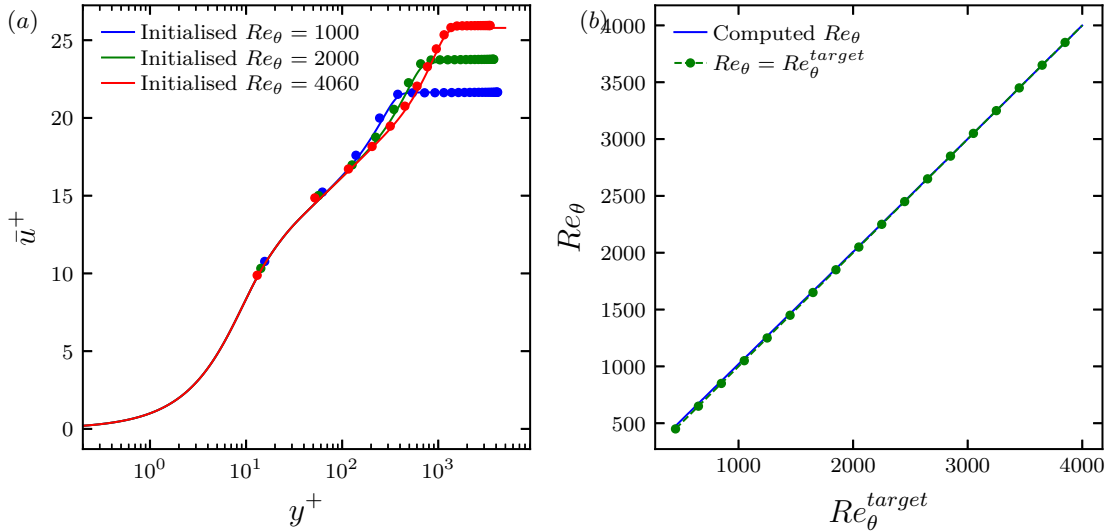


Figure 4.10: Initialisation of the streamwise mean velocity. (a) initialised \bar{u}^+ at $Re_\theta = 1000, 2000, 4060$ (lines) compared with Schlatter and Örlü [14] (markers). (b) computed Re_θ compared with target value.

correlation derived from equation (4.44) and the momentum integral equation $2 \frac{dRe_\theta}{dRe_x} = C_f$

$$Re_\theta = \left[\frac{3x}{200} Re_{\theta,0} + Re_{\theta,0}^{5/4} \right]^{4/5}. \quad (4.46)$$

The mean streamwise velocity is recovered from $\bar{u} = u_\tau \bar{u}^+$ where $u_\tau = \sqrt{C_f/2}$. The mean wall-normal velocity is determined from the computed values of \bar{u} using the integrated mean continuity equation,

$$\bar{v}(x, y) = - \int_0^y \frac{\partial \bar{u}}{\partial x} dy. \quad (4.47)$$

The resulting \bar{u}^+ is shown in figure 4.10(a) compared with DNS data [14] highlighting the similarity of the initialised flow with reference data. Figure 4.10(b) shows an almost exact overlap between a given value of Re_θ^{target} with the resulting Re_θ computed from the initialised profile indicating an effective mean flow initialisation strategy.

A numerical trip is used to initiate turbulence in the domain. This trip is a volumetric body force applied to the wall-normal momentum equation at periodic intervals in the streamwise direction. The tripping function is based on Schlatter and Örlü [225] and is already implemented in Incompact3D [226]. This forcing displaces fluid in the wall-normal direction, leading to streak generation and transition. After

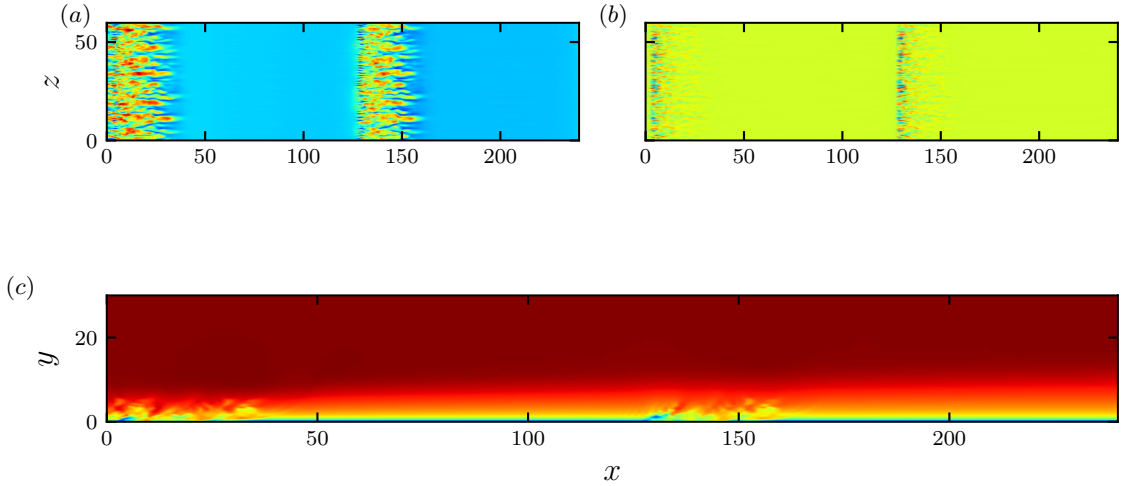


Figure 4.11: Tripping method: u and v early in the simulation showing the periodic arrays of tripping locations and the resulting turbulent structures. (a) u' $x - z$ plane, (b) v' $x - z$ plane. (c) u' $x - y$ plane

a user-defined amount of time, the forcing is removed, and the turbulence is sustained solely through the turbulent inflow described above. Figure 4.11(b) shows the periodic array of tripping locations in the wall-normal velocity shortly after the start of a simulation with the resulting near-wall streaks and turbulence visible in figures 4.11(a) and 4.11(c).

4.5.2 Specific considerations for the simulation of TBLs

In simulations of TBLs, the height of the computational domain, L_y is a parameter to be determined. L_y should not have any unintended side effects on the behaviour of turbulence within the computational domain. In their assessment of TBL simulations, Schlatter and Örlü [14] noted that the simulations that had taller and wider domains tended to perform better, highlighting the data of Simens et al. [16] and Schlatter et al. [227] as performing best. Consequently, we have used domain sizes similar to those studies with the height and width that exceeded $3\delta_{99}$ for all streamwise locations. These guidelines have also been used in other studies [228]. All cases presented in this study have $L_y \gtrsim 3 \max(\delta_{99})$ and $L_z \gtrsim 3 \max(\delta_{99})$.

The distance between the inlet and recycling planes is also an important consideration. Simens et al. [16] highlighted that the recycling-rescaling method introduced an artificial periodicity into the turbulent boundary layer, which could be observed even in the instantaneous data [222]. This periodicity was only completely eliminated if the distance between the recycling and inlet planes exceeded $x/\theta_0 > 850$. In general, they conclude that the recycling plane should be at least 20-30 boundary layer thicknesses from the inlet, as this region tends to be governed by the assumptions made to generate the inflow conditions. While it has been noted that accurate first and second-order statistics can be achieved even with relatively short distances [10, 222], it is desirable to reduce the effect as much as possible. Morgan et al. [229], studying supersonic boundary layers using the recycling-rescaling method, assessed a number of strategies for minimising these artificial periodicities and hence enabling shorter distances between the inlet and recycling planes. These include applying a spanwise shift or a reflection along the spanwise centreline to the generated inflow. Three test cases have been run to assess the effect of shifting and reflecting the inflow. The distance between the inlet and recycling planes in these tests, $L_{recy} \approx 40\delta_0$. The effect of these approaches is presented in figure 4.12, which shows the spatiotemporal autocorrelation,

$$R_{11}(x, y; \Delta t, \Delta z) = \langle u'(x, y, z, t)u'(x, y, z + \Delta z, t + \Delta t) / \overline{u'u'}(x, y) \rangle \quad (4.48)$$

at the recycling plane at $y/\delta \approx 0.5$. The temporal separation is normalised by L_{recy}/U_{conv} such that one on the abscissa scale indicates the approximate time lag for a recycled plane to reach the recycling plane. Figure 4.12(a) shows R_{11} for a case without any shift or reflection. The negative lobes, typical of the spanwise autocorrelations of u' , can be observed above and below the central peak at $\Delta t = \Delta z = 0$. Strong secondary peaks can be observed at $\Delta t U_{conv}/L_{recy} = 1$, indicating a strong correlation between the inlet and recycling planes. There does not appear to be a peak at $\Delta t U_{conv}/L_{recy} = 2$. For the $L_z/2$ shifted case (figure 4.12(b)), there is still a second peak at $\Delta t U_{conv}/L_{recy} = 1$ although it is weaker and shifted. In this case, there is a small peak at $\Delta t U_{conv}/L_{recy} = 2$. Figure 4.12(c) shows only a very minor secondary peak at $\Delta t U_{conv}/L_{recy} = 2$, indicating the periodicity has been weakened significantly and occurs at much larger Δt . which together with the relatively large L_{recy} prevents the periodicity from significantly affecting the inflow time series. Hereafter, the reflection method has been applied to the simulations of turbulent boundary layers.

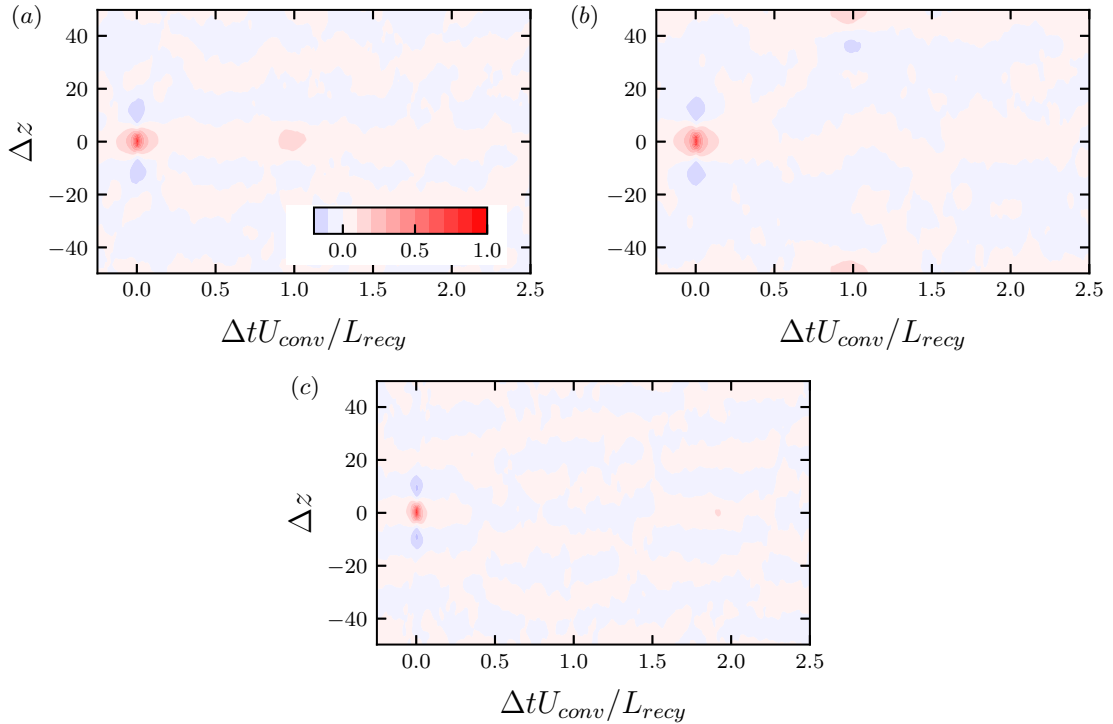


Figure 4.12: Spatiotemporal autocorrelation of the streamwise velocity showing spurious periodicities in the recycling method and several mitigation approaches. (a) Normal Recycling method. (b) Shifting the inlet plane by $L_z/2$ in the z direction. (c) Reflecting the inlet plane about $z = L_z/2$.

4.6 Computation of statistics

4.6.1 Statistic computation for different flow configurations

The present study investigates a range of flow configurations that require slightly different definitions of key statistics. Below, we will describe the discrete statistics in terms of the statistical moments of a random variable, $\phi(x, y, z; t)$ for brevity. More advanced statistics will be defined as required. For Incompact3D, all statistics have been computed on the fly with the Python packages `matplotlib`, `pgfplots` and `pyvista` used for visualisation. For CHAPSim, most statistics were calculated on the fly, with some more advanced quantities computed using saved instantaneous data.

Stationary channel flow

This flow configuration is found in the validation cases and the turbulence generator of the moving wall case. These cases are averaged in the homogeneous spanwise and

streamwise directions, in time and about the midplane. Hence, for the m^{th} statistical moment of $\phi(x, y, z; t)$

$$\overline{\phi^m}(y) = \frac{1}{N_t N_z N_x} \sum_t^{N_t} \sum_i^{N_x} \sum_k^{N_z} \phi^m, \quad (4.49)$$

where N_t is the total number of timesteps, and N_x and N_z are the number of points in the streamwise and spanwise direction, respectively. The final statistics of simulation are computed with the effect of the initial transient removed *a posteriori* such that the average between time step N_{t1} and N_{t2} is

$$\overline{\phi^m}(y) = \frac{N_{t2} \overline{\phi^m}_{t2}(y) - N_{t1} \overline{\phi^m}_{t1}(y)}{N_{t2} - N_{t1}}. \quad (4.50)$$

where $\overline{\phi^m}_{t2}$ and $\overline{\phi^m}_{t1}$ are the average (equation (4.49)) at steps N_{t2} and N_{t1} respectively. N_{t1} is determined using monitoring points and spanwise averaged quantities to assess when the flow has become stationary. The approach to stationary condition for a turbulent channel flow is shown in figure 4.13, which also highlights the rapid approach to the steady conditions using the methods discussed in section 4.4.

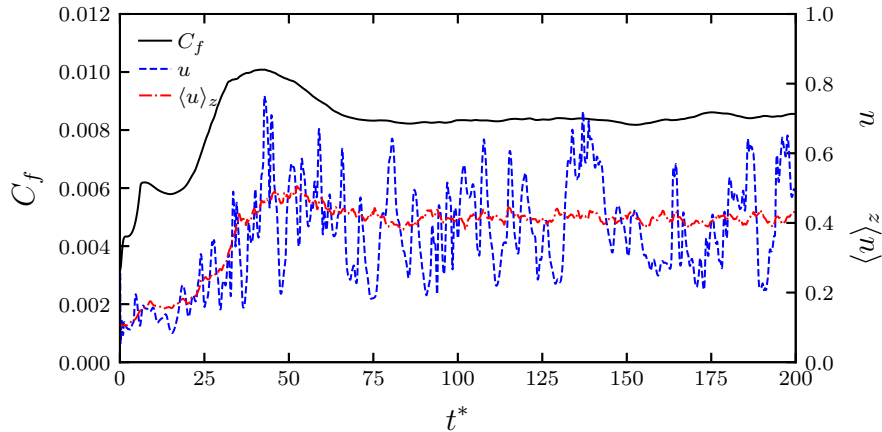


Figure 4.13: Monitoring fully developed channel flow at $Re_\tau = 180$: Instantaneous, u and spanwise averaged streamwise velocity, \bar{u} (y axis right), and skin friction coefficient C_f (y axis left).

Temporally accelerating channel flow

The temporally accelerating channel flows are also averaged in the homogeneous spanwise and streamwise directions, and about the midplane. Due to the lack of

Table 4.1: Case setup for the channel flow validation at $Re_\tau = 180$ and $Re_\tau = 395$.

	$Re_{\tau,ref}$	Re_τ	L_x	L_z	N_x	N_y	N_z	Δx^+	Δz^+	Δy_w^+	Δy_c^+
CHAPSim	180	178	10	4	540	288	360	3.3	1.98	0.242	1.87
Incompact3D 1a	180	181	18	6	540	257	240	6.04	4.53	0.401	5
Incompact3D 1b	180	182	18	6	324	181	154	10.1	7.11	0.505	8.13
Incompact3D 2	395	391	18	6	882	393	400	7.98	5.87	0.585	6.81
Vreman and Kuerten [230]	180	180	4π	$\frac{4\pi}{3}$	512	256	256	4.4	2.9		2.2
Moser et al. [231]	395	392	2π	π	256	193	192	10	6.5		6.5

stationarity in temporal acceleration, the simulations are also run multiple times and ensemble-averaged to achieve statistical convergence. $\overline{\phi^m}$ is given by

$$\overline{\phi^m}(y; t) = \frac{1}{N_e N_z N_x} \sum_e^{N_e} \sum_i^{N_x} \sum_k^{N_z} \phi^m. \quad (4.51)$$

where N_e is the number of ensembles.

Streamwise-developing flows

Streamwise developing flows such as the spatially accelerating turbulent boundary layers and moving wall accelerations are averaged in the spanwise direction and in time yielding

$$\overline{\phi^m}(x, y) = \frac{1}{N_t N_z} \sum_n^{N_t} \sum_k^{N_z} \phi^m. \quad (4.52)$$

The initial transients are removed using the same approach as stationary channel flows. The moving wall accelerations are also averaged about the midplane.

4.7 Validation and assessment of numerical tools

4.7.1 Turbulent channel flow

CHAPSim and Incompact3D are now validated for fully-developed turbulent channel flow at $Re_\tau = 180$ and $Re_\tau = 395$ against the reference DNS data of Vreman and Kuerten [230] and Moser et al. [231]. The characteristics of each case and the validating data are shown in table 4.1. Note that for $Re_\tau = 180$, Incompact3D has been validated with both a fine and coarse grid to highlight that Incompact3D can accurately reproduce statistics even at marginal resolution.

The mesh resolution is within the bounds specified in section 4.3 with the Δy^+ at the wall less than one, although the grid resolutions are somewhat coarser than the

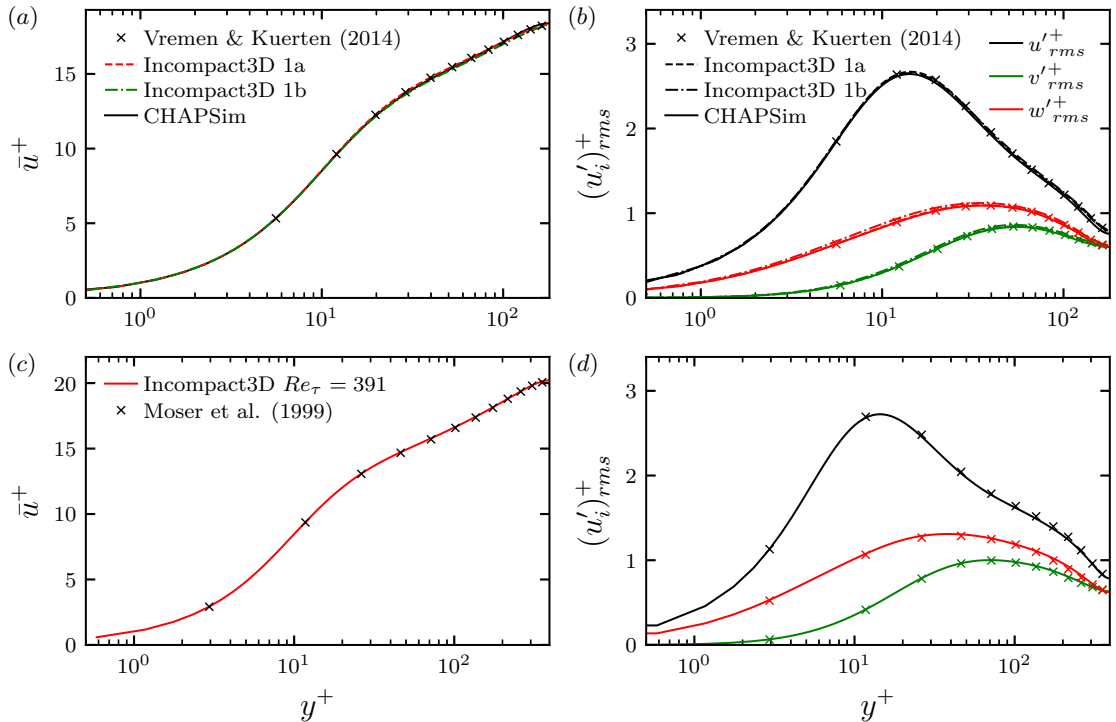


Figure 4.14: Channel flow validation: (a) \bar{u}^+ vs y^+ at $Re_\tau = 180$; (b) Normal Reynolds stresses at $Re_\tau = 180$; (c) \bar{u}^+ vs y^+ at $Re_\tau = 395$; (d) Normal Reynolds stresses at $Re_\tau = 395$.

Vreman and Kuerten [230] data. The domain sizes are larger than the comparison data, particularly for $Re_\tau = 395$. Figure 4.14 shows that for the fine mesh cases, there is excellent agreement between the solvers used herein and the reference data for the mean streamwise velocity and the RMS of the fluctuating velocity components. The agreement is still very good for the coarser mesh case, although perhaps slightly worse for w'_{rms} close to the wall. The streamwise Reynolds stress budget for $Re_\tau = 180$ is shown in figure 4.15. Good agreement is observed for both CHAPSim and Incompact3D.

4.7.2 Temporally accelerating channel flow

For the transient channel flow simulations, we compare Incompact3D with the data from He and Seddighi [15]. This case is a step-change temporal acceleration where the bulk velocity is increased linearly by a factor of 2.6 over a short duration ($\Delta t U_{b1}/\delta = 0.22$). The flow configurations for each case are shown in table 4.2, with the present case having a slightly finer mesh and larger domain sizes in the periodic directions.

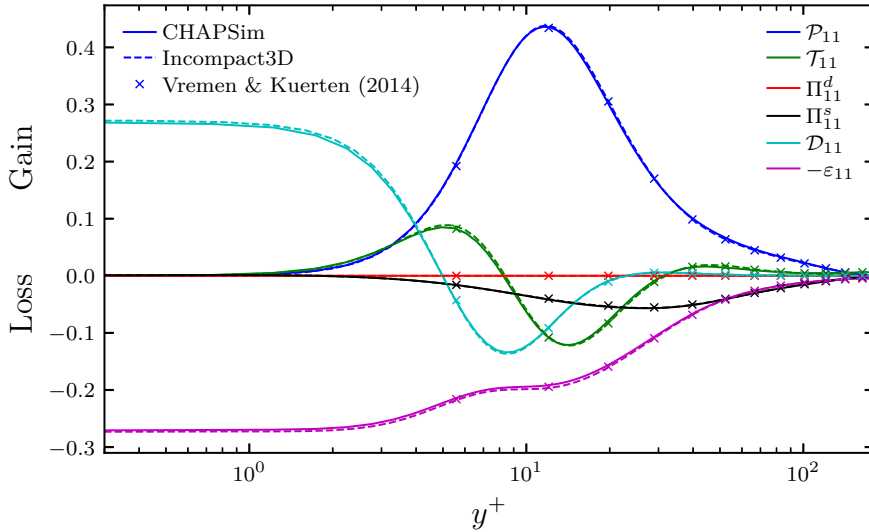


Figure 4.15: $\overline{u'u'}$ budget at $Re_\tau = 180$.

Figure 4.16 shows the skin friction coefficient and the inner-scaled mean velocity. The transition process that occurs in temporal acceleration is recovered with C_f decreasing to a minimum before increasing after the onset of transition. The present results closely correspond with He and Seddighi [15] for both the C_f and \bar{u}^+ with the strong deviation of the latter from the law of the wall during the transient captured well.

Table 4.2: Simulations configuration for temporal acceleration validation.

Case		Re_b	Re_τ	Δx^+	Δz^+	Δy_w^+	Δy_c^+	L_x	L_z
Present	Initial flow	2825	179.4	4.27	2.99	0.303	3.47	18	6
	Final flow	7404	418.3	9.96	6.97	0.706	8.09	18	6
He and Seddighi [15]	Initial flow	2818	179.3	3.2	1.9	0.16	2.78	18	5
	Final flow	7404	418	7.3	4.3	0.37	6.4	18	5

4.7.3 Zero pressure gradient TBLs

The ZPG case is summarised in table 4.3 and validated against DNS data from Spalart [17], Simens et al. [16] and Schlatter and Örlü [14], and the experimental data from Purtell et al. [18]. The inlet plane of the simulations is at $Re_\theta = 450$ with the outlet at $Re_\theta \approx 1540$. Figure 4.17 shows the development of several important parameters that were used by Schlatter and Örlü [14] to assess the quality of DNSs

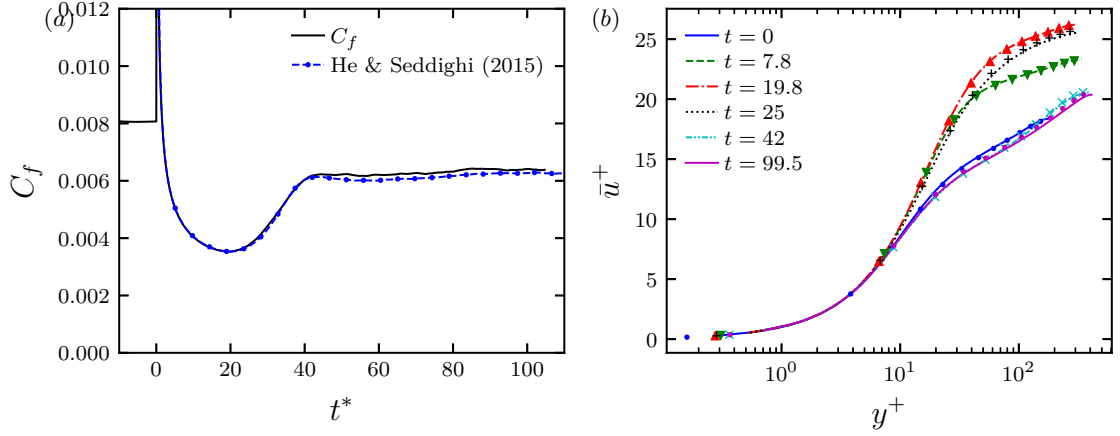


Figure 4.16: Temporal acceleration validation against He and Seddighi [15]: (a) C_f ; (b) \bar{u}^+ vs y^+ . In (b) lines indicate present results and markers indicate those from He and Seddighi [15]

of ZPGTBLs. Figure 4.17(a) shows the C_f compared with the reference data and the Smits et al. [19] correlation (solid blue), with the $\pm 5\%$ bounds (blue dashed) suggested by Schlatter and Örlü [14] also shown. After a short recovery region, C_f closely follows the reference data and the correlation of Smits et al. [19]. The recovery region for $Re_\theta < 600$ is commonly observed in turbulent boundary layer DNSs using the recycling-rescaling method and is related to assumptions used to rescale the velocity onto the inlet plane [16, 3]. In particular, the weighting function (equation (4.31)) leads to a second smaller inner peak in the streamwise Reynolds stress at the inlet plane due to the lack of scale separation between the inner and outer layers. Nonetheless, the recovery region is comparatively short and is considered in case setups. Figure 4.17(b) shows the variation of Re_τ vs Re_θ with the correlation suggested by Schlatter and Örlü [14]. After the recovery region, a close correspondence with the correlation is observed with a closer fit than the reference data.

Figure 4.17(c) compares the shape factor with the correlation from Chauhan et al. [20] for H with the $\pm 1\%$ suggested by Schlatter and Örlü [14] also shown. H is

Table 4.3: Simulation configuration for ZPG turbulent boundary layer validation. The grid resolutions indicate their worst in the domain.

	$Re_{\theta,0}$	$Re_{\theta,f}$	Δx^+	Δz^+	Δy_w^+	Δy_δ^+	L_x/δ_f	L_y/δ_f	L_z/δ_f
Present	445.9	1539	6.11	4.72	0.53	7.68	42.1	3.51	3.5

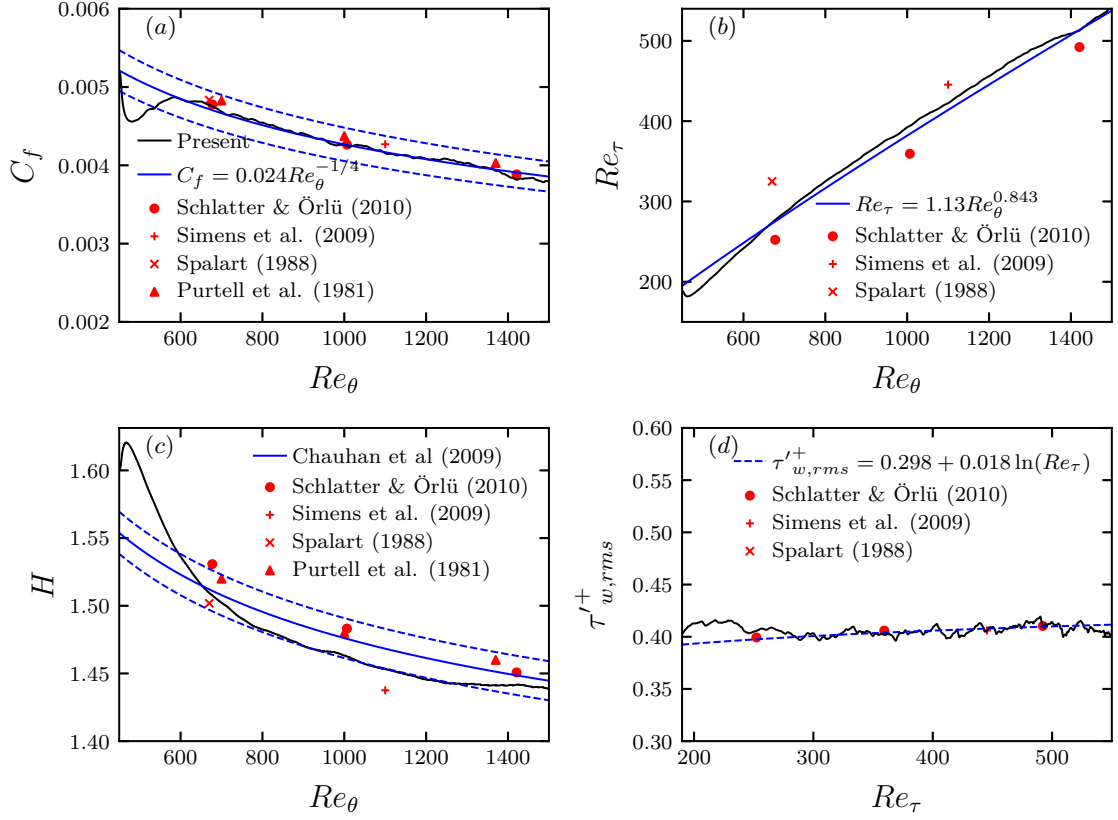


Figure 4.17: Comparison of mean flow parameters with validating data [14, 16, 17, 18]. (a) C_f compared with correlation [19]. (b) Re_θ vs Re_τ compared with correlation [14]. (c) H compared with Chauhan et al. [20] relation. (d) $\tau'_{w,rms}$ compared with relation from Schlatter and Örlü [14].

just about within 1% the Chauhan et al. [20] correlation. The recovery region is longer than for C_f (extending to $Re_\theta \approx 800$) due to H being a function of the entire velocity profile and susceptible to the slower relaxation times of the outer flow [3]. For $Re_\theta > 1300$, there appears to be a slight change in trend, suggesting that there is a region that is slightly affected by the outlet. While the effect appears to be small in the present study, it has been managed by discarding results close to the outlet, similar to previous studies [232]. Figure 4.17(d) shows $\tau'_{w,rms}$, which has been computed similarly to Schlatter and Örlü [14] using $\tau'_{w,rms} = \lim_{y^+ \rightarrow \infty} (u'_{rms}/\bar{u}^+)$. The results indicate good agreement with the correlation proposed by Schlatter and Örlü [14] and the reference data. It also indicates that the recovery region extends to $Re_\theta \approx 800$.

The mean streamwise velocity is shown in figures 4.18(a) and 4.18(c) at $Re_\theta =$

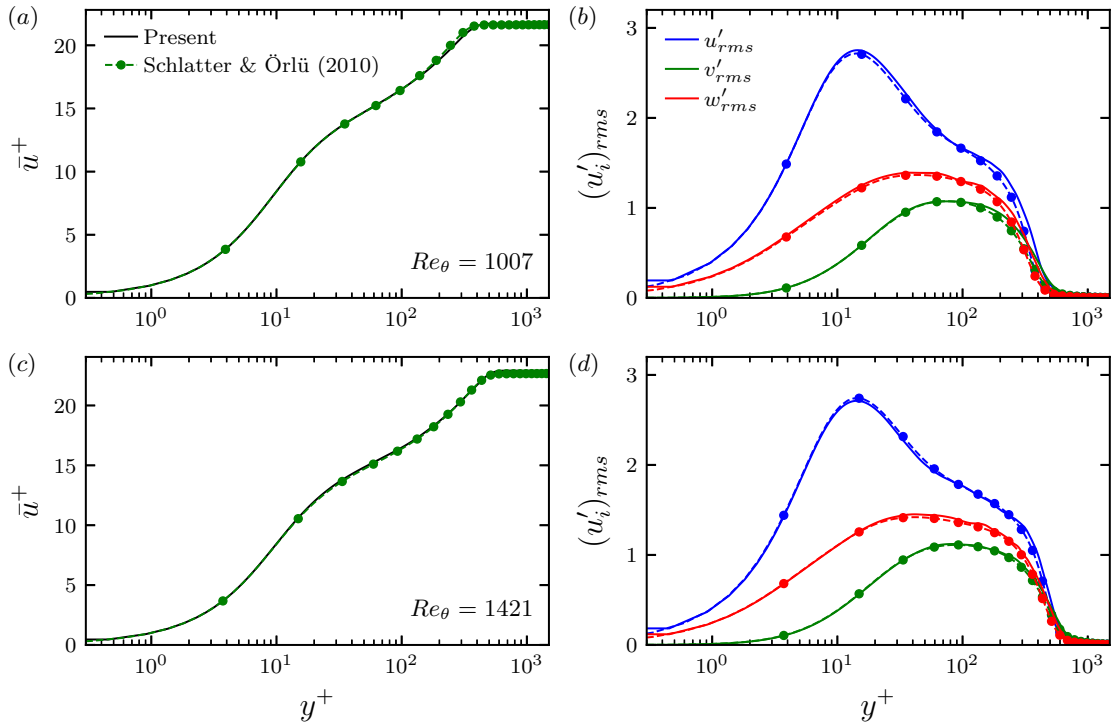


Figure 4.18: Comparison of mean velocity and normal Reynolds stresses with Schlatter and Örlü [14]. Present: solid lines. Schlatter and Örlü [14]: dashed lines with markers.

1000 and $Re_\theta = 1410$, indicating a good correspondence between the present data and Schlatter and Örlü [14]. The RMS velocity fluctuations are shown in figures 4.18(b) and 4.18(d). While there is generally good agreement, the stresses in the present results extend slightly further from the wall in the outer layer. This is likely due to the slightly higher Re_τ for a given Re_θ in the present case (figure 4.17(b)), noting that Re_τ is closer to the proposed correlation (figure 4.17(b)). The budget of $\overline{u'u'}$ is presented in figure 4.19 which indicates good agreement with Schlatter and Örlü [14] at $Re_\theta = 1000$ and $Re_\theta = 1410$.

4.7.4 Favourable pressure gradient TBLs

We validate the implementation of spatially accelerating TBLs by comparing the present method to case LES3s from Piomelli and Yuan [10]. This section comprises two parts: an assessment of the iSVV model for simulating laminarising spatial accelerations by comparing it with DNS data (section 4.7.4.1), and the comparison with Piomelli and Yuan [10] (section 4.7.4.2).

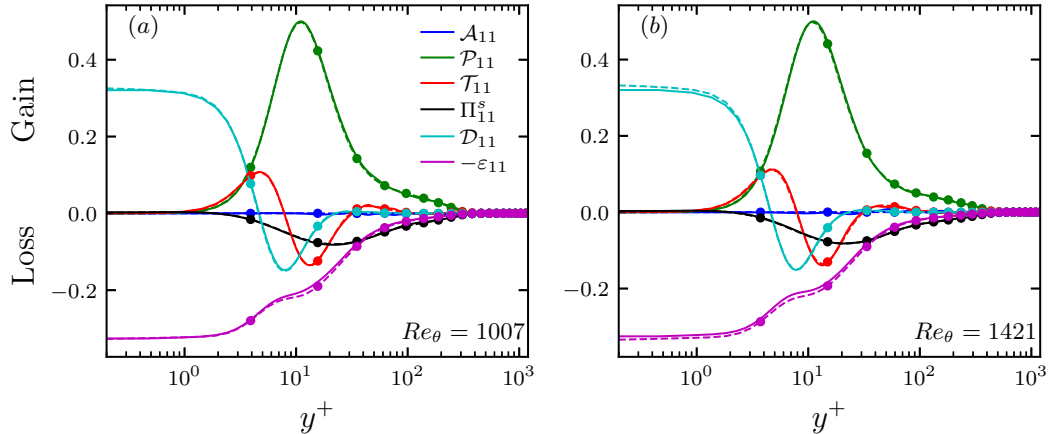


Figure 4.19: Comparison of $\overline{u'u'}$ budget with Schlatter and Örlü [14]: (a) $Re_\theta = 1000$; (b) $Re_\theta = 1410$. Solid lines indicate the present results; the dashed lines with markers indicate those of Schlatter and Örlü [14].

4.7.4.1 Applicability of iSVV method

It is important to show that the iSVV approach can capture the laminarisation process qualitatively and quantitatively, with any differences between the present implementation of spatially accelerating TBLs and Piomelli and Yuan [10] not likely to be related to the use of the iSVV model. As discussed in section 4.1.3, ν_0 must be selected, noting that the optimal value of ν_0 is unknown *a priori*. Consequently, we must ensure that flow statistics are not strongly dependent on the specific value of ν_0 or the mesh resolution and produce results comparable to DNS. A strategy is also required to use the iSVV method to ensure its results can be trusted when reference DNS is not available.

We use case 1 from chapter 6 for the DNS reference case. This case strongly laminarises, so it can be considered to reflect the physics that occurs in Piomelli

Table 4.4: Case characteristics for the iSVV tests, noting that the resolutions are the worst in the domain. Coarse case is at $\nu_0 = 20$.

	$Re_{\theta,ref}$	K_{max}	L_x	L_y	L_z	Δx^+	Δz^+	Δy_w^+	Δy_δ^+
DNS	884	6.26	59.8	2.94	3.8	9.88	6.11	0.719	6.79
$\nu_0/\nu = 20$	874	6.26	60.9	2.99	3.86	26.2	14.9	0.623	7.23
$\nu_0/\nu = 30$	879	6.25	60.9	2.99	3.86	26	14.8	0.62	7.24
$\nu_0/\nu = 50$	875	6.26	61.4	3.02	3.89	25.9	14.7	0.616	7.25
Coarse	876	6.27	60.3	2.96	3.81	47.9	20	0.821	10.5
WALE	796	7	68.3	2.48	3.09	37.5	13.3	1.08	5.07

and Yuan [10]. Table 4.4 shows a summary of the DNS reference case and all the LES cases, noting that smaller values ν_0 diverged. For reference, an LES case using the wall-adapting local eddy viscosity (WALE) [233] subgrid-scale (SGS) model has also been presented to highlight the deficiencies in using SGS viscosity models with high-order finite difference schemes, noting that this case is slightly different from the others.

We first present a qualitative comparison of the flow during laminarisation. Figure 4.20 compares an instantaneous snapshot of v' for case 1 using DNS, WALE model, and the iSVV model with $\nu_0 = 20$. In the DNS case, the typical hallmarks of laminarisation can be observed with the attenuation of the wall-normal component during laminarisation. The WALE model using the ordinary 6th-order compact scheme for the second derivative shows good behaviour during the ZPG region, but during the laminarisation, it suffers from severe small-scale oscillations similar to those observed in Dairay et al. [198]. In contrast, the iSVV model qualitatively replicates the DNS results and does not suffer from wiggles. While not a focus of this study, understanding why the WALE model suffers from such severe oscillations during laminarisation specifically should be investigated further.

Figure 4.21 shows C_f , Re_θ , and H for DNS and the iSVV model cases. All curves match the DNS results well, with the region associated with laminarisation captured excellently in all cases. The agreement is worst during retransition, with larger values of ν_0 becoming progressively worse, with the coarser mesh somewhat worse. Figure 4.22 shows the inner-scaled mean velocity and Reynolds shear stress profiles for case 1 for the DNS (lines) and iSVV cases (markers). All cases exhibit good agreement, particularly in the early stages of the acceleration. After the onset of retransition ($x \geq 500$), the cases with larger values of ν_0 have a slightly worse agreement, although they are still adequate, noting the very rapid development of the mean flow around the onset of retransition. The close results suggest that the results are not too sensitive but that lower values of ν_0 are likely to be better, providing the simulations do not diverge. Finer meshes are better, likely because they limit the influence of the spectral viscosity, with the modified wavenumber, k'' approaching the exact wavenumber for most flow scales.

As a result, the strategy we propose is that the smallest value of ν_0 that eliminates wiggles and does not diverge should be used, as this should provide the best overall agreement during the laminarisation and retransition stages. We also use mesh resolutions that are at least approximately as good as those in table 4.4, noting that the resolutions in table 4.4 represent the worst in the domain such that much of domain

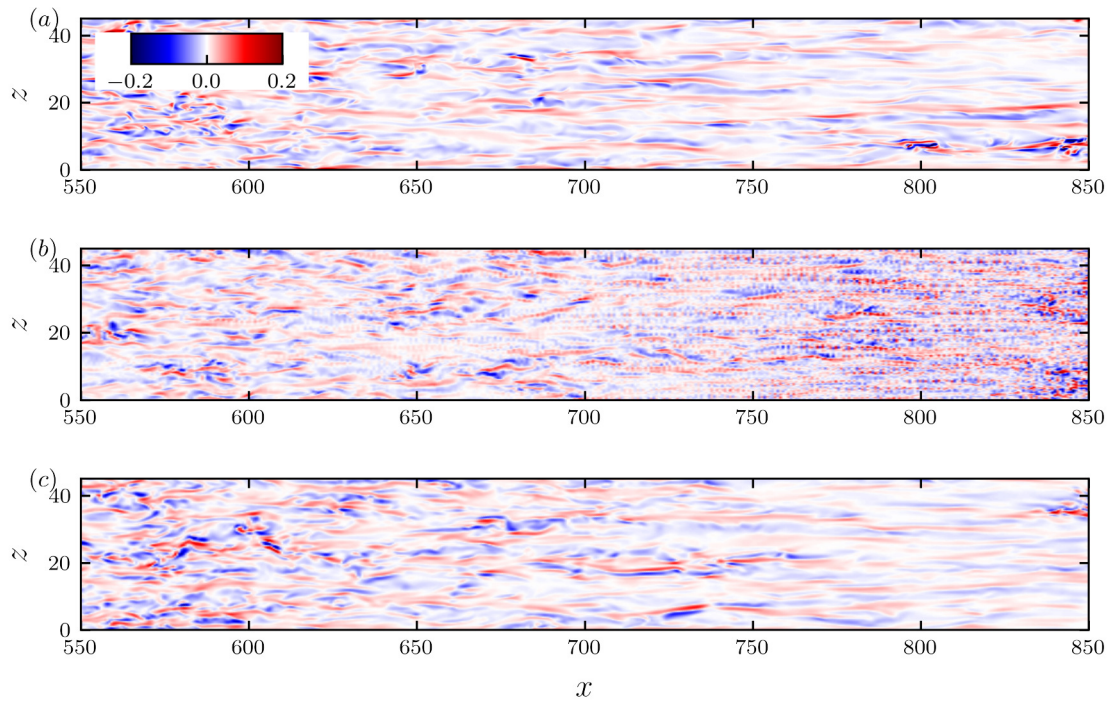


Figure 4.20: Wall-normal velocity fluctuations, v' for DNS, LES (WALE) and LES (iSVV). (a) DNS, (b) WALE, (b) iSVV.

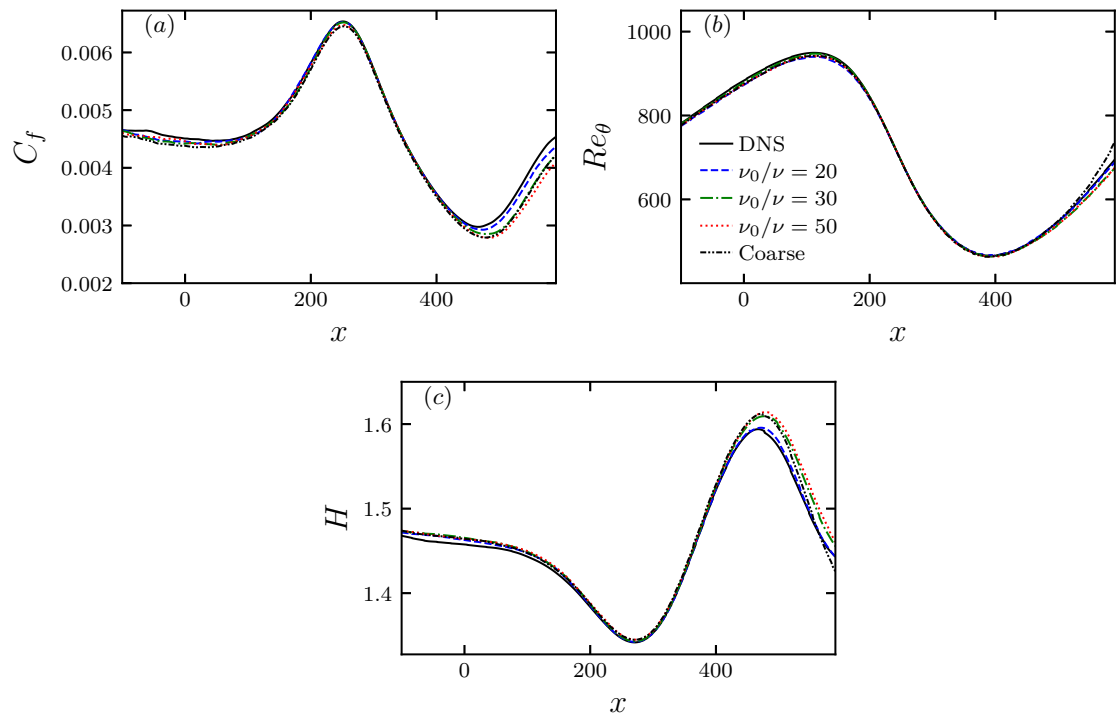


Figure 4.21: Comparison of mean flow parameters between DNS and the iSVV model for case 1 with $\nu_0 \in \{20, 30, 50\}$. (a) C_f , (b) Re_θ , and (c) H .

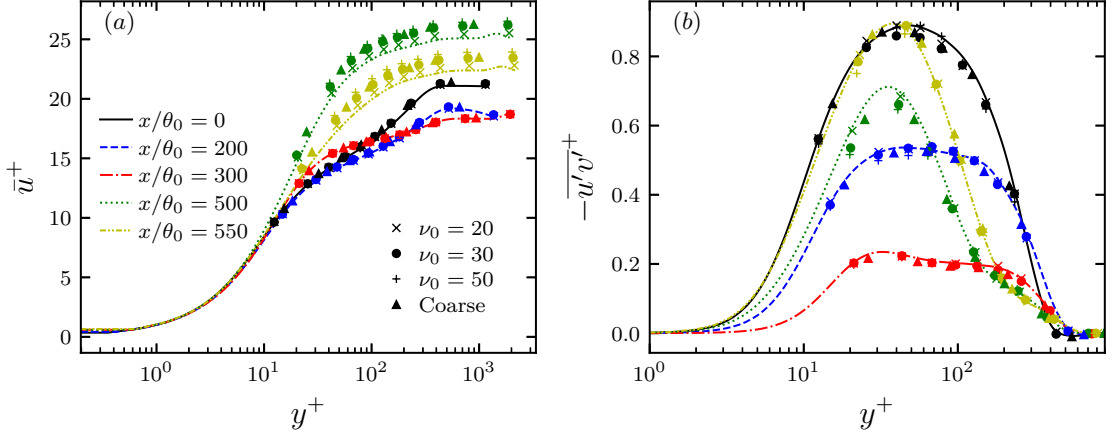


Figure 4.22: Inner-scaled mean velocity and Reynolds shear stress for DNS (lines) and iSVV models (markers). (a) \bar{u}^+ vs y^+ , (b) $-\overline{u'v'}^+$ vs y^+ .

upstream of retransition is close to DNS resolution with the influence of spectral viscosity likely to be small. Nonetheless, there is still a degree of uncertainty in the choice of ν_0 . Therefore, the iSVV model has only been used in a limited way in this study. The Adaptive Numerical Viscosity method of Mahfoze and Laizet [193] could also be adapted and tested on spatial accelerations, which would remove the need to select ν_0 for each case.

4.7.4.2 Validation

Following the policy described in section 4.1.3, $\nu_0 = 20$ and the mesh is well-resolved, with the y and z resolutions close to DNS. Case LES3s uses large eddy simulation using the Dynamic Smagorinsky model for the subgrid stresses.

Some key flow parameters for case P are shown in figure 4.23 compared with Piomelli and Yuan [10]. Figures 4.23(a) and 4.23(b) indicate that the variation of U_∞ was closely reproduced with the current method. C_f and Re_θ are presented in figures 4.23(c) and 4.23(d). Before acceleration ($x \approx 0$), Piomelli and Yuan [10]

Table 4.5: Simulation configuration of spatially accelerating turbulent boundary layer validation.

	$Re_{\theta,ref}$	L_x	L_y	L_z	Δx^+	Δz^+	Δy_w^+	Δy_δ^+
Case P	737	570	18.3	20.3	35.8	10.4	0.734	5.62
Piomelli and Yuan [10]	737				68	13	1.2	

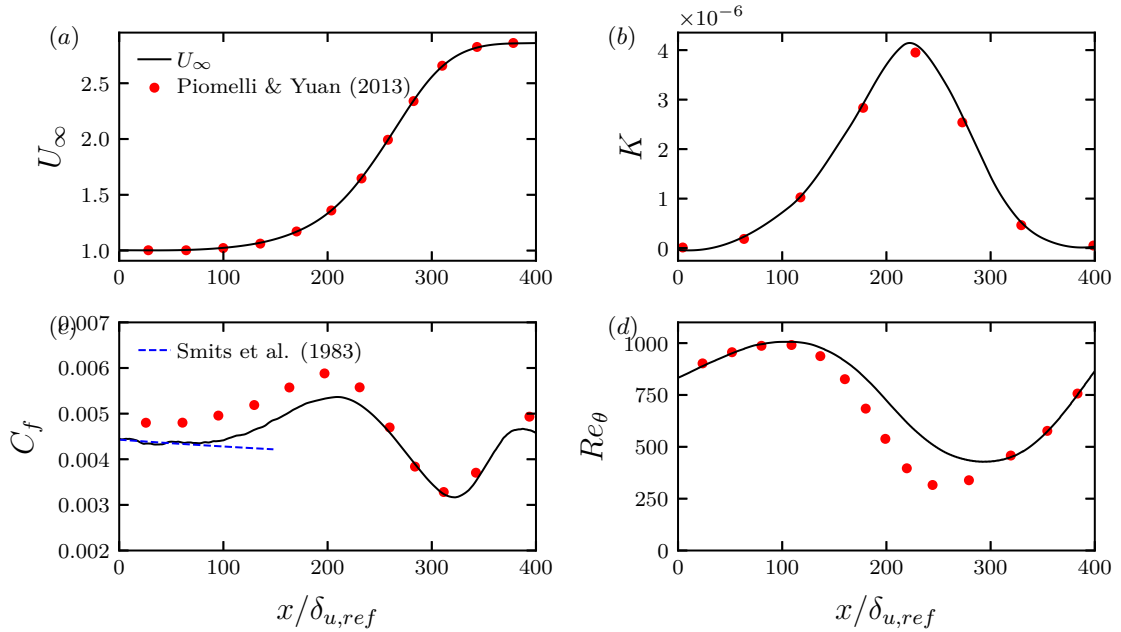


Figure 4.23: Comparison of mean flow parameter with Piomelli and Yuan [10]. (a) U_∞ , (b) K , (c) C_f , (d) Re_θ .

appears to overpredict C_f , with the present results consistent with the Smits et al. [19] correlation. After the onset of laminarisation, the skin friction coefficients in both cases overlap with the behaviour around retransition very similar. For Re_θ , the trends in both cases are similar, although there is a stronger reduction in Piomelli and Yuan [10] during the laminarisation.

The inner-scaled mean streamwise velocity are presented in figure 4.24. Figure 4.24(a) indicates that the present results and Piomelli and Yuan [10] are consistent for much of the acceleration, with the uplift of the logarithmic law observed during the laminarisation and the return to equilibrium after retransition in both cases. Consistent with the overpredicted C_f , the wake strength at $x = 0$ is noticeably smaller in Piomelli and Yuan [10], although at subsequent locations, the velocity profiles match well. The variation of the von Kármán and additive constants for case P will now be examined using the diagnostic function approach discussed in section 2.4.1. Nagib and Chauhan [60] showed that for a range of canonical flows, including spatially accelerating flows, $\kappa B = 1.6[\exp(0.1663B) - 1]$. This was subsequently confirmed for much stronger accelerations [87] and the reference case in Piomelli and Yuan [10]. Figure 4.24(b) shows close correspondence with the correlation up to the point of retransition for case P consistent with Piomelli and Yuan [10]. Figure 4.24(c) com-

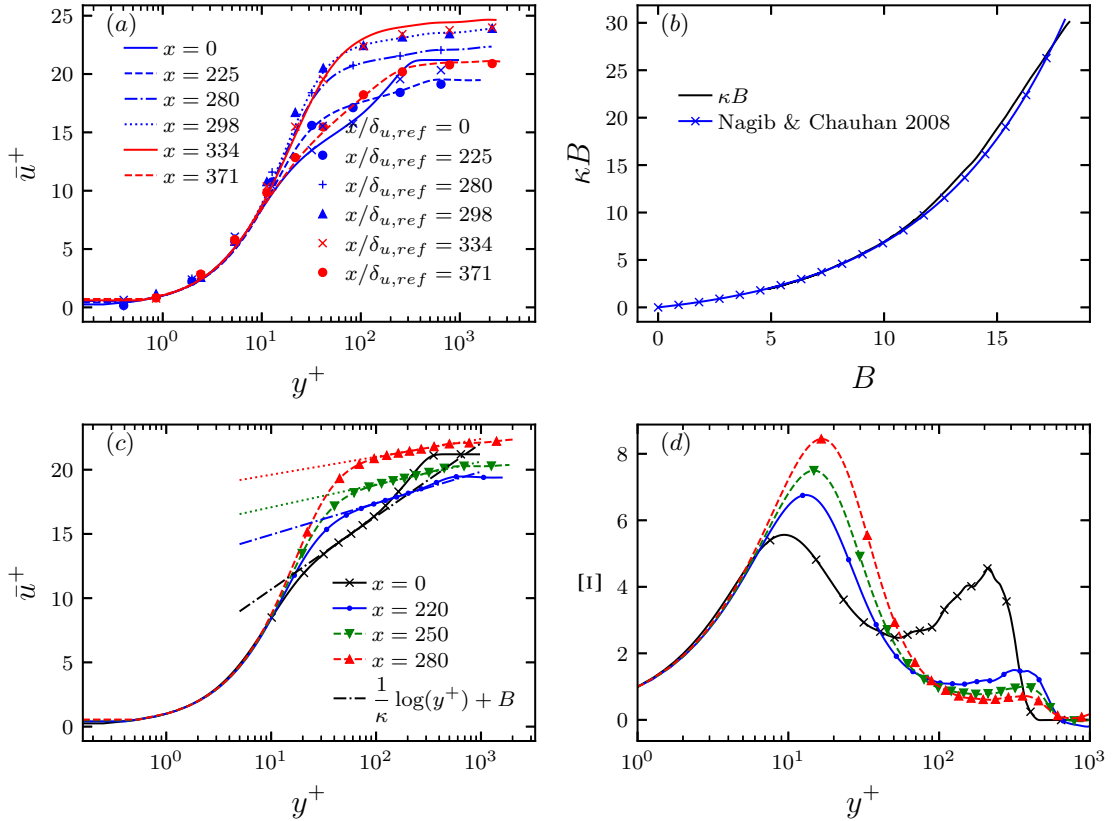


Figure 4.24: Comparison of inner-scaled mean velocity profile. (a) \bar{u}^+ , where lines represent the present results; the markers are from Piomelli and Yuan [10]. (b) shows the variation of the logarithmic law constants, κB vs. B and $\kappa B = 1.6[\exp(0.1663B) - 1]$. (c) shows the consistency of the computed logarithmic law constants with the inner scaled mean velocity. (d) shows the diagnostic function, Ξ during laminarisation for case P, with the symbols having the same meaning as (c).

compares the computed logarithmic law with \bar{u}^+ , with both agreeing well, particularly later in the acceleration. The agreement at $x = 0$ is somewhat worse, which can be investigated further by examining the diagnostic function, Ξ , which shows that Ξ only reaches a minimum at $x = 0$, similar to the lower Reynolds number channel flows in figure 2.2(b). However, a region of constant Ξ emerges as the acceleration progresses and by $x = 280$, much of the outer part of the boundary layer is essentially logarithmic. This indicates that a logarithmic region emerges in strong accelerations notwithstanding the low initial Reynolds number.

The inner-scaled Reynolds shear stress is presented in figure 4.25 with reasonable agreement between case P and Piomelli and Yuan [10], first reducing until the onset of retransition before increasing back to its typical ZPG values. However, there are

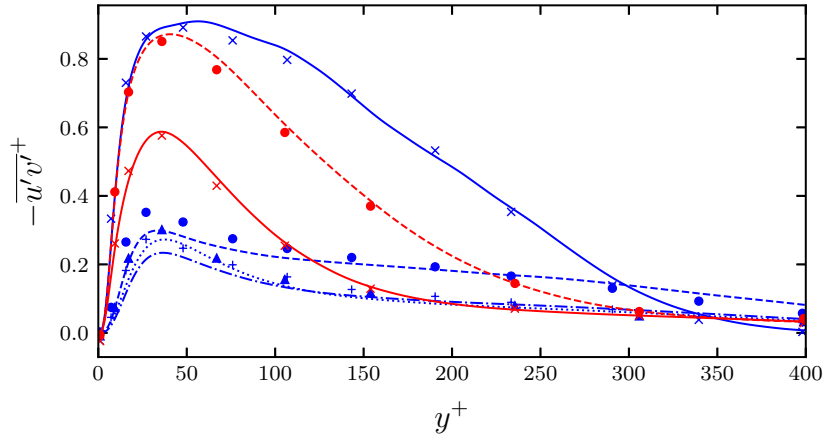


Figure 4.25: Comparison of the inner-scaled Reynolds shear stress with Piomelli and Yuan [10]. Lines and symbols are the same as figure 4.24(a).

some small differences between the cases during laminarisation ($x/\delta_{u,ref} = 225-298$). Overall, the results follow Piomelli and Yuan [10] reasonably well with the agreement of the mean flow with the correlation of Nagib and Chauhan [60] encouraging. However, the agreement is not perfect, and it is also clear that their C_f upstream of the acceleration does not match correlations for low Reynolds number TBLs. The present results highlight the need for high-quality experimental data at low Reynolds numbers to enable a more thorough validation of simulations using the method in section 4.5.

Chapter 5

A spatially accelerating flow with longitudinally contracting walls

In this chapter, an idealised spatially accelerating flow is studied where the effect of flow contraction is removed by using longitudinally accelerating moving walls to provide a relative spatial acceleration. This allows an investigation of a spatially accelerating flow where the influence of near-wall viscosity can be considered without the influence of flow contraction. The resulting flow development is consequently simpler than the spatially accelerating TBLs considered in chapter 6. A transition process is identified similar to that in temporal acceleration. In addition, it is shown that the moving wall acceleration captures some of the important aspects of the turbulence development in spatially accelerating TBLs.

5.1 Moving wall acceleration

The moving wall acceleration was implemented through a decreasing streamwise velocity boundary condition on the top and bottom walls of the channel. A schematic of this acceleration is presented in figure 5.1. This study uses a linear acceleration, which can be achieved by letting the wall velocity, $U_w(x) = -Cx$ in which C is a positive constant in the highlighted section of figure 5.1. This leads to the bulk of the fluid accelerating linearly relative to the wall as $U_b = U_a - U_w = U_a + Cx$ with U_a being the absolute bulk velocity. After the end of the acceleration, the wall velocity is maintained constant. The development of U_b , U_a , and U_w are presented in figure 5.1(c). Such an acceleration is analogous to the ramp-up accelerations frequently used in temporal acceleration [44, 47].

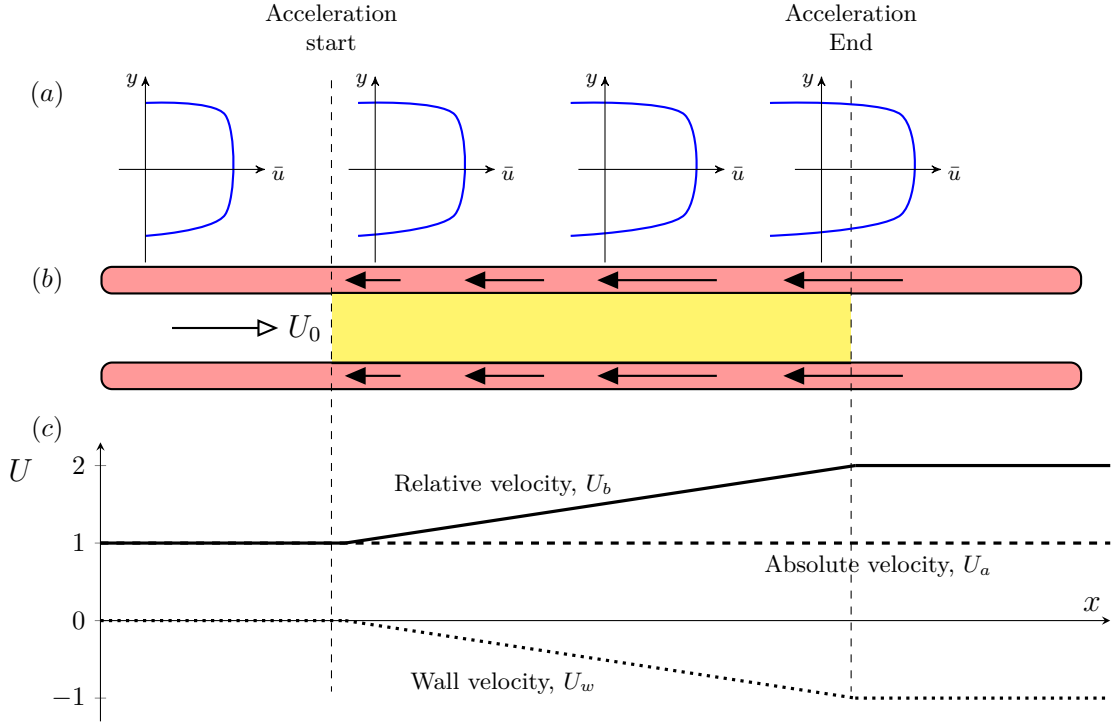


Figure 5.1: Flow acceleration caused using the moving-wall approach. (a) the absolute streamwise velocity profile at different streamwise locations. (b) the channel and its streamwise boundary condition are shown with the arrows representing the wall velocity. The shaded yellow region is the region where the acceleration is applied. (c) A plot showing the variation of the absolute velocity (dashed), wall velocity (dotted), and relative velocity (solid).

The flow created this way is naturally not equivalent to its conventional* counterpart. Instead, it is effort to study spatial flow acceleration with the influence of wall-ward contraction removed, providing an alternative to other approaches such as the laterally converging duct experiments of McEligot and co-workers [115, 114, 116, 117]. The similarities and differences between this flow and its conventional counterpart are highlighted throughout the results. It should be noted that accelerating moving wall flows have been studied in isolation previously using stability analysis (Brady and Acrivos [234] and Watson et al. [235]) and numerical simulation (Espín and Papa-georgiou [236]).

As discussed in chapter 4, CHAPSim is used in this chapter with the moving walls located in the inlet-outlet domain (figure 4.3). The turbulence generator was used for validation in the previous chapter, with proof of the sufficiency of the domain size

*In this chapter, spatially accelerating flows that include the effect of contraction, such as the spatially accelerating TBLs in chapter 6 are referred to as conventional for clarity.

Table 5.1: Details of the inlet-outlet domain presented in this study. Note that the resolutions indicate the worst resolutions in the domain.

Re_{b0}	Re_{b1}	$Re_{\tau 0}$	$Re_{\tau 1}$	ΔX	L_x	L_z	Δx^+	Δz^+	Δy_w^+	Δy_c^+	$T_s u_\tau / \delta$
2800	5600	178	325	15	30	4	6.35	3.81	0.466	3.59	10.1

shown in appendix A.1 following the considerations in section 4.3.

The computational setup of the case is shown in table 5.1. The Reynolds number of the inlet flow is $Re_0 = U_{b0}^* h^* / \nu^* = 2800$ ($Re_\tau = 178$) with wall velocity opposing the flow increasing linearly downstream for 15 half-channel heights reaching a Reynolds number based on the relative bulk velocity, $Re_1 = U_{b1}^* h^* / \nu^*$ of 5600 ($Re_\tau = 324$). The domain extends for an additional $10h$ to allow the flow to be fully developed by the outlet though the results close to the outlet are not used in the discussion to exclude any minor effects close to the boundary. The inner-scaled grid resolutions indicate their worst values in the domain and are consistent with the recommendations in section 4.3. For this chapter, statistics based on the mean velocity, such as the shape factor, H , and acceleration parameter, K are presented relative to the wall to show the effect of the relative acceleration. When mean flow statistics are presented in absolute terms, the subscript (a) is used. Velocities and lengths are normalised by the inlet bulk velocity and half-channel height, respectively, unless otherwise stated.

5.2 Mean flow

Figure 5.2 shows the wall-normal distribution of the absolute, relative, and inner-scaled mean streamwise velocity. The absolute velocity (figure 5.2(a)) is negative at the wall, and its magnitude increases with downstream distance, as expected from the accelerating moving wall, with the relative mean velocity increasing (figure 5.2(b)). Figure 5.2(c) shows that after the onset of the acceleration ($x = 0$), the inner-scaled (relative) velocity profile in the log region exhibits an uplift from the equilibrium profile reaching its highest level at around $x = 6$. After this point, it falls back and reaches the equilibrium profile before the end of the acceleration (figure 5.2(d)). Alongside the uplift, there is a slight increase in the thickness of the viscous sublayer as indicated by the larger wall-normal extent where $\bar{u}^+ = y^+$. The thickening of the viscous sublayer and the uplift and subsequent return to equilibrium of the logarithmic law are typical features of all accelerating flows, including temporal acceleration [44, 47] and spatial acceleration [98, 97].

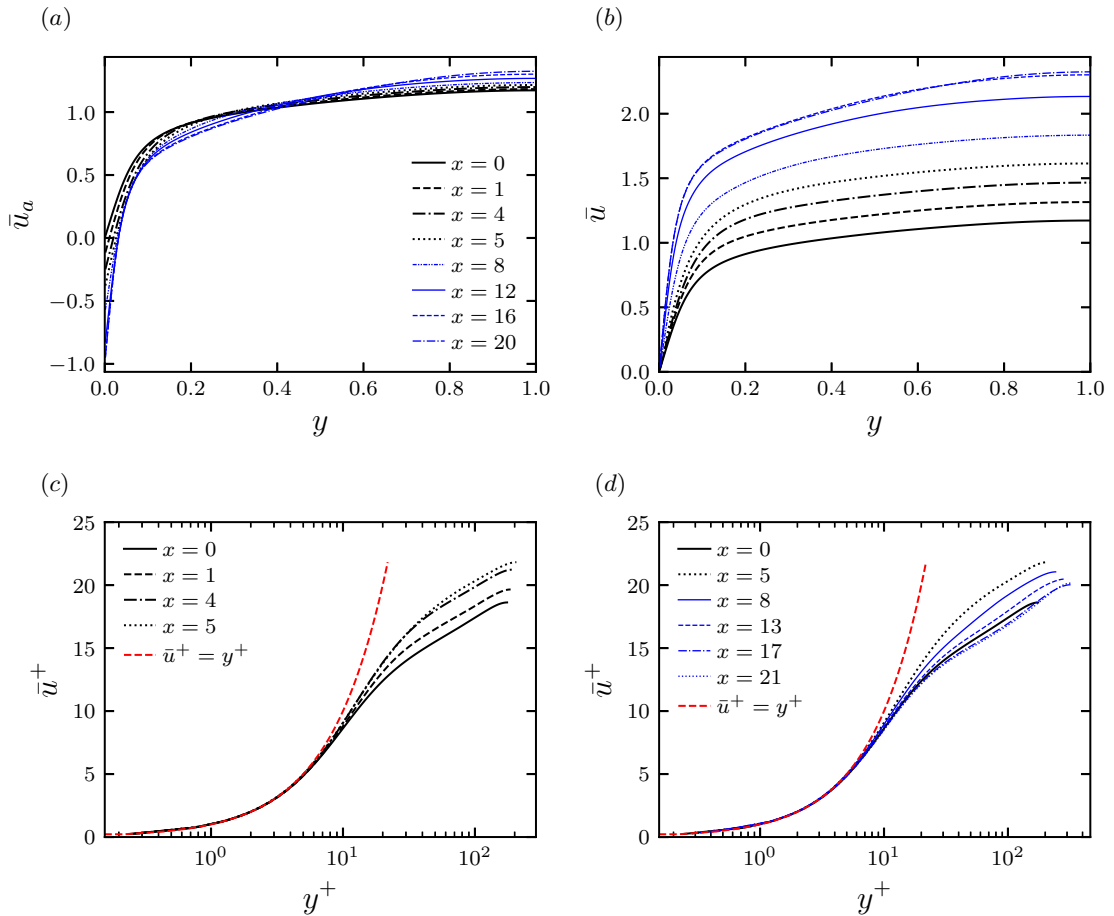


Figure 5.2: Streamwise mean velocity profile. (a): Absolute mean velocity, \bar{u}_a ; (b): Mean velocity relative to the wall, \bar{u} ; (c) inner-scaled relative mean velocity profile in the pre-transition stage ($x \leq 5$); and (d) post onset of transition ($x > 5$) including $x = 0, 5$. In figures 5.2(c) and 5.2(d), the red line is $\bar{u}^+ = y^+$.

There are some differences between the development of the mean velocity profile in the present case and conventional accelerations. In figure 5.2(c), the uplift from the equilibrium profile is relatively uniform across the channel, whereas in conventional acceleration such as Bourassa and Thomas [87] (also figure 4.24(a)) the uplift is concentrated close the wall resulting in a significant flattening of the \bar{u}^+ in the logarithmic region. A likely cause of this difference is the removal of the wall-wards contraction in the present flow, leading to a change in the mean flow structure. For example, a top wall contraction is expected to skew the mean velocity profile towards the bottom wall. As a result, the uplift occurs closer to the wall in conventional spatial acceleration. The laterally converging ducts studied by McEligot and Eckel-

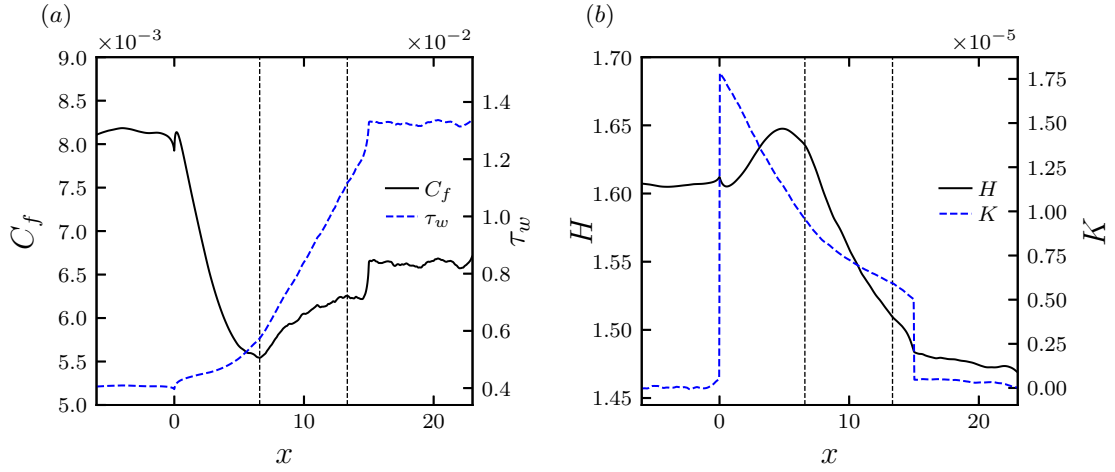


Figure 5.3: (a) shows the skin friction coefficient, C_f and wall shear stress, $\tau_w = 1/Re_0 \cdot \partial \bar{u} / \partial y$. (b) shows the shape factor, H ; and the acceleration parameter, K . As stated in section 5.1, these quantities have been calculated relative to the wall. The vertical lines indicate the onset and completion of transition using the definitions described in section 5.3.

mann [116] and temporally accelerating channel flows [44], which both lack wall-ward contraction, exhibit a similar change in the equilibrium profile to the moving wall acceleration, which supports this explanation.

A number of important flow parameters are presented in figure 5.3. Figure 5.3(b) shows that K is highest at the beginning of the acceleration and then decreases monotonically during the acceleration period due to the increasing free-stream velocity before suddenly dropping to a value close to zero on the removal of the acceleration. This distribution is substantially different from typical acceleration profiles found in previous studies, which are usually bell-shaped because the flow acceleration is increased gradually (e.g. Escudier et al. [103] or Warnack and Fernholz [102]). It should be noted, however, that the shape of the acceleration profile does not significantly affect the key features of the flow transition concerned herein as demonstrated in appendix A.2, which presents some results with a smooth acceleration profile.

The variation of the skin friction coefficient, C_f is given in figure 5.3(a), which shows that C_f decreases rapidly after the onset of the acceleration primarily due to the increasing relative bulk velocity, whereas the wall shear stress increases only mildly in the initial phase of the acceleration. C_f reaches a minimum around $x = 6$, the point where the uplift of the log region of the velocity profile reaches its maximum. The

skin friction increases after this point due to rapid increases in wall shear, reaching a peak at around $x \approx 13$. A further sudden increase occurs when the acceleration is stopped at $x = 15$, after which it remains constant until the end of the channel. Finally, the shape factor H begins to increase shortly after the acceleration before reaching a maximum at approximately the same location as the minimum in C_f before falling monotonically. Recall that the locations of the minimum and maximum of C_f and H , respectively, are broadly viewed as indications of the location of retransition in studies of accelerating flow [9, 103, 10].

5.3 Instantaneous flow

The instantaneous results highlight some of the key features in the development of the flow acceleration. Figure 5.4 shows the contours of the streamwise and wall-normal velocity fluctuations at $y^{+0} = 5$. In the pre-existing flow ($x < 0$), the ubiquitous near-wall streaky structures are clearly present, although the initial turbulence is of a much smaller magnitude than at the end of the acceleration. The streamwise fluctuation indicates that after the onset of the acceleration, the strength of the streaks mildly increases initially. Around the minimum of C_f (the dashed red line), turbulent spots start to form, as indicated by the appearance of large magnitude fluctuations of shorter spatial scale. These spots are initially localised in space, coexisting with the streaks, but grow in the spanwise and streamwise directions as they are convected downstream until the entire wall surface is covered in new turbulence. However, the wall-normal velocity fluctuations develop differently. Figure 5.4(c) indicates that the wall-normal fluctuating velocity initially does not respond until the appearance of high magnitude spots, which correspond with the large magnitude events in streamwise velocity fluctuation contour. There is a significant increase in the amplitude of both components on the formation of the turbulent spots, as shown by more frequent and much darker red and blue events. These observations are similar to those observed in studies of bypass transition such as Nagarajan et al. [11] (figure 3.4). The lack of response from v' until the formation of turbulent spots is also true in boundary layer bypass transition, but the background flow in that case is laminar, hence there are few fluctuations at all. The development is nonetheless similar.

The following interpretation is proposed to explain this development. When the mean flow is accelerated, the velocity tends to increase uniformly at all vertical locations. However, due to fluid viscosity, the flow is retarded close to the wall resulting in a new boundary layer superimposed on the existing flow, which grows downstream

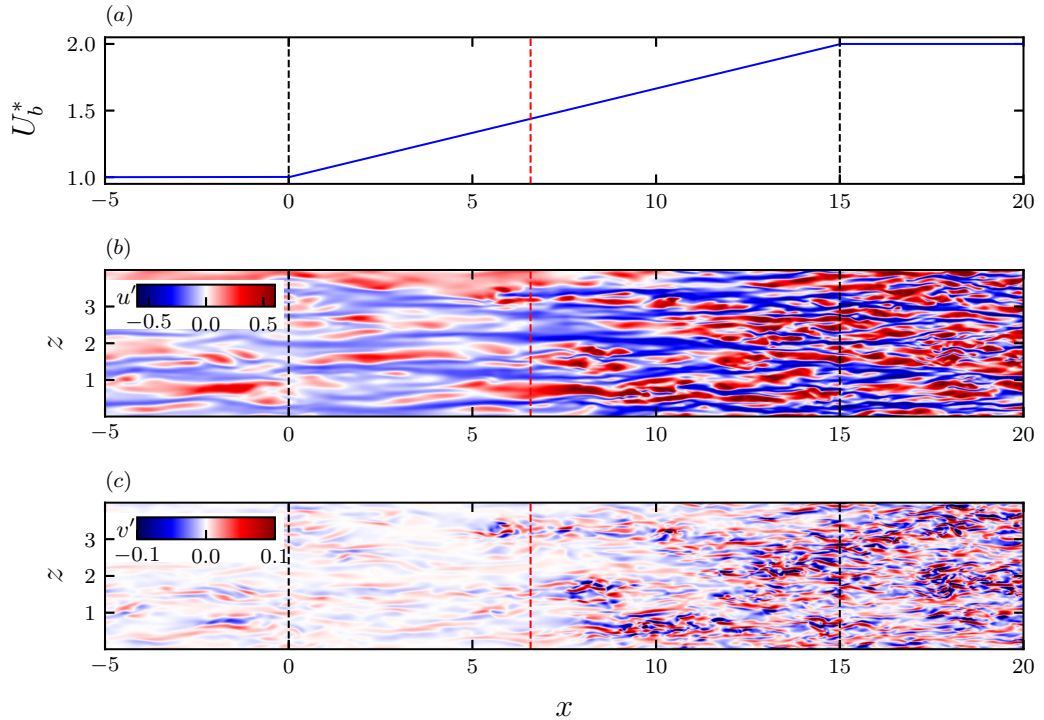


Figure 5.4: A $x - z$ plane of the streamwise (u'/U_{b0}) and wall-normal (v'/U_{b0}) fluctuating velocities at single instance in time at $y^{+0} = 4.9$. The relative bulk velocity, U_b , is shown in (a) for reference. The first black line indicates the start of the acceleration, while the final black line is the end of the acceleration. The red line indicates the approximate location of the onset of transition as indicated by the minimum in C_f .

as the effect of the acceleration is felt further from the wall. In the case of the relative acceleration studied here, the boundary layer is directly created by imposing a velocity on the wall. This can be observed in figure 5.2(a) where the mean velocity close to the wall is observed to reduce while the flow further from the wall remains nearly fixed. Viscosity subsequently causes the extent of the channel affected by the moving wall to increase with downstream distance. The new boundary layer does not significantly change the turbulent structures in the existing flow, but through the enhancement of the lift-up effect due to the increase in near-wall shear, the near-wall streaks are strengthened. With the continuing growth of the boundary layer, localised streaks break down, leading to transition. The onset of transition is typically marked by the occurrence of high frequency/high amplitude fluctuations in all three turbulence components, and this is clearly indicated by the coincident spots in the u' and v' velocity fluctuation contours. The spread and growth of these spots can

also be compared to bypass transition, where the intermittent region is linked to the coexistence of streaks and patches of broken-down flow until the entire surface of the wall is covered in new turbulence structures, which is also observed here.

In summary, the flow can be described as a three-stage development, that is, the initial pre-transition stage ($0 < x \leq 6$), the transition stage ($6 < x \leq 13$), and the fully turbulent stage ($x > 13$). Here, the onset of transition ($x = 6$) is determined using the minimum C_f , and the completion of transition ($x = 13$) is the first peak in C_f after the onset of transition. These locations have been indicated on figure 5.3. It should be noted that turbulence may still develop in the core of the flow beyond the buffer layer after the completion of transition, which is marked by the population of new turbulence in the wall region. This interpretation is analogous to the transition theory proposed by He and Seddighi [43] for temporally accelerating flows with the stages above the same as those found in studies of bypass transition [131] and temporal acceleration [43]. It should be noted in temporally accelerating flows, a similarity solution can be derived for the new boundary layer that allows accurate predictions of the mean flow from the beginning of the acceleration to the onset of transition, which provides a basis for understanding the turbulence response to the acceleration [173, 177, 12]. However, the nonlinearity of the convection terms means that analogous similarity solutions are not possible in spatially accelerating flows. Nonetheless, the concept can still provide a qualitative understanding of the flow and turbulence response from close to the onset of the acceleration by considering the response of near-wall turbulence to the development of the new boundary layer resulting from near-wall viscous effects.

It is important to consider how this interpretation can help to improve the understanding of spatially accelerating flows. Laminarisation in spatially accelerating flows occurs due to the relative domination of the pressure gradient over the turbulent stresses [9]. The present interpretation allows a qualitative description of the flow and turbulence response in accelerating flows from close to the start of the acceleration. In this interpretation, the slow response of the turbulent stresses, which leads to laminarisation, results from the delay between the onset of the acceleration and the breakdown of the strengthened near-wall streaks with the onset of transition. This transition results from the amplification of the near-wall streaks due to the development of the new boundary layer and, therefore, is a direct consequence of the acceleration. As a result, this transition can occur even in the absence of a laminar-like inner layer or before the removal of the acceleration, similar to the case studied

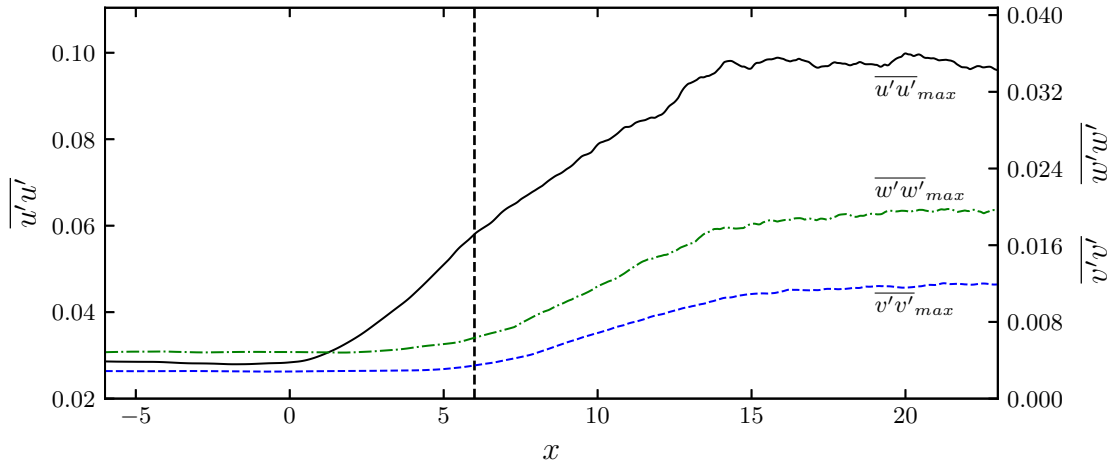


Figure 5.5: Streamwise distribution of the peak normal Reynolds stresses normalised by U_{b0}^2 . $\overline{u'u'}$ is shown on the left axis with $\overline{v'v'}$ and $\overline{w'w'}$ on the right axis. The vertical line indicates the onset of transition as indicated by the minimum in C_f

here. In the remainder of the chapter, the statistical development of the moving wall is analysed to provide a foundation for discussions in chapter 6.

5.4 Turbulence statistics

5.4.1 Reynolds stresses

The streamwise distribution of the peak normal Reynolds stresses is presented in figure 5.5, which illustrates the energy growth of the disturbances commonly used in studies of bypass transition. The figure shows that shortly after the start of the acceleration, the streamwise Reynolds stress exhibits downstream growth throughout pre-transition. This can be associated with the stretching and elongation of the streaks by the new boundary layer observed in figure 5.4 leading to an increase in the streamwise disturbance energy as energy is extracted from the mean flow. Such energy growth prior to the onset of transition is typical in bypass transition [141, 131, 139]. Also consistent with the observation in figure 5.4(c), there is a clear lack of increase in the transverse Reynolds stresses during pre-transition. The location where the transverse Reynolds stresses begin to increase is consistent with the point of transition denoted by the minimum in C_f .

The downstream growth of $\overline{u'u'}$ prior to retransition was noted to occur in several studies of spatial acceleration [110, 87]. Warnack and Fernholz [102] also showed that the development of the peak streamwise Reynolds stress exhibits downstream

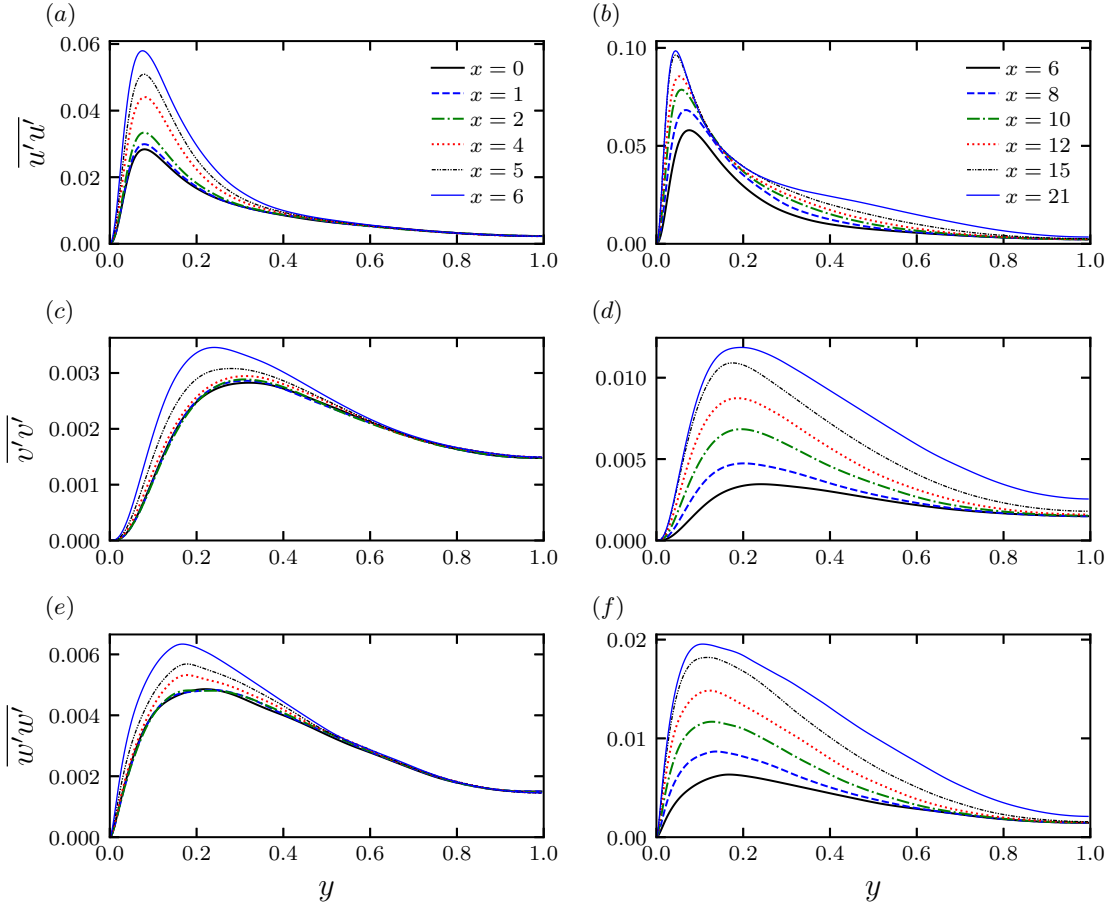


Figure 5.6: The wall-normal distribution of the normal Reynolds stresses normalised by U_{b0}^2 . The figures on the left ((a), (c), and (e)), are of x locations prior to transition and those on the right ((b), (d), and (f)) are of locations after the onset of transition. The legend in (a) is used in (c) and (e) while the legend in (b) is used in (d) and (f).

growth from near the onset of the acceleration until the onset of retransition. The continuing increase in the peak streamwise Reynolds stress after the onset of transition in the present case is likely due to the acceleration continuing to extract energy from the mean flow during and after transition. Other cases, not presented here, where transition occurs after the end of the acceleration showed a slight decline in the peak streamwise Reynolds stress after transition similarly to Warnack and Fernholz [102]. This was also observed in bypass transition [131].

The wall-normal distribution of the streamwise Reynolds stress at different downstream locations is presented in figures 5.6(a) and 5.6(b). The former shows the downstream locations prior to transition, and the latter shows those after transition.

Figure 5.6(a) indicates that during pre-transition, most of the increases in $\overline{u'u'}$ occur for $y^+ \lesssim 50$ and only increases further away from the wall after the onset of transition. This is consistent with Warnack and Fernholz [102], who also indicated that the downstream growth tends to be confined to the near-wall region in spatially accelerating flows before retransition. Figure 5.6(a) also indicates the peak in the streamwise Reynolds stress moves slightly further away from the wall, which is consistent with observations in bypass transition [139] and spatial acceleration [97]. Figure 5.6(b) shows that after the onset of transition, the peak streamwise Reynolds stress settles closer to the wall, consistent with a channel flow at higher Reynolds numbers.

Figures 5.6(c) to 5.6(f) shows the wall-normal distribution of $\overline{v'v'}$ and $\overline{w'w'}$. Consistent with figure 5.5 and the instantaneous contour plots, figures 5.6(c) and 5.6(e) indicate that $\overline{v'v'}$ and $\overline{w'w'}$ remains nearly constant through pre-transition, albeit with small increases towards the end of pre-transition. After the onset of transition, $\overline{v'v'}$ and $\overline{w'w'}$ increase over a broad wall-normal region. The wall-normal extent of the new turbulence continues to increase with downstream distance post-transition, and it is not until towards the end of the channel at $x \geq 21$ that there is an increase in $\overline{v'v'}$ and $\overline{w'w'}$ in the centre of the channel. The increase in the extent of the new turbulence with downstream distance can be similarly observed in bypass transition [138, 131] consistent with turbulence being transported away from the wall as the wall-normal extent of the new boundary layer increases and is not directly linked to the formation of turbulent spots which occurs closer to the wall. The limited changes of the transverse stresses during pre-transition in figure 5.6 are similarly observed in temporal accelerations [15, 12]. It is useful to note that conventional spatial acceleration tends to behave somewhat differently, with absolute reductions observed in strong accelerations close to the wall [10]. After transition, the spreading of new turbulence into the core resembles that observed in conventional spatial acceleration [121].

The development of the Reynolds shear stress, $-\overline{u'v'}$ is shown in figure 5.7. During pre-transition, $-\overline{u'v'}$ increases by around 60% near the wall ($y^+ \lesssim 50$). This is consistent with the delayed response of v' in figure 5.4(c) and the increases in u' being limited to the near-wall region. After transition, there are significant rises across a broad wall-normal region. Figure 5.7(b) indicates that the flow has largely redeveloped at $x = 21$ as demonstrated by the linear distribution $-\overline{u'v'}$ in the core. These results are consistent with Warnack and Fernholz [102], who similarly showed that $-\overline{u'v'}$ increases are initially limited to the near-wall region while after the onset

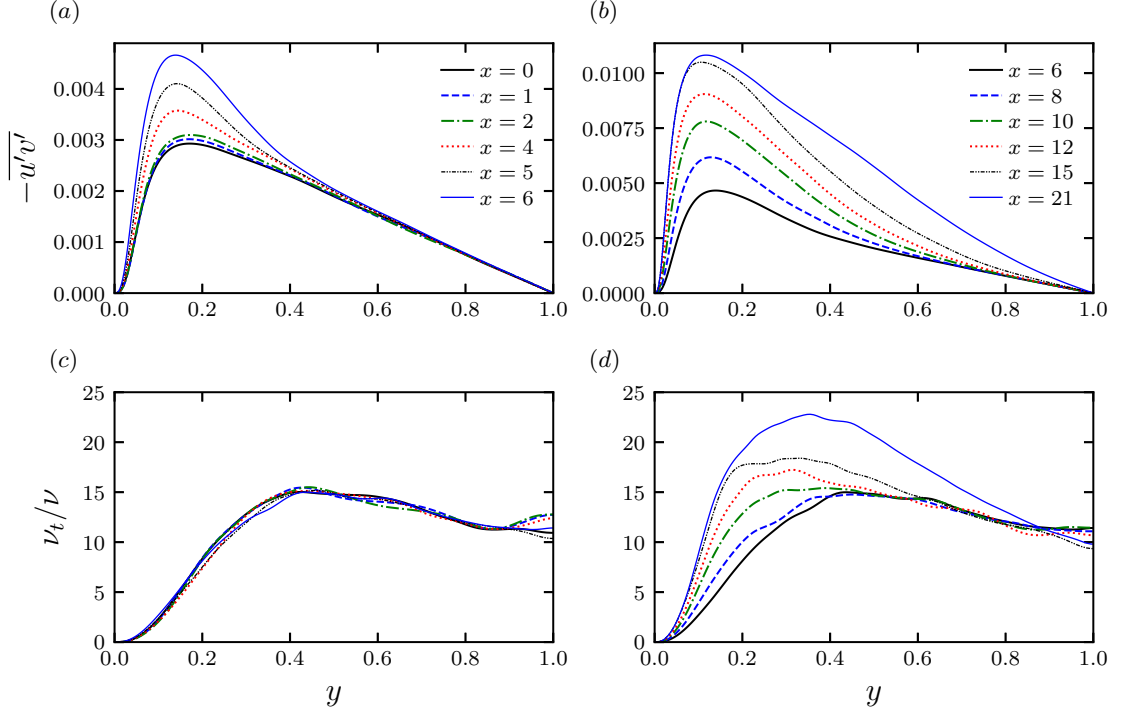


Figure 5.7: Reynolds shear stress, $-\overline{u'v'}$ ((a) and (b)) normalised by U_{b0}^2 and eddy viscosity, ν_t/ν ((c) and (d)).

of retransition, there is a broad increase, the wall-normal extent of which increases with downstream distance.

Applying the Boussinesq hypothesis and considering the dominant strain rate only, the turbulent shear stress can be written as a product of the eddy viscosity and the velocity gradient:

$$-\overline{u'v'} = \nu_t \frac{\partial \bar{u}}{\partial y}. \quad (5.1)$$

As can be inferred from the above equation, the eddy viscosity represents the mixing/diffusive effect of turbulence on the flow. Figure 5.7(c) shows that ν_t remains unchanged during pre-transition. Alongside the lack of change of the transverse components, this indicates that key elements of the near-wall turbulence processes are not significantly modified at this point beyond the strengthening of the near-wall streaks. After the onset of transition from $6 < x < 12$, figure 5.7(d) shows that ν_t is found to increase in a broad near-wall region, yet does not significantly increase in the core of the flow until the end of the transition phase of the acceleration. For $x \gtrsim 15$, the eddy viscosity increases further from the wall with the final profile similar

to the initial profile, albeit with larger values. The results for the Reynolds stresses and the eddy viscosity are very similar to those of temporal acceleration, with initial increases limited to $\overline{u'u'}$, which is followed by increases in the transverse terms and the generation of new turbulent structures with the onset of transition [43, 44].

5.4.2 Reynolds stress budgets

The contributions to the growth of the Reynolds stresses can be analysed through the budgets of the Reynolds stress transport equation. The wall-normal distribution of the streamwise budgets normalised with respect to the wall units of the initial flow ($u_{\tau,0}^4/\nu$) is shown in figure 5.8. The plot from before the onset of the acceleration at $x = 0$ depicts a typical profile for wall shear flow. After the onset of the acceleration, the production exhibits streamwise growth, indicating an increase in energy being extracted from the mean flow consistent with enhanced lift-up. Such production increases have also been noted in spatial [87] and temporal acceleration [43]. The lack of flow contraction or streamwise straining in the freestream means there is no reduction of shear production or increase in negative dilation production, unlike conventional spatial acceleration [87]. This reflects the amplification of the streaks by the mean shear associated with the newly developing boundary layer. It is also apparent that the production rises substantially during the transition phase between $x = 6$ and $x = 18$. The changes in most of the terms broadly mirror that of the production except the pressure strain, which is subdued until the onset of transition. This is significant as the pressure strain is the primary redistributive mechanism between the normal Reynolds stresses and is the sole source of the wall-normal and spanwise Reynolds stress budgets. This can provide a further explanation for the delayed increases in the transverse stresses, as the majority of the disturbance energy during pre-transition is produced in the streamwise component. This delay supports the notion that the changes during pre-transition are related to the strengthening of streaks which are primarily manifested in the streamwise velocity fluctuations. The results also imply that the turbulent spots observed in figure 5.4 are linked to intercomponent energy transfer, which is consistent with Voke and Yang [162], who highlighted the importance of the pressure strain in the process of bypass transition. The importance of energy redistribution has similarly been shown in previous studies of spatial acceleration [10] and temporal acceleration [43].

Figure 5.9 shows the streamwise development of some of the key terms of wall-normally integrated streamwise Reynolds stress budget, namely the production, dissipation, and pressure strain. In addition to the observations in figure 5.8, this figure

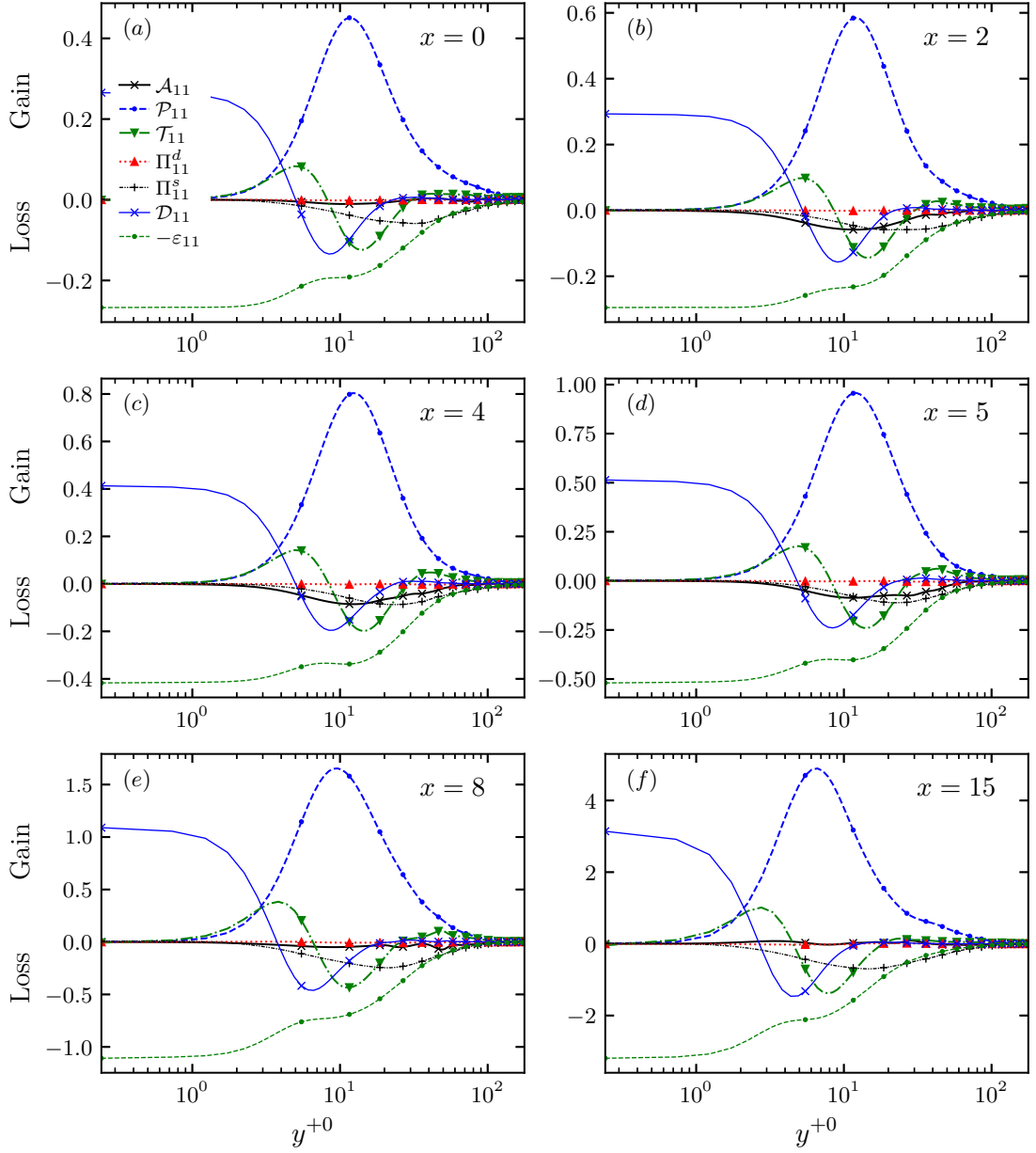


Figure 5.8: Streamwise Reynolds stress budget scaled with initial wall units, $u_{\tau,0}^*{}^4/\nu^*$.

shows that despite the large proportion of the overall increase in $\overline{u'u'}$ occurring during pre-transition, the changes of production appear significantly larger during the transition phase of the acceleration. This is consistent with the results of Jacobs and Durbin [131], although, in this study, the increase after transition is less stark due to the gradual acceleration and the relatively small velocity changes. The delayed rise of the pressure strain is also more clearly shown in this figure.

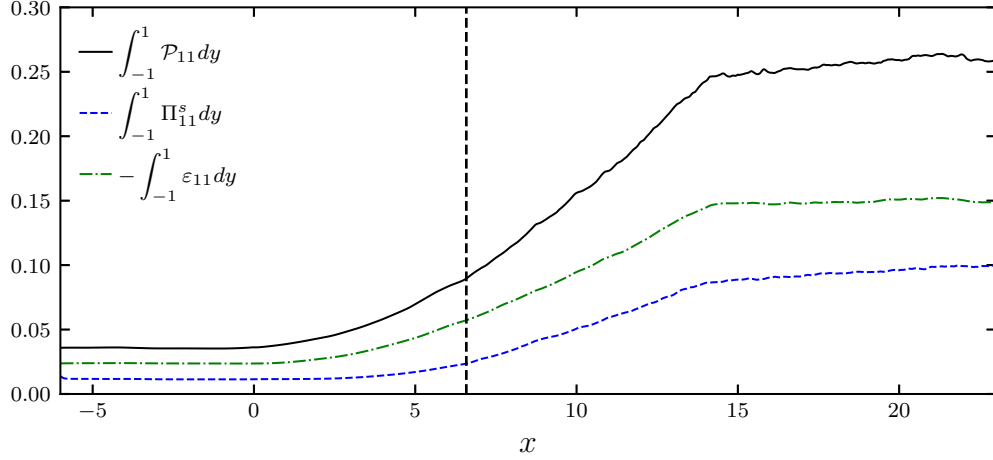


Figure 5.9: The wall-normal integral of production, pressure strain and dissipation terms of the $\overline{u'u'}$ budget normalised by $u_{\tau 0}^* 4h^*/\nu^*$. The meaning of the vertical line is the same as figure 5.5.

5.4.3 Quadrant analysis

Quadrant analysis is useful for investigating how turbulence structures change during the acceleration by looking at the different contributions (denoted $\overline{u'v'_Q}$) to the Reynolds shear stress. The coherent motions which dominate wall shear flows tend to be ejection (Q2) events ($u' < 0$ and $v' > 0$), which occur when slow-moving streaks are ejected away from the wall, and sweep (Q4) events ($u' > 0$ and $v' < 0$), which occur when fluid rushes wall-wards to replace ejected fluid. Figure 5.10 presents quadrant analysis using the hyperbolic hole method of Willmarth and Lu [21] presented in equations (5.2) and (5.3).

$$\overline{u'v'_Q}(x, y) = \lim_{T \rightarrow \infty} \frac{1}{T} \int_0^T u'v' I(x, y, t) dt \quad (5.2)$$

$$I(x, y, t) = \begin{cases} 1, & (u'v')_Q \geq hu'_{rms}v'_{rms}. \\ 0, & \text{Otherwise} \end{cases} \quad (5.3)$$

Figure 5.10 shows $\overline{u'v'_Q}/\overline{u'v'}$, the proportion of the total Reynolds shear stress at different coordinates for Q2 and Q4 giving an indication of how the significance of events in these quadrants change. The larger values of h indicate a higher threshold for events to be considered and hence show just the stronger events contributing to the Reynolds shear stress. For typical wall shear flows, sweep events tend to dominate the near-wall region for $y^+ < 12$ [61], with ejection events dominating further from the wall. This is reflected in figure 5.10 where ejection events dominate at $y^{+0} = 15$

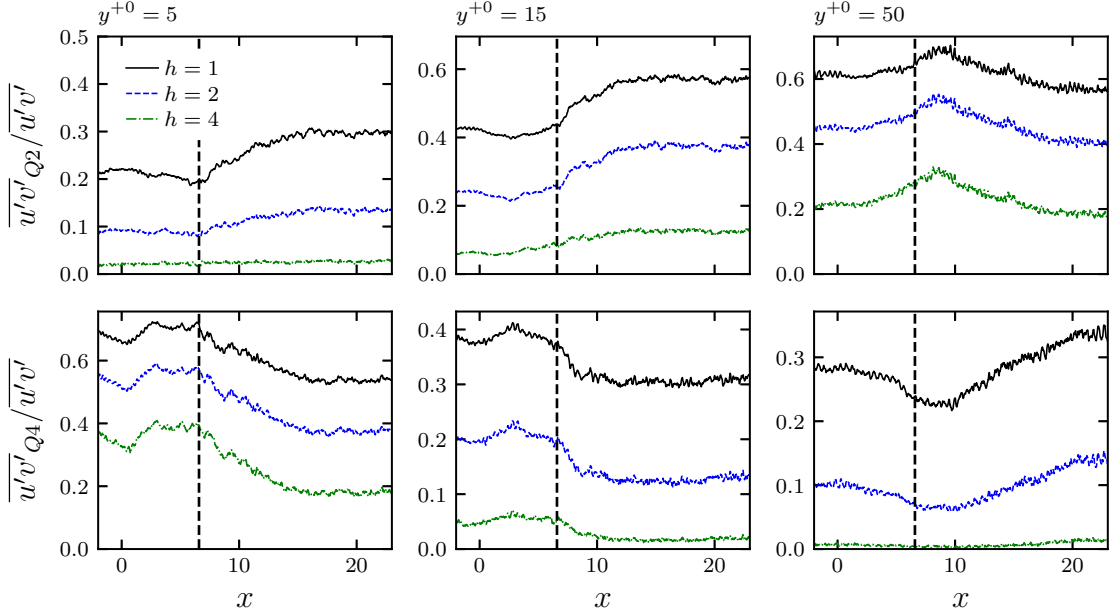


Figure 5.10: $\overline{u'v'}_{Q2}/\overline{u'v'}$ calculated using the method of Willmarth and Lu [21]. The values of the threshold h are given in the legend. The black dashed line indicates the onset of transition.

and particularly at $y^{+0} = 50$. It is interesting to note that the onset of transition is marked by a significant increase in the proportion of high-magnitude ejection events. This is signified by similar increases in the contribution to the Reynolds shear stress across all thresholds. This also indicates that the new turbulent structures created at the onset of transition are linked to the negative u' fluctuations, which is potentially consistent with the interactions on slow-moving streaks that have been found to result in streak breakdown in bypass transition [148]. Nolan et al. [161] also found a significant increase in ejection events during transition. It should be noted that the corresponding decrease in the contribution of $Q4$ events should not be considered an absolute reduction but merely a reduction in their contribution compared to $Q2$ events, and as shown in figure 5.7(b) during transition the turbulent shear stress increases substantially. The results here can also be compared to the linear temporal acceleration of Seddighi et al. [44] where transition also occurred well prior to the end of the acceleration. The results in the present study are quantitatively near-identical to that study, indicating that events contributing to $\overline{u'v'}$ are comparable in both studies.

Figure 5.11 presents the number of $Q2$ and $Q4$ events averaged over all spanwise points, which would indicate how ‘filled’ the spanwise extent of the domain is at a

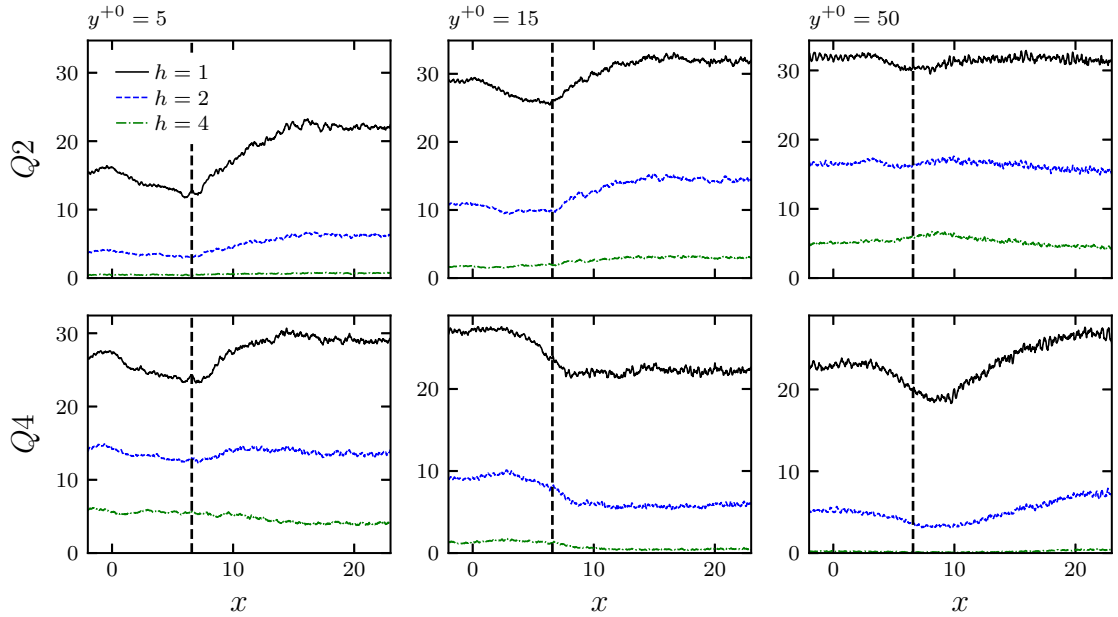


Figure 5.11: Number of distinct events using the method of Willmarth and Lu [21]. The black dashed line indicates the onset of transition.

given x and y location. More details of the algorithm and the sampling is presented in appendix A.3. During pre-transition, the number of Q_2 and Q_4 events decrease, but the number of stronger events (that is, those with $h \in \{2, 4\}$) tend to reduce by a smaller amount with $h = 4$ remaining broadly constant. It should also be noted that the threshold in equation (5.3) will increase due to increasing u'_{rms} indicating that the number of stronger events may even increase in absolute terms. As a result, these events are likely to be responsible for the increases in $\overline{u'v'}$ observed in figure 5.7. This is supported by figure 5.12, which shows the mean ratio of the duration of quadrant events, ΔT_{Q_i} to the interval between events, T_{Q_i} . The reduction of this ratio, particularly close to the wall, indicates a reduction in the dynamical significance of these events during pre-transition, although similarly with figure 5.11, this is not reflected in the stronger events. This observation is consistent with previous studies of spatial acceleration, which indicated the presence of fewer but stronger events, although the changes appear to be less severe than for conventional cases [87, 112]. After the onset of transition, both the number of events and $\Delta T_{Q_i}/T_{Q_i}$ strongly increases at the wall-normal locations closer to the wall ($y^{+0} \in 5, 15$) responding further upstream indicating that the processes which lead to the breakdown of the flow are linked to the dynamics of the near-wall region.

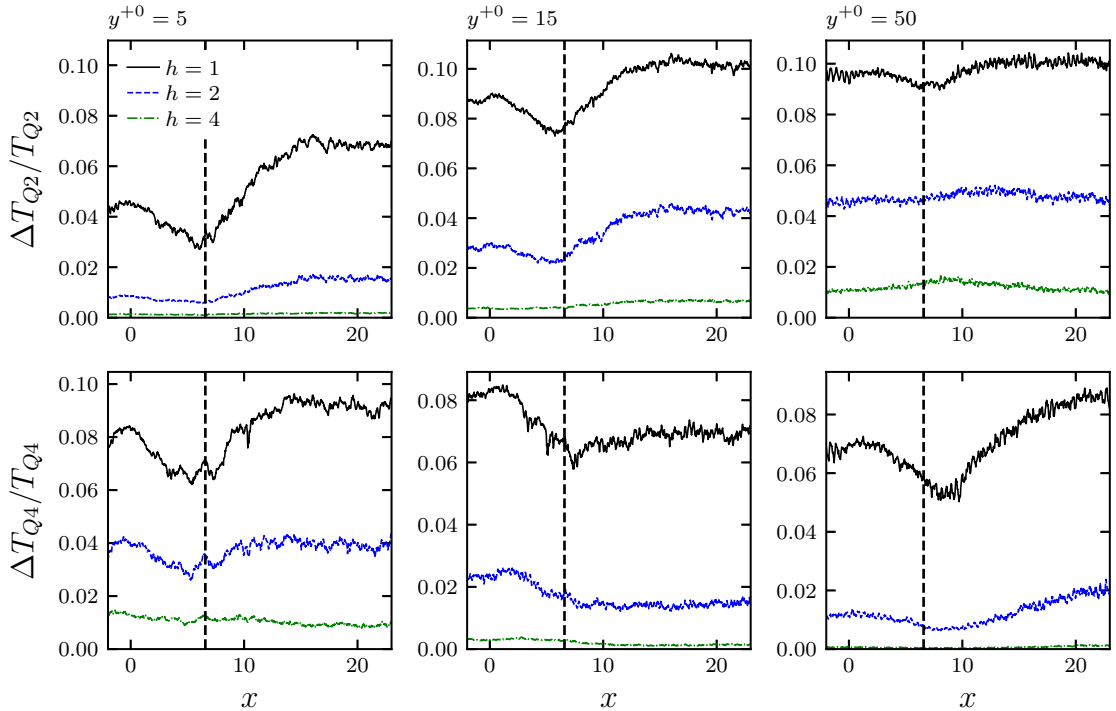


Figure 5.12: The ratio of the mean duration of quadrant events and the interval between quadrant events. The black dashed line indicates the onset of transition.

5.4.4 Correlations

Figures 5.13 and 5.14 show the autocorrelation, which can be used to understand how the scales of turbulent structures are altered by the acceleration. Figures 5.13(a) and 5.13(b) show the autocorrelation with respect to spanwise and streamwise separation, respectively defined as:

$$R_{11}(x, \Delta x) = \langle u'(x)u'(x + \Delta x) \rangle / \overline{u'^2(x)}, \quad (5.4)$$

$$R_{11}(x, \Delta z) = \langle u'(x)u'(x, \Delta z) \rangle / \overline{u'^2(x)}. \quad (5.5)$$

Figure 5.13(a) gives an indication of the spanwise spacing of the near-wall streaky structures. The spacing is calculated as $2z_{min}$, where z_{min} is the distance to the first minimum. After the start of the acceleration, there is a mild decrease in the absolute spanwise spacing. However, when presented in local wall units, the spacing increases during pre-transition. These results show similar trends to Talamelli et al. [94], who indicated that there is a reduction in the absolute spanwise spacing, but when locally scaled, the spacing increases. These variations are substantially milder in the present

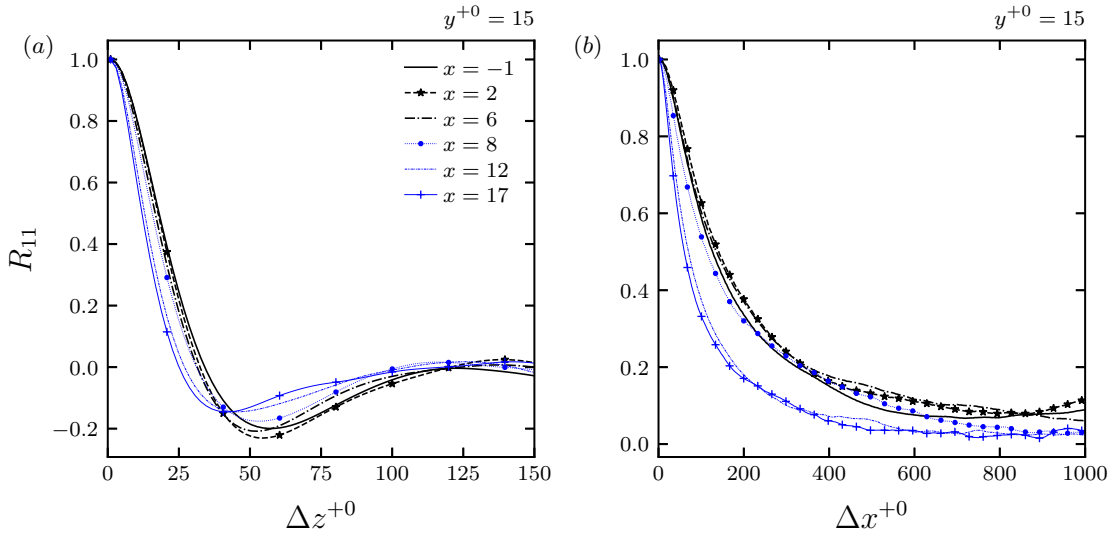


Figure 5.13: Streamwise velocity autocorrelation in the spanwise (a) and streamwise (b) directions at various streamwise locations. The blue lines are from locations after the onset of transition.

study, however. Figure 5.13(b) shows that after the onset of the acceleration, the width of the autocorrelation increases in the streamwise direction consistent with the elongation of the streaks during pre-transition. With the onset of transition, the correlation shortens consistent with the breakdown of the streaks and the generation of new turbulence, which is of shorter spatial scale than the initial turbulent flow as shown in figure 5.4(b). After the completion of transition, the streamwise scale of the turbulence is clearly far shorter than the initial flow.

Figure 5.14 shows the $\Delta z - y$ contour of the spanwise autocorrelation with only the negative values present to more closely compare with similar plots in Matsubara and Alfredsson [139]. Nonetheless, the results show a very similar trend before and during transition. It is clear that the minimum becomes more negative during the pre-transition phase, consistent with a strengthening of the streaks, although the change, in general, is relatively small, consistent with the increases of u' in figure 5.4(b). After the onset of transition, the strength of the minimum fades consistent with figure 5.13(a) due to the breakdown of the streaks during the transition phase. The development also closely resembles similar contour plots in He and Seddighi [43], which showed initial strengthening in pre-transition followed by a noticeable decline in the strength of the minimum with the onset of transition.

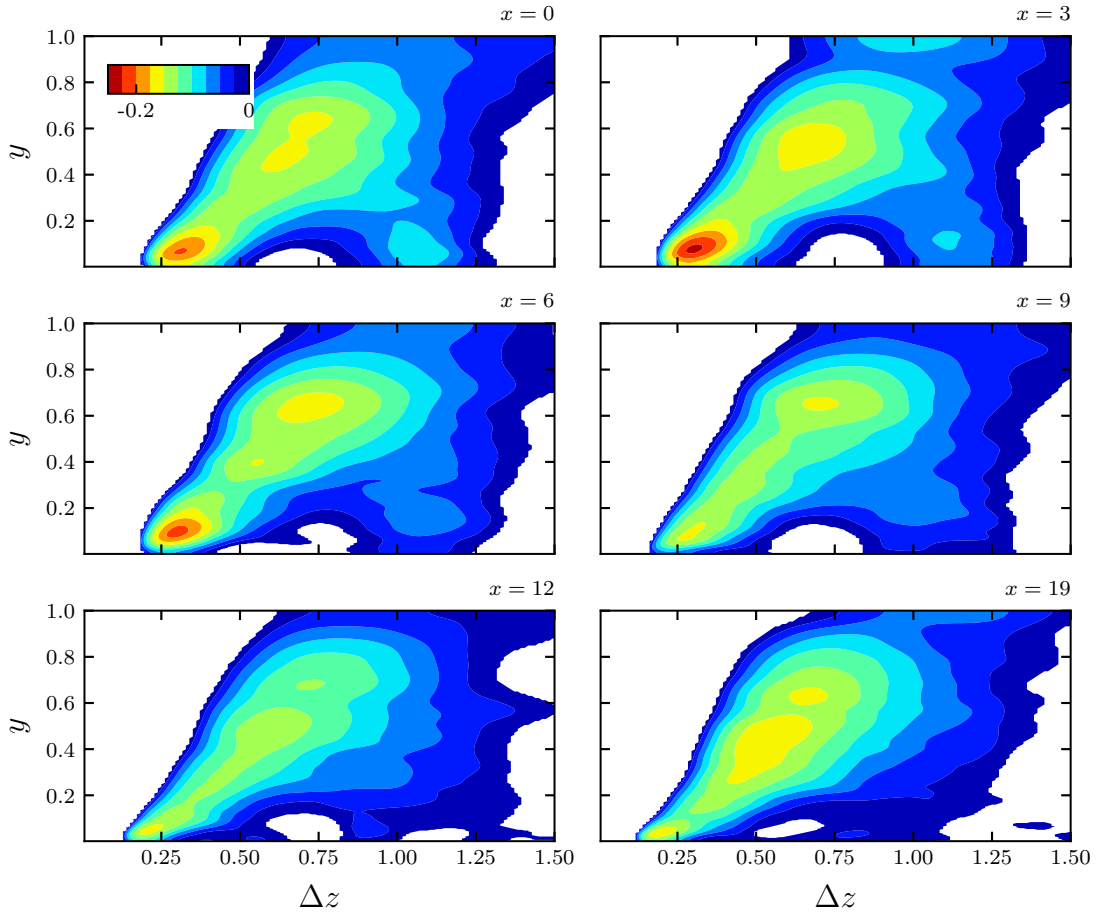


Figure 5.14: A $\Delta z - y$ contour of the spanwise autocorrelation of the streamwise velocity at streamwise locations indicated in the top right of each figure. Only the values where the autocorrelation is negative are shown for clarity.

5.4.5 Flow structures

With the strengthening of the streaks observed during pre-transition and the apparent role of low-speed streaks in the breakdown of the flow, it is useful to study the dynamics of the buffer layer where these streaks reside. The root-mean-square of the streamwise vorticity fluctuations is presented in figure 5.15, and the instantaneous streamwise vorticity is presented in figure 5.16. During the pre-transition region, figure 5.15(a) shows that until the end of this period, $\omega'_{x,rms}$ is unchanged, which is similarly indicated by figures 5.16(a) to 5.16(c). The generation of streaks is the result of the interaction between the streamwise vortices and the mean shear (the lift-up effect). The constant streamwise vorticity observed here indicates that the larger amplitude near-wall streaks during pre-transition are linked primarily to the

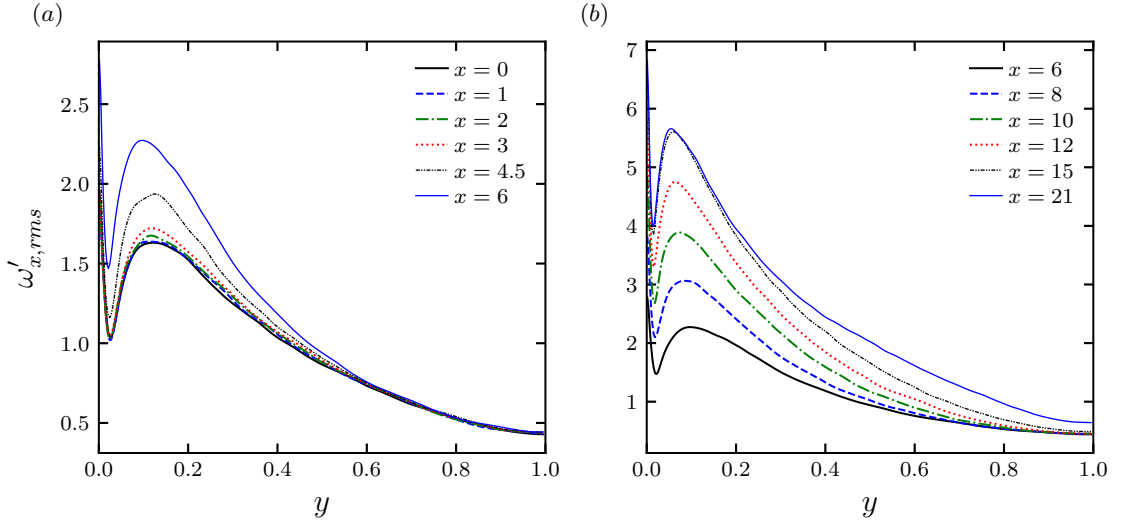


Figure 5.15: Wall-normal distribution of $\omega'_{x,rms}$ at different streamwise locations. (a) during pre-transition. (b) after the onset of transition.

increase in the mean shear, which results from the acceleration. These stronger streaks then remain stable until the onset of transition. It is conceivable that the process of generating stronger streaks through the lift-up effect may be responsible for the apparent increase in the absolute number of stronger Q2 and Q4 events observed in figure 5.11 [7].

Figure 5.15(b) shows that with the onset of transition, $\omega'_{x,rms}$ increases significantly until $x = 15$, which is also indicated by the instantaneous plots (figure 5.16). Figure 5.16(d) shows that with the onset of transition, there are localised spots of increased streamwise vorticity, which can be observed growing downstream in figures 5.16(e) and 5.16(f). Such sudden changes can be linked to the breakdown of the streaks and are a reflection of the much smaller scales of the new turbulence structures. Figure 5.17 shows a top-down view of the three-dimensional isosurfaces of the streamwise velocity fluctuations and the streamwise vorticity. This figure shows the sinuous breakdown of a near-wall streak with the onset of transition in a mechanism similar to that detailed in studies of bypass transition [149, 150]. The time frame and spatial location of the plots are shifted consistently to follow the event. At $t^* = 71.5$, a high-speed streak (green) can be observed on the $+z$ flank of the low-speed streak (blue). At this point, the streamwise vorticity ($+\omega_z$ in black, $-\omega_z$ in red) isosurfaces are barely visible (under the chosen scales used here, which is intended to show the regions of stronger vorticity). It is also important to note the increasing amplitude of

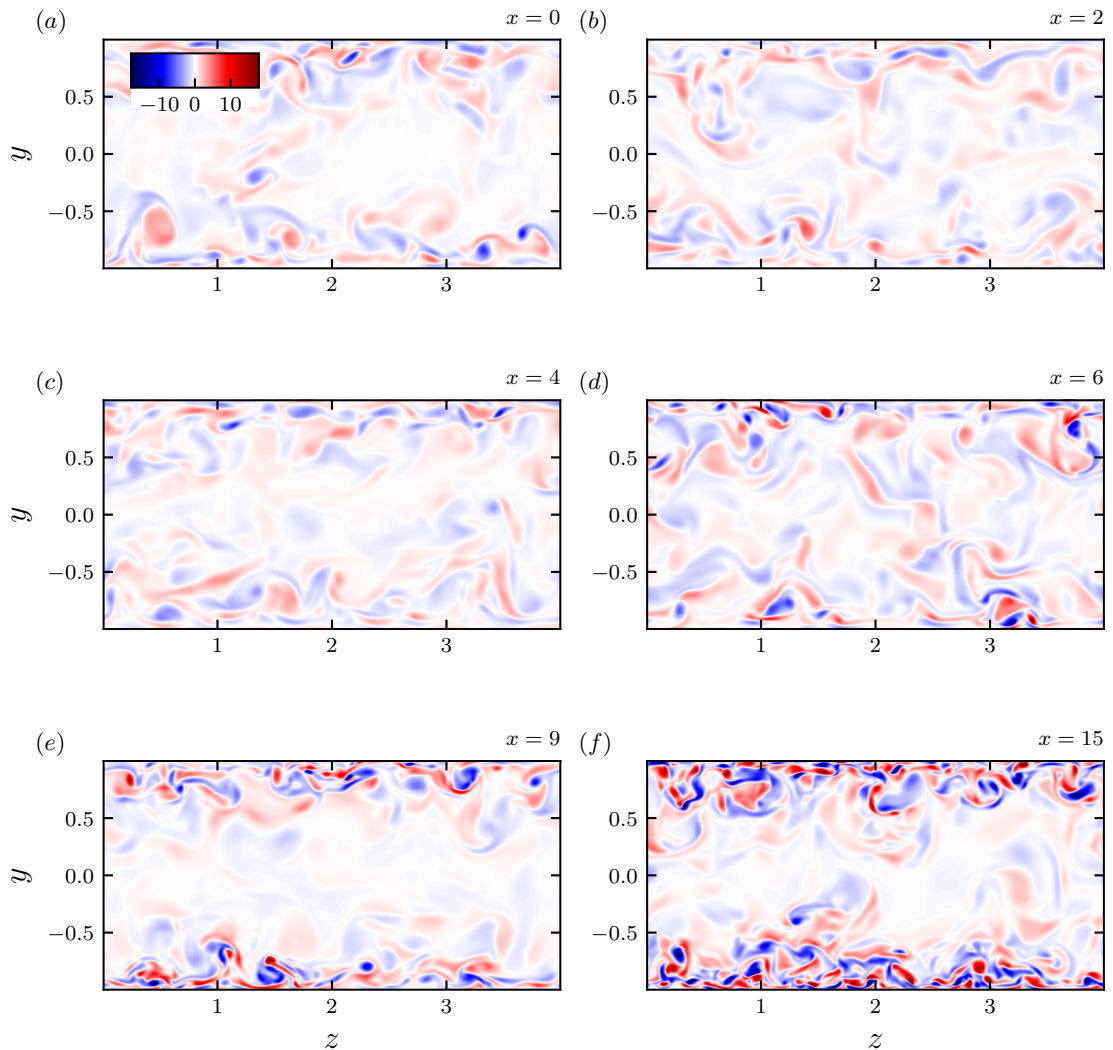


Figure 5.16: $z - y$ contours of the streamwise vorticity ω'_x at different streamwise locations.

the streaks as downstream distance increases, which is shown by the increased volume of the isosurface. This is consistent with the streamwise autocorrelation in figure 5.14. At $t^* = 72.5$, the strengthened positive u' streak can be observed catching up with the low-speed streak with the consequent generation of new streamwise vorticity. At this point, the spanwise waviness of the streaks and the patterning of the streamwise vorticity bear significant similarity to Brandt and de Lange [149]. The patterning also resembles the layout of quasi-streamwise vortices in studies of wall turbulence (figure 2.4) [7] as well as the sinuous instabilities observed in studies of temporal ac-

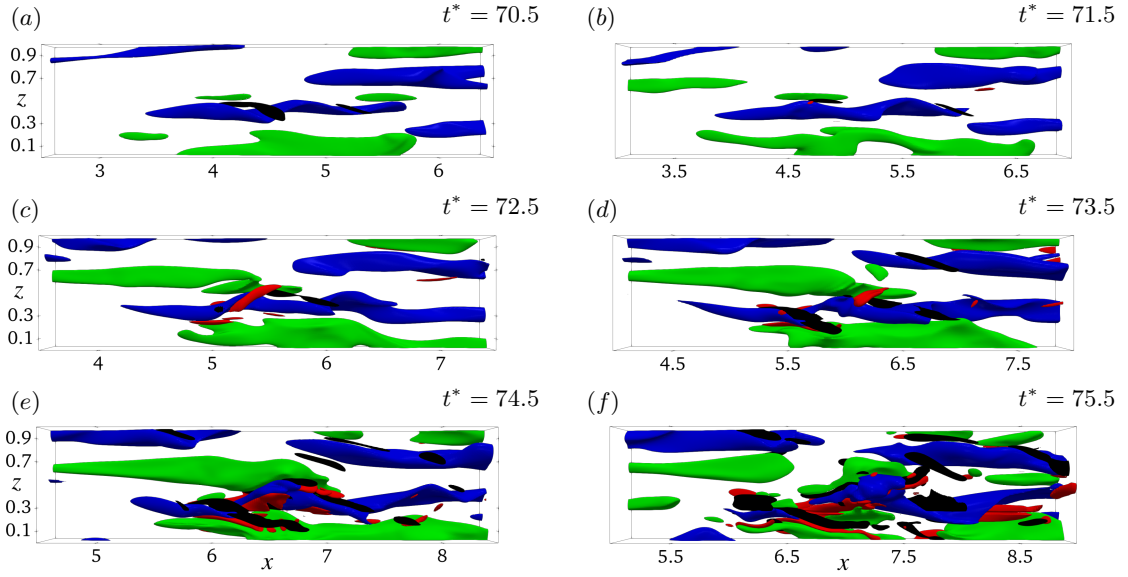


Figure 5.17: A top-down view of u' and ω'_x isosurfaces at $t^* \in \{70.5, 71.5, 72.5, 73.5, 74.5, 75.5\}$. u' surfaces: -0.31 (blue); 0.31 (green). ω'_x isosurfaces: -8 (red); 8 (black).

celeration [172]. As the instability progresses in the subsequent frames, the spanwise waviness of u' and the streamwise vorticity intensify. At $t^* = 75.5$, the low-speed fluid can be observed being ejected from the near-wall region. This indicates that the generation of new localised streamwise vorticity in figure 5.16(d) can be linked to the breakdown of the strengthened streaks that occurs with the onset of transition. This also confirms the role of low-speed streaks in the process of transition implied by the quadrant analysis. The higher energy contained in the strengthened streak makes it more susceptible to the development of instabilities on interaction with a high-speed streak. The resulting breakdown contains small scales and high magnitude disturbances characteristic of transition to a higher Reynolds number turbulent flow.

5.5 Summary and conclusion

This chapter describes a study of spatially accelerating turbulent flow based on the direct numerical simulation of a flow with longitudinally accelerating moving walls to create a relative acceleration between the fluid and the wall. This enables the influence of viscous effects on spatial acceleration to be investigated without inducing flow contraction. The flow response is characterised by the development of a new boundary layer in response to the acceleration due to viscous effects at the wall. The development of this boundary layer and the eventual transition of the flow in response

can explain the key aspects of the turbulence dynamics. Qualitative similarities were also observed with previous studies of spatially accelerating TBLs.

5.5.1 Summary of flow development

At the onset of the acceleration, a new boundary layer forms due to the influence of viscous effects, resulting in a three-stage development. The new boundary layer modulates the pre-existing near-wall streaky structures, leading to their amplification through the lift-up effect. This leads to significant growth of the streamwise Reynolds stress and turbulence kinetic energy production close to the wall. The transverse stresses are not strongly affected, with the pressure strain remaining constant. The eddy viscosity does not change at this stage, indicating that turbulence mixing is not strongly changed at this point. This region is denoted pre-transition. Eventually, streak instabilities develop on specific strengthened streaks, leading to their breakdown and the formation of turbulent spots, which marks the onset of the transition region. These spots spread in the spanwise direction as they travel downstream until the surface of the wall is covered in newly generated turbulence. The breakdown of the streaks is associated with extreme ejection and, to a lesser extent, sweep events. At this stage, the transverse stresses increase alongside large increases in the pressure strain, indicating a significant enhancement of intercomponent energy transfer. The final fully turbulent region is characterised by the diffusion of turbulence into the core of the channel, with the near-wall region not strongly altered.

5.5.2 Similarities and differences with conventional spatial acceleration

The overall development of the flow shares many similarities with conventional spatial acceleration. Among the similarities is the downstream growth of $\overline{u'u'}$ from the commencement of the acceleration and the movement of the peak away from the wall, which have been widely observed in previous studies of spatial acceleration [102, 97]. The absolute increase of production during pre-transition is also consistent with previous studies [87]. The decrease in the spanwise scale of the streaks before the onset of transition is also similar in both accelerations. Similarly, the role of pressure strain with the onset of transition mirrors that of retransition in spatially accelerating flows [10]. The increased contribution of stronger Q2 events to the Reynolds shear stress during pre-transition has also been observed in previous studies [116, 87].

While these similarities suggest similar processes could be at work in both accelerations, there are some notable differences. This includes different trends in the development of the mean velocity profile in the moving wall acceleration, which appears to be linked to the lack of flow contraction and can be observed in other accelerating flows that lack wall-normal contraction such as temporal acceleration and laterally converging ducts [44, 116]. Additionally, the constant transverse stresses during pre-transition differ somewhat from laminarising spatial accelerations, where they have been observed to reduce close to the wall [10]. These differences will be discussed in chapters 6 and 7.

Chapter 6

Transition in spatially accelerating turbulent boundary layers

This chapter presents simulations of spatially accelerating turbulent boundary layers covering a range of acceleration rates corresponding to laminarescent accelerations, where the mean flow is strongly affected by the acceleration, but the mean flow parameters do not clearly indicate a shift towards values typical of a laminar flow [86], and laminarising accelerations, where the mean flow parameters tend towards laminar-like values. There are two main objectives of this chapter. The first is to understand whether the flow is characterised by the development of a boundary layer followed by transition as for the moving wall and temporal accelerations. The second is to understand how the turbulence response changes as the acceleration rate increases.

6.1 Case setup

Simulations have been performed for a range of K both above and below the critical acceleration parameter for flow laminarisation to occur $K_{crit} = 3 \times 10^{-6}$ [87] using the method developed in section 4.5. These cases are summarised in table 6.1 with the profiles of U_∞ and K presented in figure 6.1. Cases 1 and 2 are strong accelerations with a K_{max} of 6.3×10^{-6} and 3.9×10^{-6} , respectively, and would hence be expected to begin the process of laminarisation as K exceeds K_{crit} for a downstream distance of around $100\theta_0$ in both cases. The maxima of the parameters Λ [9] and Δ_p [22], are presented in table 6.2. The values of Λ_{max} [9] are large for cases 1 and 2 but do not exceed the threshold of 50, indicating that while dominated by the pressure gradient, they are not likely to have ‘completed’ laminarisation. $\Delta_{p,max}$ exceeds the typical threshold for the onset of laminarisation for both cases [87]. Cases 3 and

Table 6.1: Case setup for the spatially accelerating TBLs. The acceleration parameter, K , is multiplied by 10^6 . Here, the lengths, L , are normalised with the maximum boundary layer thickness in the domain, showing that the height of the domain, $L_y \gtrsim 3$. The mesh resolutions represent their worst value in the domain with Δy_δ^+ , indicating the wall-normal mesh resolution at $y = \delta$.

	$Re_{\theta,ref}$	K_{max}	L_x	L_y	L_z	Δx^+	Δz^+	Δy_w^+	Δy_δ^+	$T_s u_\tau / \delta$
Case 1	883	6.26	59.4	2.91	3.77	9.88	6.11	0.719	6.98	14
Case 2	882	3.88	68.6	2.94	3.42	10.1	6.19	0.673	7.73	9.57
Case 3	869	2.36	80.8	3.09	3.08	9.8	6.07	0.695	6.45	14
Case 4	844	1.21	113	3.01	3.37	37.1	16.2	0.855	13.1	10

4 are weaker accelerations with a K_{max} of 2.4×10^{-6} and 1.2×10^{-6} , respectively, and while likely to be still strongly affected by the acceleration, are not expected to show clear indications of laminarisation. This is supported by the values of Λ_{max} and $\Delta_{p,max}$, which are below the typical laminarisation threshold values for both cases. Consequently, these cases would typically be regarded as laminarescent [93].

The streamwise coordinates of each case have been shifted in the streamwise direction such that $x = 0$ occurs at a reference plane upstream of the beginning of the acceleration. Quantities associated with the reference plane are denoted with a superscript or subscript 0. For example, y^+ at $x = 0$ is denoted y^{+0} . Velocities and lengths have been normalised by the freestream velocity, $U_{\infty,0}$, and momentum thickness, θ_0 at the reference plane unless otherwise stated. The initial Reynolds number is approximately the same in all cases with $Re_{\theta,0} = U_{\infty,0}\theta_0/\nu \approx 870$, which represents the highest Reynolds number DNS of a laminarising spatially accelerating TBL to date (to the author’s knowledge). The near-constant initial Reynolds number also means its effect on the turbulence response cannot be established in this study. The velocity ratio, $U_{\infty,1}/U_{\infty,0}$ is 2 for all cases ensuring that the turbulence response, which is anticipated to be weaker in cases 3 and 4, can be characterised unambiguously in all cases. The mesh sizes are 0.98, 1.3, 1.4, and 0.36 billion, respectively. Case 4 has been computed using the LES method discussed in section 4.1.3 with $\nu/\nu_0 = 10$

Table 6.2: Maximum pressure gradient parameters from Narasimha and Sreenivasan [9] and Patel [22] for each case.

	Case 1	Case 2	Case 3	Case 4
Λ_{max}	45	32	22	17
$\Delta_{p,max}$	-0.037	-0.028	-0.02	-0.012

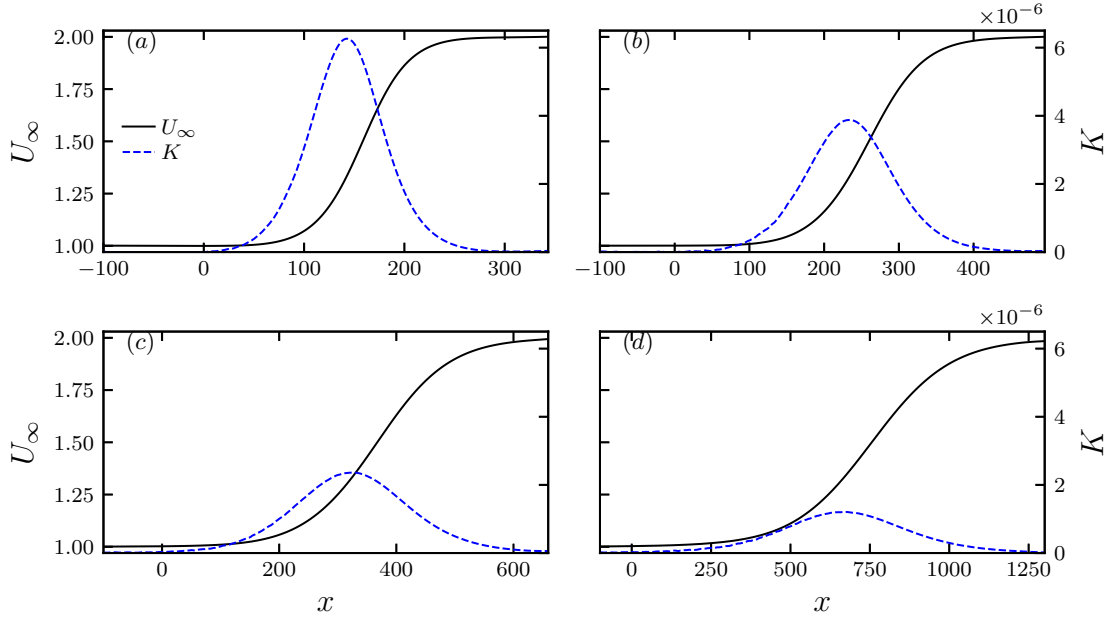


Figure 6.1: The freestream velocity, U_∞ and the acceleration parameter, K . (a): case 1. (b): case 2. (c): case 3. (d): Case 4.

following the strategy described in chapter 4 with the mesh resolution similar to the LES cases in section 4.7.4.1 and to the validation case in section 4.7. The mesh resolutions for cases 1-3 are comparable with previous DNS studies of ZPG and FPG TBLs [10, 215, 211] and follow the recommendations in section 4.3, with the values in table 6.1 representing their worst value in the domain. The resolution for the LES corresponds to previous wall-resolved LES studies [10].

6.2 Case characterisation

Figures 6.2 and 6.3 shows C_f and H to further characterise the flow regime in all cases. The ZPG case from section 4.7 is shown for comparison, showing that upstream of the acceleration, these quantities follow that of a ZPG, although H shows a small offset of around 1% in cases 1, 2 and 3. The mean velocity and the Reynolds stresses are compared with the ZPG case in appendix B.1, indicating that the acceleration only has a minor influence on the upstream flow. Similar to previous studies [10, 103], for strong acceleration (Cases 1 and 2), the C_f rapidly increases initially, reaching a maximum, followed by a rapid reduction to a minimum and a recovery. The initial increase is due to the substantial increase in velocity gradient close to the wall, which

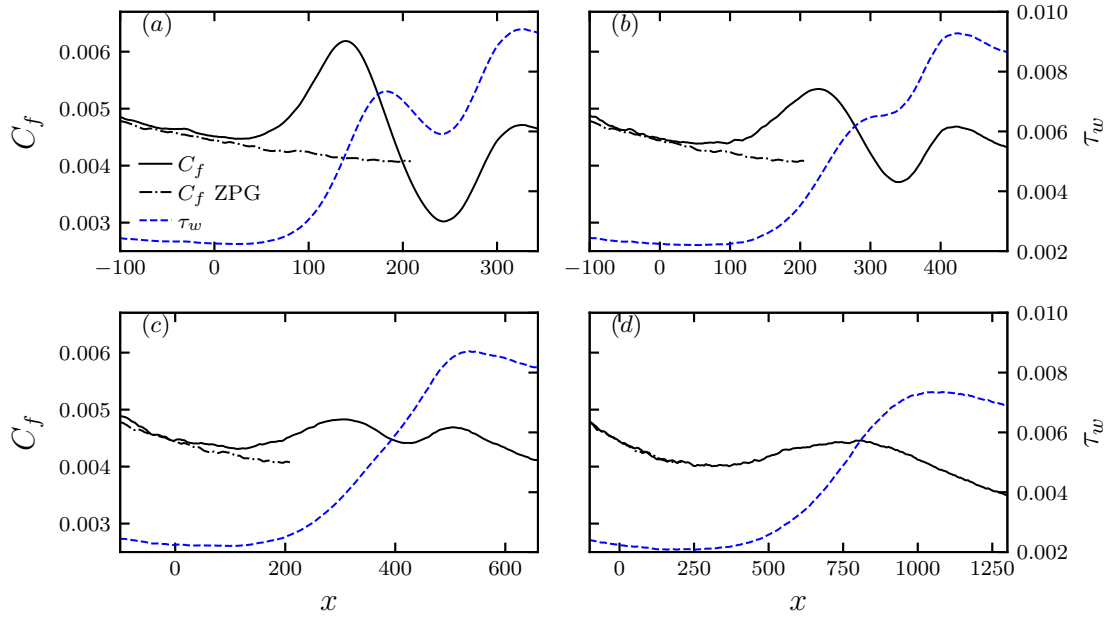


Figure 6.2: Skin friction coefficient, C_f and the wall shear stress, τ_w . (a): case 1. (b): case 2. (c): case 3. (d): Case 4. All y axis limits are fixed to highlight the influence of the acceleration in the different cases.

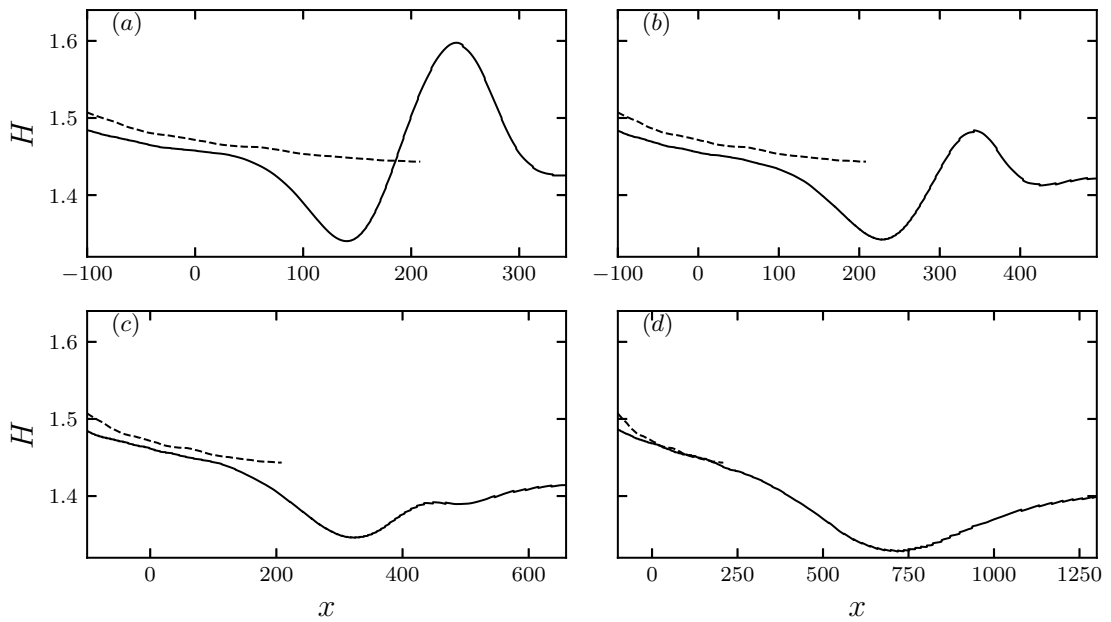


Figure 6.3: Shape factor, H . (a): case 1. (b): case 2. (c): case 3. (d): Case 4. All y axis limits are fixed to highlight the influence of the acceleration in the different cases.

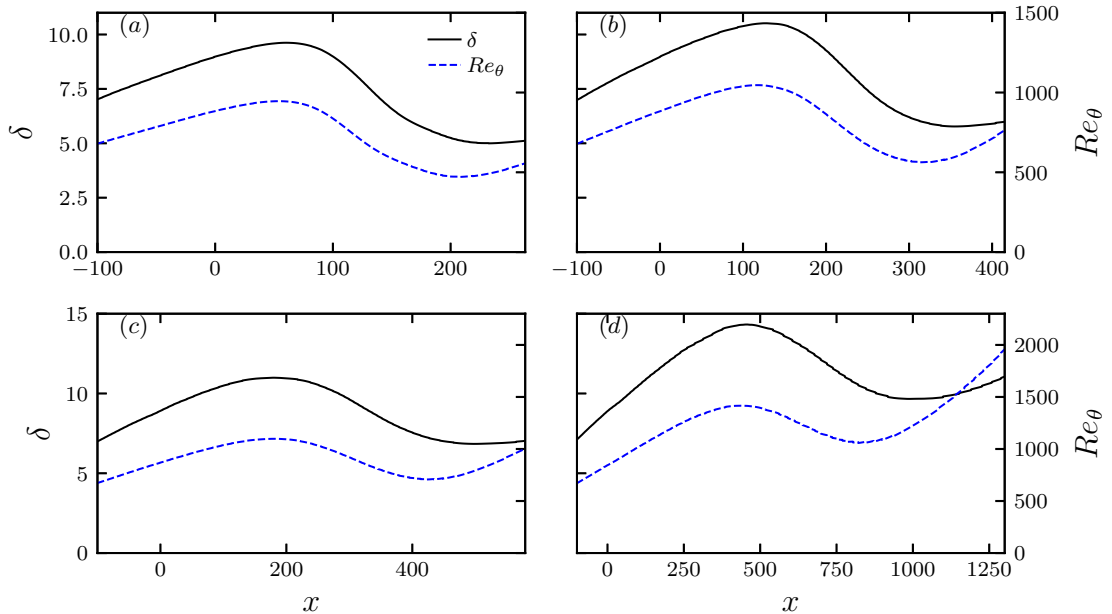


Figure 6.4: Boundary layer thickness, δ and the momentum thickness Reynolds number, Re_θ . (a): case 1. (b): case 2. (c): case 3. (d): Case 4.

can be observed in the wall-shear stress, τ_w which is also shown in figure 6.2. The subsequent reduction is caused by the increase of τ_w failing to keep up with the rapidly increasing U_∞ . In case 1, τ_w reduces in the later stages of the acceleration, likely due to a reduction in turbulence activity due to laminarisation. In the less strongly accelerated case 2, τ_w stagnates rather than reduces. The minimum of C_f is associated with the recovery of turbulence in the boundary layer, which leads to a substantial growth of the wall shear stress and signifies the onset of retransition [9]. Finally, τ_w and C_f reach a maximum and subsequently reduce monotonically. The shape factor, H shows an initial reduction followed by substantial increases towards laminar-like values similar to previous studies [9, 102], although the accelerations end before these values are reached ($H \approx 2$ in a Falkner-Skan boundary layer under contraction), with H reaching a maximum around the same location as the minimum of C_f , again indicating the onset of retransition, before returning to values more consistent with turbulent boundary layers.

In case 3, C_f exhibits similar features to the stronger accelerations, albeit with smaller variations, whereas case 4 shows no reduction in C_f . Unlike the stronger accelerations, there is no obvious change in the trend of τ_w in these cases before the maximum towards the end of the acceleration. In these cases, H reduces with the

beginning of the acceleration but shows little sign of a rapid increase towards laminar-like values, in line with the expected behaviour based on K , Λ , and Δ_p . The shape of the C_f and H curves in cases 3 and 4 are reminiscent of the laminarescent cases (1 and 3) from Fernholz and Warnack [93], which are also at similar values of K .

Figure 6.4 shows that the overall behaviour of the boundary layer thickness, δ in all cases is similar to that observed in previous studies [103, 10], with δ initially continuing the increasing trend of the upstream ZPGTBL before the effect of flow contraction becomes significant, which results in δ reducing over much of the acceleration even in the weaker accelerations. Cal and Castillo [101] associated the reduction of δ with a tendency towards the quasi-laminar state. However, it should be noted that in case 4, this reduction occurs over a considerable streamwise distance. On the other hand, δ in cases 1 and 2 reduce rapidly in a short downstream distance. These parameters also indicate cases 1 and 2 begin the process of laminarisation, whereas cases 3 and 4 exhibit behaviours consistent with laminarescence.

6.3 The transition process

In this section, the mean flow development and turbulence responses will be discussed, which will lead to the proposition that spatially accelerating TBLs can be characterised as a process of transition. Figures 6.5(a) and 6.6(a) presents the mean velocity profile for cases 1 and 3, showing that early in the acceleration (blue lines), \bar{u} tends to accelerate in a mostly uniform manner away from the wall, whereas close to the wall, there is a steep increase in the mean shear. This is more clearly observed in figures 6.5(c) and 6.6(c), which shows that the mean velocity gradient, $\tau/\tau_{w0} = \partial_y \bar{u}$ increases significantly, but only for a narrow region close to the wall ($y^{+0} \lesssim 40$). This region results from the influence of the viscosity, which acts to resist the freestream acceleration in the vicinity of the wall and represents the development of a new boundary layer that encapsulates the additional near-wall frictional effects from the acceleration. This newly developing boundary layer is analogous to that which forms in temporal and moving wall accelerations. However, there is a less obvious but important additional variation in the mean velocity distribution due to flow contraction, which causes the velocity profile to be flattened in the outer region, as indicated by the reduction of $\partial_y \bar{u}$. In case 1, the decrease in the velocity gradient is substantial, occurring even in the inner part of the boundary layer ($y^{+0} \gtrsim 30$), and by $x = 225$, the velocity profile appears essentially flat away from the wall (figure 6.5(a)). However, in case 3, where the acceleration is relatively mild, this reduction is small and occurs for

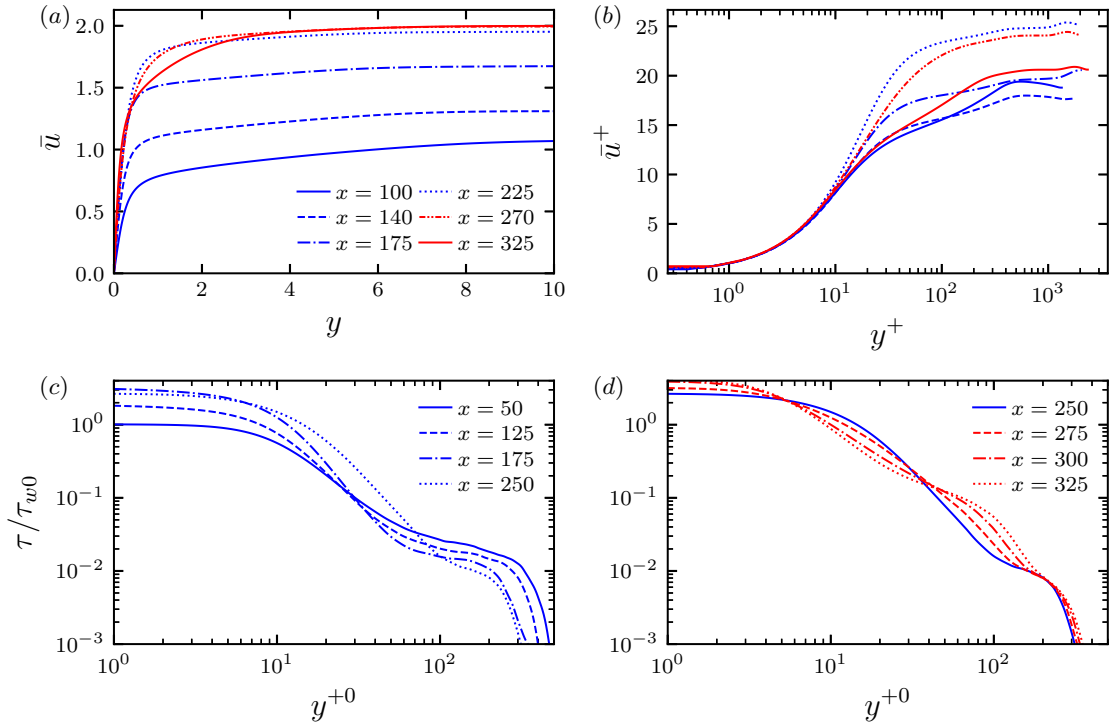


Figure 6.5: Mean flow development for case 1. (a): \bar{u} vs y , (b): \bar{u}^+ vs y^+ . τ/τ_{w0} vs y^{+0} : before transition (c); after transition (d).

$y^{+0} \gtrsim 100$. It should also be noted that the mean velocity profile would also continue developing even without acceleration, but in all the accelerations studied herein, the development associated with the onset of acceleration is much more severe.

The turbulence response in cases 1 and 3 is presented in figures 6.7 and 6.8, which show contours of the velocity fluctuations for all components at a $x - z$ plane close to the wall ($y^{+0} = 15$) with (a) in each figure showing U_∞ for reference. Figure 6.7(b) shows that as the flow travels downstream, the near-wall streaky structures in u' , which are initially faint upstream of the acceleration ($x < 100$), are amplified significantly as they travel downstream ($100 < x < 250$), resulting in long mostly unperturbed streaks which can extend for more than $50\theta_0$. The amplification of the near-wall streaks can explain this through the lift-up effect due to the increased mean shear associated with the new boundary layer, which is a typical phenomenon of the pre-transition region of accelerating flows and bypass transition. Figure 6.8(b) show that u' in case 3 responds similarly to case 1 with a strengthening of the near-wall streaks and emergence of elongated streaks by $x \approx 375$. These streaks are less prominent than in case 1 due to the weaker acceleration, meaning the increase in shear is

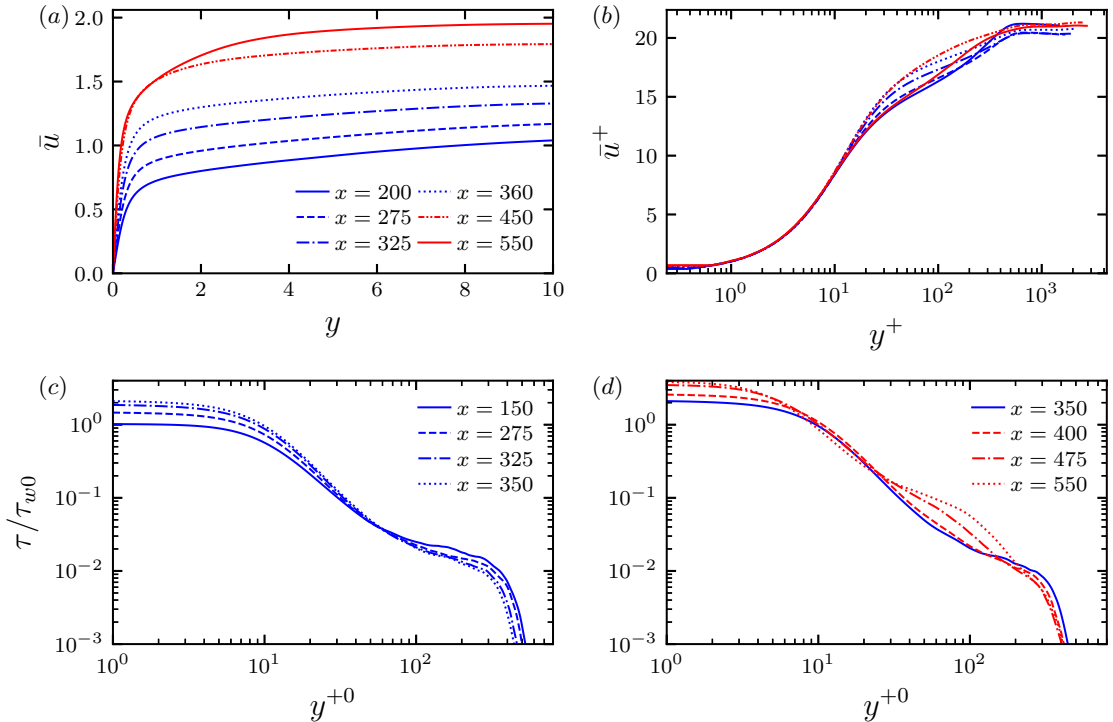


Figure 6.6: Mean flow development for case 3. (a): \bar{u} vs y , (b): \bar{u}^+ vs y^+ . τ/τ_{w0} vs y^{+0} : before transition (c); after transition (d).

less rapid. The behaviours of v' and w' are substantially different to u' . For case 3 (figures 6.8(c) and 6.8(d)), v' and w' do not vary significantly. In contrast, there is substantial attenuation of these components in case 1 (figures 6.7(c) and 6.7(d)) with the flow being largely quiescent by $x = 220$. This attenuation is related to common observations in previous studies of laminarising accelerations, including the reduction in near-wall bursting [86, 65] and the streaks appearing to be less perturbed [110], which can also be observed in figure 6.7(b).

The region of streaks amplification is terminated by the formation of localised high-intensity patches of shorter scale in u' , v' , and w' typically at the interface between the high and low-speed streaks similar to the breakdown of streaks in bypass transition [149]. In case 1, the spots are easily observed ($x \approx 250$) due to the stronger streaks at the breakdown point and the attenuated surrounding turbulence. The spots are weaker in case 3 ($x \approx 375$), being only slightly stronger than the surrounding turbulence. Hence, a spot detection algorithm, detailed in appendix B.2, has been used to identify the broken-down patches for clarity. These spots grow as they travel downstream, and by $x \approx 310$ in case 1 ($x = 500$ in case 3), the newly generated

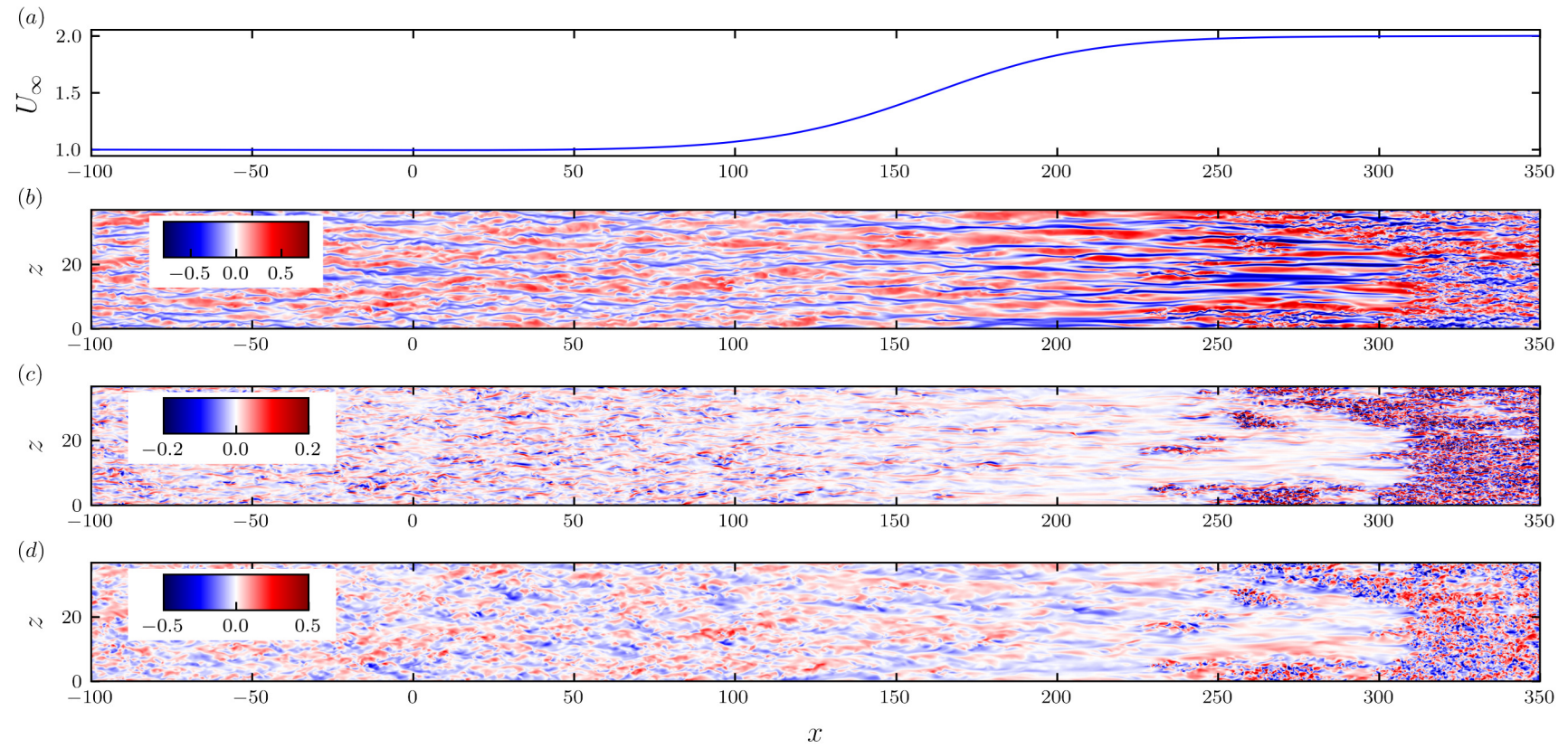


Figure 6.7: $x - z$ plane of the velocity fluctuations at $y^{+0} = 15$ for case 1. (a) U_∞ , (b) u' , (c) v' , (d) w' .

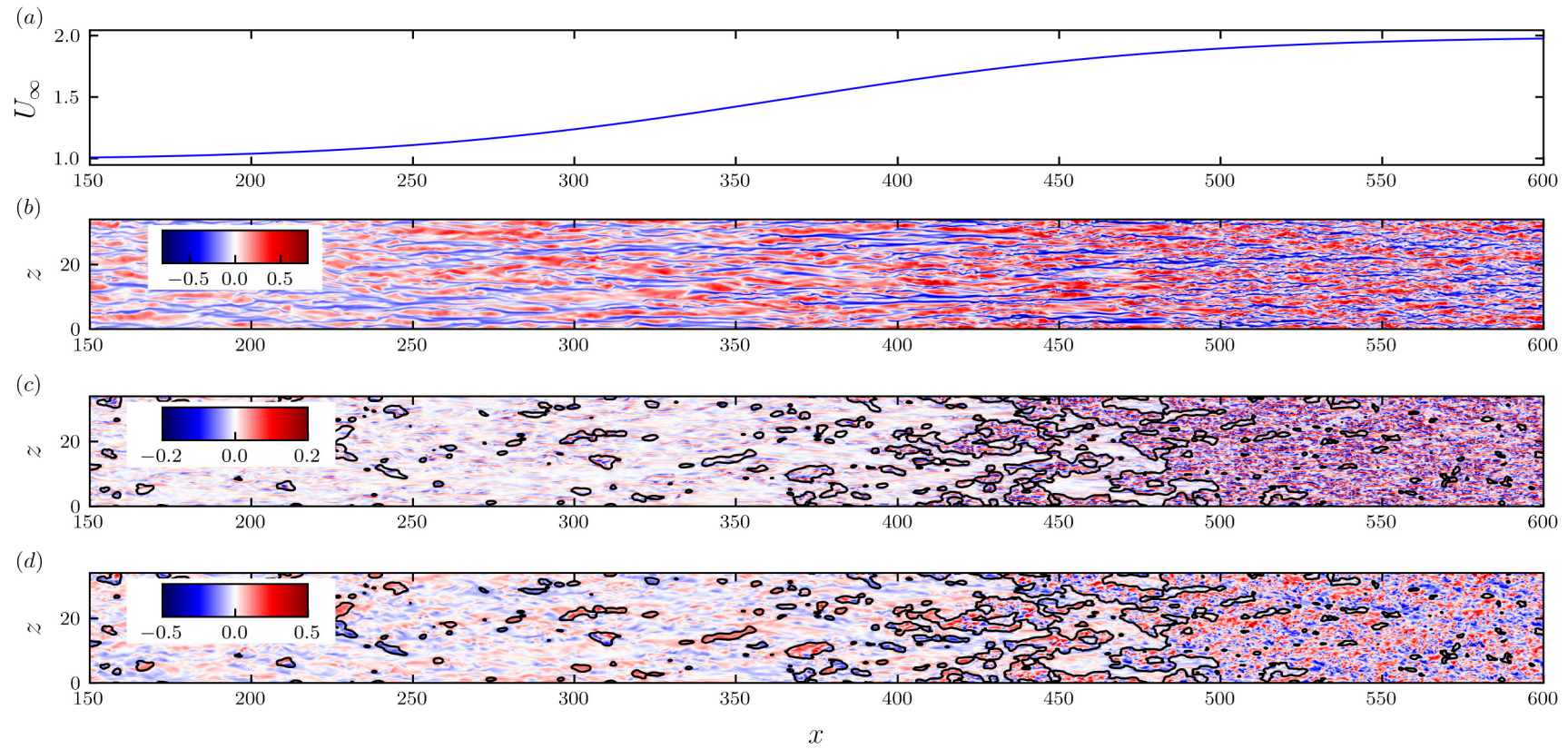


Figure 6.8: $x - z$ plane of the velocity fluctuations at $y^{+0} = 15$ for case 3. (a) U_{∞} , (b) u' , (c) v' , (d) w' .

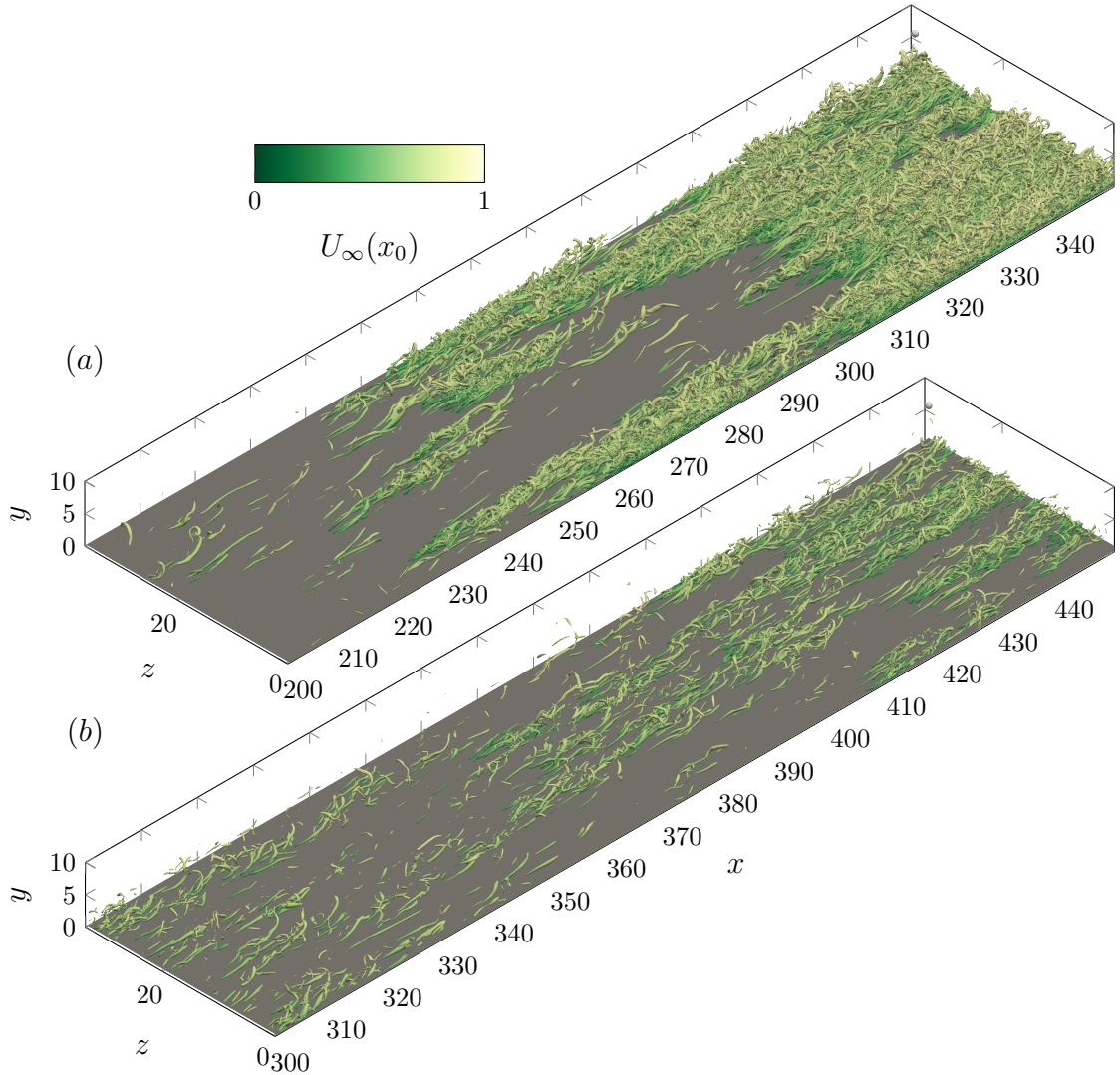


Figure 6.9: Isosurfaces of λ_2 for cases 1 and 3. (a) case 1 for $200 < x < 350$ at $\lambda_2 = -0.1$. (b) case 3 for $300 < x < 450$ at $\lambda_2 = -0.16$. The isosurfaces are coloured by the mean velocity at $x = 0$.

turbulence fills the spanwise extent of the wall. The break-up of the streaks leads to the generation of new vortical structures. Figure 6.9 shows isosurfaces of the λ_2 vortex identification criterion (section 2.3) for cases 1 and 2. Figure 6.9(a) shows the presence of the strong vortices accompanying the spots in case 1, whereas further upstream, there are few vortices due to the attenuation of transverse motions. These new vortices are predominantly hairpin-like, resembling images observed in studies of bypass transition such as Wu and Moin [144] and Wu et al. [237]. The substantial variation of the vortex density highlights the intermittent character of the near-wall turbulence around the onset of transition. For case 3 (figure 6.9(b)), a substantial

increase in the density of vortices can also be observed as the spots break down, although weaker vortical structures can still be observed upstream, reflecting the essentially unchanged transverse motions close to the wall.

The visualisation and mean flow development discussed above suggest that key elements of flow response to acceleration resemble those in a boundary layer bypass transition, similar to temporal and moving wall acceleration. The transition process can naturally be split into three distinct stages that mirror those in other accelerating flows. During the first stage, pre-transition, the turbulence response is primarily characterised by the amplification of streaks due to the modulation of near-wall structures by the new boundary layer. During this stage, a clear difference can be observed between stronger (case 1) and weaker accelerations (case 3): in the former v' and w' reduce gradually in absolute terms in the near-wall region throughout pre-transition but not in the latter, which retains a fully turbulent inner layer. These differences are discussed in more detail in later sections. The second stage is transition and is characterised by the formation and growth of turbulent spots which coexist with the amplified streaks. The final stage begins once the near-wall region is populated with the newly generated turbulence. It is useful to note that the formation of turbulent spots in case 3 (figure 6.8) occurs during the acceleration, consistent with the notion that transition is not necessarily linked to the end of the acceleration as suggested in section 5.3.

The remainder of the chapter is organised as follows. The development of the key turbulent statistics, including the Reynolds stresses and the energy budgets, are presented in section 6.4, showing that all cases undergo a process of transition. Spectra associated with the development of streamwise component are presented in section 6.5, and the mechanisms that lead to the attenuation of the transverse motions near the wall are explored in section 6.6. The conclusions are presented in section 6.7.

6.4 Reynolds stresses and higher-order statistics

6.4.1 Normal Reynolds stresses

The wall-normal distributions of the streamwise and wall-normal Reynolds stresses are presented in figures 6.10 and 6.11 normalised with reference wall units with blue lines for locations during pre-transition and red lines for those after the onset of transition (this colour scheme is used in the remainder of the chapter). This scaling has been used rather than the typical local inner or outer scaling, as many of the distinct

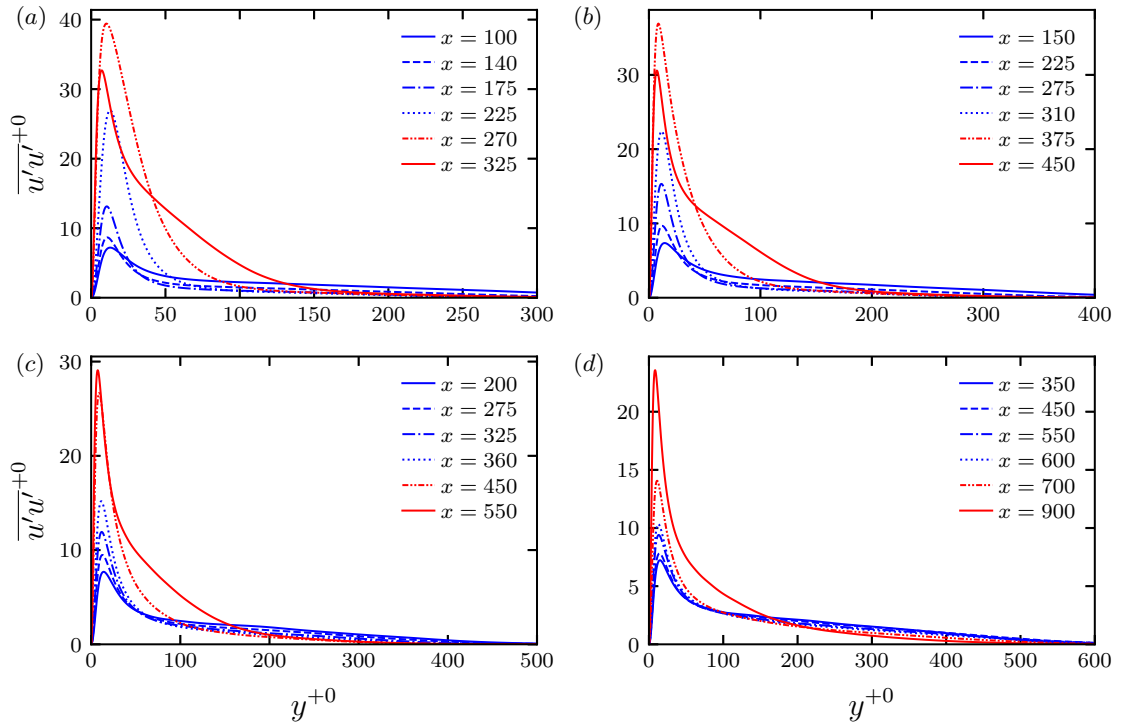


Figure 6.10: Development of $\overline{u'u'}^{+0}$ vs y^{+0} in cases 1 to 4. Blue lines indicate locations before the onset of transition, and red lines indicate those after.

differences that occur in the development of turbulence between the accelerations occur absolutely and would be masked by local scalings. The local scalings have been widely presented in previous studies and remain useful for showcasing key elements of the ‘soft’ laminarisation. During pre-transition, $\overline{u'u'}^{+0}$ exhibits substantial downstream growth in the near-wall region ($y^{+0} < 50$) in all cases due to the amplification of the streaks due to the modulation of the near-wall structures by the new boundary layer. The growth of $\overline{u'u'}^{+0}$ during pre-transition is weaker in the weaker accelerations, which is consistent with the relative prominence of the streaks observed in case 1 compared with case 3 (figures 6.7 and 6.8). Nonetheless, a notable amplification of $\overline{u'u'}^{+0}$ occurs even in case 4 (figure 6.10(d)). This absolute near-wall growth of $\overline{u'u'}^{+0}$ is also observed in previous studies across a range of acceleration rates [93, 102, 10] but has not been explicitly linked to streak amplification. Such increases in the streamwise Reynolds stress are typical of bypass transition and result from the lift-up effect [139, 135].

The response of $\overline{v'v'}^{+0}$ during pre-transition is substantially different from that of $\overline{u'u'}^{+0}$ with no (or minimal) increase in its value from before the acceleration. The re-

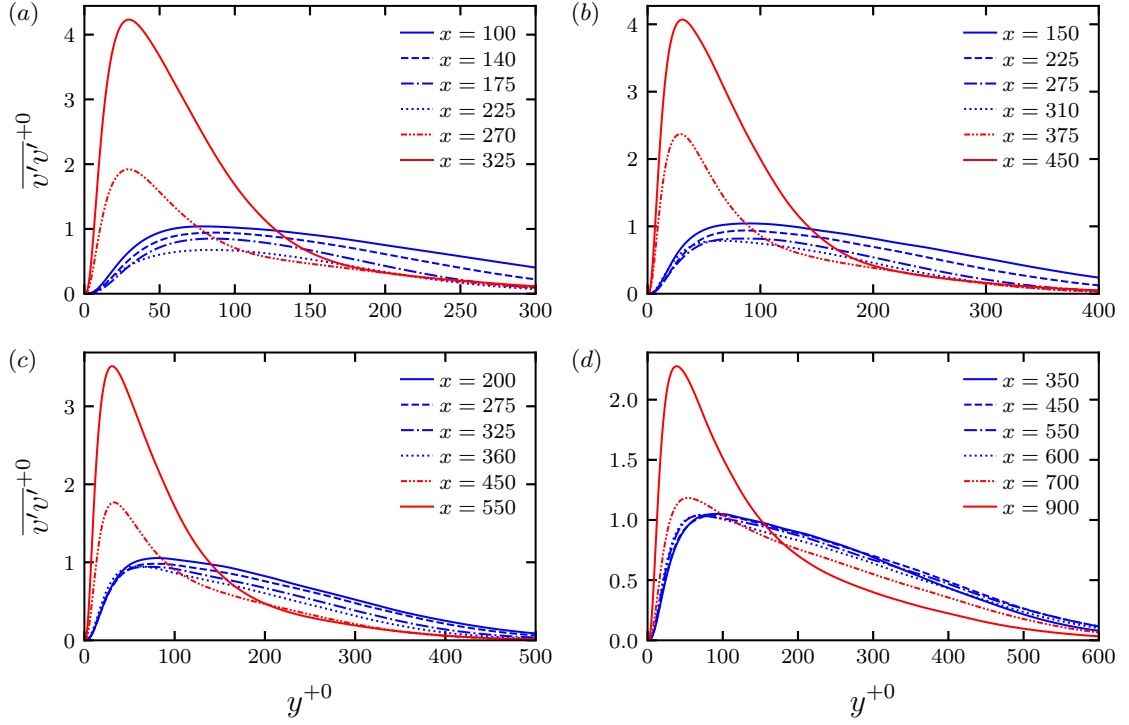


Figure 6.11: Development of $\overline{v'v'^{+0}}$ vs y^{+0} in cases 1 to 4. Blue lines indicate locations before the onset of transition, and red lines indicate those after.

sponse of $\overline{v'v'^{+0}}$ is also different in the laminarising and laminarescent cases. In cases 1 and 2, $\overline{v'v'^{+0}}$ reduces across the entire boundary layer throughout pre-transition, with the peak reducing by around 40% and 30% in cases 1 and 2, respectively. The reduction of $\overline{v'v'^{+0}}$ indicates a trend towards absolute flow laminarisation and the appearance of a more quiescent inner layer. On the other hand, $\overline{v'v'^{+0}}$ does not change substantially in the near-wall region in cases 3 and 4 during pre-transition, approximately retaining their values from further upstream, consistent with the limited changes in v' in figure 6.8(c) upstream of the formation of turbulent spots. Comparing cases 2 and 3 highlights that the behaviour of the inner layer changes drastically over comparatively modest changes in K_{max} with the reduction of $\overline{v'v'^{+0}}$ beginning early in the acceleration for case 2, whereas the near-wall region remains unchanged until transition in case 3. The mechanisms that lead to the reduction of $\overline{v'v'^{+0}}$ are explored in section 6.6.

Away from the wall ($y^{+0} \gtrsim 50$), $\overline{u'u'^{+0}}$ and $\overline{v'v'^{+0}}$ are found to decay during pre-transition for all cases as the boundary layer contracts with larger reductions observed in the stronger accelerations. The reduction of all Reynolds stresses in the outer layer

is similar to previous studies where the decay of turbulence has been observed even at low values of K [118, 105].

After the onset of transition, the wall-normal extent of the increasing $\overline{u'u'}^{+0}$ grows substantially in all accelerations, although this occurs more rapidly in the stronger accelerations. This can be linked to the formation of turbulent spots, which results in a rapid transport of turbulence away from the wall as fluid is ejected from the near-wall region. In cases 1 and 2, the peak of $\overline{u'u'}^{+0}$ is observed to decrease shortly after the onset of transition, which can similarly be observed in studies of bypass transition [139, 131]. This reduction is likely linked to the formation of turbulent spots with energy being drawn from u' and redistributed to the transverse components (shown later through the increase in pressure strain at this stage). In cases 3 and 4, however, $\overline{u'u'}^{+0}$ continues to increase after the onset of transition. This is likely because the flow undergoes transition during the acceleration, leading to sustained increases in energy extraction from the mean flow even after transition, similar to moving wall (figure 5.5) and ramp-up temporal accelerations [44].

With the onset of transition, $\overline{v'v'}^{+0}$ increases initially close to the wall in all cases due to the formation of turbulent spots on the breakdown of strengthened near-wall streaks. The near-wall peak grows progressively as these spots merge. The extent of the increased $\overline{v'v'}^{+0}$ grows as the new turbulence travels downstream, similar to $\overline{u'u'}^{+0}$. The newly generated turbulence structures reside closer to the wall, as indicated by the new $\overline{v'v'}^{+0}$ peak being located closer to the wall than its pre-transitional peak. It is interesting to note that $\overline{v'v'}^{+0}$ can continue to reduce in the region away from the wall even after the onset of transition (figure 6.11(d)), with its eventual recovery not occurring until newly generated turbulence has propagated from the wall. Overall, the characteristics of the turbulence response after the onset of transition appear essentially the same in all cases.

The streamwise development of the peak of the normal Reynolds stresses is presented in figure 6.12, which highlights the differences in the response of the normal Reynolds stresses and the similarity in the response between all cases with the downstream growth of the near-wall $\overline{u'u'}^{+0}$ due to streak strengthening and the delayed response of the $\overline{v'v'}^{+0}$ and $\overline{w'w'}^{+0}$ more clearly visible. Figures 6.12(a) and 6.12(b) also show that the absolute reduction of $\overline{v'v'}^{+0}$ and $\overline{w'w'}^{+0}$ in cases 1 and 2 begins early in the acceleration and occurs upstream of common onset markers for laminarisation such as $\min(H)$ (indicated in figures 6.12(a) and 6.12(b)), or $\max(C_f)$ (not presented). Alongside $K_{crit} = 3 \times 10^{-6}$.

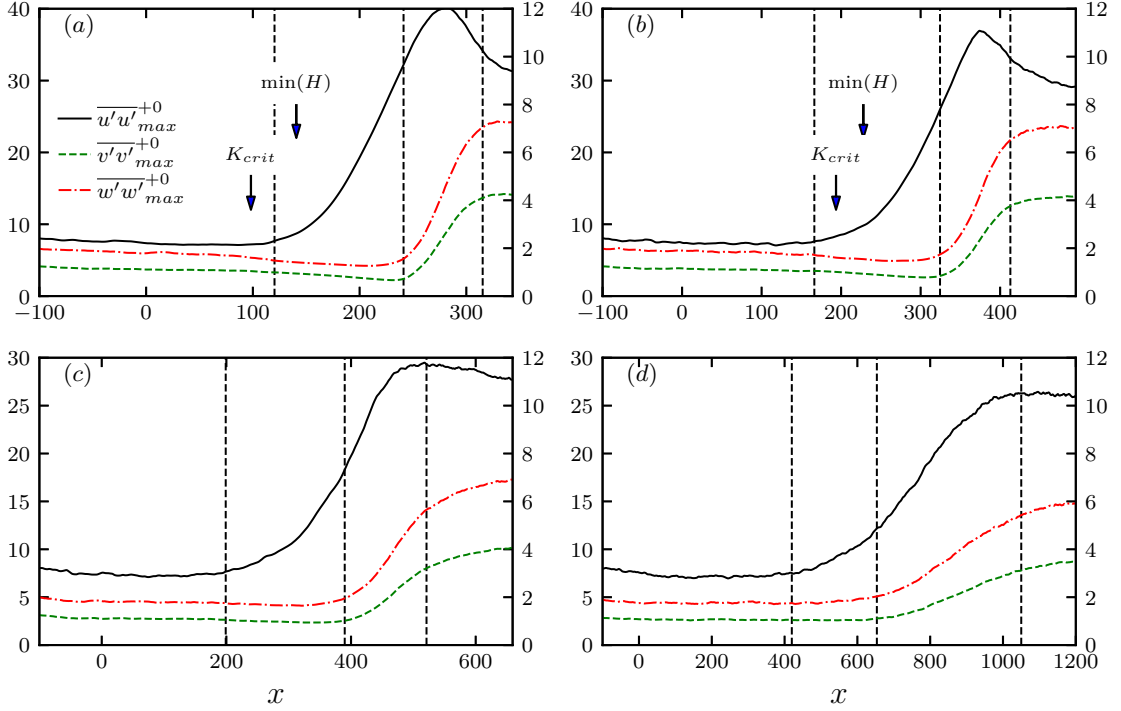


Figure 6.12: Development of peak normal Reynolds stress with x in cases 1 to 4 with the boundaries of each region from table 6.3 indicated with vertical lines. (a) case 1, (b) case 2, (c) case 3, (d) case 4.

The distinct behaviours of the normal Reynolds stresses can be used to delimit the different stages of acceleration. The onset of the pre-transition and transition are defined here using the response u' and v' , respectively, which are summarised in table 6.3. The boundaries are also shown in the table and marked in figure 6.12. The definition for the beginning of the pre-transition region is based on the fact that in this region, $\overline{u'u'}^{+0}$ tends to reduce slowly downstream in ZPGTBLs, but the acceleration reverses this trend. Consequently, the increase of $\overline{u'u'}^{+0}$ is a marker for the

Table 6.3: Limits of regions, where $\alpha = 0.07$, which ensures that $\overline{u'u'}$ and $\overline{v'v'}$ are on unambiguously increasing trajectories. The limits using the definitions from the moving wall acceleration are shown in brackets for cases 1 to 3.

	Case 1	Case 2	Case 3	Case 4	Description
Pre-transition	120	166	198	419	$\overline{u'u'} > (1 + \alpha) \min \overline{u'u'}$
Transition	241 (242)	324 (337)	389 (428)	653	$\overline{v'v'} > (1 + \alpha) \min \overline{v'v'}$
Fully turbulent	315 (326)	412 (423)	521 (505)	1050	$\max(\tau_w)$

start of pre-transition. The rapid increase of $\overline{v'v'}^{+0}$ due to the formation of turbulent spots marks the location for the onset of transition. The onset of the fully turbulent region is not clearly marked by the maxima of the normal Reynolds stresses but can be represented by the final maximum of the wall shear stress, which would tend to reduce once turbulence begins to diffuse away from the wall. This can be viewed as similar to the use of the first peak of C_f after transition onset to delimit this region in moving wall and temporal accelerations [12], although the present definition also works in case 4. The delimiters of the regions based on the definitions from the moving wall acceleration are given in brackets in table 6.3 for cases 1 to 3, indicating that where both definitions are valid, they are comparable. The resulting vertical lines in figure 6.12 further indicate how the transition process becomes less discernible as the acceleration rate reduces, with case 4 showing only limited growth of $\overline{u'u'}^{+0}$ before the onset of transition, suggesting that in sufficiently weak accelerations, the process will become undiscernible similar to temporal acceleration [45].

6.4.2 Reynolds shear stress and eddy viscosity

In the near-wall region, the Reynolds shear stress (figure 6.13), $-\overline{u'v'}^{+0}$, exhibits generally small increases close to the wall. The comparatively limited increases of $-\overline{u'v'}^{+0}$ close to the wall compared with $\overline{u'u'}^{+0}$ highlights a near-wall reduction in the Reynolds shear stress correlation coefficient (not presented), which has been reported in previous studies [10, 87] and reflects that the increase of u' during pre-transition is primarily due to the strengthening streaks and therefore not strongly correlated with v' . It is interesting to note that in the early part of the acceleration, $-\overline{u'v'}^{+0}$ increases more near the wall in the weaker accelerations, highlighting the competing mechanisms for the changes in $-\overline{u'v'}^{+0}$: the amplification of the streaks (increasing u') and the suppression of turbulence (decreasing v'). $-\overline{u'v'}^{+0}$ reduces slowly in the outer layer during pre-transition, following the behaviour of $\overline{u'u'}^{+0}$ and $\overline{v'v'}^{+0}$, noting that the absolute changes are not sudden, as expected from a ‘soft’ laminarisation.

With the onset of transition, $-\overline{u'v'}^{+0}$ mirrors the response of the normal stresses, with initial increases occurring close to the wall with the extent of the increase growing with downstream distance. The growth of $-\overline{u'v'}^{+0}$ corresponds to a significant increase in turbulent transport, substantially altering the mean flow dynamics. The influence of these changes can be observed in the mean velocity profile with the shape of \bar{u} drastically changing (figures 6.5(a) and 6.6(a)) and rapid increases in the wall-normal extent of the high-shear region as new turbulence is produced (figures 6.5(d)

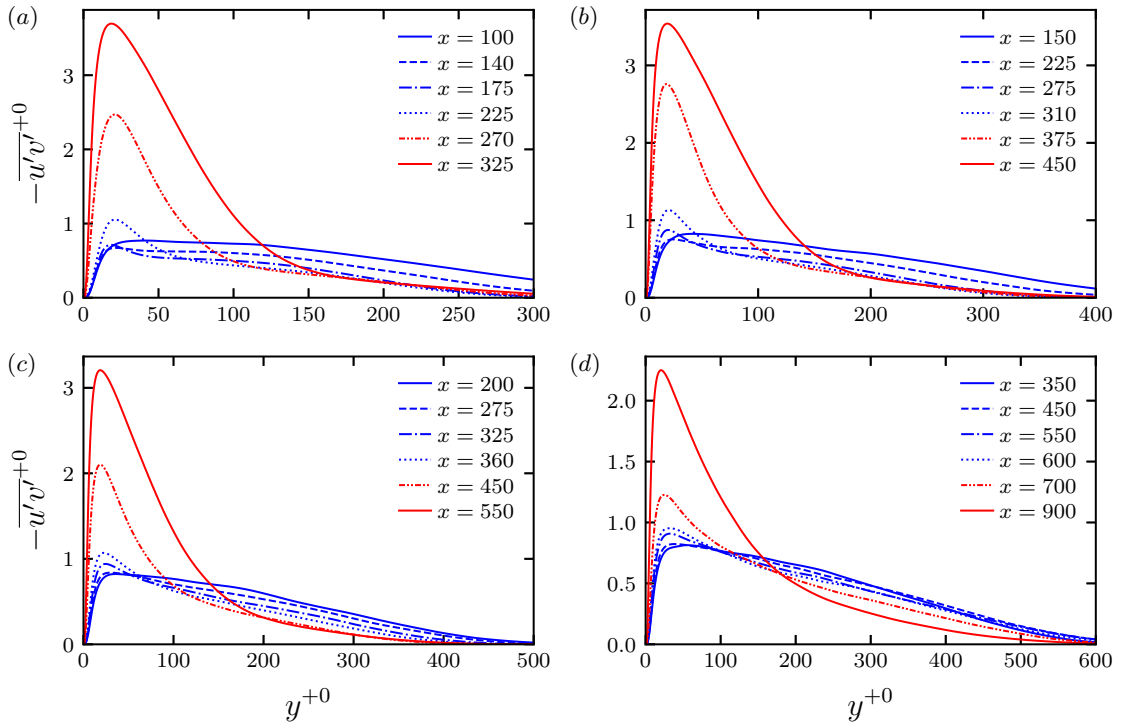


Figure 6.13: Development of $\overline{u'v'}^{+0}$ vs y^{+0} in cases 1 to 4. Blue lines indicate locations before the onset of transition, and red lines indicate those after. (a) case 1, (b) case 2, (c) case 3, (d) case 4.

and 6.6(d)). These sudden changes in the mean velocity profile are approximately coincident with the maximum uplift of the logarithmic region (figures 6.5(b) and 6.6(b)), which subsequently begins to return to equilibrium. This can also be observed in moving wall (figure 5.2) and temporal accelerations [44].

Figure 6.14 shows the eddy viscosity, ν_t . Close to the wall, ν_t almost exactly collapses onto its value from upstream during pre-transition in cases 3 and 4 (figure 6.14(c)). Alongside the nearly constant near-wall transverse stresses, this indicates that the turbulence in the inner layer does not substantially change beyond the amplification of the near-wall streaks. ν_t reduces close to the wall in cases 1 and 2, although not catastrophically, with the former reducing by around 30%. With the onset of transition, ν_t increases in the near-wall region due to the generation of new turbulence structures and the enhancement of near-wall turbulence mixing. Simultaneously, ν_t can be observed to substantially reduce further from the wall in cases 1 to 3 ($y^{+0} \approx 120$). Figure 6.13 suggests that this reduction is driven most by the change in mean shear as at this location, there has been minimal change in $-\overline{u'v'}^{+0}$. The

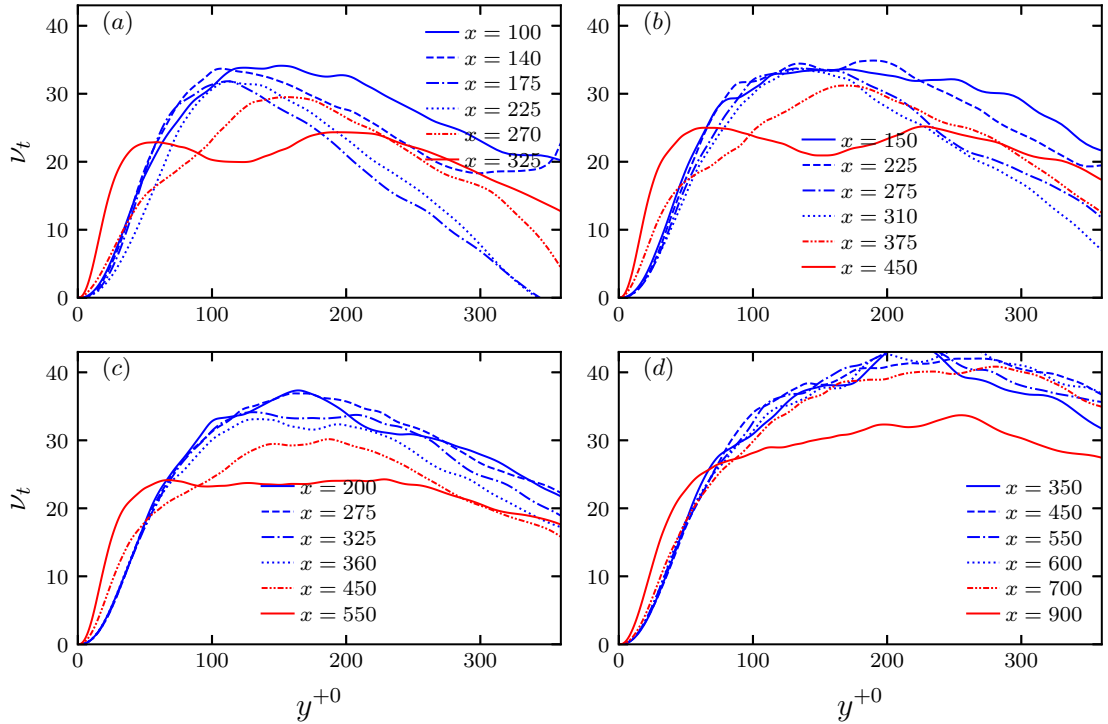


Figure 6.14: Development of ν_t vs y^{+0} in cases 1 to 4. Blue lines indicate locations before the onset of transition, and red lines indicate those after.

results from Fernholz and Warnack [93] also show a similar response of ν_t with distinctive near-wall ‘lobes’ found in both laminarescent and laminarising acceleration close to the onset of transition.

6.4.3 Kurtosis

The kurtosis, $F(v') = \overline{v'^4}/\overline{v'^2}^2$ at $y^{+0} = 15$ is presented in figure 6.15 and gives an indication of the ‘tailedness’ of the probability distribution of v' with higher values suggesting a propensity for a small number of extreme events. In each case, $F(v')$ is observed to reach a maximum around or just upstream of the onset of transition (vertical line in figure 6.15). This is a reflection of the formation of an intermittent region comprising localised turbulent spots and strengthened streaks originating from the pre-transition region, as the spots correspond with far-from-mean events leading to increases in $F(v')$. $F(v')$ subsequently reducing as these spots grow during the transition stage. Instantaneous extreme events for case 1 are shown in figure 6.16. These events are defined here by locations where $|v'| > 3.5v'_{rms}$ (blue) and $|w'| > 3.5w'_{rms}$ (red) and hence would be concentrated where the fluctuations are much larger

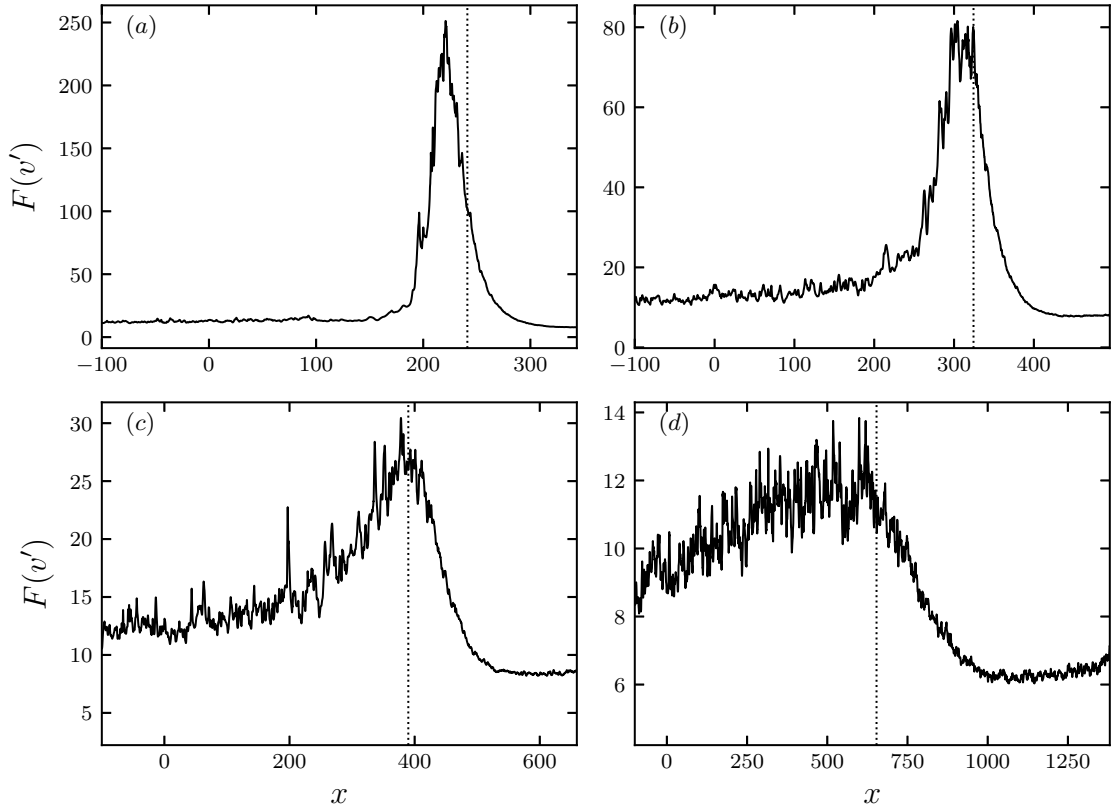


Figure 6.15: Kurtosis , $F = \overline{v'^4}/\overline{v'^2}^2$ at $y^{+0} = 15$ with a vertical line indicating the onset of transition from table 6.3. (a) case 1, (b) case 2, (c) case 3, (d) case 4.

than the local RMS value. These events are observed to be concentrated around the onset of transition as suggested by $F(v')$, being less prominent in the pre-transition and fully turbulent regions.

The peak value of the $F(v')$ is higher in the strong accelerations due to the greater prominence of the spots and the more quiescent background turbulence in the stronger accelerations, which is indicated in figures 6.7 and 6.8. A similar plot to figure 6.16 for case 3 did not show an obvious increase in extreme events around the onset of transition as the extreme events were not sufficiently prominent in that case. Similar peaks in kurtosis can be observed around transition in temporally accelerating flows [15]. Kurtosis has sometimes been reported in previous studies of spatial acceleration. Fernholz and Warnack [93] presents $F(\tau'_w)$ (figure 8), which would be expected to behave similarly to $F(v')$, for laminarescent accelerations and similarly shows peaks during the acceleration that are roughly coincident with the maximum uplift of the logarithmic region (figure 6) highlighting that there is evidence of transition in the

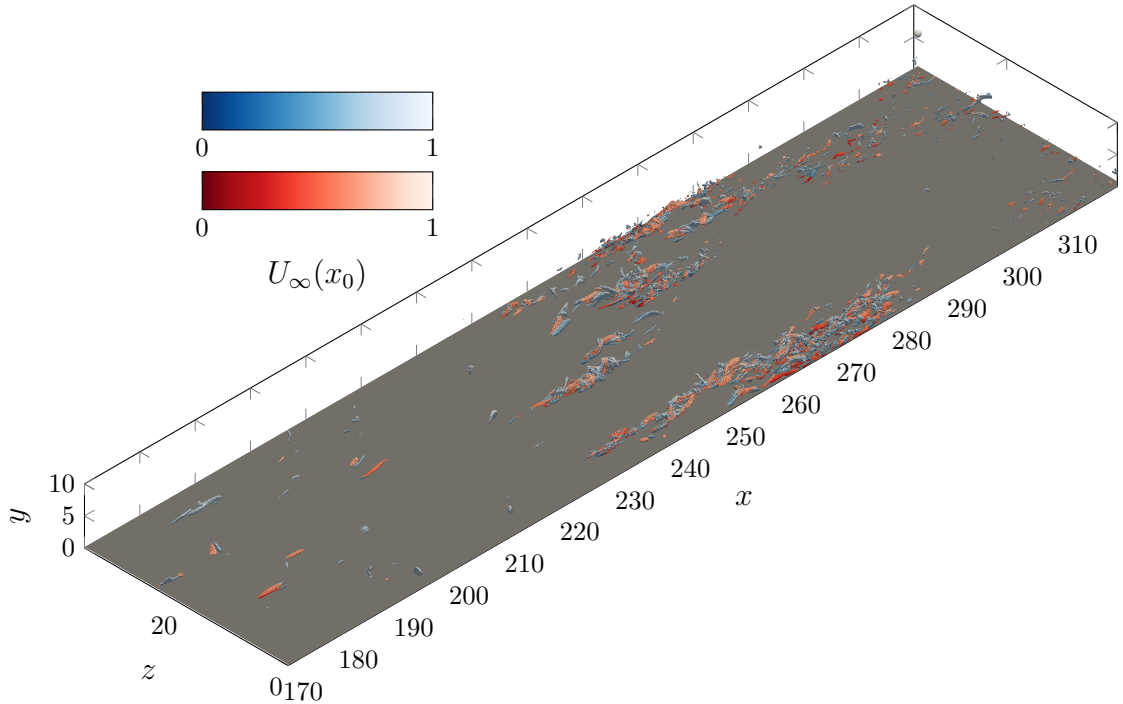


Figure 6.16: Isosurfaces of $|v'| = 3.5v'_{rms}$ (blue colourmap) and $|w'| = 3.5w'_{rms}$ (red colourmap) for case 1. The isosurfaces are shaded by the mean streamwise velocity at $x = 0$.

results of previous studies of laminarising accelerations. Warnack and Fernholz [102] similarly shows peaks of $F(\tau'_w)$ in laminarising accelerations with the decreases associated with retransition, similar to the present study.

6.4.4 Reynolds stress budgets

The streamwise Reynolds stress budgets normalised with reference wall units are presented in figure 6.17 for cases 1 (left) and 3 (right) at four streamwise stations. At the first station (figures 6.17(a) and 6.17(b)), located upstream of pre-transition (table 6.3), the budget resembles that of a ZPGTBL. During pre-transition (stations 2 and 3), the near-wall (shear) production, \mathcal{P}_{11} increases in both cases, consistent with increased energy extraction from the mean flow as a result of the strengthening near-wall streaks. A similar near-wall increase of production can also be observed in moving wall accelerations (figure 5.8) and bypass transition [131]. In stark contrast, all terms substantially reduce away from the wall ($y^{+0} \gtrsim 40$), particularly in case 1, aligning with the reduction of $\overline{u'u'}^{+0}$ observed in the outer part of the boundary layer. This can be explained by the reduction in shear production caused partly by the reducing mean shear (figures 6.5(c) and 6.6(c)), and the effect of dilational

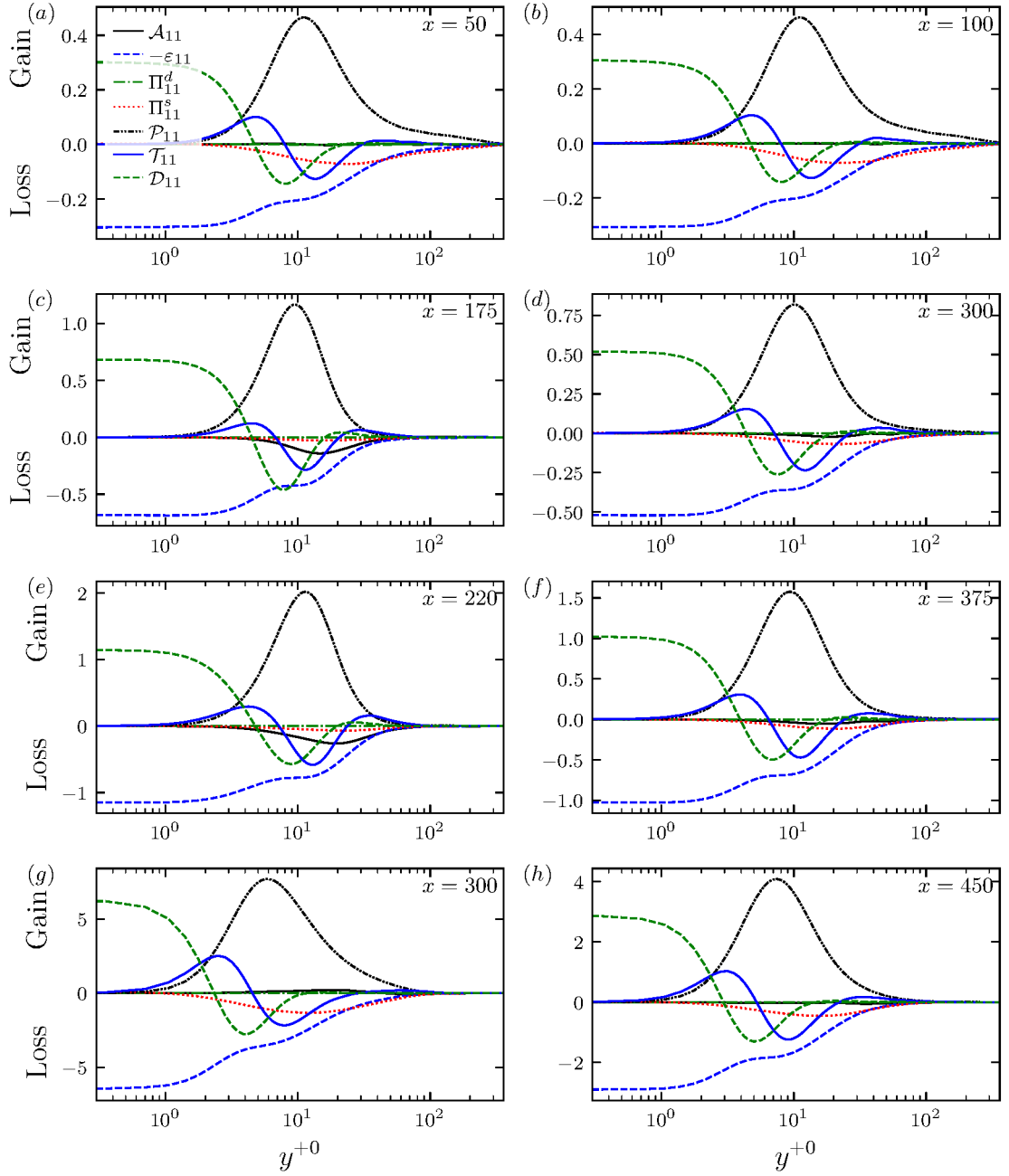


Figure 6.17: Streamwise Reynolds stress budget. Case 1 is presented on the left, and case 3 is presented on the right.

production, $-\overline{u'u'}\partial_x\bar{u}$ in transferring energy back to the mean flow as suggested by Bourassa and Thomas [87].

With the onset of transition (figures 6.17(g) and 6.17(h)), all terms increase significantly in both cases as new turbulence is generated. The increase of production with

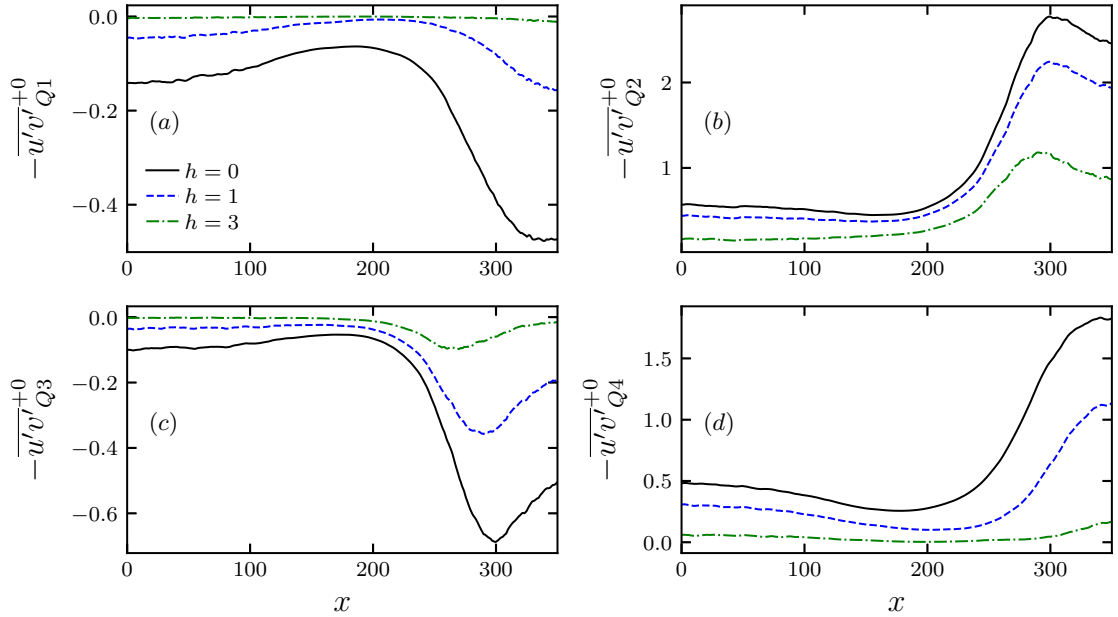


Figure 6.18: Reynolds shear stress contributions for case 1 using the hyperbolic hole method [21] with threshold, $h \in \{0, 1, 3\}$. (a) $-\overline{u'v'}_{Q1}^{+0}$, (b) $-\overline{u'v'}_{Q2}^{+0}$, (c) $-\overline{u'v'}_{Q3}^{+0}$, (d) $-\overline{u'v'}_{Q4}^{+0}$.

the onset of transition is much larger than during pre-transition, similar to bypass transition [131]. Also noticeable is the rapid response of pressure strain, Π_{11}^s , which is subdued during pre-transition, indicating a sudden increase in intercomponent energy transfer with the formation of turbulent spots in both cases. The rapid increase of pressure strain is similar to studies of temporal acceleration and bypass transition [43, 162] and is consistent with the sudden increase of the transverse stresses observed in figure 6.12. Piomelli and Yuan [10] linked the rapid increase of pressure strain with retransition after Π_{ii}^s and the transverse motions are suppressed during laminarisation. Here, the increase of Π_{ii}^s is associated with transition and occurs irrespective of the suppression of the transverse motions during pre-transition as indicated by this increase occurring in both cases 1 and 3 in figure 6.17. The behaviour of the pressure strain during pre-transition is explored in more detail in section 6.6.

6.4.5 Quadrant analysis

The contributions of Reynolds shear stress-producing events are now considered using the hyperbolic hole method (equation (5.2)) [21]. The Reynolds shear stress contributions for case 1 at $y^{+0} = 13$ are shown in figure 6.18 for $h \in \{0, 1, 3\}$. The effect

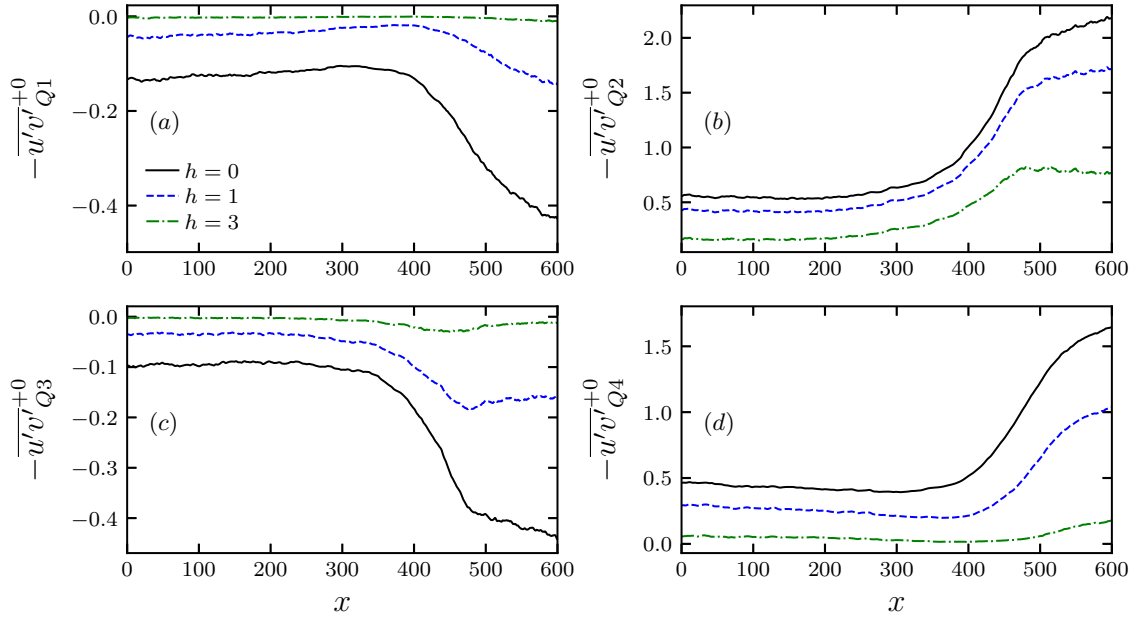


Figure 6.19: Reynolds shear stress contributions for case 3 using the hyperbolic hole method [21] with threshold, $h \in \{0, 1, 3\}$. (a) $-\overline{u'v'}_{Q1}$, (b) $-\overline{u'v'}_{Q2}$, (c) $-\overline{u'v'}_{Q3}$, (d) $-\overline{u'v'}_{Q4}$.

of the absolute turbulence reduction during pre-transition can be observed from near the beginning of the acceleration. $-\overline{u'v'}_{Q2}$ and $-\overline{u'v'}_{Q3}$ exhibit limited reductions for $h = 0$ while for $h = 1$ and $h = 3$, $-\overline{u'v'}_Q$ increases, albeit very mildly. $-\overline{u'v'}_{Q1}$ and $-\overline{u'v'}_{Q4}$ reduce strongly in the early stages of the acceleration at both $h = 0$ and $h = 1$. This is consistent with previous studies showing that Q4 (sweep) events tend to reduce more significantly than Q2 (ejection) events [87, 10]. However, by $x = 200$, the magnitude of all quadrants ($h = 0$) has started to increase, potentially due to the amplification of the streaks, where the advecting vortices associated with the lift-up effect can be linked to quadrant events [7]. With the onset of transition, there is a significant increase in all quadrants, particularly in strong Q2 events. The rapid increase of $-\overline{u'v'}_{Q2}$ with the onset of transition can be linked to the breakdown of the near-wall streaks leading to the ejection of slow-moving fluid away from the wall as discussed in chapter 5, with similar observations in bypass transition [161].

The contributions to $\overline{u'v'}$ in case 3 are shown in figure 6.19. $-\overline{u'v'}_{Q1}$ and $-\overline{u'v'}_{Q4}$ remain nearly constant in the near-wall region for all h during pre-transition, while $-\overline{u'v'}_{Q2}$ and $-\overline{u'v'}_{Q3}$ are observed to mildly increase in later stages of pre-transition ($x \gtrsim 300$). This is particularly noticeable for $-\overline{u'v'}_{Q2}$, where a similar increase is

observed at all h , indicating that extreme events drive it. These increases reflect the mild increase in $-\overline{u'v'}^{+0}$ during pre-transition (figure 6.13) and the lack of absolute attenuation of the transverse motions in the weaker accelerations. There is still an interesting parallel with the Q2 and Q3 events tending to decrease less (or increase more) than the Q1 and Q4 events. With the onset of transition ($x \gtrsim 375$), case 3 behaves similarly to case 1 with further increases in $-\overline{u'v'}_{Q2}$ at all thresholds indicative of streak breakdown. The other quadrants also increase, albeit at lower h . This behaviour again highlights that both accelerations behave similarly after the onset of transition.

6.5 Energy spectra

Figure 6.20 shows contour plots of the pre-multiplied streamwise energy spectrum, $k_z \Phi_{11}^{+0}(x, y, k_z)$ for cases 1 (left) and 3 (right). Upstream of the acceleration (figures 6.20(a) and 6.20(b)), both cases exhibit a streamwise spectrum similar to a low Reynolds number ZPGTBL with a prominent near-wall peak corresponding to the buffer layer streaks with a short spectral tail associated with streaks in the logarithmic and defect layers [227, 238]. During pre-transition (figures 6.20(c) to 6.20(f)), the buffer layer peak strengthens substantially due to the enhanced lift-up effect - similar growth at larger scales has been observed in previous studies [90, 93]. There is a tendency for the buffer layer peak to move to slightly shorter spanwise wavelengths, indicating that the streaks' spanwise spacing reduces in absolute terms as they are amplified, which is also observed in Talamelli et al. [239]. This has also been observed in temporal and moving wall accelerations during pre-transition [43]. In the logarithmic region, Φ_{11} weakens as expected by the reduction of the $\overline{u'u'}^{+0}$ away from the wall during pretransition (figure 6.10).

Figures 6.20(g) to 6.20(j) shows development of the Φ_{11} after the onset of transition. Shortly after the onset of transition (figures 6.20(g) and 6.20(h)), the near-wall peak significantly intensifies and moves to a shorter spanwise scale and closer to the wall. This is consistent with the break-up of the amplified streaks leading to the generation of new turbulence of shorter spatial scale as observed in figures 6.7 and 6.8. The recovery of turbulence in the outer part of the boundary layer can be observed through the re-emergence of the spectral tail, with the larger scale structures originating close to the wall (figures 6.20(g) and 6.20(h)) before spreading away from it (figures 6.20(i) and 6.20(j)). Compared with figures 6.20(a) and 6.20(b), a greater

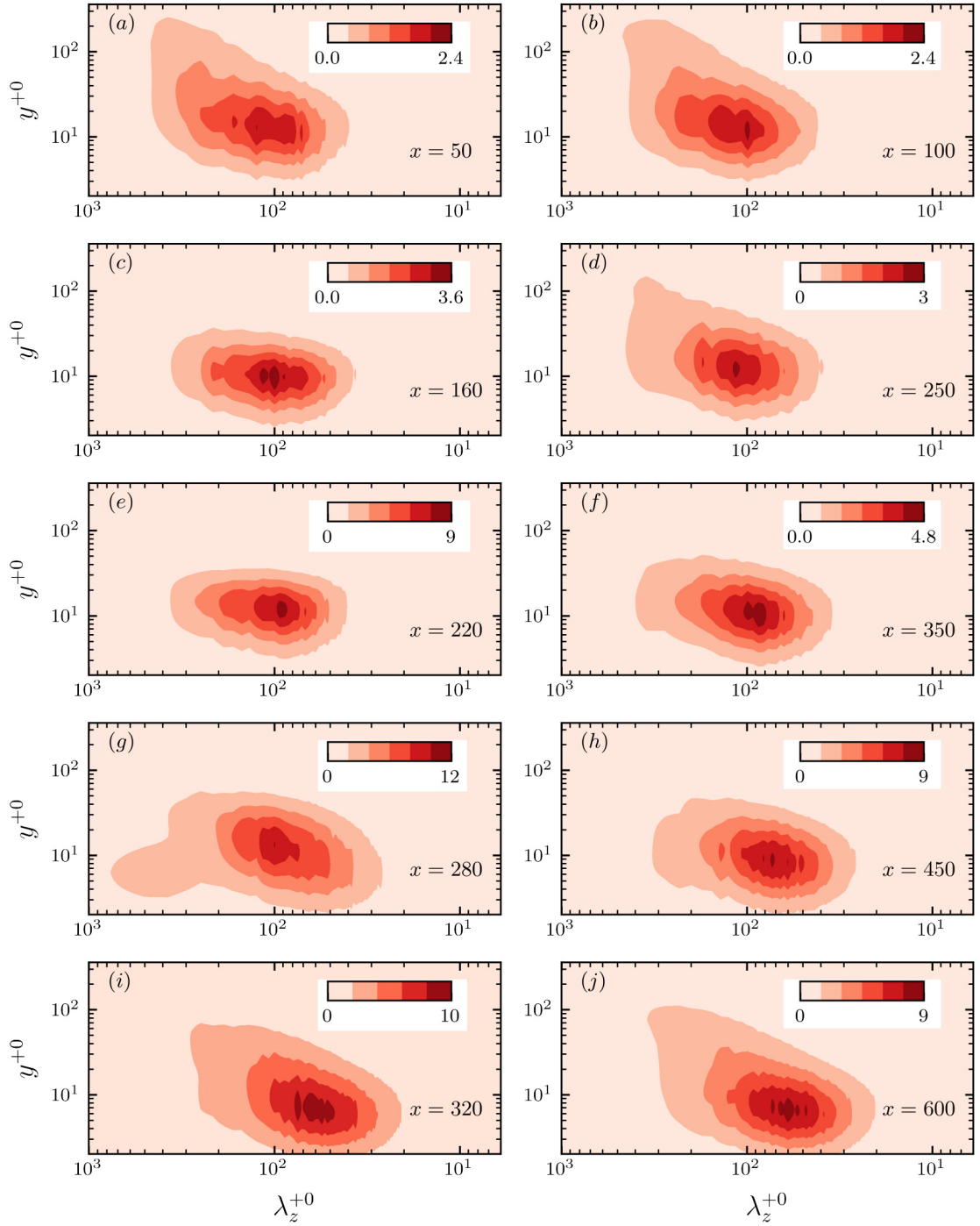


Figure 6.20: Pre-multiplied spanwise spectrum of the streamwise velocity, $k_z \Phi_{11}^{+0}(x, y, k_z)$ against referenced inner-scaled spanwise wavelength, λ_z^{+0} for cases 1 ((a), (c), (e), (g), (i)) and 3 ((b), (d), (f), (h), (j)).

range of scales can be observed with the spectral tail becoming more prominent relative to the near-wall peak due to the rapid development of a higher Reynolds number TBL. However, note that neither acceleration has fully recovered to a ZPGTBL as indicated by the lack of full re-establishment of the wake in figures 6.5(b) and 6.6(b). The results highlight the similarity of the response of u' to the acceleration in cases 1 and 3, initially characterised by streak strengthening followed by streak breakdown and the spreading of turbulence away from the wall after the transition.

6.5.1 Streak generation

Given the centrality of the streak amplification to the turbulence response, the lift-up effect is now investigated in more detail. The wall-normal vorticity, $\omega'_y \approx \partial_z u'$, in the buffer layer, is dominated by the high- and low-speed streaks, which are represented by a spanwise variation of u' . The wall-normal vorticity fluctuation transport equation can represent this,

$$\frac{\partial \omega'_y}{\partial t} = -\frac{\partial \bar{u}}{\partial y} \frac{\partial v'}{\partial z} + \dots, \quad (6.1)$$

omitting terms not related to the lift-up effect, for clarity. This term represents the interaction between the mean shear and the spanwise variation of v' - the essence of the lift-up effect. This term is also an important component of the Orr-Sommerfeld/Squires system and is partly responsible for its non-normality, which is strongly associated with transient growth and streak generation, as discussed in section 2.4.3. Numerical experiments have been performed to eliminate the streaks by damping this term [79, 78].

The changes in the lift-up effect can be examined using the transport equation for the spectral density of the wall-normal enstrophy, $\widehat{\omega}_y^2/2$, with the relevant terms derived in appendix B.3:

$$\frac{1}{2} \frac{\partial \langle \widehat{\omega}_y^2 \rangle}{\partial t} = k_z \underbrace{\text{Im} \left\{ \langle \widehat{\omega}'_y{}^* \widehat{v}' \rangle \right\}}_{\widehat{\mathcal{G}}} \frac{\partial \bar{u}}{\partial y} + \dots, \quad (6.2)$$

where * indicates the complex conjugate and $\widehat{\mathcal{G}}$ indicates the scale-by-scale changes in the lift-up effect, which has been used previously to understand streak generation in turbulent channel flows [66]. The pre-multiplied spectra, $k_z \mathcal{G}^{+0}$ is presented in figure 6.21 for cases 1 (figures 6.21(a) and 6.21(b)) and 3 (figures 6.21(c) and 6.21(d)) in the buffer layer, with locations during pre-transition on the left and those after the onset of transition on the right. During pre-transition, significant increases of

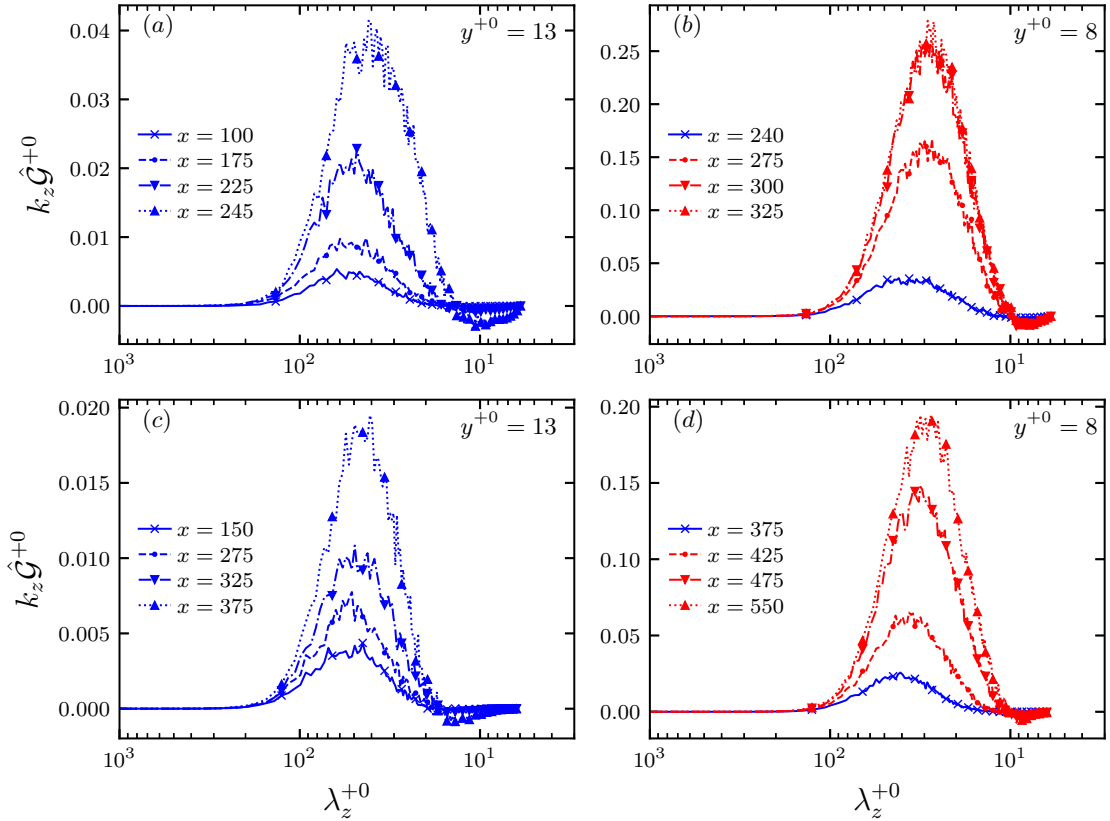


Figure 6.21: Pre-multiplied spanwise ‘lift-up’ spectrum, $k_z \hat{\mathcal{G}}^{+0}$ against referenced inner-scaled spanwise wavelength, λ_z^{+0} for cases 1 ((a) and (b)) and 3 ((c) and (d)). Locations during pre-transition are on the left at $y^{+0} = 13$, and locations after the onset of transition are on the right at $y^{+0} = 8$.

\mathcal{G}^{+0} can be observed in both accelerations, indicative of enhanced lift-up as the near-wall structures are modulated by the new boundary layer. The peak of \mathcal{G}^{+0} can be observed to move to slightly smaller wavelengths consistent with the observed shift of the near-wall spectral peak in figure 6.20. Interestingly, in case 1, there is a region of negative \mathcal{G}^{+0} at $\lambda_z^{+0} \approx 10$ that is not present in case 3. This may be linked with the less perturbed streaks in figure 6.7(b), although a spectral analysis of the full \widehat{w}'_y transport equation would be required to understand the smaller scale processes completely. These results highlight the importance of the lift-up effect to turbulence development in the pre-transition region in cases 1 and 3.

With the onset of transition, large increases in \mathcal{G}^{+0} are observed in both cases with a substantial further shift towards smaller wavelengths, again reflecting the changes in the near-wall Φ_{11} peak and the generation of new turbulence, which would be

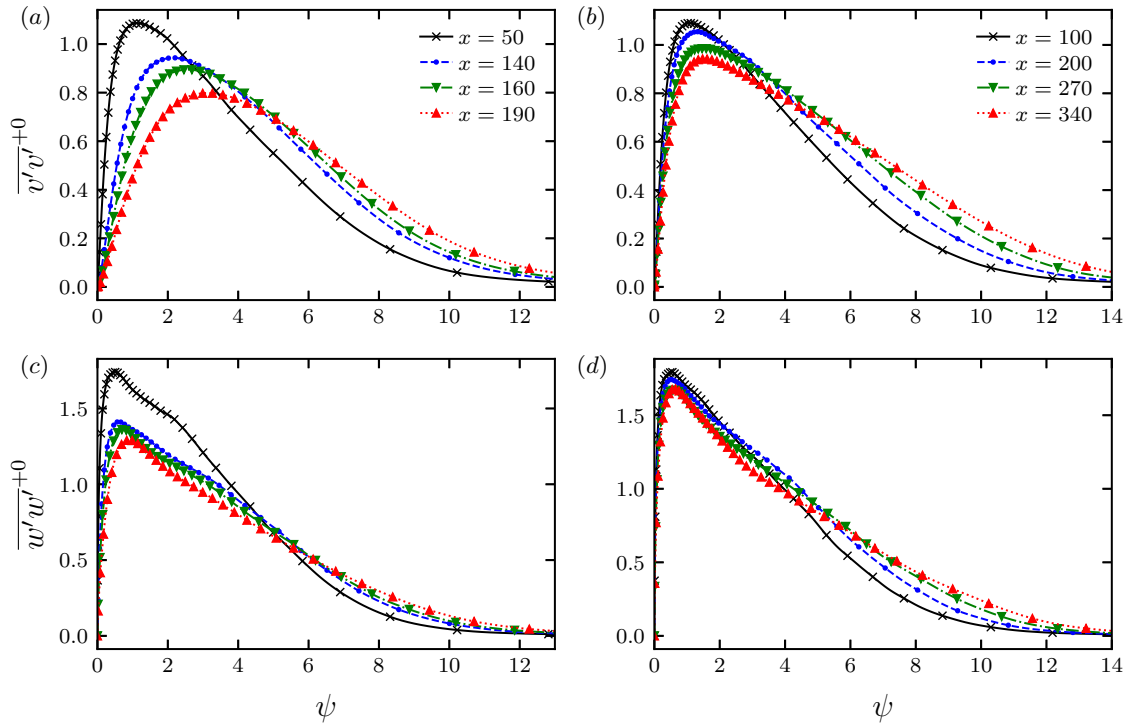


Figure 6.22: $\overline{v'v'}^{+0}$ and $\overline{w'w'}^{+0}$ against streamfunction ψ for cases 1 (left) and 3 (right).

associated with the formation of streaks of a much shorter scale than in the pre-transition flow. The large increase of \mathcal{G}^{+0} is likely caused by the rapid reduction of spanwise scale and hence $\omega'_y \approx \partial_z u'$.

6.6 Transverse stresses

The reduction of the transverse Reynolds stresses in the inner layer is an important feature of cases that tend to laminarise, and it is plausible that such an attenuation could delay the onset of transition, which may explain why retransition is usually observed after the relaxation of the acceleration in laminarising accelerations [9, 103]. Section 6.4 showed that the behaviour of the transverse components in the inner layer changes significantly between cases 2 and 3, with $\overline{v'v'}^{+0}$ and $\overline{w'w'}^{+0}$ essentially remaining unchanged in cases 3 and 4 with substantial attenuation in cases 1 and 2. This section primarily focuses on the behaviour of transverse stresses in the inner layer and the mechanisms that lead to it, with some limited discussion of the outer layer turbulence where its behaviour was deemed relevant to the near-wall turbulence.

Figure 6.22 shows $\overline{v'v'^{+0}}$ and $\overline{w'w'^{+0}}$ for cases 1 (left) and 3 (right) at locations during pre-transition against the streamfunction, ψ defined as

$$\psi(y) = \int_0^y \bar{u}(x, y') dy', \quad (6.3)$$

with lines of constant ψ indicating the mean streamlines. $\overline{v'v'^{+0}}$ and $\overline{w'w'^{+0}}$ do not significantly change in case 3, with some limited near-wall reduction in $\overline{v'v'^{+0}}$ observed close to the wall. $\overline{v'v'^{+0}}$ and $\overline{w'w'^{+0}}$ increase mildly in the outer boundary layer, which has been noted in previous studies [97, 9]. In case 1, $\overline{w'w'^{+0}}$ and particularly $\overline{v'v'^{+0}}$ reduce substantially. However, it is also clear that $\overline{v'v'^{+0}}$ and $\overline{w'w'^{+0}}$ behave differently, with the peak of $\overline{w'w'^{+0}}$ reducing along its mean streamline and settling closer to the wall as the flow contracts. On the other hand, the peak of $\overline{v'v'^{+0}}$ moves across its mean streamline and settles somewhat further from the wall (figure 6.11(a)) as it reduces. This suggests that there are processes in strong accelerations that particularly affect $\overline{v'v'^{+0}}$. The differences between $\overline{v'v'^{+0}}$ and $\overline{w'w'^{+0}}$ can be observed in previous results, but this has not been previously reported [9, 10].

6.6.1 Pressure strain

Figure 6.23 shows the pressure strain in the normal components, Π_{ii}^s scaled with reference wall units for cases 1 (left) and 3 (right). For case 3, Π_{ii}^s remains roughly fixed in absolute terms during pre-transition (figures 6.23(d) and 6.23(f)) in the near-wall region compared to its value upstream of the acceleration (figure 6.23(b)), which indicates that the near-wall intercomponent energy transfer processes are largely unaffected by the acceleration during pre-transition. This is consistent with the limited changes observed in $\overline{v'v'^{+0}}$ and $\overline{w'w'^{+0}}$ close to the wall in figure 6.11 and highlights that beyond the amplification of the streaks, the near-wall turbulence is not strongly affected by the acceleration during pre-transition in this case. Further from the wall, Π_{ii}^s reduces in all components, in line with the steady decline of all stresses in the outer layer. In contrast, in case 1, Π_{ii}^s reduces significantly during pre-transition close to the wall, corresponding with the reduction of the transverse stresses near the wall in figure 6.22. However, figures 6.23(c) and 6.23(e) shows that the response of Π_{22}^s differs significantly from the other two. While Π_{11}^s and Π_{33}^s are smaller during pre-transition, they retain their shape. However, Π_{22}^s changes completely, becoming an energy sink across the entire boundary layer by $x = 160$ and indicates a substantive change in the energy transfer processes in the wall-normal component. Figure 6.23 also shows that the dilation production of v' , $\mathcal{P}_{22} = -\overline{v'v'}\partial_y\bar{v}$ becomes the primary

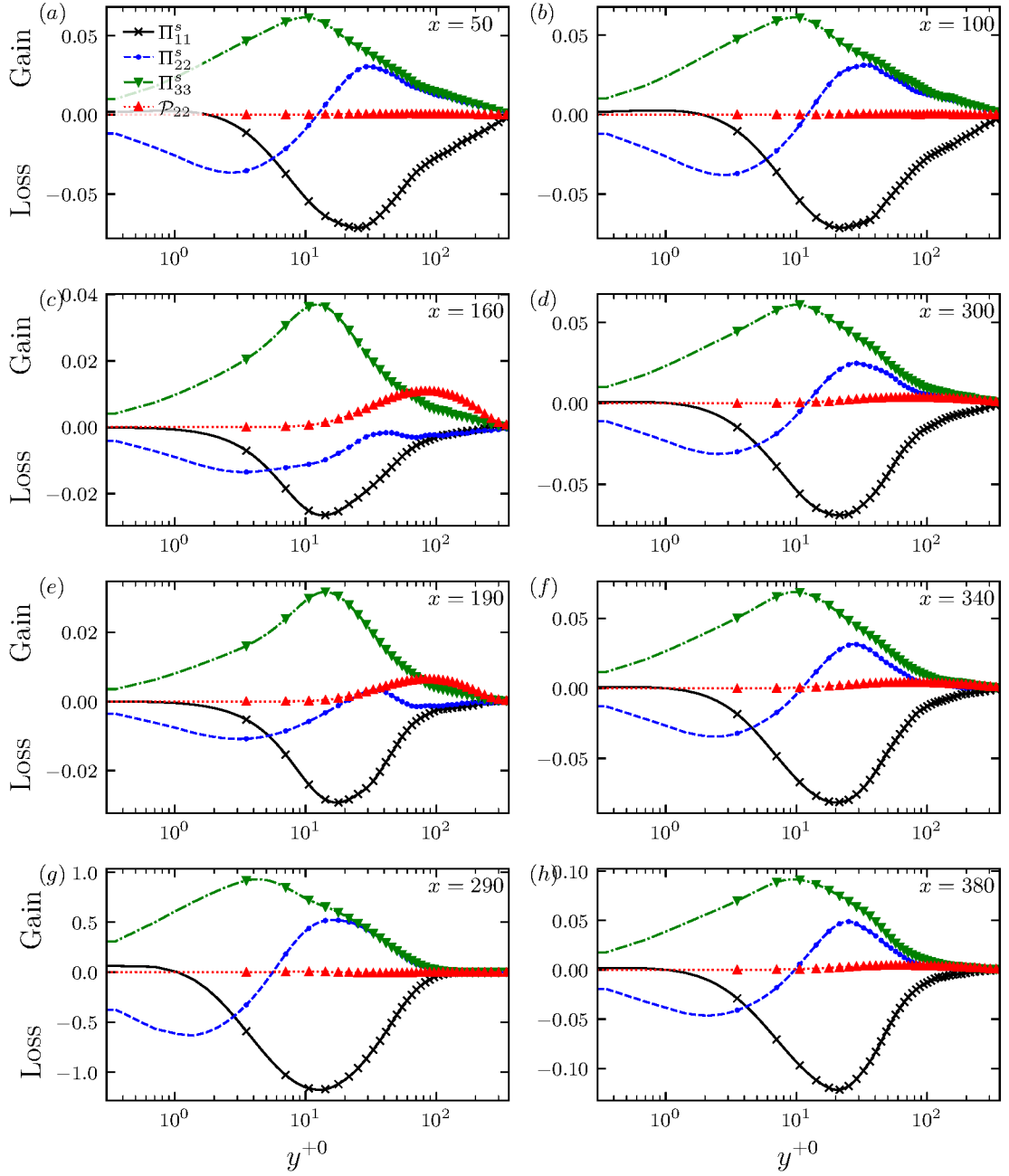


Figure 6.23: Pressure strain components, Π_{ii}^s and wall-normal dilational production, \mathcal{P}_{22} for cases 1 (left) and 3 (right).

source of the wall-normal Reynolds stress budget away from the wall. The negative Π_{22}^s suggests that it acts to redistribute this energy to the other components. The ‘splating’ peak close to the wall, where $\Pi_{22}^s < 0$, is caused by the inviscid blocking of packets of v' by the wall [240, 241], is observed to increase in wall-normal extent,

but its amplitude is smaller. The differences between the response of Π_{22}^s and Π_{33}^s are reminiscent of homogeneous shear flows undergoing streamwise acceleration where Π_{22}^s is observed to become negative, with Π_{33}^s remaining positive [242]. As discussed in section 6.4.4, with the onset of transition, Π_{ii}^s increases significantly in both cases, with this increase starting near the wall, further highlighting the similarity between these cases after the onset of transition.

6.6.2 Spectral analysis of Reynolds stress budget

To better understand the energy transfer processes, particularly for the wall-normal component, the spectrum of the Reynolds stress transport equation can be examined, giving insight into the scales of energy transfer. Such analysis has previously been used in turbulent channel flows [243, 244, 245]. Here, we focus on the pressure strain spectra for the wall-normal and spanwise components and the dilational production terms.

$$\widehat{\Pi}_{22}^s = 2 \operatorname{Re} \left\{ \left\langle \widehat{p}^* \frac{\partial \widehat{v}}{\partial y} \right\rangle \right\} \quad (6.4a)$$

$$\widehat{\Pi}_{33}^s = -2k_z \operatorname{Im} \left\{ \left\langle \widehat{p}^* \widehat{w} \right\rangle \right\} \quad (6.4b)$$

$$\widehat{\mathcal{P}}_{22} = 2 \operatorname{Re} \left\{ \left\langle \widehat{v}'^2 \right\rangle \frac{\partial \bar{u}}{\partial x} \right\} \quad (6.4c)$$

where * indicates the complex conjugate. The derivations of the terms in equation (6.4) are given in appendix B.4. The pressure strain terms, $\widehat{\Pi}_{22}^s$ and $\widehat{\Pi}_{33}^s$ from equations (6.4a) and (6.4b) are presented in figure 6.24 for case 1, noting that during pre-transition there is no appreciable change for case 3 for any component. Figure 6.24(a) shows the distribution for $\widehat{\Pi}_{22}^s$ in a ZPG boundary layer which resembles that in turbulent channel flow [245]. The splatting peak can be observed close to the wall ($y^{+0} \lesssim 10$) where $\widehat{\Pi}_{22}^s < 0$. Splatting is mostly a result of the transfer of energy from v' to w' as these motions are typically linked to the quasi-streamwise vortices [245]. Further from the wall, $\widehat{\Pi}_{22}^s$ contains a large positive region that is associated with the transfer of energy from u' ; $\widehat{\Pi}_{33}^s$ is essentially positive across the boundary layer.

During pre-transition, the amplitude of $\widehat{\Pi}_{22}^s$ and $\widehat{\Pi}_{33}^s$ has substantially reduced at all wavelengths and heights. The main positive peak for both components reduce by approximately 60%, indicating that the processes that transfer energy from u' to v' and w' are weaker but that the substantial differences between Π_{22}^s and Π_{33}^s during pre-transition are not related to it. The shape of $\widehat{\Pi}_{33}^s$ has not changed substantially by $x =$

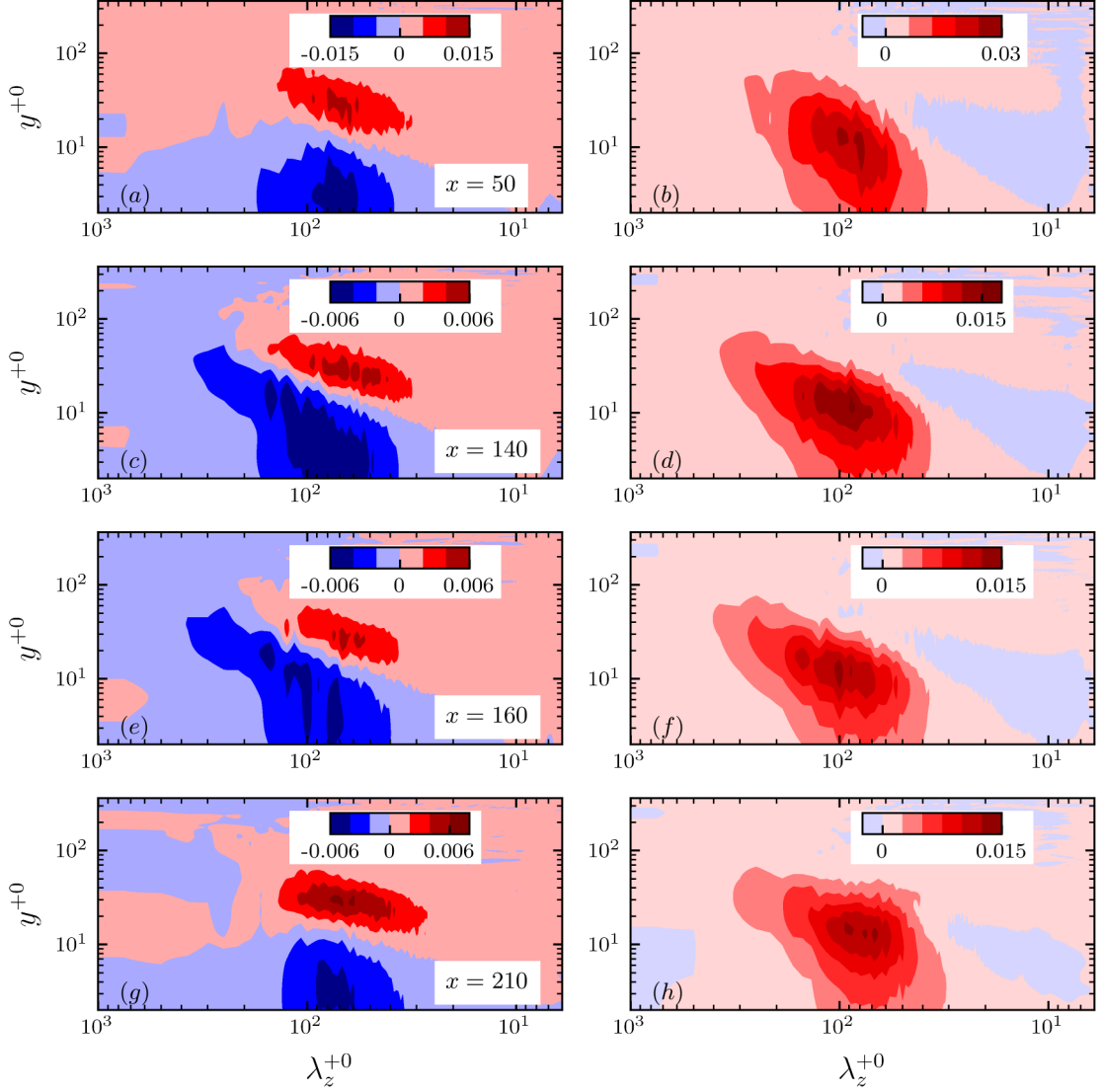


Figure 6.24: Pre-multiplied pressure-strain spectra for case 1. Wall-normal component, $\widehat{\Pi}_{22}^{s+0}$ (left) and spanwise component, $\widehat{\Pi}_{33}^{s+0}$ (right).

160. In contrast, at large wavelengths, $\widehat{\Pi}_{22}^{s+0}$ becomes a sink at all heights, suggesting that there are processes that specifically affect the wall-normal component. Close to the wall, the splatting peak has become more prominent and occupies a region further from the wall. The spanwise scale of the splatting peak suggests that the structures being blocked are wider than the typical near-wall structures present in the buffer layer, where the streamwise vortices typically of order 50 wall units [66]. The enhanced blocking may explain why $\overline{v'v'}^{+0}$ moves away from the wall while $\overline{w'w'}^{+0}$ tends to follow the mean streamlines (figure 6.22). As the acceleration progresses, this negative peak

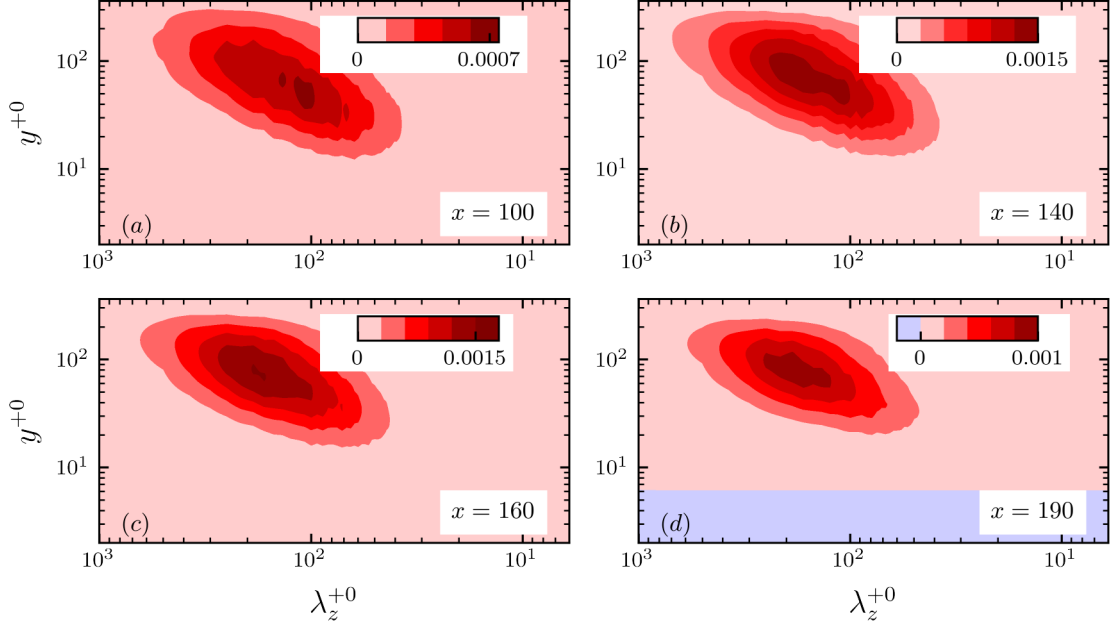


Figure 6.25: Pre-multiplied wall-normal dilational production, $\widehat{\mathcal{P}}_{22}^{+0}$ spectra for case 1.

in $\widehat{\Pi}_{22}^s$ strengthens until $x \approx 160$, which corresponds to the maximum $d_x U_\infty$ and $-V_\infty$ (maximum flow contraction). The weakening of the negative splatting peak is also linked to the small recovery of Π_{22}^s close to the wall in figure 6.23(e). Figure 6.25 shows the spectrum of the wall-normal dilation production (equation (6.4c)), which shows that the negative region of $\widehat{\Pi}_{22}^s$ further from the wall corresponds with where $\widehat{\mathcal{P}}_{22} > 0$ (figure 6.25) confirming that pressure strain acts to redistribute energy directly extracted from the mean flow due to flow contraction. The peak of $\widehat{\mathcal{P}}_{22}$ reaches its maximum at $x \approx 160$, where the negative region of $\widehat{\Pi}_{22}^s$ has its maximum extent, which is consistent with the direct dependence of (equation (6.4c)). It should be noted that the extended splatting peak is not collocated with the increased production because $\widehat{\mathcal{P}}_{22}$ acts further from the wall and is everywhere much weaker than the splatting peak. Instead, the prominent splatting peak at large spanwise scales in figure 6.24 indicates that large-scale wall-ward ($v' < 0$) motions that are redirected by the wall are responsible for the significantly different behaviour of Π_{22}^s close to the wall.

The large-scale incursions from the freestream, identified in Piomelli and Yuan [10], are a potential candidate, particularly as these would be expected to peak around the maximum $-V_\infty$. These wall-ward motions correspond primarily to Q4

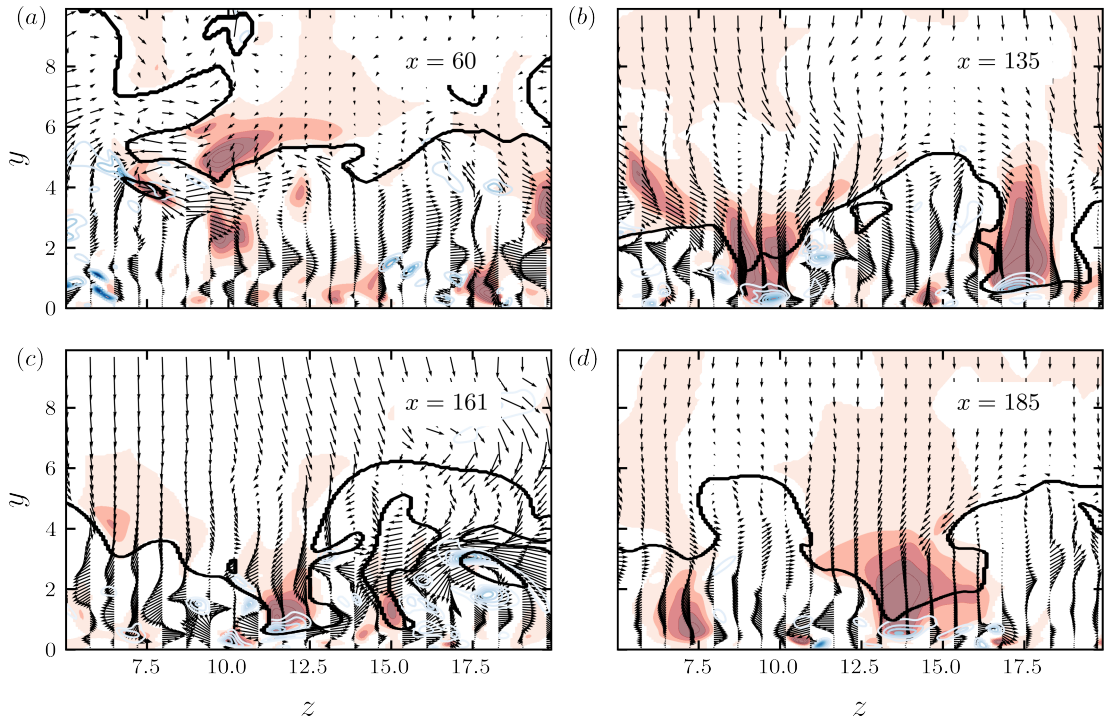


Figure 6.26: $z - y$ plane of instantaneous velocity vectors for case 1 superimposed with contours of $p'\partial_y v' < 0$ (blue lines). Filled contours represent $u'v'$ corresponding Q4 events. The thick black lines indicates where $u = 0.92U_\infty$

events. Figure 6.26 shows the instantaneous velocity vectors in the $z - y$ plane at streamwise locations during pre-transition superimposed with contour plots showing $u'v'$ corresponding with Q4 events. We also show events that contribute to energy being transferred away from v' ($2p'\partial_y v' < 0$) as blue line contours. To highlight the incursions from the freestream, a thick black line is used to indicate where $u = 0.92U_\infty$.

At $x = 60$, the flow is only slightly deviating from ZPG with patches of Q4, and $p'\partial_y v' < 0$ occurring throughout the boundary layer. Individual events are typically small-scale and localised, and there does not appear to be a clear correspondence between these events. At $x = 135$, the boundary layer has become more quiescent with fewer small-scale events. Vertical vectors show the influence of flow contraction with the incursion of unperturbed fluid into the boundary layer from the freestream. Much of the small-scale Q4 events of the ZPGTBL have disappeared, with large regions of Q4 events resulting from incursions from the outer flow. As these motions approach the wall, wide patches of $p'\partial_y v' < 0$ overlap with the bottom edges of these events. This is indicative of splatting with negative v' being slowed as these motions impinge

on the wall resulting in negative $\partial_y v'$ and Q4 events being associated with local adverse pressure gradients [246, 105] resulting in positive p' , and hence negative $2p'\partial_y v'$. At these locations, the black contour line approaches the wall, indicating that these impinging motions originate in the freestream. At subsequent downstream stations, similar events can be observed close to the wall. The presence of these large incursions and the wide regions of $p'\partial_y v' < 0$ conforms with the wide structures implicated in figure 6.24. The incursion of unperturbed flow is also reminiscent of low- K sink flows [105], where distorted outer layer vortices act to transport quiescent flow into the near-wall region, which may also contribute to the more quiescent appearance of the inner layer.

While similar observations can be found in other planes and at other times, time-resolved conditional averaging of these structures (along the lines of Lozano-Durán et al. [247, 248]) is required to confirm that these motions have the correct characteristics. In particular, whether these motions' spanwise scale and wall-normal location correspond with the extended splatting peak in figure 6.24. It is also useful to confirm whether these motions, on average, reach their maximum intensity near $\min(V_\infty)$ as expected from the maximum of the splatting peak.

6.6.3 Rapid pressure

The above mechanisms can help to explain the substantially different behaviour of the wall-normal pressure strain but do not explain the general reduction of all three pressure strain components, which is much larger than the enhanced splatting peak or the dilational production. Furthermore, both of these mechanisms reach their maxima around $x \approx 160$, while $\overline{v'v'}^{+0}$ and $\overline{w'w'}^{+0}$ continue to reduce until the onset of transition at $x \approx 270$. The positive peak of $\hat{\Pi}_{22}^s$ and $\hat{\Pi}_{33}^s$ reduces by approximately the same amount during pre-transition, indicating that there are also mechanisms that act on all three components. One possible mechanism proposed by Piomelli and Yuan [10], is that the reduction of Π_{ii}^s is caused by the reduction of the rapid pressure fluctuations, p'_r . The pressure fluctuations, p' , can be decomposed into rapid and slow, p'_s components:

$$p' = p'_s + p'_r. \quad (6.5)$$

These can be defined through the Poisson equations

$$\nabla^2 p'_s = - \underbrace{\frac{\partial u'_i}{\partial x_j} \frac{\partial u'_j}{\partial x_i}}_{f_s}, \quad (6.6)$$

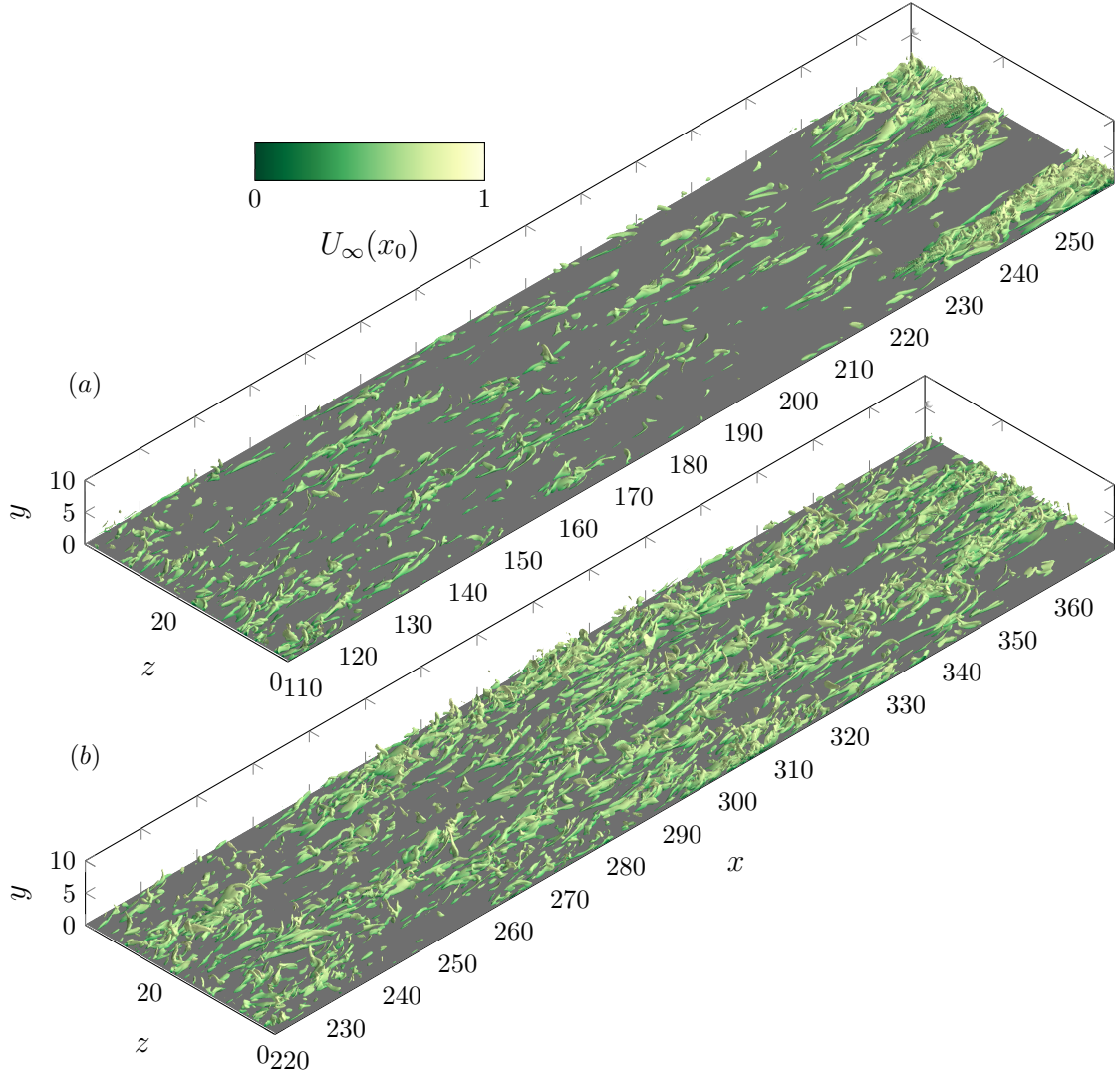


Figure 6.27: Isosurfaces of the source of the rapid pressure, $f_r = 0.03$ for cases 1 and 3 for streamwise locations upstream of the onset of transition. The isosurfaces are coloured by the mean streamwise velocity at $x = 0$.

$$\nabla^2 p'_r = \underbrace{-2 \frac{\partial \bar{u}_i}{\partial x_j} \frac{\partial u'_j}{\partial x_i}}_{f_r} \approx -2 \frac{\partial \bar{u}}{\partial y} \frac{\partial v'}{\partial x}. \quad (6.7)$$

The direct dependence of equation (6.7) on the mean velocity gradients means that it responds rapidly to changes in the mean flow [61, 10]. Piomelli and Yuan [10] showed that the source of equation (6.7), f_r reduces significantly in a strong acceleration whereas f_s does not and so proposed that the reductions in f_r lead to reductions in p'_r and consequently Π_{ii} . Given the sudden near-wall drastic reduction of the pressure strain in the inner layer in case 1 but not case 3, any mechanism responsible for this reduction should appear in the former but not the latter. The importance of the

mechanism proposed by Piomelli and Yuan [10] can be assessed by comparing f_r in cases 1 and 3. The isosurface of $f_r = 0.03$ upstream of the onset of transition is presented in figure 6.27. Note that f_r and f_s are related to the Q criterion for vortex identification as $Q = \nabla^2 p / 2$ [10]. f_r reduces substantially in case 1, as indicated by the appearance of large regions which are sparsely populated with isosurfaces in figure 6.27(a), similarly to Piomelli and Yuan [10]. However, case 3 does not show any significant reductions in f_r , which suggests that the reduction in f_r and consequently p_r is a plausible mechanism to explain the mostly isotropic reductions of pressure strain that occur in strong spatial accelerations.

The likely physical mechanism of this process is indicated by the dominant term in f_r : $-2\partial_y \bar{u} \partial_x v'$, which reveals a direct dependence on the mean velocity gradient. Figure 6.5(c) shows that in strong accelerations, $\partial_y \bar{u}$ reduces substantially down to $y^{+0} \approx 30$ suggesting that the buffer layer processes, which exist up to $y^{+0} \lesssim 80$ [79], would be substantially affected, while in case 3 (figure 6.6(c)), the reduction is limited and only occurs away from the wall $y^{+0} \gtrsim 100$. While this suggests that the reduction in f_r is a plausible mechanism to explain the mostly isotropic reductions of the pressure strain, further work is required. In particular, the relationship between the reduction of f_r and p'_r and whether it can explain the behaviour of Π_{ii}^s , which is complicated by the nonlocality of p'_r .

6.7 Summary and Conclusion

In this chapter, numerical simulations of spatially accelerating TBLs have been reported, covering a wide range of acceleration rates. A new understanding of spatial acceleration is proposed that characterises the flow and turbulence response as a transition process that occurs in response to the development of a new boundary layer. This boundary layer is formed as a consequence of the acceleration, with the resulting flow bearing substantial similarities to bypass transition. This description incorporates observations of laminarising and much weaker laminarescent cases. The range of accelerations studied also allowed an investigation of the differences between stronger and weaker accelerations, with an absolute attenuation of transverse motions close to the wall in the former but not the latter, with several potential mechanisms investigated.

6.7.1 Summary of near-wall transition process

As the flow accelerates, a new boundary layer forms as viscous effects resist the freestream acceleration, leading to a confined region of high mean shear. The enhanced mean shear amplifies the near-wall streaks as they travel downstream through the lift-up effect. In all cases, the increasing amplitude of the near-wall streaks can be observed through the persistent growth of the streamwise Reynolds stress in a limited near-wall region. At this stage, there is a mild decrease in the absolute spanwise scale of these streaks. The enhanced lift-up can be observed through the spectra of the ‘lift-up’ term in the wall-normal vorticity equation, with the changes in its amplitude and spanwise scale aligning with the changes of u' . During this region, the rise of turbulence kinetic energy is entirely due to the streaks as energy is extracted from the mean flow, with no significant accompanying increases in the wall-normal Reynolds stress, which either remains essentially constant or decays. Close to the wall, the Reynolds shear stress generally exhibits no or limited increases in this region, which is linked to the increasing amplitude of the streaks not being strongly correlated with v' . Further from the wall, all turbulent stresses decay. This region is denoted as pre-transition.

The onset of transition is caused by the breakdown of these strengthened streaks with the appearance of localised, high-intensity spots in all three components. In strong accelerations, the breakdown mechanism appears to resemble a streak instability process with disturbances originating at the interface of the streaks. In the weaker accelerations, the mechanism is more difficult to discern, but the statistical and visual characteristics of the breakdown are essentially identical across all cases. This includes large increases in the transverse stresses initially close to the wall before spreading away from it, which is due to a sudden rise in the pressure strain indicative of an increase in intercomponent energy transfer. A sudden change in the energy spectrum is also observed, with the near-wall peak moving closer to the wall and to a shorter spanwise scale. There is also a large increase in all quadrant events, particularly ejection events, indicative of a significant rise in wall-normal momentum transport. The onset of transition is also linked to a significant increase in the eddy viscosity near the wall, which had been subdued during pre-transition. The formation of spots is also related to a peak of the kurtosis of v' in all cases. Once the newly generated turbulence covers the spanwise extent of the wall, the flow enters the ‘fully turbulent’ region, which is characterised by the diffusion of turbulence away from the wall, noting that the spread of the new turbulence dictates the recovery of the outer layer in all cases.

The transition process described above characterises the overarching turbulence response in all cases investigated, with important features such as the formation of turbulent spots not previously reported in laminarescent accelerations to the author’s knowledge. Distinctive onset markers for transition reported in this study can also be observed in previous studies, including a peak in kurtosis and near-wall lobes in the eddy viscosity [102].

6.7.2 Comparison of spatial accelerations with different K

We now discuss the important differences between the laminarising (cases 1 and 2) and laminarescent (cases 3 and 4) accelerations. While all accelerations exhibit a flattening of the mean velocity profile away from the wall linked to boundary layer contraction, this effect is much stronger in the laminarising accelerations, with flattening observed down to the buffer layer.

The absolute attenuation of transverse motions in the inner layer in strong accelerations has been investigated, revealing strikingly different behaviours between v' and w' . While the pressure strain in all three components reduces, this reduction is more substantial for v' . We have identified several potential mechanisms that specifically affect v' associated with a sink at large scales in the pressure strain spectrum of v' . In the first mechanism, large-scale motions originating in the freestream impinge on the wall and are inviscidly blocked, leading to a transfer of energy from v' to w' and u' . Second, energy is directly extracted from the mean flow by v' , which is subsequently redistributed. We have also investigated a mechanism proposed by Piomelli and Yuan [10], which can reduce the pressure strain in all three components by reducing the rapid pressure Poisson equation source. The current results suggest this is a plausible mechanism to explain the near-wall reduction of the pressure strain, but further work is required to confirm this.

In contrast to the inner layer, the outer layer behaves similarly in all accelerations, exhibiting a slow decay during pre-transition. This decay is observed to be stronger as the acceleration rate increases. From a statistical perspective, this reduction can be explained by the decrease of production in the outer layer as suggested by Bourassa and Thomas [87]. However, further work examining the systematic behaviour of coherent structures in this region would be beneficial.

There are also some differences in the transition process between the stronger and weaker accelerations. Cases 3 and 4 undergo transition during the acceleration where K remains close to its peak value. In contrast, cases 1 and 2 transition after the relaxation of the acceleration, similar to previous studies of laminarising spatial

acceleration. This may be related to the stabilisation of the streaks due to the attenuation of transverse motions in the inner layer in those cases, leading to delayed transition.

6.7.3 Laminarisation: where are we?

In this new understanding of spatial acceleration, the ‘soft’ laminarisation in spatially accelerating flows results from the delay between the beginning of the acceleration and the onset of transition. While transition occurs even in cases that do not laminarise, in those cases, the pressure gradient is not strong enough to render the turbulent stresses negligible to the mean flow dynamics. The absolute attenuation of the turbulent stresses in the inner layer only occurs in strong accelerations, which further diminishes the role of turbulence in the mean flow dynamics and may delay the onset of transition, resulting in an extended streamwise region where the turbulent stresses are negligible.

It is also useful to consider the conceptual differences between this interpretation and previous studies. Laminarisation in spatially accelerating flows is usually considered in terms of the progressive shift of the boundary layer between its asymptotic states: the initial ZPGTBL and the quasi-laminar boundary layer where the two-layer model of Narasimha and Sreenivasan [9] is valid. In the present study, we consider the flow and turbulence response to be dominated by the incremental change of the mean velocity profile, which is dominated by the development of the new boundary layer. The new boundary layer amplifies the streamwise component in the form of near-wall streaks, whose break-up is ultimately responsible for the onset of transition. This contrasts with the previous studies that have considered u' to be passively advected from upstream and not driving the turbulence response to the acceleration [10, 121].

Retransition is usually regarded as a consequence of flow laminarisation and is indicative of the recovery of the inner layer to the turbulent state. The present study shows that this transition occurs across a range of acceleration rates irrespective of the state of the inner layer. The onset of transition has the same characteristics as previous observations of retransition, being associated with intermittency and originating close to the wall [112, 10, 121]. We have also shown that the onset of transition can help to explain the return to equilibrium of the inner-scaled mean velocity profile across all cases simulated.

It is also important to note that while cases 1 and 2 represent large values of K , these accelerations have not been sustained for a significant streamwise distance. Somewhat longer accelerations such as those of Piomelli and Yuan [10] and case 2 from Warnack and Fernholz [102] appear to behave similarly to those studied herein.

However, extreme accelerations such as Bourassa and Thomas [87] (where $\Lambda_{max} \approx 2800$) may exhibit somewhat different behaviour, with their results implying that in sufficiently strong accelerations, $\overline{v'v'}$ can increase more (or reduce less) than $\overline{u'u'}$. On the other hand, case 4 implies that the transition process may become undiscernible in sufficiently weak accelerations with all three turbulence components responding similarly. Therefore, further investigation of even weaker accelerations should also be considered.

It is also useful to consider what influence the initial Reynolds number has on the transition process and the attenuation of the transverse motions. Narasimha and Sreenivasan [40] suggested that TBLs would likely begin to laminarise at lower values of K as Reynolds number increases with some experimental results tentatively supporting this [249]. However, a study has yet to systematically investigate Reynolds number effects in spatially accelerating flows, with the initial Re_θ in FPGTBLs much smaller than experiments of ZPGTBLs. With the initial Reynolds number nearly constant in this study, we are not able to investigate its influence on transition or the attenuation of the transverse motions.

Chapter 7

A comparison of spatially and temporally accelerating flows

Previous studies of temporal acceleration have highlighted the similarities and differences between these accelerations, both in terms of mean flow parameters and the turbulence response [46, 47, 12, 48]. However, no direct detailed comparisons of the spatially and temporally accelerating flows have been made to date. In the context of the previous chapter, where it was established that the turbulence response to the spatial acceleration has many similarities to its temporal counterpart, we directly compare these accelerations at comparable acceleration rates to understand the differences in mean flow and turbulence response. This study has three primary objectives: First, to develop and assess a temporal analogy for the strong spatial accelerations (cases 1 and 2 from chapter 6) to facilitate a comparison between the accelerations. Second, to compare the mean flow development and important mean flow parameters, such as C_f and H , explaining the key differences. Third, to explore the differences in the turbulence response, particularly the transverse motions where chapter 6 suggested processes occur in spatial acceleration that would not be present in temporal acceleration.

7.1 Comparison approach

7.1.1 Initial flow

A comparison between spatial and temporal acceleration must begin at the conditions of the flows upstream of the acceleration: a ZPGTBL and a stationary turbulent channel flow, respectively. Most comparisons of these flows have maintained approximately the same friction Reynolds number in each case - essentially making an analogy between the boundary layer thickness and the half-channel height [250, 232]. Previous

Table 7.1: Characteristics of channel flow cases at low Reynolds number to be compared with ZPGTBL from chapter 4.

	Re_c	Re_τ	L_x	L_z	N_x	N_y	N_z	Δx^+	Δz^+	Δy_w^+	Δy_c^+
Case C1	6792	344	18	6	648	385	360	9.56	5.74	0.401	8
Case C2	7286	366	18	6	648	385	360	10.2	6.1	0.427	8.52

studies, over a wide range of Reynolds numbers ($580 \leq Re_\tau \leq 3000$) have found that with approximately matched Re_τ , there are similarities close to the wall for the inner-scaled mean velocity and streamwise turbulent statistics with the inner-scaled transverse stresses typically being larger in TBLs compared with channels. In the present study, we are comparing accelerating flows at lower Reynolds numbers than the studies above. As a result, we have simulated two stationary channel flows at low Reynolds number to compare with the ZPGTBL from section 4.7: one at $Re_\tau \approx 340$ (case C1) to compare with matched Re_τ (like previous studies), and a second with matched $Re_c \approx 7280$ (case C2), which is relevant for the comparison approach developed in section 7.1.2. The summary of these cases is given in table 7.1, indicating reasonable grid resolution.

Figure 7.1(a) presents the inner-scaled mean velocities for cases ZPG, C1 and C2. There is good agreement between all cases up to the edge of the logarithmic region ($y^+ \lesssim 100$). Further from the wall, there are deviations between the channels and TBL due to the presence of the wake in the outer layer of the TBL, which can similarly be observed in figure 2.2(a). The lower Reynolds number and reduced scale separation mean that the mean velocity profiles overlap for a greater proportion of the boundary layer ($y/\delta \lesssim 0.3$) compared with the comparisons at higher Re_τ such as Monty et al. [250]. The relatively low Reynolds number of the present simulations leads to a small velocity defect, implying the influence of the higher momentum outer region in the TBL may increase with Reynolds number as the velocity defect becomes more prominent. Figure 7.1(b) shows the RMS streamwise velocity fluctuations. All cases collapse for much of the channel/TBL with reasonable agreement observed even into the outer part of the boundary layer, although deviations can be observed towards the outer edge of the TBL, which is consistent with higher Reynolds number studies [232, 250]. It should also be highlighted that the RMS velocity fluctuations in ZPGTBLs go to zero in the freestream, whereas for channels, the domain is bounded with turbulence developing on the opposing wall, meaning that the velocity fluctuations do not reduce to zero at the centreline. The inner peak of u'_{rms}^+ exhibits a very good collapse, which is significant given the role of the streamwise streaks in

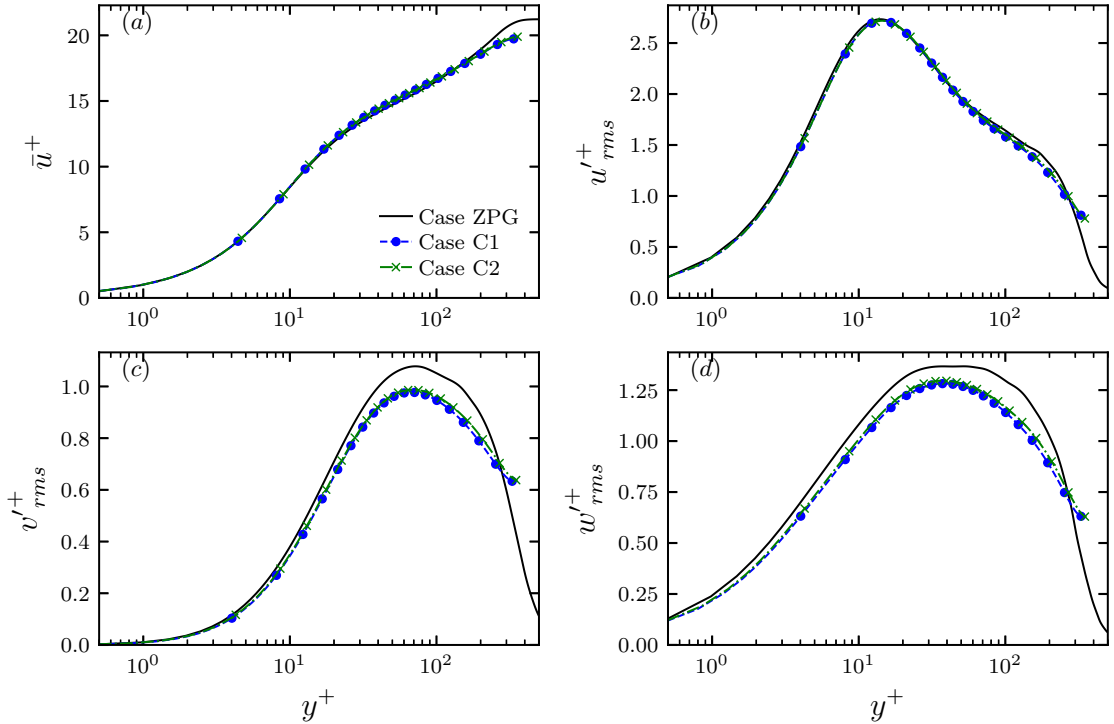


Figure 7.1: Variation of first and second-order statistics for the low Reynolds number channel and TBLs: (a) \bar{u}^+ vs y^+ ; (b) $\overline{u'u'^+}$ vs y^+ ; (c) $\overline{v'v'^+}$ vs y^+ ; (d) $\overline{w'w'^+}$ vs y^+ .

temporal and spatial acceleration, indicating the streaks upstream of the acceleration are similar.

The transverse Reynolds stresses are presented in figures 7.1(c) and 7.1(d). Consistent with previous studies, the transverse motions are stronger in TBLs across the flow. The location of maximum excess for v'^+_{rms} and w'^+_{rms} between the TBL and the channels is at $y/\delta \approx 0.3$ which is generally similar to previous studies at higher Reynolds number, although it is perhaps somewhat further from the wall [232, 251]. The excess appears to be somewhat larger in the present case compared with higher Reynolds number comparisons [232]. Consistent with Jiménez and Hoyas [252], v'^+_{rms} and w'^+_{rms} tend to peak closer to the wall in the channel flows compared with the TBLs.

Figure 7.2 shows the skewness, $S(u')$ and kurtosis, $F(u')$ of the streamwise velocity fluctuations showing that for much of the channel/TBL, there is good agreement in both flows similar to previous studies [250], although there appears to be some deviation in the viscous sublayer (this region is not resolved in Monty et al. [250]). In the outer layer, both flows behave consistently with previous studies of channel and

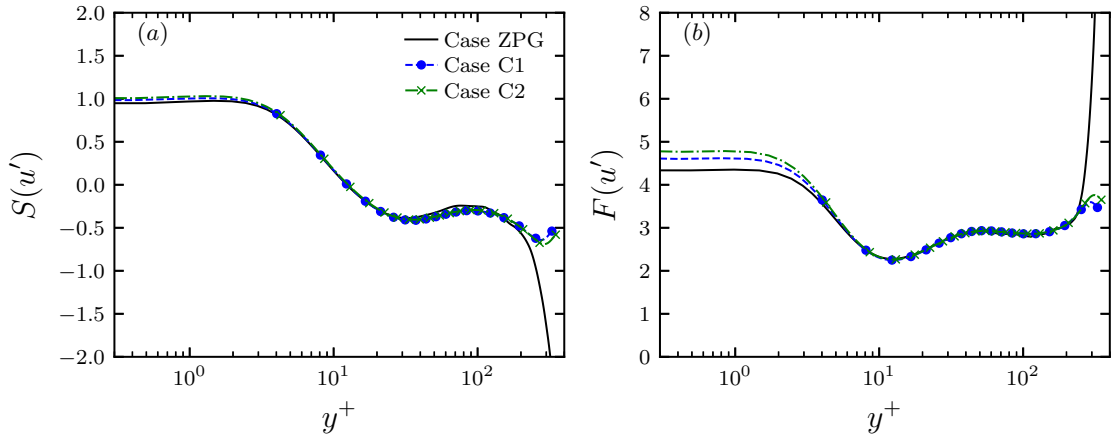


Figure 7.2: Higher order statistics: (a): skewness of u' , $S(u')$; (b): kurtosis of u' , $F(u')$.

boundary layer flows [250]. Overall, the similarity of one-point turbulence statistics between the channel flows and TBLs is comparable to previous studies conducted at higher Reynolds numbers. There is also good agreement between cases C1 and C2 suggesting that the difference in the initial turbulence between these different Reynolds numbers is negligible.

7.1.2 Matched accelerations

While comparisons of spatial and temporal acceleration have not previously been performed, there have been many comparisons of temporally developing and spatially developing flows, mostly to reduce the computational cost, as the streamwise direction can be treated as periodic in the temporal case. Early uses of the temporal analogy to investigate flows that ordinarily develop in space include transitional flows where the flow statistics and turbulent structures have been found to match their spatially developing counterparts [253, 254, 255]. Recently, temporal analogies have been applied to turbulent boundary layers. Kozul et al. [228] created a temporally developing TBL using an impulsively started moving wall and a numerical trip, resulting in good agreement with its spatial counterpart for the first and second-order statistics, even at low Reynolds numbers. Numerical studies of three-dimensional TBLs also typically use a temporal analogy where they are represented by a channel flow with a suddenly applied spanwise pressure gradient or moving wall [256, 257, 258, 259].

This study compares spatially and temporally accelerating flows with a matched acceleration parameter, K , of the two flows at a given streamwise location/convective

distance. K is chosen as it is an important parameter that is often reported in studies of both accelerations. It should be emphasised that, unlike some of the studies above, we are not attempting to create accelerations with equivalent statistics but to evaluate the similarities and differences of spatial and temporal accelerations of the same value of a chosen control parameter, K .

The acceleration parameters for spatially accelerating TBLs and temporally accelerating channel flows are

$$K = \frac{\nu^*}{U_\infty^{*2}} \frac{dU_\infty^*}{dx^*} \qquad K = \frac{\nu^*}{U_c^{*3}} \frac{dU_c^*}{dt^*}, \quad (7.1)$$

respectively. To compare the time development of the temporal acceleration with the spatial acceleration, a convective distance is defined [171],

$$X_c^* = \int_0^{t^*} U_c^*(\tau^*) d\tau^*, \quad (7.2)$$

Equation (7.2) can be considered analogous to the definition used in Kozul et al. [228] for temporally developing TBLs, where $X_c^* = U_w^* t^*$, albeit with a time-varying convection velocity in this case. The choice of U_c^* as the convection velocity is physically relevant due to the tendency of temporally accelerating channel flows to accelerate uniformly across the channel for much of the acceleration.

A characteristic length is required to compare X_c^* from the temporal acceleration and x^* from the spatial acceleration. Here, we use the half-channel height, h^* and the 99% boundary layer thickness at a reference plane upstream of the acceleration, δ_0^* . The fixed value of δ_0^* used in this study ensures that x varies monotonically. In principle, h^* could be matched to a smaller value than δ_0^* to reflect the reducing outer scale, although in appendix C.1.1, it is shown that this should not change at least the early stage excursions of the mean flow parameters. It also should be noted that neither the location of the reference plane nor the choice of the boundary layer thickness appreciably affects the results (appendices C.1.2 and C.1.3). Hereafter, lengths in the accelerations will be normalised by these values unless otherwise stated.

Alongside matching the accelerating parameter, K , we also match the scaled centreline velocity of the channel with the scaled freestream velocity at a given convective distance.

$$U_c(X_c) = U_\infty(x). \quad (7.3)$$

where $U_c = U_c^*/U_{c0}^*$ and $U_\infty = U_\infty^*/U_{\infty0}^*$. Matching K , equation (7.3), and matching the half-channel height and initial boundary layer thickness places a condition on the

Reynolds number of the channel. Substituting equation (7.3) into equation (7.1), noting that from equation (7.2) $d_t = U_c dX_c$

$$K = \frac{1}{Re_{\delta 0}} \frac{1}{U_\infty^2} \frac{dU_\infty}{dx}, \quad K = \frac{1}{Re_{c0}} \frac{1}{U_c^2} \frac{dU_c}{dX_c}. \quad (7.4)$$

where $Re_{\delta 0} = U_{\infty,0}^* \delta_0^* / \nu$ and $Re_{c0} = U_{c,0}^* h^* / \nu$. Therefore, for K to match at a given X_c and x , $Re_{c0} = Re_{\delta 0}$. This requires the initial Reynolds number to differ from those used in previous turbulent channel flow and TBL comparisons, where Re_τ is more common. Section 7.1.1 shows that the same similarities in the initial flow also exist for matched Re_c at the low Reynolds numbers in this study. Equations (7.2) and (7.3) allow further analogies to be made between the temporal and spatial accelerations. Firstly, the scaled freestream/centreline inertia is approximately equal in each acceleration.

$$U_\infty \frac{dU_\infty}{dx} \approx U_c \frac{dU_c}{dX_c} \equiv \frac{dU_c}{dt}. \quad (7.5)$$

Using the mean momentum balance at the freestream/centreline. For spatial acceleration (neglecting small terms),

$$-\frac{d\bar{p}_\infty}{dx} \approx U_\infty \frac{dU_\infty}{dx} \quad (7.6)$$

For temporal acceleration,

$$U_c \frac{dU_c}{dX_c} = -\frac{d\bar{p}_c}{dx} - \frac{\partial \overline{u'v'}}{\partial y} \Big|_c. \quad (7.7)$$

Decomposing the pressure gradient using $d_x \bar{p}_c^\wedge(t) = d_x \bar{p}_c(t) - d_x \bar{p}_c(t=0)$ and noting that $-\overline{u'v'}$ at the centreline does not change in temporally accelerating flows until the re-establishment of the linear Reynolds shear stress profile at the end of the fully turbulent region [43] and that $d_x \bar{p}_c(t=0) = \partial_y \overline{u'v'}(t=0, y=1)$

$$-\frac{d\bar{p}_c^\wedge}{dx} \approx U_c \frac{dU_c}{dX_c}, \quad (7.8)$$

where physically $\partial_x \bar{p}_c^\wedge$ is the driving pressure gradient associated with the temporal acceleration. From equation (7.5),

$$\frac{d\bar{p}_\infty}{dx} \approx \frac{d\bar{p}_c^\wedge}{dx}. \quad (7.9)$$

It should be noted that in non-zero pressure gradient TBLs, the mean velocity above the edge of the boundary layer is not exactly constant due to the non-uniformity of the pressure gradient that results from the effect of flow contraction [260], meaning

Table 7.2: Details of the temporally accelerating simulations. ΔT is the time from the start of the acceleration to where it has reached 90% of its final value. K is multiplied by 10^6 . Resolutions represent their worst values during the simulations.

Case		Re_c	Re_τ	K_{max}	ΔT	Δx^+	Δz^+	Δy_w^+	Δy_c^+	L_x	L_z
Case 1T	Initial	7784	388	6.3	12.8	5.5	3.9	0.4	3.9	18	6
	Final	15600	698			9.8	7.0	0.7	7.0	18	6
Case 2T	Initial	7842	389	3.9	20.2	5.5	3.9	0.4	3.9	18	6
	Final	15692	697			9.8	7.0	0.7	7.0	18	6

that equations (7.5) and (7.9) can only match approximately. It also means that the U_c must be matched to a ‘particular’ U_∞ , and hence this means that there is some uncertainty in the K profile in spatially accelerating flows. In this study, we take $U_\infty = \bar{u}(y = 1.1 \max(\delta_{99}))$. This point was chosen such that it was far enough from the wall that \bar{u} was not varying significantly, but close enough that equation (7.9) is approximately valid within the boundary layer/channel. Other more systematic approaches to determining U_∞ , such as using the diagnostic plot [260], have been considered but were not found to work in such strong favourable pressure gradients. A more detailed explanation and assessment is given in appendix C.1.4 with testing indicating that the choice of U_∞ does not significantly affect the results, with only some small quantitative differences observed in case 1.

In summary, the temporal acceleration has been matched to the spatial acceleration at a given X_c through (i) the acceleration parameter, K ; (ii) the scaled freestream/centerline velocity (equation (7.3)), noting that the half-channel height and initial boundary layer thickness have been used to scale X_c and x in the temporal and spatial accelerations, respectively. As a consequence, the scaled pressure gradient and the streamwise inertia match at the centreline/freestream. The initial Reynolds number ($Re_{\delta_0} = Re_{c0}$) also match. Other approaches for matching the accelerations include using different acceleration parameters, such as the Narasimha and Sreenivasan [9] pressure gradient parameter, Λ . The development of alternative acceleration parameters will be considered in the results.

7.2 Simulation setup

The details of the temporal acceleration simulations in this chapter are outlined in table 7.2, showing cases 1T and 2T, the analogous accelerations for cases 1 and 2.

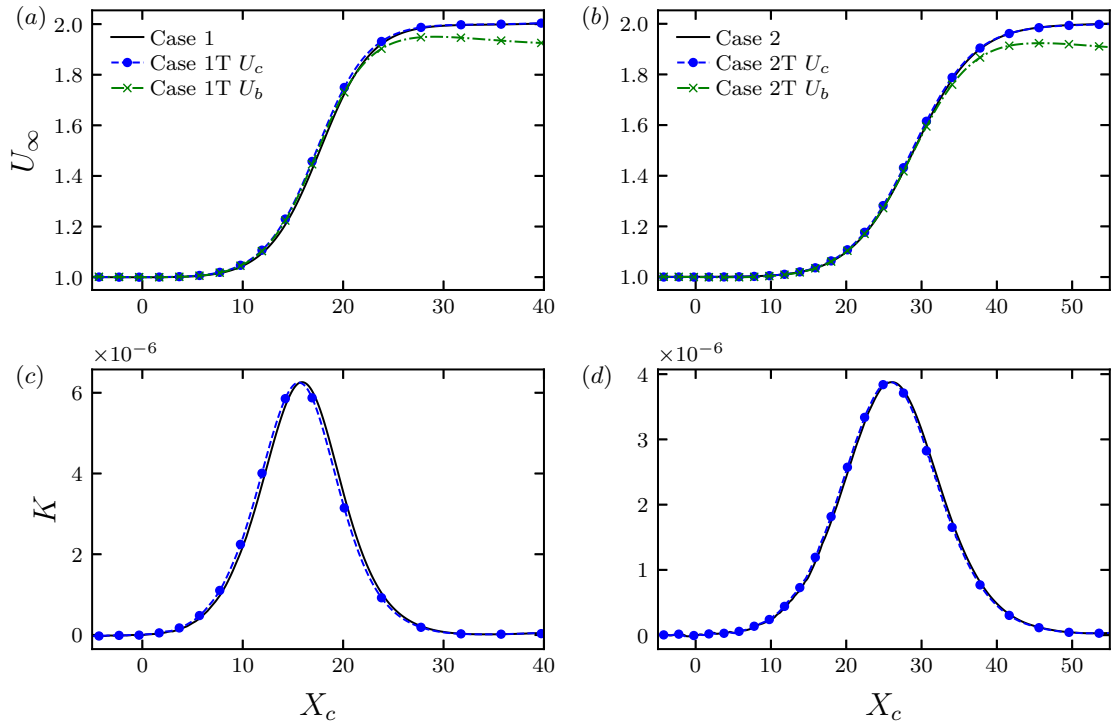


Figure 7.3: Freestream/centreline velocity and acceleration parameter. (a) U_∞ and U_c for cases 1 and 1T. (b) U_∞ and U_c for cases 2 and 2T. The bulk velocity, U_b for the channel flows is also presented, shifted upwards so that it initially overlaps with U_c . (c) K for cases 1 and 1T. (d) K for cases 2 and 2T. The legend in (a) applies to (c) and the legend in (b) applies to (d).

The details of the spatial acceleration cases are presented in table 6.1 with these cases rescaled using δ at the same reference location. Equation (7.3) specifies that the centreline velocity of the channel is matched to the freestream velocity. This is achieved by dynamically modifying the pressure gradient of the channel to ensure that at every time step, the cross-sectionally averaged centreline velocity matches the desired freestream velocity of the spatial accelerations with the error between these values of $O(10^{-6})$. U_c is presented for cases 1T and 2T against X_c in figures 7.3(a) and 7.3(b) showing that it matches $U_\infty(x)$ at all locations. Figures 7.3(c) and 7.3(d) show that K also matches at a given X_c .

Figure 7.3 shows that the bulk velocity, U_b , also approximately matches U_∞ in the early stages of the acceleration due to the new boundary layer being thin during the pre-transition region. The number of mesh points (N_x, N_y, N_z) is $1280 \times 649 \times 600$ for both cases leading to mesh resolutions that are similar to previous studies of

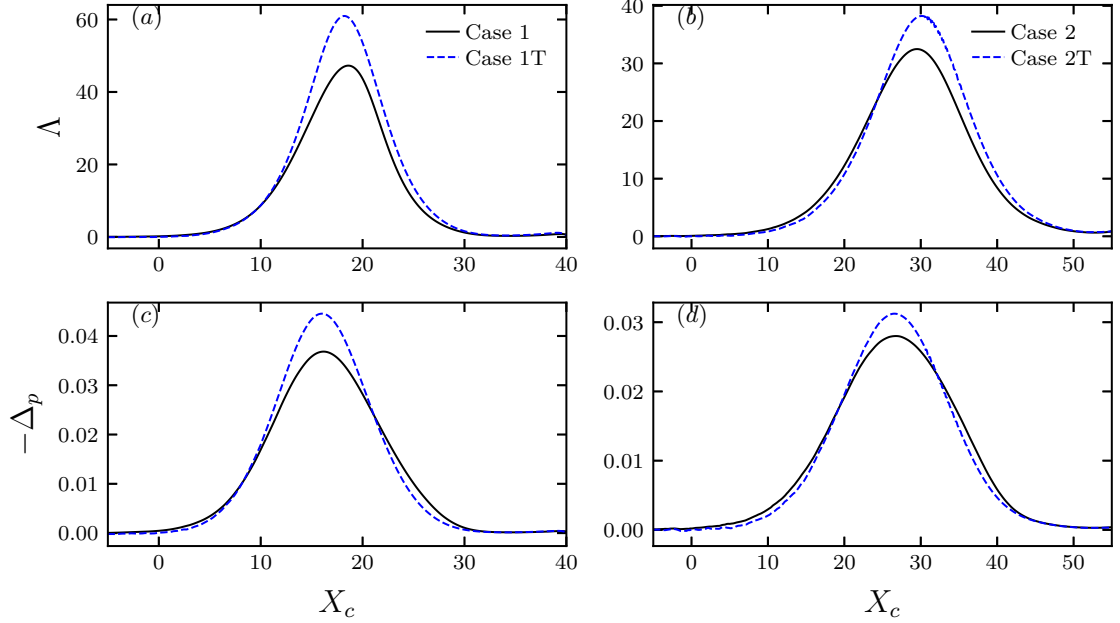


Figure 7.4: Comparison of other acceleration parameters. Λ [9] (a), (b). Δ_p [22] (c), (d). Cases 1 and 1T: (a) (c). Cases 2 and 2T: (b) (d).

temporally accelerating channel flow [43, 44]. Three ensembles have been run for cases 1T and 2T.

7.3 Mean flow response

Figure 7.4 shows the development of the pressure gradient parameters $\Lambda = -(\delta/\tau_{w0})d_x\bar{p}_\infty$ and $\Delta_p = (\nu/u_\tau^3)d_x\bar{p}_\infty$ [9, 22] for cases 1 and 2, where for temporal acceleration, $\Lambda = -(h/\tau_{w0})d_x\bar{p}_c^\wedge$ and $\Delta_p = (\nu/u_\tau^3)d_x\bar{p}_c^\wedge$. Λ is larger in case 1T compared with case 1. This is largely due to the substantial reduction of δ , which is somewhat offset by the smaller value of τ_{w0} in spatial accelerations. For cases 2 and 2T, the peak values of Λ and Δ_p are also larger for the temporal accelerations. Matching these acceleration parameters represents alternatives to the approach discussed in section 7.1.2. The larger values in the temporal acceleration indicate that if these parameters were matched, the resulting temporal accelerations would be weaker than those presented herein.

Figure 7.5 presents several important mean flow parameters for cases 1 (left) and 2 (right). The wall shear stress, τ_w for cases 1 and 2 is presented in figures 7.5(a)

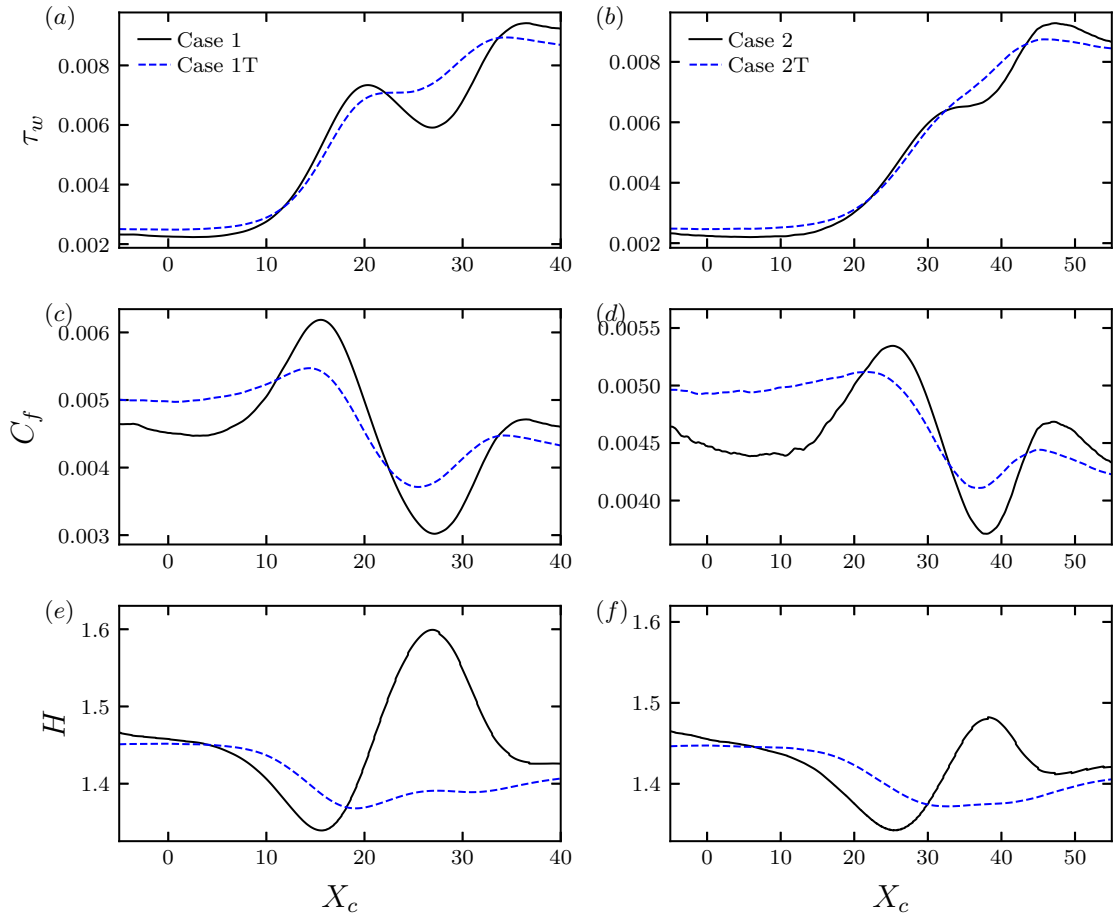


Figure 7.5: Comparison of mean flow parameters. Skin friction coefficient C_f (c) (d). Shape factor H (e) (f). Cases 1 and 1T: (c) (e). Cases 2 and 2T: (d) (f)

and 7.5(b). In case 1T, τ_w follows the four-stage development described in Oluwadare and He [261] for strong temporal accelerations. During pre-transition, τ_w rapidly increases due to the formation of the new boundary layer before stagnating for a short time. This results from the tendency of the τ_w to reduce as the new boundary layer grows, combined with the lack of further substantial increases in bulk velocity to maintain the rapid increase of τ_w . Case 1 follows a similar development initially, although τ_w increases earlier and somewhat more strongly than for case 1T. Next, instead of reaching a plateau as in case 1T, τ_w in case 1 reduces rapidly after reaching a peak. At the onset of transition, ($X_c \approx 29$ in case 1; $X_c \approx 27$ in case 1T), τ_w increases rapidly in both cases as new turbulence is generated. τ_w is similarly observed to increase earlier in case 2 than in case 2T (figure 7.5(b)). From ($22 \lesssim X_c \lesssim 33$),

both cases nearly collapse for a region comprising much of the overall increase in τ_w . Case 2T behaves more similarly to the slower accelerations from Oluwadare and He [261], with little stagnation of τ_w , whereas in case 2, τ_w stagnates without obvious reduction.

Figures 7.5(c) and 7.5(d) shows the skin friction coefficient for cases 1 and 2, where $C_f = 2\tau_w/(\rho U_c^2)$ for the temporal acceleration cases. For $X_c < 0$, the initial C_f is lower in the spatial accelerations, reflecting the fuller velocity profile and absence of the wake in stationary channel flows. C_f also slowly decreases with downstream distance in the spatial accelerations due to the downstream growth of the boundary layer in the upstream TBL, whereas temporal acceleration cases are stationary. After the onset of the accelerations, C_f in case 1 increases significantly in the spatial acceleration, overshooting case 1T in the early stages. As $U_c = U_\infty$, these differences derive just from the changes in τ_w , which increases slightly earlier in case 1. By $X_c \approx 16$, τ_w increases somewhat more rapidly in case 1 than case 1T, but both accelerations exhibit similar trends. However, pointwise, τ_w is significantly larger in case 1. Hence, normalisation by U_∞^2 accentuates these differences, meaning the changes of C_f appear substantially larger in the spatial accelerations. For case 2, the early stages of the acceleration are also characterised by significant increases in C_f , which reflects the small increases in τ_w at $X_c \approx 20$ where the increase of U_∞ is modest. C_f subsequently reduces substantially in all accelerations, although more strongly in the spatial acceleration. C_f reaches a minimum indicating the onset of transition. The location of transition in the temporal and spatial acceleration is similar, although it appears slightly delayed in the spatial accelerations.

The shape factor, H , is presented in figures 7.5(e) and 7.5(f) and can be observed to behave similarly after the start of the acceleration, with an initial decrease followed by an increase towards the end of the pre-transition region. However, the initial reduction in cases 1 and 2 occurs earlier and stronger than for cases 1T and 2T. The subsequent increase is far larger in cases 1 and 2, where H increases towards laminar-like values, whereas cases 1T and 2T exhibit only a mild increase. These much stronger excursions in the spatial acceleration agree with the observations of Greenblatt and Moss [47]. Overall, the mean flow parameters in both accelerations show general similarities. However, the spatial accelerations tend to respond earlier and more strongly to the increases in freestream velocity than their temporal counterparts.

Figures 7.6(a) and 7.6(b) shows the mean streamwise velocity, \bar{u} for cases 1 and 1T with blue lines indicating locations before the onset of transition and red lines

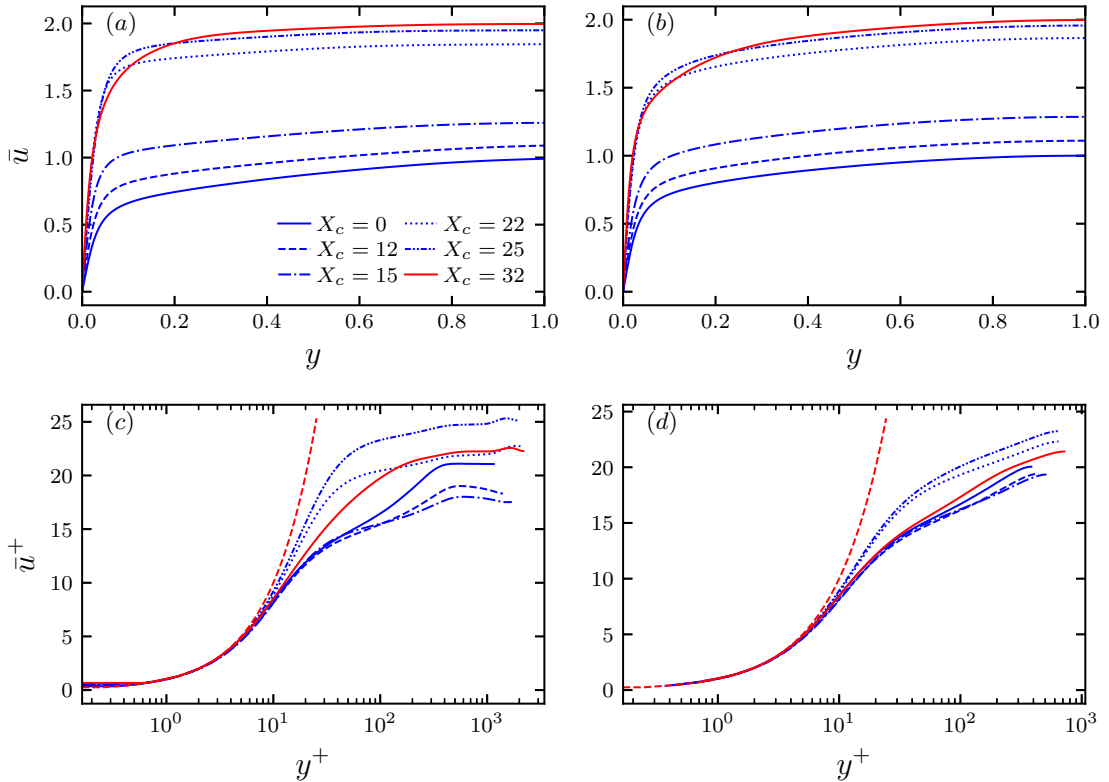


Figure 7.6: Comparison of mean velocity: (a) \bar{u} case 1; (b) \bar{u} case 1T; (c) \bar{u}^+ case 1; (d) \bar{u}^+ case 1T.

indicating those after. Hereafter, we focus predominantly on cases 1 and 1T because the mean flow and turbulence response in cases 2 and 2T are generally similar. From the matching strategy, U_c and U_∞ are the same. The effect of flow contraction can be observed in case 1 with the uplift from the $X_c = 0$ line at $X_c = 12$ larger at $y = 0.1$ than in the freestream. This trend continues, and by $X_c = 22$, \bar{u} has been significantly flattened in case 1. In contrast, case 1T accelerates uniformly and largely retains its velocity gradient from further upstream. The flattening of the velocity profile helps to explain the stronger and earlier increases of τ_w in spatial acceleration: the contraction results in a stronger effective acceleration being felt in the near-wall region, consequently leading to larger velocity gradients there to satisfy the no-slip condition. The inner-scaled mean velocity profile is presented in figures 7.6(c) and 7.6(d) for cases 1 and 1T. At $X_c = 0$, the differences in the initial flow can be observed with the strong wake component visible in case 1. The inner-scaled mean velocity profile for case 1 shows that in the early stages of the acceleration $X_c \leq 15$,

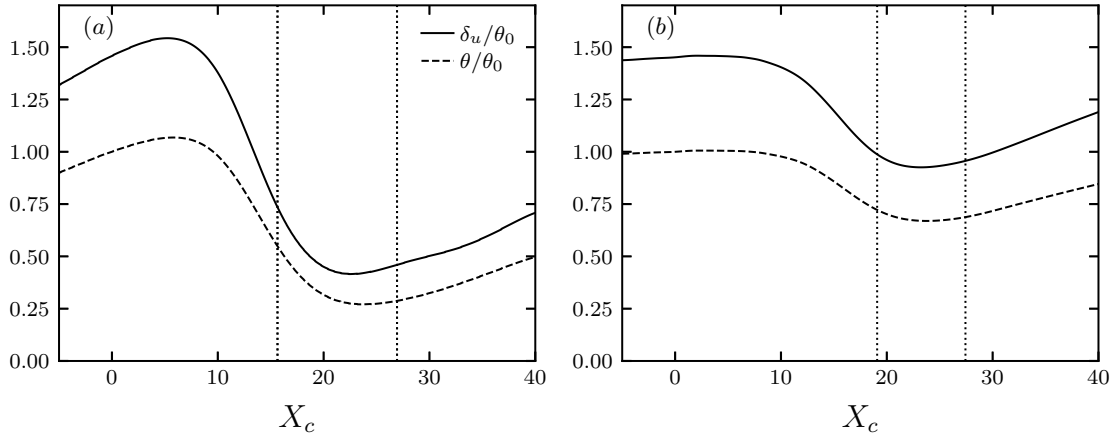


Figure 7.7: Development of integral thicknesses in cases 1 (a) and 1T (b).

the reduction of velocity gradient is mostly associated with the destruction of the wake with the uplift of the logarithmic law observed for $X_c > 15$. There are some similar general trends in case 1T (figure 7.6(d)) with \bar{u}^+ reducing below the $X_c = 0$ line for $X_c \leq 15$ before exhibiting some mild uplift. However, case 1T lacks the distinctive skew towards the wall, with the uplift occurring relatively evenly across the logarithmic region, which can be compared with the uplift of the logarithmic law in moving wall accelerations (figure 5.2). The much larger variations of \bar{u}^+ in case 1 compared with case 1T conforms with the larger variation of C_f in figure 7.5 ($C_f = 2/U_\infty^{+2}$). In both cases, the onset of transition is approximately associated with the maximum uplift from the logarithmic law as discussed in chapter 6.

The flow contraction has an important influence on the development of the shape factor in each acceleration. Figure 7.7 presents the integral thicknesses for cases 1 (left) and 1T (right) normalised by the momentum thickness at the reference plane, θ_0 . For reference, the location of the $\min(H)$ during pretransition and the $\max(H)$ associated with the onset of transition are indicated by vertical lines. Figure 7.7 shows that for $X_c < 22$, δ_u and θ reduce, although the former reduces more strongly. This can be explained by considering a location where $\bar{u}/U_\infty = 0.7$ initially and becomes $\bar{u}/U_\infty = 0.9$ due to the flattening of the velocity profile (or just the increasing centre-line velocity without a change in absolute velocity defect for temporal acceleration): the contribution to δ_u goes from $0.3 \rightarrow 0.1$ whereas θ goes from $0.21 \rightarrow 0.09$, leading to a reduction of H . The flattening of the velocity profile results in larger and earlier reductions of δ_u and θ , causing earlier and stronger reductions of H in cases 1 and 2 compared with cases 1T and 2T (figure 7.5). However, as the acceleration progresses,

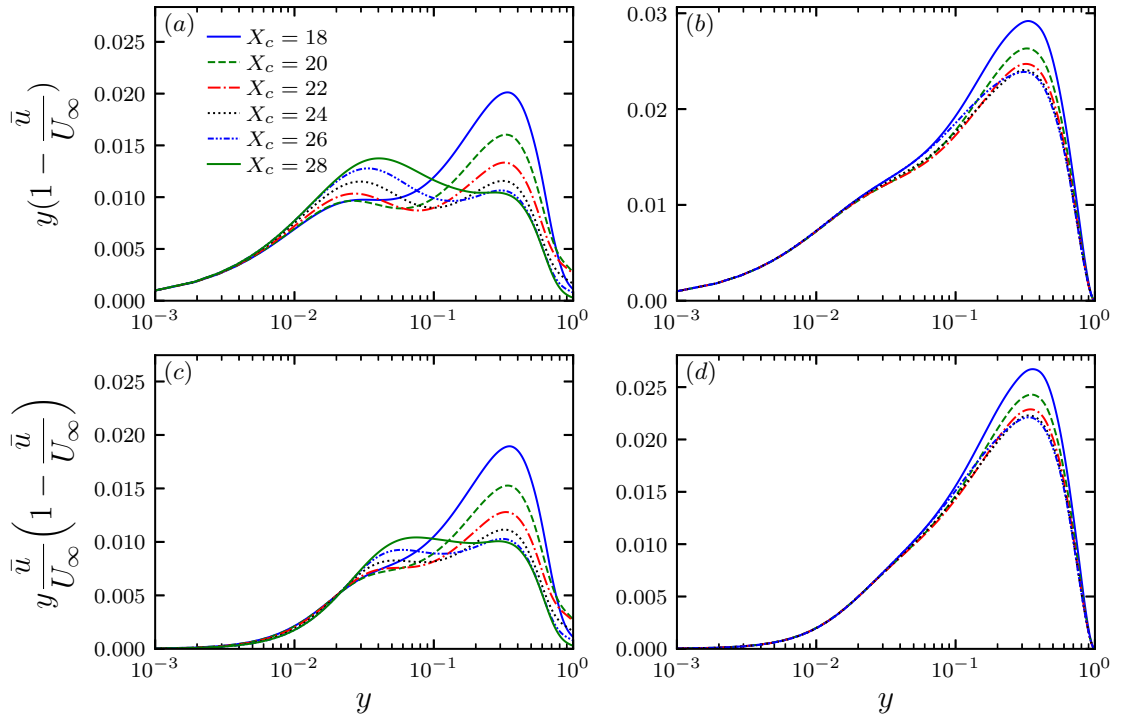


Figure 7.8: Comparison of integral thickness integrands pre-multiplied by y . $1 - \bar{u}/U_\infty$ (a) (b). $(\bar{u}/U_\infty)(1 - \bar{u}/U_\infty)$ (c) (d). Case 1: (a) (c). Case 1T: (b) (d)

\bar{u}/U_∞ will approach one away from the wall. Therefore, δ_u and θ would tend to reduce by a similar amount, although the decrease of the former is always greater than the latter. This comparable reduction of δ_u and θ can be observed around H_{min} in figures 7.7(a) and 7.7(b). This comparable decrease helps explain why H begins to increase in both accelerations. From the quotient rule

$$\theta^2 \frac{dH}{dx} = \theta \frac{d\delta_u}{dx} - \delta_u \frac{d\theta}{dx}. \quad (7.10)$$

From equation (7.10), where θ is reducing, H will increase when

$$H > \frac{d\delta_u}{dx} / \frac{d\theta}{dx}. \quad (7.11)$$

As a result, as both thicknesses decrease at the roughly same rate, the RHS of equation (7.11) will approach 1, and as $H_{min} > 1.3$ in cases 1 and 1T, H will begin to increase. This effect applies to both cases 1 and 1T, explaining why H increases in both accelerations towards the end of the pre-transition region. However, the contraction should result in this increase being stronger in the spatial accelerations due

to the larger reductions of the integral thicknesses (figure 7.7). The influence of the mean velocity on the integral thicknesses can also be investigated by examining their integrands. Figure 7.8 shows locations during pre-transition where H is increasing. The abscissa is plotted logarithmically to highlight the near-wall region. Therefore, the integrands have been premultiplied by y such that the area under the curve still visually represents the integral thicknesses. In the outer part of the flow ($y > 0.1$), the effect of the reducing velocity defect can be observed in both accelerations with stronger decreases in spatial acceleration, consistent with the flattening of the velocity profile. However, close to the wall, there appears to be a region in case 1 where both the δ_u and θ integrands are increasing that is not present in case 1T. This indicates an expansion in the near-wall region, which will be investigated in more detail in the next section. The expansion has the opposite effect of the flattening mean velocity profile, leading to δ_u beginning to increase (or reduce less) than θ , thus increasing H .

7.4 Momentum balance

The non-dimensional mean momentum equations for spatial and temporal acceleration are

$$\underbrace{\bar{u} \frac{\partial \bar{u}}{\partial x}}_{-\mathcal{I}_{C1}} + \underbrace{\bar{v} \frac{\partial \bar{u}}{\partial y}}_{-\mathcal{I}_{C2}} = \underbrace{-\frac{\partial \bar{p}}{\partial x}}_{\mathcal{P}} + \underbrace{\frac{1}{Re_{\delta 0}} \left[\frac{\partial^2 \bar{u}}{\partial x^2} + \frac{\partial^2 \bar{u}}{\partial y^2} \right]}_{\mathcal{V}} - \underbrace{\frac{\partial \bar{u}'^2}{\partial x} - \frac{\partial \bar{u}'v'}{\partial y}}_{\mathcal{T}}, \quad (7.12)$$

$$\underbrace{\frac{\partial \bar{u}}{\partial t}}_{-\mathcal{I}_T} = \underbrace{-\frac{\partial \bar{p}}{\partial x}}_{\mathcal{P}} + \underbrace{\frac{1}{Re_{e0}} \frac{\partial^2 \bar{u}}{\partial y^2}}_{\mathcal{V}} - \underbrace{\frac{\partial \bar{u}'v'}{\partial y}}_{\mathcal{T}}. \quad (7.13)$$

where $Re_{\delta 0} = Re_{e0}$. Of particular interest is the behaviour of the inertial terms with \mathcal{I}_{C1} and \mathcal{I}_T representing the streamwise accelerations in the spatial and temporal accelerations. Spatial accelerations have the additional \mathcal{I}_{C2} term representing the influence of the wall-normal contraction and expansion. These terms are balanced on the RHS by the pressure gradient, \mathcal{P} , viscous diffusion, \mathcal{V} and turbulence diffusion, \mathcal{T} .

Figure 7.9 shows the momentum balance for cases 1 (left) and 1T (right) at the same convective/downstream distance. At $X_c = 0$, we can observe the differences between the flows before the accelerations. In case 1T (figure 7.9(b)), \mathcal{P} balances \mathcal{T} away from the wall, while in case 1 (figure 7.9(a)), \mathcal{T} is mostly balanced by \mathcal{I}_{C1} , which is positive indicating that the outer flow is being decelerated as the boundary layer grows. The \mathcal{V} and \mathcal{T} balance close to the wall in both accelerations. In

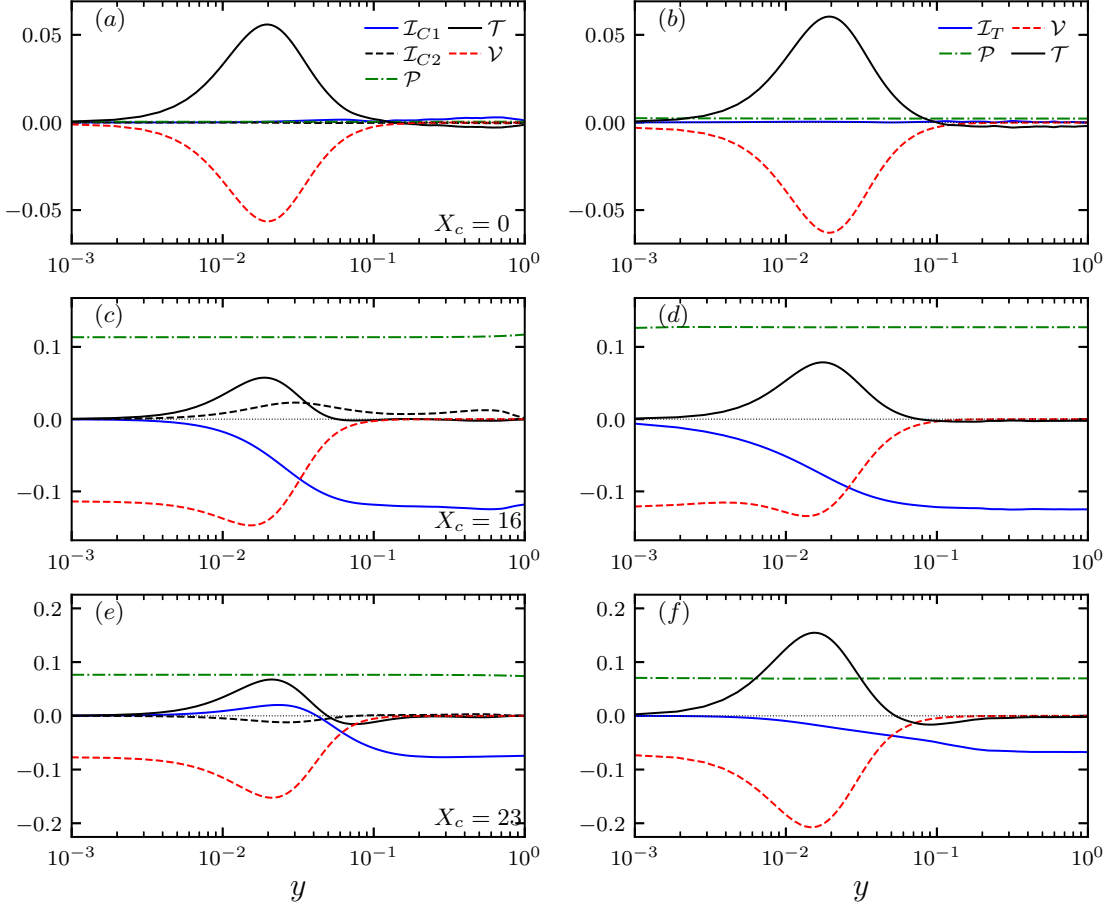


Figure 7.9: Momentum balance during pre-transition. Cases 1 and 1T are presented on the left and right, respectively. Streamwise locations: $X_c = 0$ (a) and (b); $X_c = 16$ (c) and (d); $X_c = 23$ (e) and (f).

figures 7.9(c) to 7.9(f), the momentum balances are presented at locations during pre-transition. As expected from the comparison approach, the pressure gradient across the channel/boundary layer approximately matches, although small deviations can be observed, for example, at $X_c = 16$ due to slight non-uniformity in the pressure gradient in FPGTBLs (see appendix C.1.4). Similarly, the streamwise inertia terms also approximately match at the freestream. We can also see that at the wall, the viscous diffusion matches in both cases, consistent with taking the force balance at the wall and the approximately equal pressure gradient.

At $X_c = 16$, \mathcal{I}_T is essentially constant for much of the wall-normal extent, which conforms with the uniform increase of the mean velocity in figure 7.6(b) and acts to

balance the increasing pressure gradient. In case 1, the \mathcal{I}_{C1} is also mostly balanced by the increasing pressure gradient away from the wall. However, the magnitude of \mathcal{I}_{C1} is slightly larger than the pressure gradient in the outer part of the boundary layer and is larger there than in the freestream, which can be linked to the flow accelerating faster in the outer boundary layer than at the freestream (figure 7.6(a)). At this stage, \mathcal{I}_{C1} and \mathcal{I}_T have similar general shapes. The ‘excess’ \mathcal{I}_{C1} in the outer layer is balanced mainly by wall-normal convection term, \mathcal{I}_{C2} , which is consistent with the flow contraction being responsible for the flattening of the velocity profile. Closer to the wall, \mathcal{V} typically has a similar shape in both accelerations, with case 1 slightly larger than case 1T at $X_c = 16$.

More substantial differences emerge between the accelerations in the late pre-transition stage ($X_c = 23$). For case 1T, the momentum balance has not substantially changed from $X_c = 16$, albeit with a moderate increase in \mathcal{T} . In contrast, there have been substantial changes in case 1. Close to the wall ($y \approx 0.02$), the fluid has also started to mildly decelerate ($\mathcal{I}_{C1} > 0$), despite the continuing freestream acceleration, with the flow beginning to expand ($\bar{v} > 0$) and \mathcal{I}_{C2} becoming negative close to the wall. This expansion is consistent with the increase of the δ_u integrand in figure 7.8 and it is evident that a similar expansion is not observed in the matched temporal acceleration (figure 7.9(f)). The expansion can also explain the tendency for τ_w to reduce more strongly in the later stages of pre-transition in the spatial accelerations (figures 7.5(a) and 7.5(b)).

We consider there to be two main mechanisms that may lead to this near-wall expansion. First, by $X_c = 23$, the effect of flow contraction has substantially diminished as indicated by $\mathcal{I}_{C2} \approx 0$ away from the wall, with $\min V_\infty$ at $X_c \approx 18$. Consequently, as the acceleration begins to relax, the flow in the near-wall region, which has been substantially thinned due to the contraction, begins to expand. Second, the subdued turbulence mixing by this point means that there is less momentum transport into the near-wall region by the turbulent fluctuations. This is indicated by \mathcal{T} being noticeably weaker in case 1 compared with case 1T, consistent with the near-wall region becoming more laminar-like and the turbulent stresses not substantially contributing to the mean flow dynamics. The comparatively short region of acceleration in the present study means that it is difficult to determine definitively between these mechanisms.

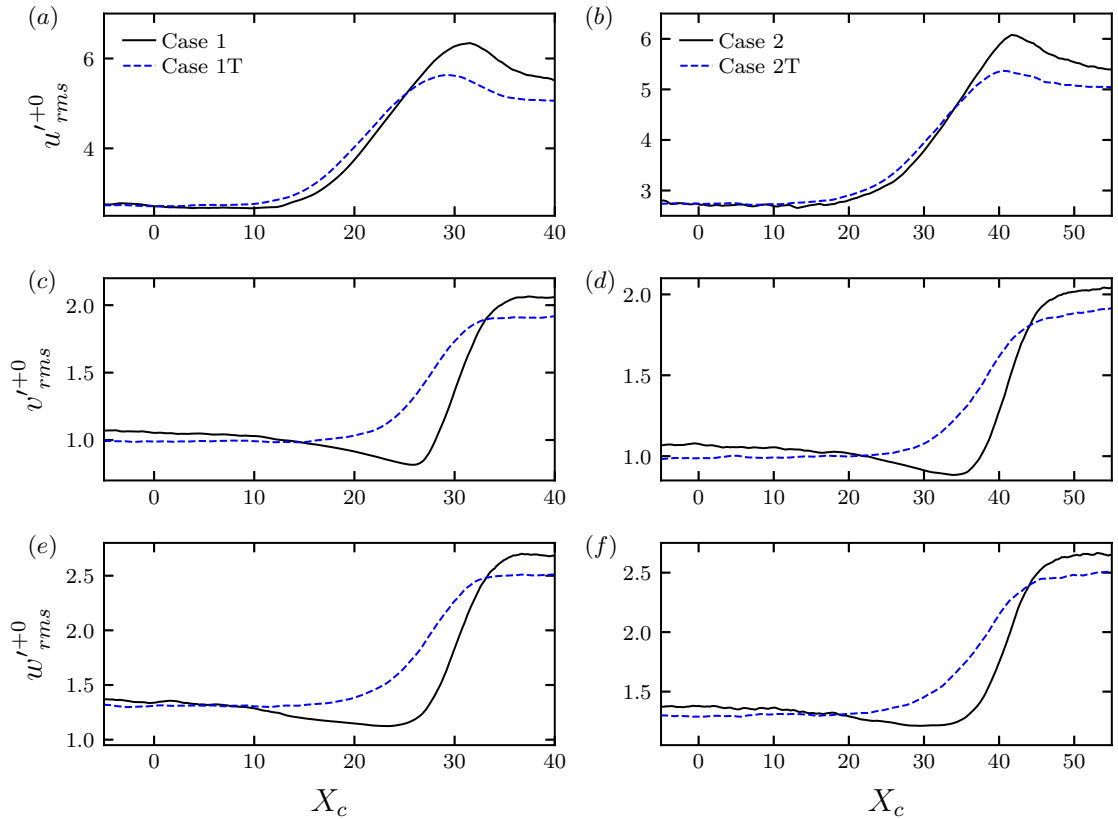


Figure 7.10: Maxima of RMS velocity fluctuations for cases 1 and 1T (left), and cases 2 and 2T (right). $u'_{rms}{}^{+0}$ (a) (b); $v'_{rms}{}^{+0}$ (c) (d); $w'_{rms}{}^{+0}$ (e) (f).

7.5 Turbulence response

The maxima of the RMS of the velocity fluctuations are presented in figure 7.10 for cases 1 and 2. Upstream of the acceleration, the peak of $u'_{rms}{}^{+0}$ for spatial and temporal acceleration collapse as expected from figure 7.1(b). After the beginning of the acceleration, the near-wall maximum of $u'_{rms}{}^{+0}$ follow very similar trajectories with the temporal acceleration slightly larger than their spatial counterparts. The agreement in case 2 is somewhat better than in case 1. At $X_c \approx 25$ in case 1T ($X_c \approx 35$ in case 2T), the rate of increase of $\max(u'_{rms}{}^{+0})$ decreases substantially whereas the spatial accelerations continue to increase until somewhat later. This difference reflects the slightly earlier onset of transition in the temporal acceleration. The onset of transition leads to increased intercomponent energy transfer, drawing energy from u' . Consequently, the earlier transition results in an earlier decrease of u'_{rms} in the temporal accelerations. Upstream of the acceleration, the peak of transverse components, $v'_{rms}{}^{+0}$

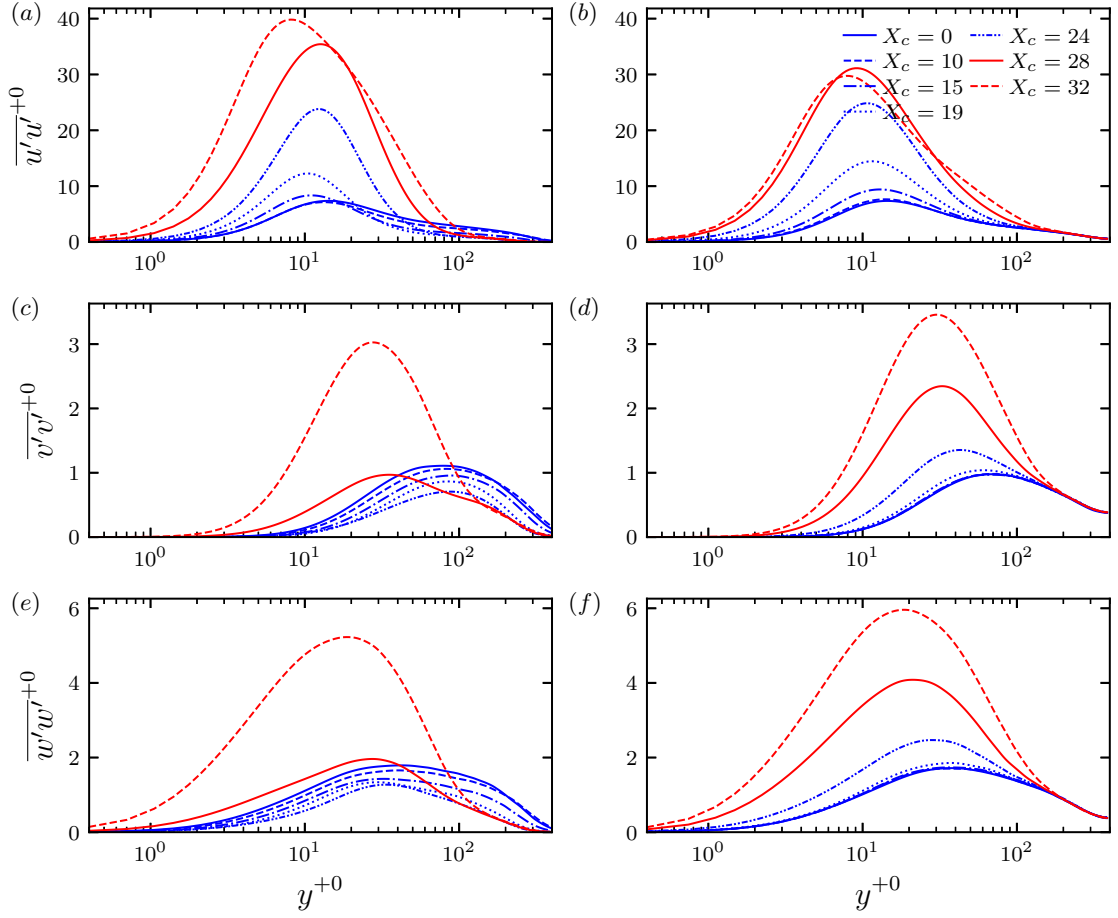


Figure 7.11: Wall normal distributions of $\overline{v'v'^{+0}}$ ((c)(d)) and $\overline{w'w'^{+0}}$ ((e)(f)) for cases 1 (left) and 1T (right.)

and w'_{rms}^{+0} are larger in the spatial accelerations as expected from previous studies [232] (see also figure 7.1). However, v'_{rms}^{+0} and w'_{rms}^{+0} reduce substantially in absolute terms in the spatial accelerations during pre-transition, whereas the temporal accelerations remain approximately constant.

Figure 7.11 presents the wall-normal distribution of the normal Reynolds stresses for cases 1 and 1T, with blue lines indicating locations during pre-transition and red lines indicating those after. The similar values of the near-wall peak of $\overline{u'u'}$ during pre-transition in cases 1 and 1T can also be observed here, with the growth indicative of the increasing amplitude of the near-wall streaks. However, further from the wall, there are significant differences between cases 1 and 1T. While case 1 reduces substantially, case 1T remains at its value from before the acceleration for $y^{+0} > 50$. The behaviour of the transverse components during pre-transition is also very different

(figures 7.10(c) to 7.10(f)). While case 1 attenuates substantially across the boundary layer during pre-transition, case 1T remains unchanged until the onset of transition. With the onset of transition, transverse components increase substantially in both accelerations, initially close to the wall, then further away from it. The significant differences in the response of $\overline{v'v'}^{+0}$ and $\overline{w'w'}^{+0}$ between the spatial and temporal accelerations are consistent with the mechanisms for the absolute reduction of the transverse stresses in spatial acceleration being closely tied to the contraction of the boundary layer.

These similarities and differences in the turbulence response can also be observed in the velocity fluctuations. Figure 7.12 shows u' and v' for cases 1 and 1T. For case 1, an $x - z$ plane near the wall is shown, with the corresponding plane in case 1T generated from a line probe in the z direction, which is converted to a plane of $X_c - z$ for comparison with case 1. Figure 7.12 also shows $z - y$ at the same downstream/convective distance for both cases with two planes during pre-transition and one plane located after the onset of transition.

The similarity in the response of the streamwise component close to the wall in cases 1 and 1T is shown in figures 7.12(a) and 7.12(b), with the $x - z$ plane showing the increase in the amplitude of the near-wall streaks, as expected in the pre-transition stage of the accelerations. The streaky structures in the spatial acceleration are noticeably less perturbed than for the temporal acceleration, reflecting the absolute attenuation of transverse motions in the former but not the latter. The $z - y$ planes in figures 7.12(a) and 7.12(b) also indicate how further from the wall there are significant differences, with u' reducing and the turbulence becoming confined to a thin region close to the wall for case 1. However, for case 1T, u' is not significantly changed away from the wall in any of the $z - y$ planes. The differences in the wall-normal component during pre-transition can also be observed with v' attenuating for case 1 (figure 7.12(c)) and remaining at approximately the same amplitude in case 1T (figure 7.12(d)). The onset of transition can also be observed in both cases with the formation of higher intensity, shorter scale motions at $X_c \approx 25$. These spots are more prominent in case 1 due to the attenuation of the transverse motions, with the spots forming slightly further downstream in case 1 consistent with the somewhat delayed minimum in C_f in figure 7.5. The differences in the turbulence response away from the wall can similarly be observed in the wall-normal velocity fluctuations.

The similarities and differences in the turbulence structures can also be considered in an averaged sense. The $\Delta x - y$ autocorrelation of the streamwise velocity fluctuation, $R_{11}(\Delta x, y, y_0; t)$ has frequently been used to characterise the average extent and

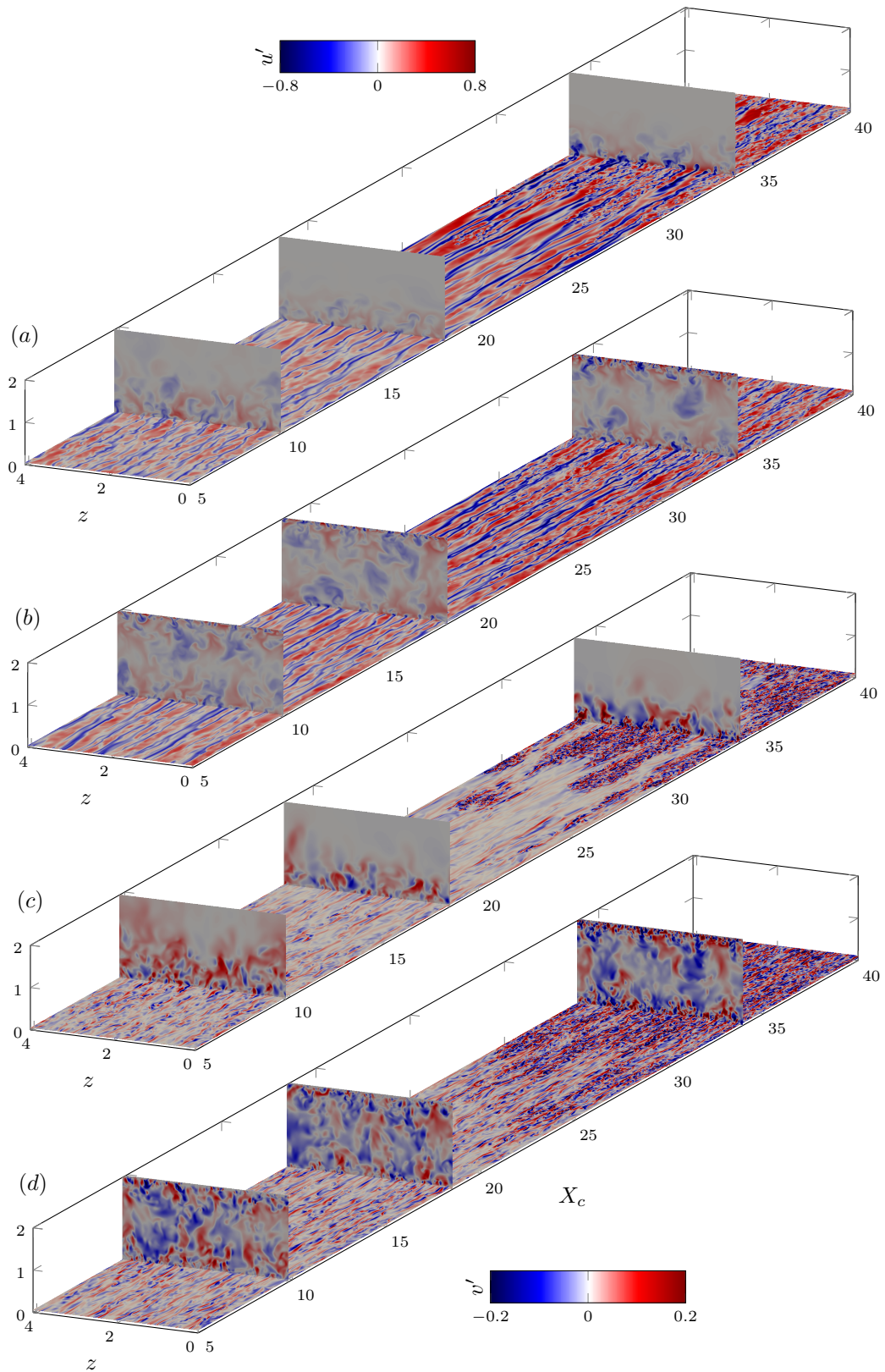


Figure 7.12: Comparison of the velocity fluctuations for cases 1 and 1T at an $x - z$ plane close to the wall and at various $z - y$ planes. (a) u' case 1, (b) u' case 1T, (c) v' case 1, (d) v' case 1T. The colourmap for u' is presented in the top left, the colourmap for v' is shown in the bottom right.

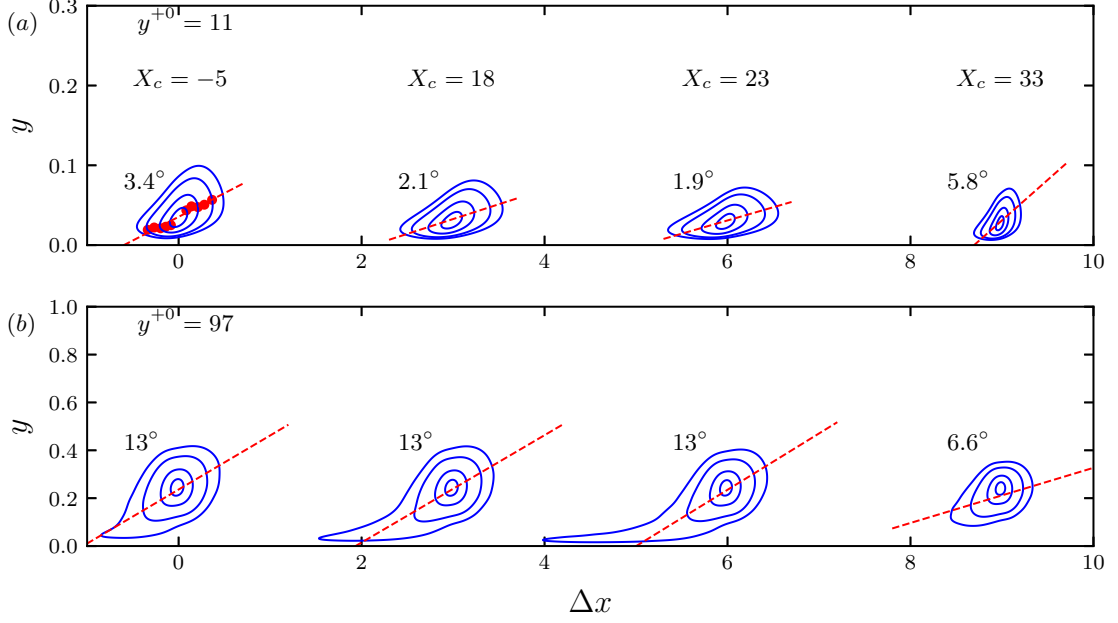


Figure 7.13: $\Delta x - y$ streamwise velocity autocorrelation, $R_{11}(\Delta x, y, y_0; t)$ for case 1T at $y^{+0} = 11$ (a) and $y^{+0} = 97$ (b) for $X_c \in -5, 18, 23, 33$ with subsequent stations shifted by 3 to the right. Inclination computed using the method of Volino et al. [23] is given to the left of R_{11} . At ($y^{+0} = 11, X_c = -5$), the points used to compute the inclination angle are marked with red dots.

shape of turbulent structures in boundary layers and channels [23, 48]. In the present study, R_{11} has been computed with

$$R_{11}(\Delta x, y, y_0; t) = \frac{1}{u'u'} \mathcal{F}^{-1} \left[\left\langle \widehat{u}'^*(k_x, y_0, t) \widehat{u}'(k_x, y, t) \right\rangle \right], \quad (7.14)$$

employing the relationship between the spectral density and the autocovariance (equation (2.17)). In this case, $\langle \rangle$ indicates spanwise and ensemble averaging of the spectral density. The changes in turbulent structures can be summarised by the structure inclination angle, ϕ , developed by Volino et al. [23]. ϕ is determined by least-squares fitting the points furthest from $(\Delta x, y - y_0) = (0, 0)$ for the contours of R_{11} at $(0.5, 0.6, 0.7, 0.8, 0.9)$ both upstream and downstream of the autocorrelation peak to $y = m\Delta x + c$ with $\phi = \tan^{-1}(m)$. The points selected for the least-squares fit for $X_c = -5$ are indicated by red dots in figure 7.13(a).

In the present study, R_{11} has not been computed for the spatial accelerations, but the substantial reduction of the inclination angle throughout the boundary layer has been widely reported [118, 105, 215]. Figure 7.13 shows the development of R_{11}

in the buffer layer (figure 7.13(a)) and logarithmic layer (figure 7.13(b)) during the acceleration in case 1T. Before the start of the acceleration ($X_c = -1$), the structures close to the wall ($y^{+0} = 10$) are nearly aligned with the streamwise direction, although R_{11} shows they are slightly lifted at their downstream end. As the acceleration progresses, these structures tilt further toward the wall, exhibiting a notable reduction in inclination angle by $X_c = 23$. This results from the increase in mean shear, which causes these structures to elongate as their downstream (upwards tilted) end is subject to higher streamwise velocities and is ‘pulled’ away from the upstream end, which is closer to the wall and moving more slowly. After the onset of transition, the inclination increases significantly.

In the logarithmic region, R_{11} is associated with the inclination of logarithmic layer streaks and their associated vortical structures. The nature of these vortical structures is still debated [262], although they have often been represented as packets of hairpin vortices [263, 264]. At ($y^{+0} = 97$), the shape of R_{11} does not substantially change during pre-transition (figure 7.13(b)) as indicated by the comparatively small changes in inclination angle, which remains similar to values observed in the logarithmic layer of stationary turbulent channel flows [265]. R_{11} is still substantially distorted towards the bottom left of the contours as the roots of these structures, which are embedded in the near-wall region, are sheared. The comparatively small distortion of R_{11} is because, in temporal accelerations, the flow accelerates without deformation outside the new boundary layer, as indicated in figure 7.6(b). However, in spatial acceleration, the streamwise acceleration elongates these structures in the streamwise direction and flow contraction pushes these structures towards the wall. This leads to the turbulent structures in the outer flow being strongly distorted and a reduction of inclination angle across the boundary layer.

In summary, the turbulence response shares some important similarities associated with the transition process, such as the response of u'_{rms} and the eventual increase of the transverse components with the onset of transition, which occurs at similar locations. However, there are substantial differences in the behaviour of the turbulent stresses and structures away from the wall. This indicates that it is unlikely that there is a common mechanism, such as those proposed in Yuan and Piomelli [49] and Mangavelli and Yuan [48], that can fully explain laminarisation in both accelerations.

7.6 Discussion

7.6.1 Influence of the initial flow

Given the different nature of the flow before the accelerations, we can consider the potential influence that this may have on the flow development during the acceleration. One notable difference is the streamwise inhomogeneity of the TBL upstream of the spatial acceleration, contrasting with the fully developed channel flow in the temporal accelerations. For cases 1 and 2, this should not strongly affect the results, as the flow development after the onset of acceleration dwarfs that before it. Furthermore, it can be shown that modestly changing the location of the reference plane does not substantially affect the comparison (see appendix C.1). However, in weaker accelerations, where the influence of the acceleration is less severe, this difference may be more relevant. Another difference is the presence of the wake in TBLs, which results in a fuller mean velocity profile in the temporal accelerations before the acceleration. The less full mean velocity profile in the upstream TBL likely reinforces the significance of flow contraction in spatial accelerations, as the larger initial velocity deficit leads to more substantial excursions in the mean flow parameters as the mean velocity profile is flattened. Significantly, the elimination of the wake represents one of the earliest changes in the inner-scaled mean velocity (figure 7.6(c)). Additionally, there are differences in the initial turbulence, particularly the larger transverse motions in ZPGTBLs compared with channels [232]. This is not expected to substantially contribute to the different turbulence responses during pre-transition, as the streamwise acceleration and flow contraction are much more important.

7.6.2 Assessment of the comparison approach

The purpose of the comparison approach developed in section 7.1 was to facilitate comparison between spatial and temporal accelerations. The chosen approach offers several advantages. First, the matching of U_c and U_∞ ensured that the changes in C_f can be related directly to τ_w , highlighting that the significant differences in the former could be associated with seemingly limited differences in the trends of the latter. It also allows a comparison of the mean velocity by ensuring that the scaled freestream/centreline velocities are the same. This, in turn, enables differences between the uniformly increasing mean velocity in temporal acceleration and the flattening mean velocity profile in spatial acceleration to be observed. Second, the approximate matching of the scaled pressure gradients means that the momentum balance could be compared at each X_c , with many terms approximately equal at the

freestream or the wall. Third, the matched acceleration parameter, K means that the accelerations could be considered nominally equivalent in terms of a quantity that has been used previously to characterise both accelerations. As noted in section 7.3, it is possible to match other parameters, but figure 7.4 suggests it is unlikely to lead to different conclusions as it would lead to weaker accelerations and even weaker excursions of the mean flow parameters.

Another advantage of the comparison approach is that the resulting temporal acceleration shares many overarching similarities with its spatial counterpart. These similarities include the overall behaviour of τ_w until the late stages of pre-transition, the similar location of transition onset, and the variation of the near-wall peak of u'_{rms} . While such similarities were not strictly necessary for drawing general conclusions regarding the similarities and differences between the accelerations, they facilitated a meaningful pointwise comparison of the accelerations for much of the pre-transition region. It should be noted that such similarities may not occur at different values of K . Weaker accelerations are more likely to be affected by the differences in the initial flow, while stronger or more sustained accelerations may result in a more extended ‘late pre-transition’ region where more substantial differences in the momentum balance and H were observed.

7.7 Summary and Conclusions

In this chapter, we compared laminarising spatially accelerating TBLs (cases 1 and 2) with temporally accelerating channel flows (cases 1T and 2T) by matching the acceleration parameter, K . For the temporal acceleration cases, we used a convective distance, X_c , where the channel centerline velocity was used as the convection velocity. The comparison approach was effective in facilitating the comparison between the accelerations. The resulting temporal accelerations have similar overarching responses in the development of mean flow parameters and some aspects of the turbulence response as their spatial counterparts. However, flow contraction plays a significant role in spatial acceleration, resulting in much more pronounced variations of the mean flow parameters and significant differences in the transverse turbulent stresses during pre-transition. The main conclusions are summarised below.

- With the onset of the acceleration, C_f initially increases before falling rapidly until the onset of transition in both cases, but the variations are far stronger in the spatial accelerations. The primary reason for this is the contraction of the boundary layer, with the mean velocity close to the wall accelerating faster

than the freestream, meaning the near-wall region is affected by the increasing U_∞ earlier and more strongly than its temporal counterpart. The contraction is reinforced by the initially less full mean velocity profile in the spatial case, leading to a lower initial C_f , which rapidly increases as the velocity profile flattens.

- Similarly, H tends to follow similar trends in both accelerations with more pronounced variations in the spatial accelerations. It is shown that the reduction of the velocity defect relative to the freestream/centreline velocity is responsible for both the initial decrease in H and its subsequent increases in the later stages of pre-transition. Again, flow contraction leads to a more substantial reduction of the velocity defect, contributing to the more significant changes in H .
- In spatial accelerations, the momentum balance exhibits a distinct change of behaviour in the late pre-transition stage, characterised by an expansion of the near-wall flow as the freestream continues to accelerate. Similar behaviours are not observed in their temporal counterparts. This expansion likely plays a significant role in the more notable increases in H and the more substantial decreases in τ_w during this stage. Two possible (not mutually exclusive) mechanisms were identified: (i) the flow beginning to relax as the influence of contraction diminished, and (ii) the subdued turbulence, meaning less turbulent mixing in the near-wall region. However, due to the relatively short accelerations in this study, further simulations or experiments are required to understand their relative importance fully.
- The streamwise turbulent stresses behave similarly close to the wall in spatial and temporal accelerations, with the peak values nearly collapsing throughout pre-transition. In contrast, further from the wall, the streamwise component reduces strongly in the former.
- The transverse motions exhibit significant differences, remaining constant in temporal accelerations while reducing substantially in spatial accelerations. This supports the notion that the absolute attenuation of transverse stresses and the streamwise component away from the wall in spatial accelerations is closely tied to the contraction of the boundary layer. Additionally, distinctions in the development of turbulent structures in the outer flow have been highlighted. After the onset of transition, both accelerations behave similarly.

Chapter 8

Conclusions and future work

8.1 Conclusions

In this study, we have investigated spatially accelerating turbulent flows to improve the understanding of the turbulence dynamics, particularly the processes that lead to the emergence of laminarisation, which has remained enigmatic for decades and is present in many engineering applications. The main finding of this study is the flow and turbulence response of spatially accelerating turbulent boundary layers across a wide range of acceleration rates are dominated by the development of a new boundary layer and the eventual transition of the flow in response. This was first investigated through a simplified spatial acceleration, driven by longitudinally accelerating moving walls, which enabled a study of the development of the new boundary layer and the turbulence response without the influence of flow contraction (chapter 5). This simplified flow has been characterised by a transition process and exhibited many similarities to both spatially and temporally accelerating flows. We subsequently investigated spatially accelerating TBLs, which include the influence of flow contraction, over a range of acceleration rates from the weak laminarescent to the strongly laminarising regimes (chapter 6). A transition process was identified in all cases as a result of the near-wall increases in mean shear. Important differences were found in the turbulence response of laminarescent and laminarising cases, with the turbulence in the inner layer freezing in the former, while in the latter, it attenuates significantly. The mechanisms for the differences have been explored. Lastly, we have directly compared spatially accelerating TBLs and temporally accelerating channel flow with matched acceleration parameter, K (chapter 7). It has been found that flow contraction results in spatially accelerating flows exhibiting earlier and larger excursions in the mean flow parameters such as C_f and H and leads to substantial differences in the turbulence development, particularly away from the wall. While

many aspects of spatially accelerating flows remain enigmatic and require further study, we believe this work has shed light on some of the fundamental processes in these flows. Below, we summarise each of the results chapters.

8.1.1 Moving wall acceleration

The flow response in the moving wall acceleration is characterised by the development of a new boundary layer followed by transition. As such, the process can be described as a three-stage development: pre-transition, transition, and fully turbulent, similar to temporal acceleration. During pre-transition, the new boundary layer amplifies the near-wall streaks through the lift-up effect without significantly affecting the transverse components. At the onset of the transition stage, these streaks break down due to localised instabilities developing of specific streaks. This leads to the formation of turbulent spots, which spread in the spanwise direction until the wall is covered in new turbulence. The newly generated turbulence propagates away from the wall during the fully turbulent stage. The moving wall acceleration shares many similarities with conventional spatially accelerating flows that include flow contraction, such as the downstream growth of the streamwise Reynolds stress, changes in the spanwise scales of the streaks before transition, and the role of pressure strain in the recovery of turbulence during transition. The similarities suggested that similar mechanisms could be present in the more complex acceleration where contraction effects are present. The flow also shares considerable similarities with temporally accelerating flows.

8.1.2 Spatially accelerating turbulent boundary layers

Four spatially accelerating TBLs were simulated with peak acceleration parameter K ranging from 1.2×10^{-6} to 6.3×10^{-6} , which is among the widest range of acceleration rates studied using numerical simulation to date enabling a detailed evaluation of the changes in turbulence dynamics as acceleration rate increases. The two weaker accelerations could be classified as laminarescent, in which the flows exhibit some departures from the turbulent state but do not show clear signs of laminarisation. The two stronger accelerations are consistent with laminarising spatial accelerations. The main conclusions are

- The development of the mean velocity in all cases can be characterised in two parts: (i) the development of a new boundary layer due to the resistance provided by viscous effects to freestream acceleration and (ii) a flattening of the mean velocity away from the wall due to flow contraction, which becomes

stronger as acceleration rate increases such that in the strongest acceleration, the mean shear reduces down to the buffer layer.

- All four cases undergo a transition process similar to that described for the moving wall acceleration, with the onset of transition marking the recovery of turbulence in the boundary layer. This recovery is linked to the generation of new turbulence close to the wall, which subsequently spreads away from it, with the turbulence in the outer layer not increasing until the new turbulence has propagated from the wall. In all cases, transition onset can be associated with the maximum uplift from the logarithmic law, an important observation in spatially accelerating flows.
- During pre-transition, the transverse stresses behave differently in the laminarising and laminarising accelerations, with the former remaining frozen in absolute terms and the latter strongly attenuating. The same difference is also observed for the streamwise component but only away from the wall.
- For the laminarising accelerations, the wall-normal pressure strain has been found to behave differently from the other components, becoming negative for much of the boundary layer, which was linked to the ‘splating’ of large-scale wall-ward motions from the freestream and the redistribution of energy extracted directly from the mean flow by flow contraction.

8.1.3 Comparison of spatially and temporally accelerating flows

Matched temporally accelerating channel flows have been created for the laminarising spatial accelerations by matching the acceleration parameter, K and the scaled freestream/centreline velocities to understand the similarities and differences in the development of mean flow parameters and turbulence between the accelerations. C_f and H have been found to have similar trends in both accelerations. However, the variations are much more significant in the spatial accelerations. There are two main reasons for this: First, the flattening of the velocity profile in spatial accelerations results in the flow close to the wall accelerating faster than the freestream, meaning that the mean flow parameters tend to respond earlier and more strongly than their temporal counterparts. Second, the momentum balance showed that in the late pre-transition stage, the near-wall region in the spatial acceleration expands, resulting in strong increases in H and reductions in τ_w .

The precise cause of the expansion is unclear, but it is likely to result from either the subdued turbulence in the spatial acceleration or the relaxation of the flow contraction towards the end of the acceleration, although these should not be mutually exclusive. The near-wall peak streamwise stress nearly collapses between the spatial and temporal accelerations. However, the transverse stresses across the boundary layer and the streamwise stress away from the wall behave differently, with turbulence in the temporal accelerations roughly collapsing onto their values from before the acceleration. However, in the spatial accelerations, they attenuate absolutely. Significant differences have been observed in the turbulent structures in the logarithmic layer of the temporal acceleration compared with previous studies of spatial accelerations.

8.2 Proposed future work

There are three areas that should be investigated in future work. (i) More simulations and experiments of spatially accelerating TBLs to extend the range of acceleration further and to consider additional physics. (ii) Studying accelerations with geometries closer to those in engineering applications, particularly those accompanied by curvature. (iii) Work to improve the understanding of the near-wall turbulence processes that lead to transition occurring in spatially and temporally accelerating flows. These are detailed below.

Further simulations and experiments of spatially accelerating TBLs should include stronger, more sustained accelerations and weaker accelerations. As discussed in chapter 6, experimental works such as Bourassa and Thomas [87] have accelerations that have been sustained for far longer with much larger freestream velocity ratios of around (10). Their results suggest that differences in the turbulence response compared with this study may emerge in such strong acceleration rates. It is likely that extreme cases such as Bourassa and Thomas [87] will remain computationally unfeasible for the foreseeable future and will require experimental investigation, potentially supported by simulations using the present code at more moderate acceleration rates and Reynolds numbers. Additionally, weaker accelerations should also be simulated to ascertain if and at what acceleration rates the transition process described herein becomes indiscernible.

It would also be useful to consider a broader range of initial Reynolds numbers to understand what influence this has on transition and the attenuation of the transverse motions in spatially accelerating TBLs. Spatial accelerations with additional physics,

such as heat transfer, should also be investigated. Some of the early works on spatial acceleration, such as Moretti and Kays [95], noted that laminarisation was responsible for heat transfer deterioration. However, few studies have since investigated this in detail. Future simulations could also consider using more advanced analyses to characterise the transition process, such as using the budget of the Kármán-Howarth-Monin equation to improve the understanding of energy redistribution around transition onset.

Simulations should also be performed on accelerating flows with more complex geometries to understand how the presence of curvature may alter the transition process. Many applications discussed in chapter 1, such as the leading edge slat, also include significant curvature. These could include simulations or experiments of Gaussian bumps or curved hills, where there is already a significant body of research [38, 266, 267].

Lastly, the transition process in accelerating flows has been established, with the mean and turbulence responses explained in this framework. However, we believe that this new understanding could be further linked to the turbulence re-generation cycle, which already has a significant body of research. The link between the turbulence regeneration cycle and the present transition concept may be established with the aid of stability analysis, which could focus particularly on the amplification of the streaks and their breakdown. This is out of the scope of the present study but may be a valuable future research topic.

Appendix A

Moving wall acceleration

A.1 Details of the turbulence generator

The sufficiency of the domain size in periodic directions is confirmed using the two-point correlation. Figure A.1 shows the streamwise autocorrelation in the periodic streamwise and spanwise directions. These plots show that the correlation is close to zero by the half-width and half-length of the channel, indicating that the turbulence generator size is sufficient.

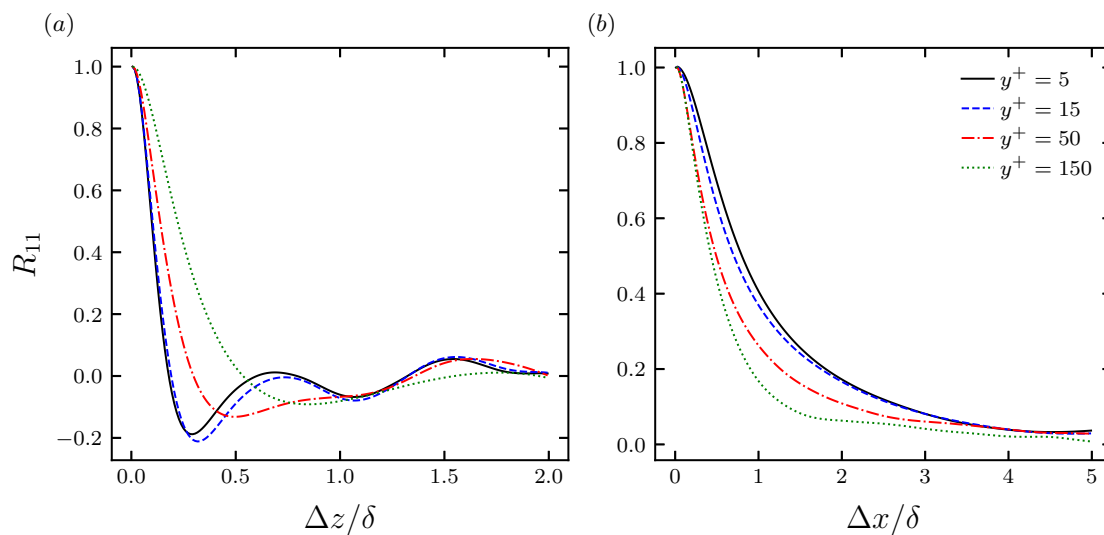


Figure A.1: Streamwise autocorrelation for turbulence generator at $y^+ \in \{5, 15, 50, 150\}$. (a) spanwise direction. (b) streamwise direction.

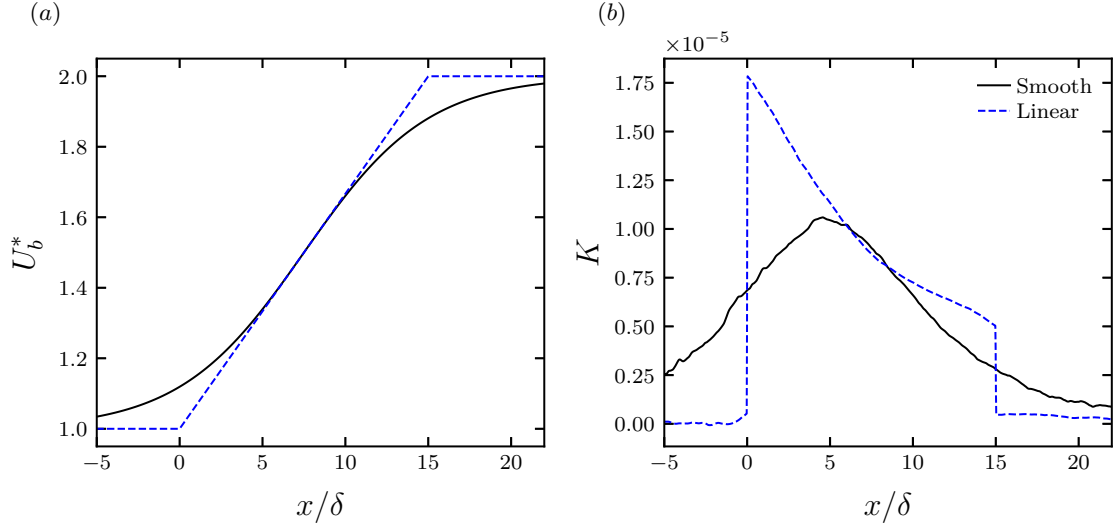


Figure A.2: Smooth case compared with the case presented in the paper. (a) Relative bulk velocity. (b) Acceleration parameter.

A.2 Moving-wall acceleration with a smooth and gradual flow increase

Some results are presented below of a smooth moving wall acceleration, which shows that the overall phenomena, including the location of transition, are largely unchanged compared to the linear acceleration presented in the main body of the paper. In order to create an equivalent smooth acceleration, a tanh function was used such that the acceleration, dU/dx in the middle of the acceleration is the same as the linear case, and the velocity of both cases was the same in the middle of the acceleration. Enforcing these conditions results in:

$$U(x) = U_0 - U_w(x) = U_0 + \frac{\Delta U}{2} \left[\tanh \left(\frac{2x}{\Delta x} + 1 \right) + 1 \right], \quad (\text{A.1})$$

where x is the downstream distance from the nominal onset of the acceleration in the equivalent linear case. Δx is the streamwise length of the acceleration in the equivalent linear acceleration case. The resulting bulk velocity profile and acceleration parameter distributions for the smooth case compared with the case presented in the study are shown in figure A.2. It can be observed that the peak K observed in figure 5.3 is now absent in the ‘smooth’ case, which shows a shape more similar to those exhibited in conventional flows. Figure A.3 shows that the general behaviour of the skin friction coefficient and shape factor in the two cases are similar. In

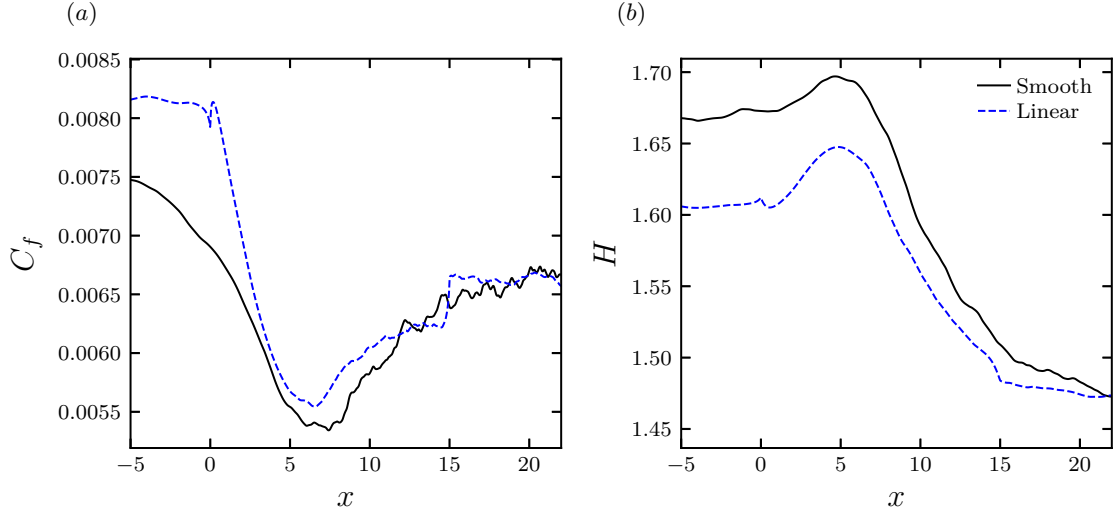


Figure A.3: Smooth case compared with the case presented in the paper. (a) Skin friction coefficient. (b) Shape factor.

particular, the locations of the minimum C_f and peak H are similar in the two flows, which indicates that the smoothing of the flow acceleration profile does not change the key transition features of the flows presented in the main body of the chapter. The parameters in figure A.3 show some detailed different behaviour before transition, which can explain the longer acceleration in the smooth case. Preliminary results from $\overline{u'u'_{max}}$ and $\overline{v'v'_{max}}$ (not presented) also show similar trends to the results presented in the paper.

A.3 Algorithm for quadrant events

The quadrant event statistics were computed from saved instantaneous data with a time interval between samples $\Delta t_s = 0.5h/U_{b0}$. This corresponds to $\Delta t_s^{+0} = 6$ with a maximum $\Delta t_s^+ = 20$ near the completion of transition. In the early stages of the pre-transition, this spacing should be capable of adequately resolving nearly all quadrant events, while during the transition region, the dynamically significant events in the buffer layer, which typically have lifetimes $\Delta t^+ \approx 30$ [248] should be captured. This algorithm considers the events passing a fixed point in the domain with the result averaged over spanwise locations, indicating how ‘full’ the domain is with these events. An event begins at threshold h at sample n when $I(x, y, z; t) = 1$ (equation (5.3)) at n and $I(x, y, z; t) = 0$ at $n - 1$. The average event duration, ΔT_{Qi} ,

is given by the total time at a point where $I(x, y, z; t) = 1$ divided by the number of new events. The average interval between events, T_{Qi} , is given by the total time that statistics are accrued divided by the number of new events.

Appendix B

Transition in spatially accelerating TBLs

B.1 Conditions upstream of acceleration

Figure B.1 shows the mean velocity and the normal Reynolds stresses at the reference plane. There is a good agreement with the ZPG data from chapter 4, indicating that the use of a single domain has not substantially affected the inflow generation in these cases, with the statistics still consistent with ZPG data. Nonetheless, in the future, it is recommended that the inflow data be created with separate precursor simulations to completely eliminate the possibility of feedback between the acceleration and the inflow generation.

B.2 Spot detection algorithm

A simple spot detection algorithm was used in this study with the quantity of interest being

$$D = |v'| + |w'|, \quad (\text{B.1})$$

which is the quantity used in the transition study of Nolan and Zaki [165] to detect turbulent spots. The criterion for spot detection was defined as

$$D - D_{rms,0} > 0.15(\max(D_{rms}) - D_{rms,0}), \quad (\text{B.2})$$

where $D_{rms} = v'_{rms} + w'_{rms}$. This threshold is similar to that used in the conditional averaging of temporally accelerating flows performed by Mathur et al. [172]. This is different from Nolan and Zaki [165] because their detection method [268] was less effective due to the turbulence present before transition, although more sophisticated versions of the Otsu [268] thresholding method may have worked adequately. The

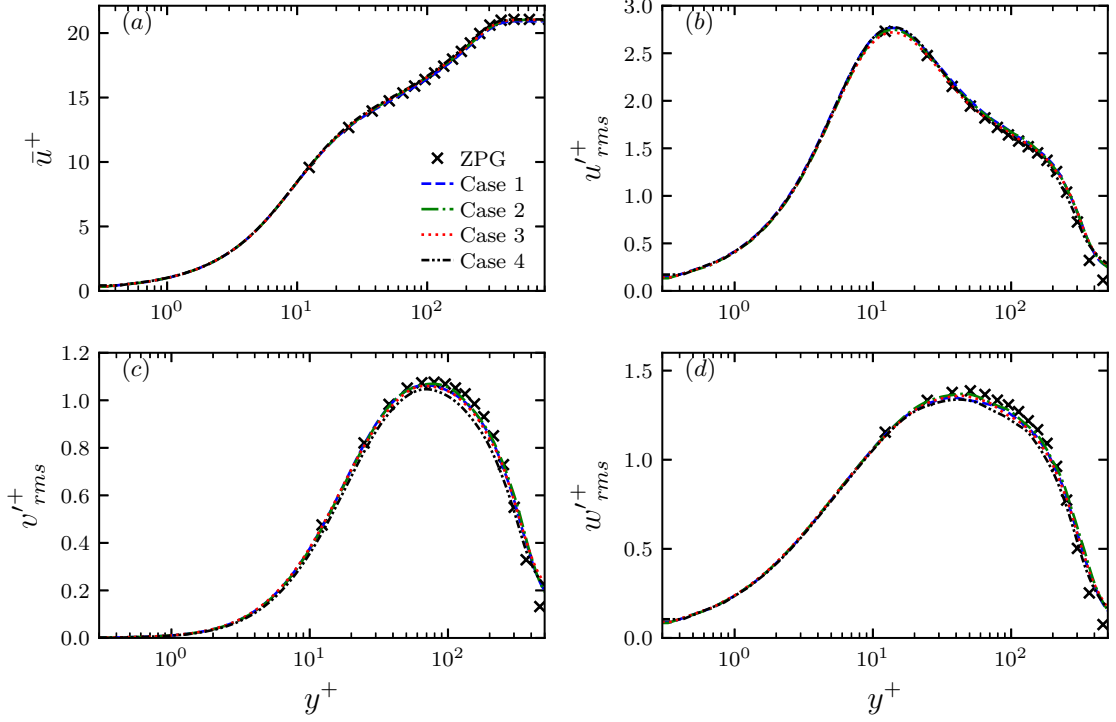


Figure B.1: Comparison of the reference plane of cases 1 to 4 with ZPG case from chapter 4

criterion is depicted as lines on figures 6.8(c) and 6.8(d), indicating that the spots are accurately captured with some false positives due to the relatively low prominence of the turbulent spots compared with the background turbulent. Given that the purpose of this spot detection algorithm is as a visual aid only, these false positives are unimportant.

B.3 Derivation of $\widehat{\mathcal{G}}$

The wall-normal vorticity fluctuation, considering the dominant term only

$$\omega'_y = \frac{\partial u'}{\partial z} - \frac{\partial w'}{\partial x} \approx \frac{\partial u'}{\partial z} \quad (\text{B.3})$$

To derive the transport equation for ω'_y , we start with the streamwise Navier-Stokes (NS) and Reynolds-averaged NS equations, omitting the pressure, viscous, and turbulence transport terms.

$$\frac{\partial u}{\partial t} = -u \frac{\partial u}{\partial x} - v \frac{\partial u}{\partial y} = \dots \quad (\text{B.4})$$

$$\frac{\partial \bar{u}}{\partial t} = -\bar{u} \frac{\partial \bar{u}}{\partial x} - \bar{v} \frac{\partial \bar{u}}{\partial y} + \dots \quad (\text{B.5})$$

Differentiating equations (B.4) and (B.5) by z yields

$$\frac{\partial}{\partial t} \frac{\partial u}{\partial z} = \frac{\partial \omega_y}{\partial t} = -\frac{\partial}{\partial z} \left(u \frac{\partial u}{\partial x} \right) - \frac{\partial}{\partial z} \left(v \frac{\partial u}{\partial y} \right) + \dots \quad (\text{B.6})$$

$$\frac{\partial}{\partial t} \frac{\partial \bar{u}}{\partial z} = \frac{\partial \bar{\omega}_y}{\partial t} = -\frac{\partial}{\partial z} \left(\bar{u} \frac{\partial \bar{u}}{\partial x} \right) - \frac{\partial}{\partial z} \left(\bar{v} \frac{\partial \bar{u}}{\partial y} \right) + \dots \quad (\text{B.7})$$

Subtracting equation (B.7) from equation (B.6) and noting that $\omega' = \omega - \bar{\omega}$ gives

$$\frac{\partial \omega'_y}{\partial t} = -\frac{\partial}{\partial z} \left(u \frac{\partial u}{\partial x} - \bar{u} \frac{\partial \bar{u}}{\partial x} \right) - \underbrace{\frac{\partial}{\partial z} \left(v \frac{\partial u}{\partial y} - \bar{v} \frac{\partial \bar{u}}{\partial y} \right)}_A + \dots \quad (\text{B.8})$$

Considering just term A in equation (B.8)

$$-\frac{\partial}{\partial z} \left(v \frac{\partial u}{\partial y} - \bar{v} \frac{\partial \bar{u}}{\partial y} \right) = -\frac{\partial}{\partial z} \left(v' \frac{\partial \bar{u}}{\partial y} + \bar{v} \frac{\partial u'}{\partial y} + v' \frac{\partial u'}{\partial y} \right) \quad (\text{B.9})$$

Considering just the first term on the RHS of equation (B.9) and applying the product rule

$$-\frac{\partial}{\partial z} \left(v' \frac{\partial \bar{u}}{\partial y} \right) = -\frac{\partial v'}{\partial z} \frac{\partial \bar{u}}{\partial y} - v' \frac{\partial^2 \bar{u}}{\partial y \partial z} \Rightarrow \frac{\partial \omega'_y}{\partial t} = -\frac{\partial v'}{\partial z} \frac{\partial \bar{u}}{\partial y} + \dots \quad (\text{B.10})$$

The spectral density of the wall-normal enstrophy is given by

$$\frac{1}{2} \frac{\partial \langle \widehat{\omega}'_y{}^2 \rangle}{\partial t} = \frac{1}{2} \frac{\partial \langle \widehat{\omega}'_y{}^* \widehat{\omega}'_y \rangle}{\partial t} = \frac{1}{2} \left\langle \widehat{\omega}'_y{}^* \frac{\partial \widehat{\omega}'_y}{\partial t} + \widehat{\omega}'_y \frac{\partial \widehat{\omega}'_y{}^*}{\partial t} \right\rangle \quad (\text{B.11})$$

First, take the Fourier transform of equation (B.10) in the z direction, noting that $\partial_z \widehat{\omega}'_y = ik_z \widehat{\omega}'_y$

$$\frac{\partial \widehat{\omega}'_y}{\partial t} = -\frac{\partial v'}{\partial z} \frac{\partial \bar{u}}{\partial y} + \dots = -ik_z \widehat{v}' \frac{\partial \bar{u}}{\partial y}. \quad (\text{B.12})$$

Multiplying equation (B.12) by complex conjugate of $\widehat{\omega}'_y$, $\widehat{\omega}'_y{}^*$ and averaging in time gives

$$\left\langle \widehat{\omega}'_y{}^* \frac{\partial \widehat{\omega}'_y}{\partial t} \right\rangle = -ik_z \left\langle \widehat{\omega}'_y{}^* \widehat{v}' \right\rangle \frac{\partial \bar{u}}{\partial y} + \dots \quad (\text{B.13})$$

Taking the complex conjugate of equation (B.13), adding it to equation (B.13), and dividing by 2 gives

$$\frac{1}{2} \frac{\partial \langle \widehat{\omega}'_y{}^2 \rangle}{\partial t} = -\frac{1}{2} \left[ik_z \left\langle \widehat{\omega}'_y{}^* \widehat{v}' \right\rangle + ik_z \left\langle \widehat{\omega}'_y \widehat{v}'^* \right\rangle \right] \frac{\partial \bar{u}}{\partial y} = k_z \text{Im} \left\{ \left\langle \widehat{\omega}'_y{}^* \widehat{v}' \right\rangle \right\} \frac{\partial \bar{u}}{\partial y} \quad (\text{B.14})$$

B.4 Derivation of terms in the spectral Reynolds stress transport equation

Beginning with the Navier-Stokes and RANS equations, showing only those terms required to derive the production and pressure strain spectra

$$\frac{\partial u_i}{\partial t} + u_k \frac{\partial u_i}{\partial x_k} = -\frac{\partial p}{\partial x_i} + \dots \quad (\text{B.15})$$

$$\frac{\partial \bar{u}_i}{\partial t} + \bar{u}_k \frac{\partial \bar{u}_i}{\partial x_k} = -\frac{\partial \bar{p}}{\partial x_i} + \dots \quad (\text{B.16})$$

Applying the Reynolds decomposition, $u_i = \bar{u}_i + u'_i$ to equation (B.15) yields

$$\frac{\partial \bar{u}_i}{\partial t} + \frac{\partial u'_i}{\partial t} = -\bar{u}_k \frac{\partial \bar{u}_i}{\partial x_k} - u'_k \frac{\partial \bar{u}_i}{\partial x_k} - \bar{u}_k \frac{\partial u'_i}{\partial x_k} - u'_k \frac{\partial u'_i}{\partial x_k} - \frac{\partial \bar{p}}{\partial x_i} - \frac{\partial p'}{\partial x_i} + \dots \quad (\text{B.17})$$

Subtracting equation (B.16) from equation (B.17) gives

$$\frac{\partial u'_i}{\partial t} = -u'_k \frac{\partial \bar{u}_i}{\partial x_k} - \bar{u}_k \frac{\partial u'_i}{\partial x_k} - u'_k \frac{\partial u'_i}{\partial x_k} - \frac{\partial p'}{\partial x_i} + \dots \quad (\text{B.18})$$

Taking the Fourier transform in z and retaining only the terms needed to derive the production and pressure strain terms gives

$$\frac{\partial \hat{u}'_i}{\partial t} = -\hat{u}'_k \frac{\partial \bar{u}_i}{\partial x_k} - \frac{\partial \hat{p}'}{\partial x_i} + \dots \quad (\text{B.19})$$

The spectral transport equation is given by

$$\frac{\partial \langle \hat{u}'_i{}^* \hat{u}'_j \rangle}{\partial t} = \underbrace{\left\langle \hat{u}'_i{}^* \frac{\partial \hat{u}'_j}{\partial t} \right\rangle}_{\text{A}} + \underbrace{\left\langle \hat{u}'_j \frac{\partial \hat{u}'_i{}^*}{\partial t} \right\rangle}_{\text{B}} \quad (\text{B.20})$$

For term A, we reindex equation (B.19) with i becoming j and multiply by $\hat{u}'_i{}^*$. This gives

$$\hat{u}'_i{}^* \frac{\partial \hat{u}'_j}{\partial t} = -\hat{u}'_i{}^* \hat{u}'_k \frac{\partial \bar{u}_j}{\partial x_k} - \hat{u}'_i{}^* \frac{\partial \hat{p}'}{\partial x_j} + \dots \quad (\text{B.21})$$

For term B, we take the complex conjugate of equation (B.19) and multiply by \hat{u}'_j

$$\hat{u}'_j \frac{\partial \hat{u}'_i{}^*}{\partial t} = -\hat{u}'_j \hat{u}'_k{}^* \frac{\partial \bar{u}_i}{\partial x_k} - \hat{u}'_j \frac{\partial \hat{p}'^*}{\partial x_i} + \dots \quad (\text{B.22})$$

For the production term, the first terms on the RHS of equations (B.21) and (B.22) are added together and averaged in time

$$\hat{\mathcal{P}}_{ij} = -\langle \hat{u}'_i{}^* \hat{u}'_k \rangle \frac{\partial \bar{u}_j}{\partial x_k} - \langle \hat{u}'_j \hat{u}'_k{}^* \rangle \frac{\partial \bar{u}_i}{\partial x_k} \quad (\text{B.23})$$

The pressure strain, $\widehat{\Pi}_{ij}^s$ is recovered from the velocity-pressure gradient term

$$-\widehat{u}_i^* \frac{\partial \widehat{p}'}{\partial x_j} = \widehat{p}' \frac{\partial \widehat{u}_i'^*}{\partial x_j} - \frac{\partial \widehat{u}_i'^* \widehat{p}'}{\partial x_j} \quad (\text{B.24})$$

$$-\widehat{u}_j \frac{\partial \widehat{p}'^*}{\partial x_i} = \widehat{p}'^* \frac{\partial \widehat{u}_j'}{\partial x_i} - \frac{\partial \widehat{p}'^* \widehat{u}_j'}{\partial x_i} \quad (\text{B.25})$$

Gathering the first terms of the RHS of equations (B.24) and (B.25) and averaging in time gives

$$\widehat{\Pi}_{ij}^s = \left\langle \widehat{p}' \frac{\partial \widehat{u}_i'^*}{\partial x_j} + \widehat{p}'^* \frac{\partial \widehat{u}_j'}{\partial x_i} \right\rangle \quad (\text{B.26})$$

Hence, the wall-normal dilational production and the wall-normal and spanwise pressure strain spectra are given by

$$\widehat{\mathcal{P}}_{22} = -2 \operatorname{Re} \left\{ \left\langle \widehat{v}'^2 \right\rangle \right\} \frac{\partial \bar{v}}{\partial y} = 2 \operatorname{Re} \left\{ \left\langle \widehat{v}'^2 \right\rangle \right\} \frac{\partial \bar{u}}{\partial x} \quad (\text{B.27})$$

$$\widehat{\Pi}_{22}^s = 2 \operatorname{Re} \left\{ \left\langle \widehat{p}'^* \frac{\partial \widehat{v}'}{\partial y} \right\rangle \right\} \quad (\text{B.28})$$

$$\widehat{\Pi}_{33}^s = 2 \operatorname{Re} \left\{ \left\langle \widehat{p}'^* \frac{\partial \widehat{w}'}{\partial z} \right\rangle \right\} = -2k_z \operatorname{Im} \left\{ \left\langle \widehat{p}'^* \widehat{w}' \right\rangle \right\} \quad (\text{B.29})$$

Appendix C

Comparison of spatially and temporally accelerating flows

C.1 Stokes first problem

Here, we discuss a method for approximating the wall shear stress to indicate how the temporal accelerations may behave in slightly different configurations. Previous studies have used Stokes' first problem to predict flow development during pre-transition [15, 12]. This model assumes that the perturbation mean velocity, $\bar{u}^\wedge(y, t) = \bar{u}(y, t) - \bar{u}(y, 0)$, follows the laminar solution for an impulsively accelerated flow from rest. This model of temporally accelerating flows is derived in Sundstrom and Cervantes [176], assuming that the change in turbulent transport during pre-transition is negligible. This model cannot capture the transition region but is capable of giving a good indication of the flow development in its early stages and is useful for assessing the matching decisions in section 7.1.2.

For an arbitrary centreline velocity profile [12], the perturbation flow, $\bar{u}^\wedge(y, t) = \bar{u}(y, t) - \bar{u}(y, 0)$ is given by

$$\bar{u}^\wedge(y, t) = \int_0^t \frac{dU_c}{d\tau} \operatorname{erfc} \left(y \sqrt{\frac{Re}{4(t-\tau)}} \right) d\tau. \quad (\text{C.1})$$

It can be easily shown that the perturbation wall shear stress, τ_w^\wedge , is given by the extended Stokes' solution:

$$\tau_w^\wedge = \frac{1}{Re} \frac{\partial \bar{u}^\wedge}{\partial y} = \int_0^t \frac{dU_c}{dt} \frac{1}{\sqrt{\pi Re(t-\tau)}} d\tau \quad (\text{C.2})$$

The total wall shear stress is given by $\tau_w = \tau_{w0} + \tau_w^\wedge$. The initial wall shear stress

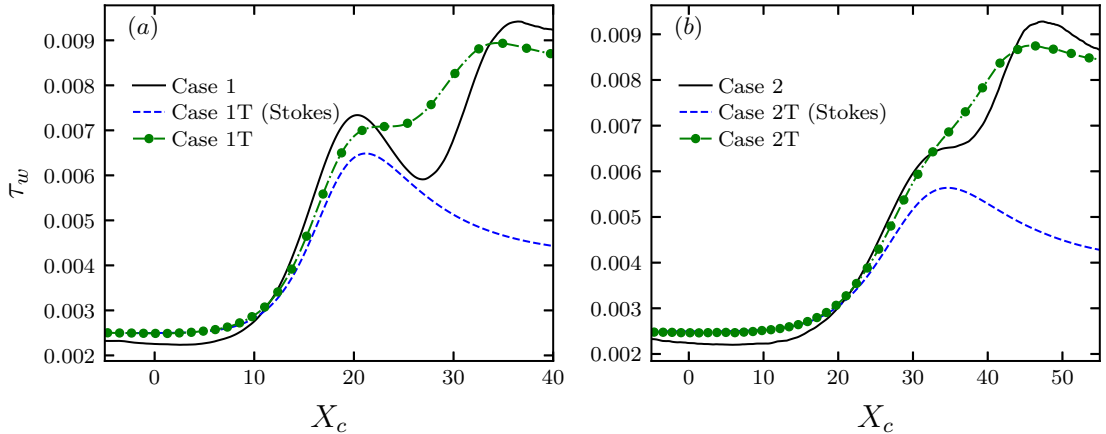


Figure C.1: Validation of the laminar model for pre-transition region. (a) Case 1. (b) Case 2.

is estimated from the following correlation for C_f in channel flows [269].

$$\sqrt{\frac{1}{C_f}} = a \log(2Re_b \sqrt{C_f}) + b, \quad (\text{C.3})$$

where $a = 3.53$ and $b = 1.78$. Note that in this chapter, we use Re_c rather than Re_b . Consequently, we approximate $Re_c = 1.13Re_b$, which was found to be reasonable based on existing channel flow data at low Reynolds numbers. Figure C.1 compares this approach with cases 1 and 2.

A reasonable agreement is observed between the model and the temporal accelerations in case 1, with a worse prediction in case 2. The underpredictions result mostly from neglecting changes to the turbulent transport in the laminar model, noting that, in reality, the eddy viscosity remains constant during pretransition. This is a good approximation in stronger acceleration but is less effective in weaker accelerations because the changes in the turbulent transport are more dynamically significant in the latter. Hence, the better agreement with case 1T than case 2T. The approximation of the initial τ_w is excellent.

C.1.1 Different reference heights

In this section, we consider the influence of choosing a reference height different from the boundary layer thickness. The primary motivation for this is to account for the reduction of the boundary layer thickness by selecting a reference height for the TBL that is smaller than the reference boundary layer thickness but still matching the

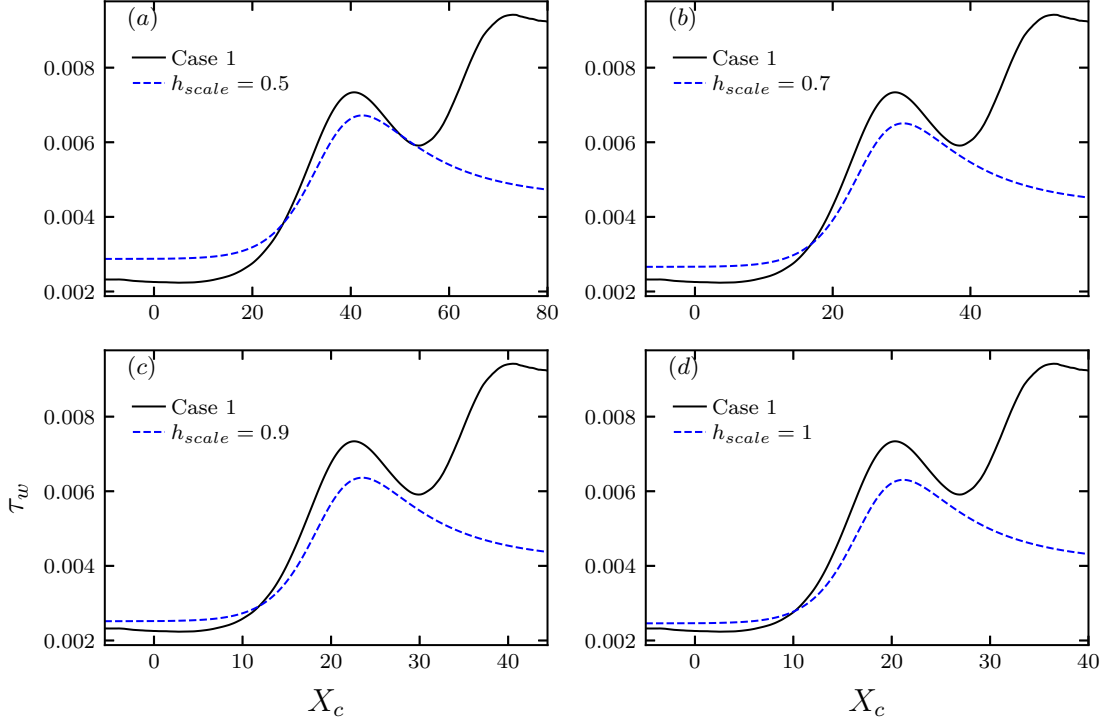


Figure C.2: Comparison of extended Stokes' solution for different reference heights.

accelerations in the same manner. The reference height is given by $h_{\text{ref}}\delta_{99,0}$. We can compare the development of the flows with different reference heights. This leads to the scalings compared with the method used in section 7.1.2:

$$t = \frac{t_{\text{ref}}}{h_{\text{ref}}} \quad X_c = \frac{X_{c,\text{ref}}}{h_{\text{ref}}}, \quad (\text{C.4})$$

with the resulting initial Reynolds number from equation (7.4) $Re_{c0} = h_{\text{ref}}Re_{c,\text{ref}}$. Substituting into equation (C.2)

$$\tau_w^\wedge \left(\frac{t_{\text{ref}}}{h_{\text{ref}}} \right) = \int_0^{t_{\text{ref}}} \frac{h_{\text{ref}}}{h_{\text{ref}}} \frac{dU_c}{d\tau_{\text{ref}}} \frac{1}{\sqrt{\pi \frac{h_{\text{ref}}}{h_{\text{ref}}} Re_{c,\text{ref}} (t_{\text{ref}} - \tau_{\text{ref}})}} d\tau_{\text{ref}}. \quad (\text{C.5})$$

This shows that the change in τ_w^\wedge should be the same as for the original case, albeit with the time stretched a factor $1/h_{\text{ref}}$. However, the different initial Reynolds numbers mean that τ_{w0} would be different. Nonetheless, the excursions would be the same initially, where the extended Stokes' solution is valid. A comparison of case 1 with different choices of h_{ref} is shown in figure C.2, confirming that the excursions of τ_w should be the same in the initial stages of the acceleration but lower values of h_{ref} have higher initial wall shear stress as their Reynolds numbers are lower.

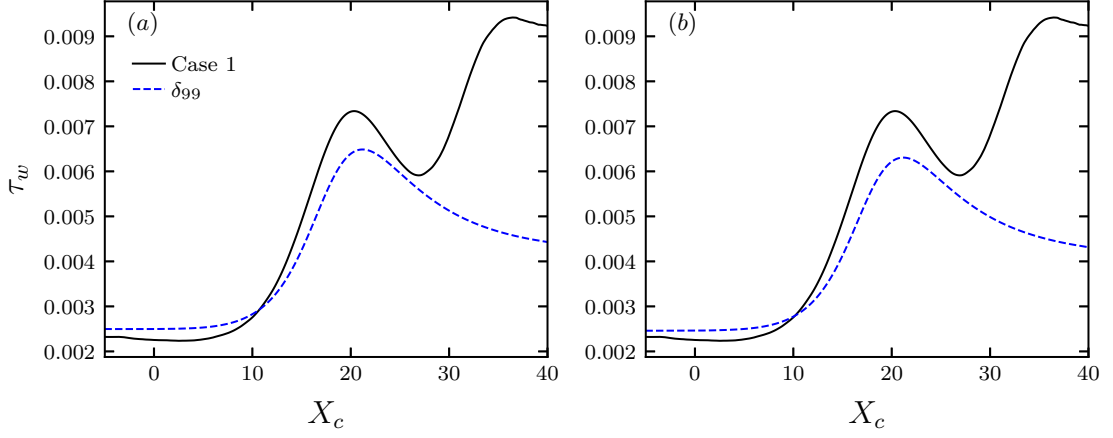


Figure C.3: Comparison of case 1 with laminar models using different definitions of the boundary layer thickness. (a) 99% thickness. (b) 99.5% thickness.

C.1.2 Different boundary layer thickness definitions

Figure C.3 compares the use of the 99% and 99.5% thicknesses for case 1 using the laminar model above, keeping all other elements of the comparison approach the same. For the 99% thickness $Re_c = 7773$ and for the 99.5% thickness $Re_c = 8380$. The results indicate that using a different definition of boundary layer thickness would not make a significant difference, with the figures barely distinguishable.

C.1.3 Different reference planes

Figure C.4 compares case 1 with laminar models at different reference planes upstream of the acceleration. Four different locations have been tested at $300\theta_0$, $350\theta_0$, $400\theta_0$, and $450\theta_0$ from the inlet plane, with the results indicating that the matched accelerations are not very sensitive to the location of the reference plane.

C.1.4 Different freestream velocities

As discussed in section 7.1.2, the mean velocity is not exactly constant in the freestream of a non-zero pressure gradient TBL due to significant non-uniformities in the pressure gradient. The pressure gradient can be decomposed into wall and non-uniform components. The wall-normal momentum equation is given by

$$\bar{u} \frac{\partial \bar{v}}{\partial x} + \bar{v} \frac{\partial \bar{v}}{\partial y} = -\frac{\partial \bar{p}}{\partial y} + \frac{1}{Re} \left[\frac{\partial^2 \bar{v}}{\partial x^2} + \frac{\partial^2 \bar{v}}{\partial y^2} \right] - \frac{\partial \overline{u'v'}}{\partial x} - \frac{\partial \overline{v'^2}}{\partial y} \quad (\text{C.6})$$

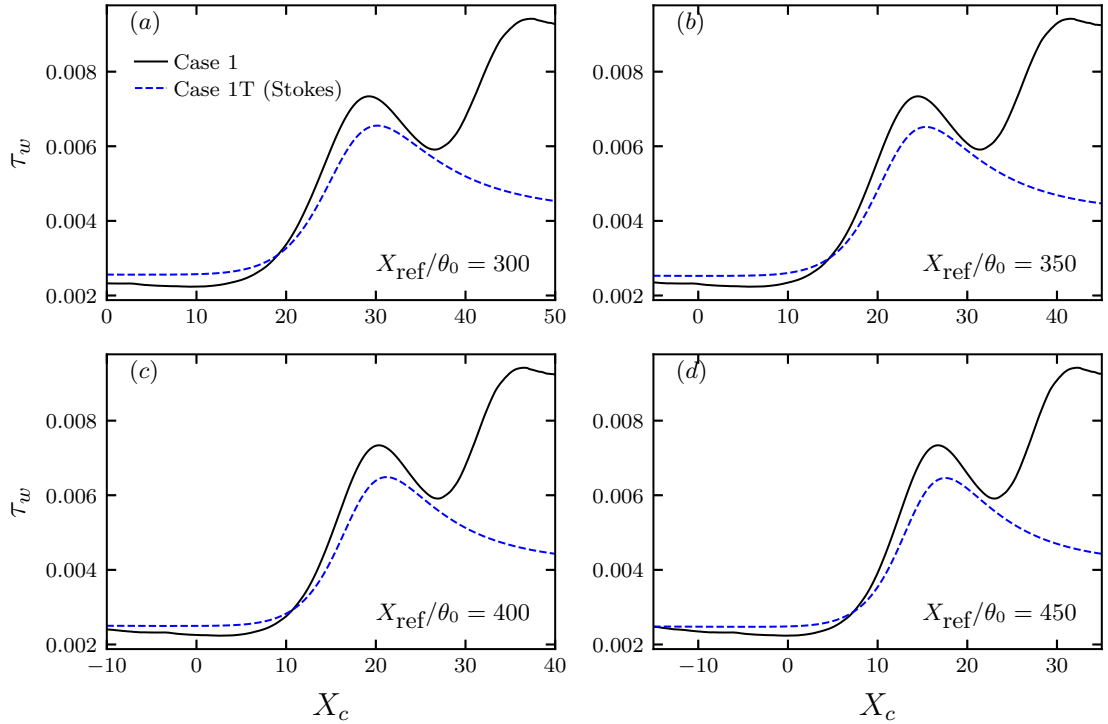


Figure C.4: Comparison of case 1 with different reference plane locations. (a) $x/\theta_0 = 300$, (b) $x/\theta_0 = 350$, (c) $x/\theta_0 = 400$, (d) $x/\theta_0 = 450$.

The non-uniform pressure is determined by integrating equation (C.6) from the wall

$$\bar{p}(x, y) - \bar{p}(x, 0) = - \int_0^y \left[\bar{u} \frac{\partial \bar{v}}{\partial x} + \bar{v} \frac{\partial \bar{v}}{\partial y} + \frac{\partial \overline{u'v'}}{\partial x} \right] dy - \bar{v}^2. \quad (\text{C.7})$$

The total streamwise pressure gradient is given by

$$\underbrace{-\frac{\partial \bar{p}(x, y)}{\partial x}}_{\mathcal{P}} = \underbrace{-\frac{\partial \bar{p}(x, 0)}{\partial x}}_{\mathcal{P}_w} + \underbrace{\frac{\partial}{\partial x} \left[\int_0^y \bar{u} \frac{\partial \bar{v}}{\partial x} + \bar{v} \frac{\partial \bar{v}}{\partial y} + \frac{\partial \overline{u'v'}}{\partial x} dy \right]}_{\mathcal{P}_{conv}} + \frac{\partial \bar{v}^2}{\partial x}. \quad (\text{C.8})$$

In ZPGTBLs, only the last term of \mathcal{P}_{conv} is significant. However, in FPGTBLs, the convection terms can become very large due to the high wall-normal mean velocities associated with flow contraction. The terms of equation (C.8) are shown in figure C.5 at two locations during pre-transition for case 1, alongside the perturbation pressure gradient, \mathcal{P}^\wedge from case 1T. Figure C.5 highlights how significant the freestream pressure distortions can be and how choosing a different definition of U_∞ has the potential to have a significant effect on the matched pressure gradients.

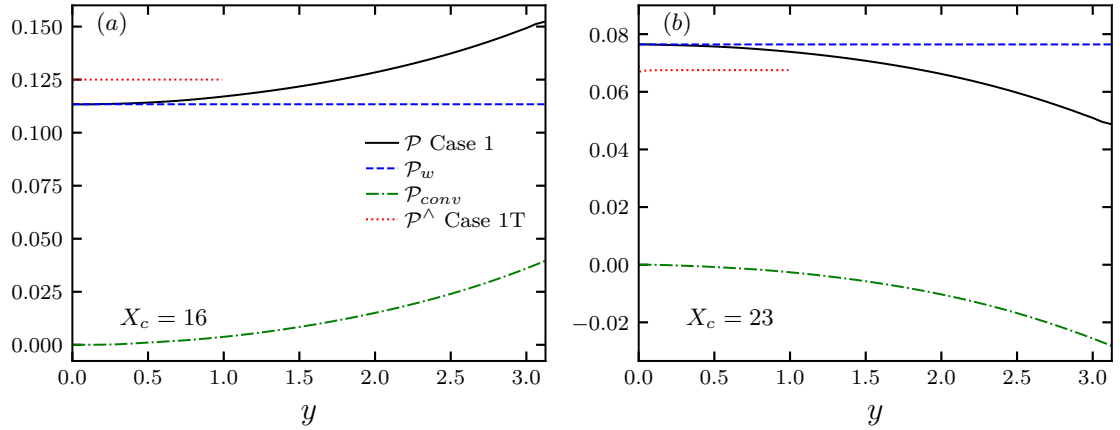


Figure C.5: Pressure gradient at two locations during pre-transition showing the terms of equation (C.8). (a) $X_c = 16$, (b) $X_c = 23$.

We can use the laminar model to understand the influence of choosing different definitions of U_∞ on the response of the wall shear stress. The method used in this chapter is $U_\infty(x) = \bar{u}(x, 1.1 \max(\delta_{99}))$. Figure C.6 shows case 1 compared with the laminar model for four different values of wall-normal distance. Note that the non-uniformity is much weaker in case 2 compared with case 1. We observe that the response of τ_w becomes stronger as the reference height becomes further from the wall, although temporal cases are still much weaker than case 1 and that the matching of the pressure gradient within the boundary layer in section 7.4 would be worse. This indicates that changing the freestream velocity definition is unlikely to change the general conclusions but may change the detailed flow development.

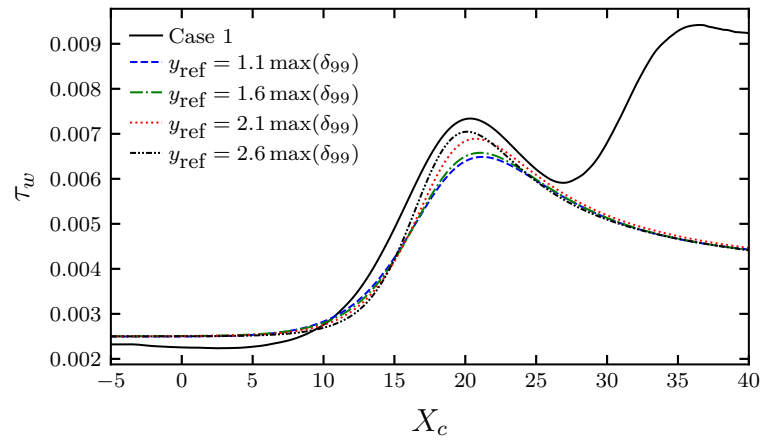


Figure C.6: Comparison of case 1 with different definitions of U_∞ computed using the extended Stokes' solution.

Bibliography

- [1] C.P. van Dam. The aerodynamic design of multi-element high-lift systems for transport airplanes. *Progress in Aerospace Sciences*, 38:101–144, 2 2002.
- [2] Sergio Hoyas and Javier Jiménez. Scaling of the velocity fluctuations in turbulent channels up to $Re_\tau = 2003$. *Physics of Fluids*, 18:011702, 2006.
- [3] Juan A. Sillero, Javier Jiménez, and Robert D. Moser. One-point statistics for turbulent wall-bounded flows at Reynolds numbers up to $\delta^+ \approx 2000$. *Physics of Fluids*, 25:105102, 10 2013.
- [4] Myoungkyu Lee and Robert D. Moser. Direct numerical simulation of turbulent channel flow up to $Re_\tau \approx 5200$. *Journal of Fluid Mechanics*, 774:395–415, 6 2015.
- [5] Matteo Bernardini, Sergio Pirozzoli, and Paolo Orlandi. Velocity statistics in turbulent channel flow up to $Re_\tau = 4000$. *Journal of Fluid Mechanics*, 742:171–191, 2014.
- [6] R. F. Blackwelder and R. E. Kaplan. On the wall structure of the turbulent boundary layer. *Journal of Fluid Mechanics*, 76:89–112, 1976.
- [7] J. Jeong, F. Hussain, W. Schoppa, and J. Kim. Coherent structures near the wall in a turbulent channel flow. *Journal of Fluid Mechanics*, 332:185–214, 1997.
- [8] John Kim. Physics and control of wall turbulence for drag reduction. *Philosophical Transactions of the Royal Society A: Mathematical, Physical and Engineering Sciences*, 369:1396–1411, 4 2011.
- [9] R. Narasimha and K. R. Sreenivasan. Relaminarization in highly accelerated turbulent boundary layers. *Journal of Fluid Mechanics*, 61:417–447, 1973.

- [10] Ugo Piomelli and Junlin Yuan. Numerical simulations of spatially developing, accelerating boundary layers. *Physics of Fluids*, 25:101304: 1–21, 2013.
- [11] S. Nagarajan, S. K. Lele, and J. H. Ferziger. Leading-edge effects in bypass transition. *Journal of Fluid Mechanics*, 572:471–504, 2 2007.
- [12] A. Mathur, S. Gorji, S. He, M. Seddighi, A. E. Vardy, T. O’Donoghue, and D. Pokrajac. Temporal acceleration of a turbulent channel flow. *Journal of Fluid Mechanics*, 835:471–490, 1 2018.
- [13] G. S. Karamanos and G. E. Karniadakis. A Spectral Vanishing Viscosity Method for Large-Eddy Simulations. *Journal of Computational Physics*, 163: 22–50, 9 2000.
- [14] Philipp Schlatter and Ramis Örlü. Assessment of direct numerical simulation data of turbulent boundary layers. *Journal of Fluid Mechanics*, 659:116–126, 9 2010.
- [15] S. He and M. Seddighi. Transition of transient channel flow after a change in Reynolds number. *Journal of Fluid Mechanics*, 764:395–427, 2 2015.
- [16] Mark P. Simens, Javier Jiménez, Sergio Hoyas, and Yoshinori Mizuno. A high-resolution code for turbulent boundary layers. *Journal of Computational Physics*, 228:4218–4231, 6 2009.
- [17] Philippe R. Spalart. Direct simulation of a turbulent boundary layer up to $R_\theta = 1410$. *Journal of Fluid Mechanics*, 187:61–98, 1988.
- [18] L. P. Purtell, P. S. Klebanoff, and F.T. Buckley. Turbulent boundary layer at low Reynolds number. *Physics of Fluids*, 24:802–811, 5 1981.
- [19] A. J. Smits, N. Matheson, and P. N. Joubert. Low-Reynolds-Number Turbulent Boundary Layers in Zero and Favorable Pressure Gradients. *Journal of Ship Research*, 27:147–157, 9 1983.
- [20] Kapil A. Chauhan, Peter A. Monkewitz, and Hassan M. Nagib. Criteria for assessing experiments in zero pressure gradient boundary layers. *Fluid Dynamics Research*, 41:021404, 3 2009.
- [21] W. W. Willmarth and S. S. Lu. Structure of the Reynolds stress near the wall. *Journal of Fluid Mechanics*, 55:65–92, 9 1972.

- [22] V. C. Patel. Calibration of the Preston tube and limitations on its use in pressure gradients. *Journal of Fluid Mechanics*, 23:185–208, 1965.
- [23] R. J. Volino, M. P. Schultz, and K. A. Flack. Turbulence structure in rough- and smooth-wall boundary layers. *Journal of Fluid Mechanics*, 592:263–293, 12 2007.
- [24] M. Falcone and S. He. A spatially accelerating turbulent flow with longitudinally contracting walls. *Journal of Fluid Mechanics*, 945:A23, 8 2022.
- [25] M. Falcone and S. He. The evolution of turbulence in spatially accelerating turbulent boundary layers. *To be submitted*, 2024.
- [26] M. Falcone and S. He. A comparison of spatially and temporally accelerating flows. *To be submitted*, 2024.
- [27] Matthew Falcone and Shuisheng He. A Spatially Accelerating Turbulent Flow with Longitudinally Moving Walls. In *Progress in Turbulence IX*, pages 109–114. Springer, 2021.
- [28] Matthew A Falcone and Shuisheng He. A comparison of spatial and temporal acceleration in turbulent channel flows. *12th International Symposium on Turbulence and Shear Flow Phenomena (TSFP12)*, pages 1–6, 2022.
- [29] Long P. Yip, Paul M.H.W. Vijgen, Jay D. Hardin, and C. P. van Dam. In-Flight pressure measurements on a subsonic transport high-lift wing section. *Journal of Aircraft*, 32:529–538, 1995.
- [30] A. Séraudie, J. Perraud, and F. Moens. Transition measurement and analysis on a swept wing in high lift configuration. *Aerospace Science and Technology*, 7:569–576, 12 2003.
- [31] Jean Perraud, Alain Séraudie, and Frédéric Moens. Transition on a High-Lift Swept Wing in the European Project EUROLIFT. *Journal of Aircraft*, 41: 1183–1190, 9 2004.
- [32] P. R. Viswanath, R. Mukund, R. Narasimha, and J. D. Crouch. Relaminarization on Swept Leading Edges Under High-Lift Conditions. *AIAA Journal*, 44: 2621–2629, 11 2006.

- [33] R. Mukund, P. R. Viswanath, R. Narasimha, A. Prabhu, and J. D. Crouch. Relaminarization in highly favourable pressure gradients on a convex surface. *Journal of Fluid Mechanics*, 566:97–115, 2006.
- [34] Robert Edward Mayle. The Role of Laminar-Turbulent Transition in Gas Turbine Engines. In *Proceedings of the ASME Turbo Expo*, volume 5, pages 1–28. American Society of Mechanical Engineers Digital Collection, 3 1991.
- [35] Pasquale Cardamone. *Aerodynamic Optimisation of Highly Loaded Turbine Cascade Blades for Heavy Duty Gas Turbine Applications*. PhD thesis, Universität der Bundeswehr München, 2 2006.
- [36] H. P. Hodson. Boundary Layer and Loss Measurements on the Rotor of an Axial-Flow Turbine. *Journal of Engineering for Gas Turbines and Power*, 106:391–399, 4 1984.
- [37] H. D. Ammari, N. Hay, and D. Lampard. Effect of Acceleration on the Heat Transfer Coefficient on a Film-Cooled Surface. *Journal of Turbomachinery*, 113:464–471, 7 1991.
- [38] Riccardo Balin and K. E. Jansen. Direct numerical simulation of a turbulent boundary layer over a bump with strong pressure gradients. *Journal of Fluid Mechanics*, 918:14, 2021.
- [39] K. R. Sreenivasan. Laminarescent, relaminarizing and retransitional flows. *Acta Mechanica*, 44:1–48, 1982.
- [40] R. Narasimha and K.R. Sreenivasan. Relaminarization of Fluid Flows. *Advances in Applied Mechanics*, 19:221–309, 1 1979.
- [41] M. A. Badri Narayanan. An experimental study of reverse transition in two-dimensional channel flow. *Journal of Fluid Mechanics*, 31:609–623, 2 1968.
- [42] Emily L. Manchester, Selene Pirola, Mohammad Yousuf Salmasi, Declan P. O’Regan, Thanos Athanasiou, and Xiao Yun Xu. Analysis of Turbulence Effects in a Patient-Specific Aorta with Aortic Valve Stenosis. *Cardiovascular Engineering and Technology*, 12:438–453, 8 2021.
- [43] S. He and M. Seddighi. Turbulence in transient channel flow. *Journal of Fluid Mechanics*, 715:60–102, 1 2013.

- [44] M. Seddighi, S. He, A. E. Vardy, and P. Orlandi. Direct Numerical Simulation of an Accelerating Channel Flow. *Flow, Turbulence and Combustion*, 92:473–502, 1 2014.
- [45] Seo Yoon Jung and Kyoungyoun Kim. Transient behaviors of wall turbulence in temporally accelerating channel flows. *International Journal of Heat and Fluid Flow*, 67:13–26, 10 2017.
- [46] D. Greenblatt and E. A. Moss. Pipe-flow relaminarization by temporal acceleration. *Physics of Fluids*, 11:3478–3481, 11 1999.
- [47] David Greenblatt and Edward A. Moss. Rapid temporal acceleration of a turbulent pipe flow. *Journal of Fluid Mechanics*, 514:65–75, 9 2004.
- [48] S. C. Mangavelli and J. Yuan. Effects of form-induced velocity in rough-wall turbulent channel flows. *Journal of Turbulence*, pages 1–22, 2022.
- [49] J. Yuan and U. Piomelli. Numerical simulation of a spatially developing accelerating boundary layer over roughness. *Journal of Fluid Mechanics*, 780:192–214, 2015.
- [50] Alexander J. Smits and Ivan Marusic. Wall-bounded turbulence. *Physics Today*, 66:25–30, 9 2013.
- [51] G K Batchelor. *An Introduction to Fluid Dynamics*. Cambridge University Press, 1967.
- [52] Ronald L. Panton. Overview of the self-sustaining mechanisms of wall turbulence. *Progress in Aerospace Sciences*, 37:341–383, 5 2001.
- [53] S K Robinson. Coherent Motions in the Turbulent Boundary Layer. *Annual Review of Fluid Mechanics*, 23:601–639, 1 1991.
- [54] Jinhee Jeong and Fazle Hussain. On the identification of a vortex. *Journal of Fluid Mechanics*, 285:69, 2 1995.
- [55] J C R Hunt, A A Wray, and P Moin. Eddies, Streams, and Convergence Zones in Turbulent Flows. *Proceedings of the Summer Program 1988, Center for Turbulence Research*, 1988.

- [56] J. Zhou, R. J. Adrian, S. Balachandar, and T. M. Kendall. Mechanisms for generating coherent packets of hairpin vortices in channel flow. *Journal of Fluid Mechanics*, 387:353–396, 5 1999.
- [57] C. B. Millikan. A critical discussion of turbulent flow in channels and circular tubes. *Proc. 5th Int. Congress on Applied Mechanics (Cambridge, MA, 1938)*, pages 386–392, 1938.
- [58] Ronald L. Panton. Review of Wall Turbulence as Described by Composite Expansions. *Applied Mechanics Reviews*, 58:1–36, 1 2005.
- [59] Javier Jiménez and Robert D. Moser. What are we learning from simulating wall turbulence? *Philosophical Transactions of the Royal Society A: Mathematical, Physical and Engineering Sciences*, 365:715–732, 3 2007.
- [60] Hassan M. Nagib and Kapil A. Chauhan. Variations of von Kármán coefficient in canonical flows. *Physics of Fluids*, 20:101518, 10 2008.
- [61] Stephen B Pope. *Turbulent Flows*. Cambridge University Press, 2000.
- [62] Donald Coles. The law of the wake in the turbulent boundary layer. *Journal of Fluid Mechanics*, 1:191–226, 1956.
- [63] James M. Wallace. Quadrant Analysis in Turbulence Research: History and Evolution. *Annual Review of Fluid Mechanics*, 48:131–158, 1 2016.
- [64] Javier Jiménez. Coherent structures in wall-bounded turbulence. *Journal of Fluid Mechanics*, 842:P1, 5 2018.
- [65] S. J. Kline, W. C. Reynolds, F. A. Schraub, and P. W. Runstadler. The structure of turbulent boundary layers. *Journal of Fluid Mechanics*, 30:741–773, 12 1967.
- [66] Javier Jiménez, Juan C. del Álamo, and Oscar Flores. The large-scale dynamics of near-wall turbulence. *Journal of Fluid Mechanics*, 505:179–199, 4 2004.
- [67] Ron F. Blackwelder and Helmut Eckelmann. Streamwise vortices associated with the bursting phenomenon. *Journal of Fluid Mechanics*, 94:577–594, 1979.
- [68] Fabian Waleffe. On a self-sustaining process in shear flows. *Physics of Fluids*, 9:883, 6 1997.

- [69] T. Ellingsen and E. Palm. Stability of linear flow. *Physics of Fluids*, 18:487–488, 9 1975.
- [70] M. T. Landahl. A note on an algebraic instability of inviscid parallel shear flows. *Journal of Fluid Mechanics*, 98:243–251, 1980.
- [71] Lloyd N. Trefethen, Anne E. Trefethen, Satish C. Reddy, and Tobin A. Driscoll. Hydrodynamic stability without eigenvalues. *Science*, 261:578–584, 7 1993.
- [72] Peter J. Schmid. Nonmodal Stability Theory. *Annual Review of Fluid Mechanics*, 39:129–162, 12 2006.
- [73] Kathryn M. Butler and Brian F. Farrell. Three-dimensional optimal perturbations in viscous shear flow. *Physics of Fluids A: Fluid Dynamics*, 4:1637, 6 1992.
- [74] Gregory Pujals, Manuel García-Villalba, Carlo Cossu, and Sebastien Depardon. A note on optimal transient growth in turbulent channel flows. *Physics of Fluids*, 21:44, 1 2009.
- [75] Juan C. del Álamo and Javier Jiménez. Linear energy amplification in turbulent channels. *Journal of Fluid Mechanics*, 559:205–213, 2006.
- [76] W. Schoppa and F. Hussain. Coherent structure generation in near-wall turbulence. *Journal of Fluid Mechanics*, 453:57–108, 2002.
- [77] Matteo de Giovanetti, Hyung Jin Sung, and Yongyun Hwang. Streak instability in turbulent channel flow: the seeding mechanism of large-scale motions. *Journal of Fluid Mechanics*, 832:483–513, 12 2017.
- [78] Javier Jiménez. The streaks of wall-bounded turbulence need not be long. *Journal of Fluid Mechanics*, 945:R3, 8 2022.
- [79] Javier Jiménez and Alfredo Pinelli. The autonomous cycle of near-wall turbulence. *Journal of Fluid Mechanics*, 389:335–359, 6 1999.
- [80] Yongyun Hwang. Near-wall turbulent fluctuations in the absence of wide outer motions. *Journal of Fluid Mechanics*, 723:264–288, 2013.
- [81] Joseph Sternberg. The Transition From A Turbulent To A Laminar Boundary Layer. Technical report, Ballistics Research Laboratory, 1954.

- [82] D. G. Wilson and J. A. Pope. Convective Heat Transfer to Gas Turbine Blade Surfaces. *Proceedings of the Institution of Mechanical Engineers*, 168:861–876, 6 1954.
- [83] B E Launder. The turbulent boundary layer in a strongly negative pressure gradient. *MIT Gas Turbine Laboratory TR 71*, 1963.
- [84] B. E. Launder. Laminarization of the Turbulent Boundary Layer in a Severe Acceleration. *Journal of Applied Mechanics*, 31:707–708, 12 1964.
- [85] B. E. Launder. *Laminarization of the Turbulent Boundary Layer by Acceleration*. PhD thesis, MIT Gas Turbine Laboratory, 1964.
- [86] F A Schraub and S J Kline. A Study of the Structure of the Turbulent Boundary Layer with and without Longitudinal Pressure Gradients. Technical report, Stanford university, Ca. Thermosciences Div., 1965.
- [87] C. Bourassa and F. O. Thomas. An experimental investigation of a highly accelerated turbulent boundary layer. *Journal of Fluid Mechanics*, 634:359–404, 2009.
- [88] M. B. Jones, Ivan Marusic, and A. E. Perry. Evolution and structure of sink-flow turbulent boundary layers. *Journal of Fluid Mechanics*, 428:1–27, 2 2001.
- [89] B. E. Launder and W. P. Jones. Sink flow turbulent boundary layers. *Journal of Fluid Mechanics*, 38:817–831, 10 1969.
- [90] W. P. Jones and B. E. Launder. Some properties of sink-flow turbulent boundary layers. *Journal of Fluid Mechanics*, 56:337–351, 11 1972.
- [91] B E Launder and H S Stinchcombe. Non-normal similar boundary layers. *Imperial College (London, England) Mechanical Engineering Department TWF/TN/21*, 1967.
- [92] M. A. Badri Narayanan and V. Ramjee. On the criteria for reverse transition in a two-dimensional boundary layer flow. *Journal of Fluid Mechanics*, 35: 225–241, 1 1969.
- [93] H. H. Fernholz and D. Warnack. The effects of a favourable pressure gradient and of the Reynolds number on an incompressible axisymmetric turbulent boundary layer. Part 1. The turbulent boundary layer. *Journal of Fluid Mechanics*, 359:329–356, 3 1998.

- [94] Alessandro Talamelli, Nicola Fornaciari, K Johan A Westin, and P Henrik Alfredsson. Experimental investigation of streaky structures in a relaminarizing boundary layer. *Journal of Turbulence*, 3:27–29, 2001.
- [95] P.M. Moretti and W.M. Kays. Heat transfer to a turbulent boundary layer with varying free-stream velocity and varying surface temperature—an experimental study. *International Journal of Heat and Mass Transfer*, 8:1187–1202, 9 1965.
- [96] L. H. Back, P. F. Massier, and H. L. Gier. Convective heat transfer in a convergent-divergent nozzle. *International Journal of Heat and Mass Transfer*, 7:549–568, 5 1964.
- [97] Ron F. Blackwelder and Leslie S. G. Kovasznay. Large-scale motion of a turbulent boundary layer during relaminarization. *Journal of Fluid Mechanics*, 53: 61–83, 5 1972.
- [98] V. C. Patel and M. R. Head. Reversion of turbulent to laminar flow. *Journal of Fluid Mechanics*, 34:371–392, 11 1968.
- [99] Hermann Schlichting and Klaus Gersten. *Boundary-layer theory*. Springer, 2000.
- [100] Shivsai Ajit Dixit and O. N. Ramesh. Pressure-gradient-dependent logarithmic laws in sink flow turbulent boundary layers. *Journal of Fluid Mechanics*, 615: 445–475, 2008.
- [101] Raúl Bayoán Cal and Luciano Castillo. Similarity analysis of favorable pressure gradient turbulent boundary layers with eventual quasilaminarization. *Physics of Fluids*, 20:105106, 10 2008.
- [102] D. Warnack and H. H. Fernholz. The effects of a favourable pressure gradient and of the Reynolds number on an incompressible axisymmetric turbulent boundary layer. Part 2. The boundary layer with relaminarization. *Journal of Fluid Mechanics*, 359:357–381, 3 1998.
- [103] M. P. Escudier, A. Abdel-Hameed, M. W. Johnson, and C. J. Sutcliffe. Laminarisation and re-transition of a turbulent boundary layer subjected to favourable pressure gradient. *Experiments in Fluids*, 25:491–502, 10 1998.

- [104] Zambri Harun, Jason P. Monty, Romain Mathis, and Ivan Marusic. Pressure gradient effects on the large-scale structure of turbulent boundary layers. *Journal of Fluid Mechanics*, 715:477–498, 1 2013.
- [105] Pranav Joshi, Xiaofeng Liu, and Joseph Katz. Effect of mean and fluctuating pressure gradients on boundary layer turbulence. *Journal of Fluid Mechanics*, 748:36–84, 2014.
- [106] M. A. Badri Narayanan, S. Rajagopalan, and R. Narasimha. Experiments on the fine structure of turbulence. *Journal of Fluid Mechanics*, 80:237–257, 1977.
- [107] D. S. Finnicum and T. J. Hanratty. Effect of favorable pressure gradients on turbulent boundary layers. *AIChE Journal*, 34:529–540, 4 1988.
- [108] H. T. Kim, S. J. Kline, and W. C. Reynolds. The production of turbulence near a smooth wall in a turbulent boundary layer. *Journal of Fluid Mechanics*, 50:133–160, 11 1971.
- [109] Philippe R. Spalart. Numerical study of sink-flow boundary layers. *Journal of Fluid Mechanics*, 172:307–328, 11 1986.
- [110] Ugo Piomelli, Elias Balaras, and Andrea Pascarelli. Turbulent structures in accelerating boundary layers. *Journal of Turbulence*, 1:N1, 1 2000.
- [111] Corey Bourassa. *An Experimental Investigation of an Accelerated Turbulent Boundary Layer*. PhD thesis, University of Notre Dame, 5 2006.
- [112] Masashi Ichimiya, Ikuo Nakamura, and Shintaro Yamashita. Properties of a relaminarizing turbulent boundary layer under a favorable pressure gradient. *Experimental Thermal and Fluid Science*, 17:37–48, 5 1998.
- [113] R. E. Falco. Coherent motions in the outer region of turbulent boundary layers. *Physics of Fluids*, 20:S124, 8 1977.
- [114] F. W. Chambers, H. D. Murphy, and D. M. McEligot. Laterally converging flow. Part 2. Temporal wall shear stress. *Journal of Fluid Mechanics*, 127:403–428, 2 1983.
- [115] H. D. Murphy, F. W. Chambers, and D. M. McEligot. Laterally converging flow. Part 1. Mean flow. *Journal of Fluid Mechanics*, 127:379–401, 2 1983.

- [116] Donald M. McEligot and Helmut Eckelmann. Laterally converging duct flows. Part 3. Mean turbulence structure in the viscous layer. *Journal of Fluid Mechanics*, 549:25–59, 2 2006.
- [117] Donald M. McEligot, Robert S. Brodkey, and Helmut Eckelmann. Laterally converging duct flows. Part 4. Temporal behaviour in the viscous layer. *Journal of Fluid Mechanics*, 634:433–461, 2009.
- [118] Shivsai Ajit Dixit and O. N. Ramesh. Large-scale structures in turbulent and reverse-transitional sink flow boundary layers. *Journal of Fluid Mechanics*, 649:233–273, 4 2010.
- [119] J. Yuan and U. Piomelli. Numerical simulations of sink-flow boundary layers over rough surfaces. *Physics of Fluids*, 26:015113, 2014.
- [120] Giuseppe de Prisco, Anthony Keating, and Ugo Piomelli. Large-Eddy Simulation of Accelerating Boundary Layers. In *45th AIAA Aerospace Sciences Meeting and Exhibit*. American Institute of Aeronautics and Astronautics, 1 2007.
- [121] Pascal Bader, Manuel Pschernig, Wolfgang Sanz, Jakob Woisetschläger, Franz Heitmeir, Walter Meile, and Günter Brenn. Experimental Investigation of Boundary Layer Relaminarization in Accelerated Flow. *Journal of Fluids Engineering, Transactions of the ASME*, 140, 8 2018.
- [122] P. Bradshaw. A note on reverse transition. *Journal of Fluid Mechanics*, 35:387–390, 1 1969.
- [123] Moon Joo Lee, John Kim, and Parviz Moin. Structure of turbulence at high shear rate. *Journal of Fluid Mechanics*, 216:561–583, 1990.
- [124] G. B. Schubauer and H. K. Skramstad. Laminar Boundary-Layer Oscillations and Stability of Laminar Flow. *Journal of the Aeronautical Sciences*, 14:69–78, 8 1947.
- [125] P G Drazin and W H Reid. *Hydrodynamic Stability*. Cambridge University Press, 2004.
- [126] H. L. Dryden. Airflow in the boundary layer near a plate. In *NACA Rep. 562*. National Advisory Committee for Aeronautics, 1936.

- [127] G. I. Taylor. Some recent developments in the study of turbulence. In *Fifth Intl Congress for Applied Mathematics*, pages 294–310. Wiley, 1939.
- [128] M. V. Morkovin. Bypass transition to turbulence and research Desiderata. In *In NASA. Lewis Research Center Transition in Turbines*, pages 161–204, 7 1985.
- [129] P S Klebanoff. Effect of free-stream turbulence on a laminar boundary layer. In *Bulletin of the American Physical Society*, volume 16, page 1323, 1971.
- [130] J. M. Kendall. EXPERIMENTAL STUDY OF DISTURBANCES PRODUCED IN A PRE-TRANSITIONAL LAMINAR BOUNDARY LAYER BY WEAK FREESTREAM TURBULENCE. *American Society of Mechanical Engineers (Paper)*, 1985.
- [131] R. G. Jacobs and P. A. Durbin. Simulations of bypass transition. *Journal of Fluid Mechanics*, 428:185–212, 2 2001.
- [132] Paul A. Durbin. Perspectives on the Phenomenology and Modeling of Boundary Layer Transition. *Flow, Turbulence and Combustion*, 99:1–23, 7 2017.
- [133] J. C.R. Hunt and P. A. Durbin. Perturbed vortical layers and shear sheltering. *Fluid Dynamics Research*, 24:375–404, 6 1999.
- [134] K. P. Nolan and E. J. Walsh. Particle image velocimetry measurements of a transitional boundary layer under free stream turbulence. *Journal of Fluid Mechanics*, 702:215–238, 7 2012.
- [135] Luca Brandt. The lift-up effect: The linear mechanism behind transition and turbulence in shear flows. *European Journal of Mechanics - B/Fluids*, 47:80–96, 9 2014.
- [136] David W. Wundrow and M. E. Goldstein. Effect on a laminar boundary layer of small-amplitude streamwise vorticity in the upstream flow. *Journal of Fluid Mechanics*, 426:229–262, 1 2001.
- [137] K. J.A. Westin, A. A. Bakchinov, V. V. Kozlov, and P. H. Alfredsson. Experiments on localized disturbances in a flat plate boundary layer. Part 1. The receptivity and evolution of a localized free stream disturbance. *European Journal of Mechanics - B/Fluids*, 17:823–846, 11 1998.

- [138] K. J.A. Westin, A. V. Boiko, B. G.B. Klingmann, V. V. Kozlov, and P. H. Alfredsson. Experiments in a boundary layer subjected to free stream turbulence. Part 1. Boundary layer structure and receptivity. *Journal of Fluid Mechanics*, 281:193–218, 1994.
- [139] M. Matsubara and P. H. Alfredsson. Disturbance growth in boundary layers subjected to free-stream turbulence. *Journal of Fluid Mechanics*, 430:149–168, 3 2001.
- [140] Paul Andersson, Martin Berggren, and Dan S. Henningson. Optimal disturbances and bypass transition in boundary layers. *Physics of Fluids*, 11:134–150, 1 1999.
- [141] Paolo Luchini. Reynolds-number-independent instability of the boundary layer over a flat surface: optimal perturbations. *Journal of Fluid Mechanics*, 404:289–309, 2 2000.
- [142] Pierre Ricco, Edmond J. Walsh, Flavio Brighenti, and Donald M. McEligot. Growth of boundary-layer streaks due to free-stream turbulence. *International Journal of Heat and Fluid Flow*, 61:272–283, 10 2016.
- [143] S. J. Leib, David W. Wundrow, and M. E. Goldstein. Effect of free-stream turbulence and other vortical disturbances on a laminar boundary layer. *Journal of Fluid Mechanics*, 380:169–203, 2 1999.
- [144] Xiaohua Wu and Parviz Moin. Direct numerical simulation of turbulence in a nominally zero-pressure-gradient flat-plate boundary layer. *Journal of Fluid Mechanics*, 630:5–41, 2009.
- [145] D. Lengani, D. Simoni, J. O. Pralits, K. Đurović, L. de Vincentiis, D. S. Henningson, and A. Hanifi. On the receptivity of low-pressure turbine blades to external disturbances. *Journal of Fluid Mechanics*, 937:A36, 4 2022.
- [146] Victor Ovchinnikov, Meelan M. Choudhari, and Ugo Piomelli. Numerical simulations of boundary-layer bypass transition due to high-amplitude free-stream turbulence. *Journal of Fluid Mechanics*, 613:135–169, 10 2008.
- [147] Xiaohua Wu. New Insights into Turbulent Spots. *Annual Review of Fluid Mechanics*, 55:45–75, 1 2023.

- [148] Luca Brandt, Philipp Schlatter, and Dan S. Henningson. Transition in boundary layers subject to free-stream turbulence. *Journal of Fluid Mechanics*, 517: 167–198, 10 2004.
- [149] Luca Brandt and H. C. de Lange. Streak interactions and breakdown in boundary layer flows. *Physics of Fluids*, 20:024107, 2008.
- [150] Philipp Schlatter, Luca Brandt, H. C. de Lange, and Dan S. Henningson. On streak breakdown in bypass transition. *Physics of Fluids*, 20:101505, 10 2008.
- [151] Ming Dong and Xuesong Wu. On continuous spectra of the Orr–Sommerfeld/Squire equations and entrainment of free-stream vortical disturbances. *Journal of Fluid Mechanics*, 732:616–659, 10 2013.
- [152] Masahito Asai, Masayuki Minagawa, and Michio Nishioka. The instability and breakdown of a near-wall low-speed streak. *Journal of Fluid Mechanics*, 455: 289–314, 3 2002.
- [153] J. Mans, E. C. Kadijk, H. C. de Lange, and A. A. Van Steenhoven. Breakdown in a boundary layer exposed to free-stream turbulence. *Experiments in Fluids*, 39:1071–1083, 12 2005.
- [154] Paul Andersson, Luca Brandt, Alessandro Bottaro, and Dan S. Henningson. On the breakdown of boundary layer streaks. *Journal of Fluid Mechanics*, 428: 29–60, 2001.
- [155] Nicholas J. Vaughan and Tamer A. Zaki. Stability of zero-pressure-gradient boundary layer distorted by unsteady Klebanoff streaks. *Journal of Fluid Mechanics*, 681:116–153, 2011.
- [156] Tamer A. Zaki. From Streaks to Spots and on to Turbulence: Exploring the Dynamics of Boundary Layer Transition. *Flow, Turbulence and Combustion*, 91:451–473, 10 2013.
- [157] M. J. P. Hack and T. A. Zaki. Streak instabilities in boundary layers beneath free-stream turbulence. *Journal of Fluid Mechanics*, 741:280–315, 2 2014.
- [158] J. Mans, H. C. de Lange, and A. A. van Steenhoven. Sinuous breakdown in a flat plate boundary layer exposed to free-stream turbulence. *Physics of Fluids*, 19, 8 2007.

- [159] G. Balamurugan and A. C. Mandal. Experiments on localized secondary instability in bypass boundary layer transition. *Journal of Fluid Mechanics*, 817: 217–263, 4 2017.
- [160] Domhnaill Hernon, Edmond J. Walsh, and Donald M. McEligot. Experimental investigation into the routes to bypass transition and the shear-sheltering phenomenon. *Journal of Fluid Mechanics*, 591:461–479, 11 2007.
- [161] K. P. Nolan, E. J. Walsh, and D. M. McEligot. Quadrant analysis of a transitional boundary layer subject to free-stream turbulence. *Journal of Fluid Mechanics*, 658:310–335, 9 2010.
- [162] Peter R Voke and Zhiyin Yang. Numerical study of bypass transition . *Physics of Fluids*, 7:2256–2264, 1995.
- [163] M. F. Blair. Boundary-Layer Transition in Accelerating Flows With Intense Freestream Turbulence: Part 2—The Zone of Intermittent Turbulence. *Journal of Fluids Engineering*, 114:322–332, 9 1992.
- [164] Joshua R. Brinkerhoff and Metin I. Yaras. Numerical investigation of transition in a boundary layer subjected to favourable and adverse streamwise pressure gradients and elevated free stream turbulence. *Journal of Fluid Mechanics*, 781: 52–86, 10 2015.
- [165] Kevin P. Nolan and Tamer A. Zaki. Conditional sampling of transitional boundary layers in pressure gradients. *Journal of Fluid Mechanics*, 728:306–339, 8 2013.
- [166] Olaf Marxen and Tamer A. Zaki. Turbulence in intermittent transitional boundary layers and in turbulence spots. *Journal of Fluid Mechanics*, 860:350–383, 2 2019.
- [167] E. B. Shuy. Wall shear stress in accelerating and decelerating turbulent pipe flows. *Journal of Hydraulic Research*, 34:173–183, 1996.
- [168] Naoki Shiibara, Hajime Nakamura, and Shunsuke Yamada. Unsteady characteristics of turbulent heat transfer in a circular pipe upon sudden acceleration and deceleration of flow. *International Journal of Heat and Mass Transfer*, 113: 490–501, 10 2017.

- [169] Hajime Nakamura, Riku Saito, and Shunsuke Yamada. Delay in response of turbulent heat transfer against acceleration or deceleration of flow in a pipe. *International Journal of Heat and Fluid Flow*, 85:108661, 10 2020.
- [170] Toshiro Maruyama, Toshiaki Kuribayashi, and Tokuro Mizushima. THE STRUCTURE OF THE TURBULENCE IN TRANSIENT PIPE FLOWS. *Journal of Chemical Engineering of Japan*, 9:431–439, 12 1976.
- [171] S. He and J. D. Jackson. A study of turbulence under conditions of transient flow in a pipe. *Journal of Fluid Mechanics*, 408:1–38, 4 2000.
- [172] Akshat Mathur, Mehdi Seddighi, and Shuisheng He. Transition of Transient Channel Flow with High Reynolds Number Ratios. *Entropy*, 20:375, 5 2018.
- [173] L. R. Joel Sundstrom and Michel J. Cervantes. Laminar similarities between accelerating and decelerating turbulent flows. *International Journal of Heat and Fluid Flow*, 71:13–26, 6 2018.
- [174] Byron Guerrero, Martin F. Lambert, and Rey C. Chin. Transient dynamics of accelerating turbulent pipe flow. *Journal of Fluid Mechanics*, 917:A43, 6 2021.
- [175] Koji Fukagata, Kaoru Iwamoto, and Nobuhide Kasagi. Contribution of Reynolds stress distribution to the skin friction in wall-bounded flows. *Physics of Fluids*, 14:L73–L76, 11 2002.
- [176] L. R. Joel Sundstrom and Michel J. Cervantes. The self-similarity of wall-bounded temporally accelerating turbulent flows. *Journal of Turbulence*, 19:49–60, 1 2018.
- [177] S. He, C. Ariyaratne, and A. E. Vardy. Wall shear stress in accelerating turbulent pipe flow. *Journal of Fluid Mechanics*, 685:440–460, 10 2011.
- [178] S. He and C. Ariyaratne. Wall Shear Stress in the Early Stage of Unsteady Turbulent Pipe Flow. *Journal of Hydraulic Engineering*, 137:606–610, 5 2011.
- [179] B. S. Oluwadare. *Experimental Study of Turbulence in Transient Channel Flows*. PhD thesis, University of Sheffield, 2019.
- [180] F. Javier García García and Pablo Fariñas Alvariño. On an analytical explanation of the phenomena observed in accelerated turbulent pipe flow. *Journal of Fluid Mechanics*, 881:420–461, 12 2019.

- [181] Sai C. Mangavelli, Junlin Yuan, and Giles J. Brereton. Effects of surface roughness topography in transient channel flows. *Journal of Turbulence*, 22:434–460, 2021.
- [182] Steven A. Orszag and G. S. Patterson. Numerical Simulation of Three-Dimensional Homogeneous Isotropic Turbulence. *Physical Review Letters*, 28:76, 1 1972.
- [183] John Kim, Parviz Moin, and Robert Moser. Turbulence statistics in fully developed channel flow at low Reynolds number. *Journal of Fluid Mechanics*, 177:133–166, 4 1987.
- [184] Parviz Moin and Krishnan Mahesh. DIRECT NUMERICAL SIMULATION: A Tool in Turbulence Research. *Annual Review of Fluid Mechanics*, 30:539–578, 1 1998.
- [185] A. G. Kravchenko and P. Moin. On the effect of numerical errors in large Eddy simulations of turbulent flows. *Journal of Computational Physics*, 131:310–322, 3 1997.
- [186] Sanjiva K. Lele. Compact finite difference schemes with spectral-like resolution. *Journal of Computational Physics*, 103:16–42, 11 1992.
- [187] Sylvain Laizet and Eric Lamballais. High-order compact schemes for incompressible flows: A simple and efficient method with quasi-spectral accuracy. *Journal of Computational Physics*, 228:5989–6015, 2009.
- [188] Paul Bartholomew, Georgios Deskos, Ricardo A.S. Frantz, Felipe N. Schuch, Eric Lamballais, and Sylvain Laizet. Xcompact3D: An open-source framework for solving turbulence problems on a Cartesian mesh. *SoftwareX*, 12:100550, 7 2020.
- [189] Alexandre Joel Chorin. Numerical Solution of the Navier-Stokes Equations. *Mathematics of Computation*, 22:745, 10 1968.
- [190] J. Kim and P. Moin. Application of a fractional-step method to incompressible Navier-Stokes equations. *Journal of Computational Physics*, 59:308–323, 6 1985.
- [191] R. Temam. Remark on the pressure boundary condition for the projection method. *Theoretical and Computational Fluid Dynamics*, 3:181–184, 12 1991.

- [192] J. Blair Perot. An Analysis of the Fractional Step Method. *Journal of Computational Physics*, 108:51–58, 9 1993.
- [193] Omar A. Mahfoze and Sylvain Laizet. Non-explicit large eddy simulations of turbulent channel flows from $Re_\tau = 180$ up to $Re_\tau = 5,200$. *Computers & Fluids*, 228:105019, 10 2021.
- [194] Haecheon Choi and Parviz Moin. Effects of the computational time step on numerical solutions of turbulent flow. *Journal of Computational Physics*, 113: 1–4, 1994.
- [195] H. Aref and S. Balachandar. *A First Course in Computational Fluid Dynamics*. Cambridge University Press, 10 2017.
- [196] A. B. Cain, J. H. Ferziger, and W. C. Reynolds. Discrete orthogonal function expansions for non-uniform grids using the fast fourier transform. *Journal of Computational Physics*, 56:272–286, 11 1984.
- [197] Suhas V. Pantankar. *Numerical Heat Transfer and Fluid Flow*. Taylor-Francis, 1980.
- [198] Thibault Dairay, Eric Lamballais, Sylvain Laizet, and John Christos Vassilicos. Numerical dissipation vs. subgrid-scale modelling for large eddy simulation. *Journal of Computational Physics*, 337:252–274, 5 2017.
- [199] J. Smagorinsky. GENERAL CIRCULATION EXPERIMENTS WITH THE PRIMITIVE EQUATIONS. *Monthly Weather Review*, 91:99–164, 3 1963.
- [200] Massimo Germano, Ugo Piomelli, Parviz Moin, and William H. Cabot. A dynamic subgrid-scale eddy viscosity model. *Physics of Fluids A: Fluid Dynamics*, 3:1760–1765, 7 1991.
- [201] Mehdi Seddighi-Moormani. *Study of turbulence and wall shear stress in unsteady flow over smooth and rough wall surfaces*. PhD thesis, University of Aberdeen, 2011.
- [202] Wei Wang and Shuisheng He. Mechanisms of buoyancy effect on heat transfer in horizontal channel flow. *The 7th International Symposium on Supercritical Water-Cooled Reactors (ISSCWR-7)*, pages 15–18, 2015.

- [203] J. He, R. Tian, P.X. Jiang, and S. He. Turbulence in a heated pipe at supercritical pressure. *Journal of Fluid Mechanics*, 920:45, 2021.
- [204] S. He, K. He, and M. Seddighi. Laminarisation of flow at low Reynolds number due to streamwise body force. *Journal of Fluid Mechanics*, 809:31–71, 12 2016.
- [205] Paolo Orlandi. *Fluid flow phenomena: a numerical toolkit*, volume 55. Springer Science and Business Media, 2000.
- [206] J. H. Williamson. Low-storage Runge-Kutta schemes. *Journal of Computational Physics*, 35:48–56, 3 1980.
- [207] K. C. Kim and R. J. Adrian. Very large-scale motion in the outer layer. *Physics of Fluids*, 11:417–422, 2 1999.
- [208] N. Hutchins and Ivan Marusic. Evidence of very long meandering features in the logarithmic region of turbulent boundary layers. *Journal of Fluid Mechanics*, 579:1–28, 2007.
- [209] Juan C. del Álamo, Javier Jiménez, Paulo Zandonade, and Robert D. Moser. Scaling of the energy spectra of turbulent channels. *Journal of Fluid Mechanics*, 500:135–144, 2004.
- [210] Gary N Coleman and Richard D Sandberg. A Primer on Direct Numerical Simulation of Turbulence-Methods, Procedures and Guidelines. Technical report, Aerodynamics & Flight Mechanics Research Group, University of Southampton, 2010.
- [211] P. Schlatter, R. Örlü, Q. Li, G. Brethouwer, H. M.J. Fransson, V. A. Johansson, H. P. Alfredsson, and S. D. Henningson. Turbulent boundary layers up to $Re_\theta = 2500$ studied through simulation and experiment. *Physics of Fluids*, 21:051702, 5 2009.
- [212] Thomas S. Lund, Xiaohua Wu, and Kyle D. Squires. Generation of Turbulent Inflow Data for Spatially-Developing Boundary Layer Simulations. *Journal of Computational Physics*, 140:233–258, 1998.
- [213] Guillermo Araya, Luciano Castillo, and Fazle Hussain. The log behaviour of the Reynolds shear stress in accelerating turbulent boundary layers. *Journal of Fluid Mechanics*, 775:189–200, 6 2015.

- [214] Guillermo Araya, Luciano Castillo, and Fazle Hussain. DNS of turbulent boundary layers in the quasi-laminarization process. In *ERCRAFT Series*, volume 23, pages 63–71. Springer Netherland, 2016.
- [215] G. Araya and D. Rodriguez. Visualization and assessment of turbulent coherent structures in laminarescent boundary layers. *Journal of Visualization*, 21:191–202, 4 2018.
- [216] Guillermo Araya, Kenneth E. Jansen, and Luciano Castillo. Inlet condition generation for spatially developing turbulent boundary layers via multiscale similarity. *Journal of Turbulence*, 10:N36, 1 2009.
- [217] Guillermo Araya, Luciano Castillo, Charles Meneveau, and Kenneth Jansen. A dynamic multi-scale approach for turbulent inflow boundary conditions in spatially developing flows. *Journal of Fluid Mechanics*, 670:581–605, 3 2011.
- [218] William K. George and Luciano Castillo. Zero-Pressure-Gradient Turbulent Boundary Layer. *Applied Mechanics Reviews*, 50:689–729, 12 1997.
- [219] David B. de Graaff and John K. Eaton. Reynolds-number scaling of the flat-plate turbulent boundary layer. *Journal of Fluid Mechanics*, 422:319–346, 11 2000.
- [220] V. Kitsios, A. Sekimoto, C. Atkinson, J. A. Sillero, G. Borrell, A. G. Gungor, J. Jiménez, and J. Soria. Direct numerical simulation of a self-similar adverse pressure gradient turbulent boundary layer at the verge of separation. *Journal of Fluid Mechanics*, 829:392–419, 10 2017.
- [221] T. B. Nickels. Inner scaling for wall-bounded flows subject to large pressure gradients. *Journal of Fluid Mechanics*, 521:217–239, 12 2004.
- [222] Jae Hwa Lee and Hyung Jin Sung. Direct numerical simulation of a turbulent boundary layer up to $Re_\theta = 2500$. *International Journal of Heat and Fluid Flow*, 32:1–10, 2 2011.
- [223] D. B. Spalding. A single formula for the “law of the wall”. *Journal of Applied Mechanics, Transactions ASME*, 28:455–458, 9 1960.
- [224] Paolo Luchini. Structure and interpolation of the turbulent velocity profile in parallel flow. *European Journal of Mechanics - B/Fluids*, 71:15–34, 9 2018.

- [225] Philipp Schlatter and Ramis Örlü. Turbulent boundary layers at moderate Reynolds numbers: Inflow length and tripping effects. *Journal of Fluid Mechanics*, 710:5–34, 11 2012.
- [226] Carlos Diaz-Daniel, Sylvain Laizet, and J. Christos Vassilicos. Wall shear stress fluctuations: Mixed scaling and their effects on velocity fluctuations in a turbulent boundary layer. *Physics of Fluids*, 29:055102, 5 2017.
- [227] Philipp Schlatter, Qiang Li, Geert Brethouwer, Arne V. Johansson, and Dan S. Henningson. Simulations of spatially evolving turbulent boundary layers up to $Re_\theta = 4300$. *International Journal of Heat and Fluid Flow*, 31:251–261, 6 2010.
- [228] M. Kozul, D. Chung, and J. P. Monty. Direct numerical simulation of the incompressible temporally developing turbulent boundary layer. *Journal of Fluid Mechanics*, 796:437–472, 6 2016.
- [229] Brandon Morgan, Johan Larsson, Soshi Kawai, and Sanjiva K. Lele. Improving Low-Frequency Characteristics of Recycling/Rescaling Inflow Turbulence Generation. *AIAA Journal*, 49:582–597, 3 2011.
- [230] A. W. Vreman and J. G.M. Kuerten. Comparison of direct numerical simulation databases of turbulent channel flow at $Re_\tau = 180$. *Physics of Fluids*, 26:015102, 2014.
- [231] Robert D. Moser, John Kim, and Nagi N. Mansour. Direct numerical simulation of turbulent channel flow up to $Re_\tau = 590$. *Physics of Fluids*, 11:943–945, 4 1999.
- [232] Javier Jiménez, Sergio Hoyas, Mark P. Simens, and Yoshinori Mizuno. Turbulent boundary layers and channels at moderate Reynolds numbers. *Journal of Fluid Mechanics*, 657:335–360, 2010.
- [233] F Nicoud and F Ducros. Subgrid-Scale Stress Modelling Based on the Square of the Velocity Gradient Tensor. *Flow, Turbulence and Combustion*, 62:183–200, 9 1999.
- [234] J. F. Brady and A. Acrivos. Steady flow in a channel or tube with an accelerating surface velocity. An exact solution to the Navier—Stokes equations with reverse flow. *Journal of Fluid Mechanics*, 112:127, 11 1981.

- [235] E. B. B. Watson, W. H. H. Banks, M. B. Zaturka, and P. G. Drazin. On transition to chaos in two-dimensional channel flow symmetrically driven by accelerating walls. *Journal of Fluid Mechanics*, 212:451, 3 1990.
- [236] Leonardo Espín and Demetrios T. Papageorgiou. Flow in a channel with accelerating or decelerating wall velocity: A comparison between self-similar solutions and Navier-Stokes computations in finite domains. *Physics of Fluids*, 21:1–17, 11 2009.
- [237] Xiaohua Wu, Parviz Moin, James M. Wallace, Jinhie Skarda, Adrián Lozano-Durán, and Jean-Pierre Hickey. Transitional–turbulent spots and turbulent–turbulent spots in boundary layers. *Proceedings of the National Academy of Sciences*, 114, 7 2017.
- [238] Juan C. del Álamo and Javier Jiménez. Spectra of the very large anisotropic scales in turbulent channels. *Physics of Fluids*, 15:L41, 2003.
- [239] A. Talamelli, K. J.A. Westin, and P. H. Alfredsson. An experimental investigation of the response of hot-wire X-probes in shear flows. *Experiments in Fluids*, 28:425–435, 2000.
- [240] Blair Perot and Parviz Moin. Shear-free turbulent boundary layers. Part 1. Physical insights into near-wall turbulence. *Journal of Fluid Mechanics*, 295:199, 7 1995.
- [241] A. Dejoan and Mike A. Leschziner. Separating the effects of wall blocking and near-wall shear in the interaction between the wall and the free shear layer in a wall jet. *Physics of Fluids*, 18:065110, 6 2006.
- [242] K. R. Sreenivasan. The effect of contraction on a homogeneous turbulent shear flow. *Journal of Fluid Mechanics*, 154:187–213, 1985.
- [243] Igor A. Bolotnov, Richard T. Lahey, Donald A. Drew, Kenneth E. Jansen, and Assad A. Oberai. Spectral analysis of turbulence based on the DNS of a channel flow. *Computers & Fluids*, 39:640–655, 4 2010.
- [244] Yoshinori Mizuno. Spectra of energy transport in turbulent channel flows for moderate Reynolds numbers. *Journal of Fluid Mechanics*, 805:171–187, 10 2016.

- [245] Myoungkyu Lee and Robert D. Moser. Spectral analysis of the budget equation in turbulent channel flows at high Reynolds number. *Journal of Fluid Mechanics*, 860:886–938, 2 2019.
- [246] A. S. W. Thomas and M. K. Bull. On the role of wall-pressure fluctuations in deterministic motions in the turbulent boundary layer. *Journal of Fluid Mechanics*, 128:283–322, 1983.
- [247] Adrián Lozano-Durán, Oscar Flores, and Javier Jiménez. The three-dimensional structure of momentum transfer in turbulent channels. *Journal of Fluid Mechanics*, 694:100–130, 3 2012.
- [248] Adrián Lozano-Durán and Javier Jiménez. Time-resolved evolution of coherent structures in turbulent channels: Characterization of eddies and cascades. *Journal of Fluid Mechanics*, 759:432–471, 11 2014.
- [249] J. L. Nash-Webber and G. C. Oates. An Engineering Approach to the Design of Laminarizing Nozzle Flows. *Journal of Basic Engineering*, 94:897–903, 12 1972.
- [250] J. P. Monty, N. Hutchins, H. C.H. Ng, I. Marusic, and M. S. Chong. A comparison of turbulent pipe, channel and boundary layer flows. *Journal of Fluid Mechanics*, 632:431–442, 2009.
- [251] Matthias H. Buschmann and Mohamed Gad-El-Hak. Normal and cross-flow Reynolds stresses: Differences between confined and semi-confined flows. *Experiments in Fluids*, 49:213–223, 7 2010.
- [252] Javier Jiménez and Sergio Hoyas. Turbulent fluctuations above the buffer layer of wall-bounded flows. *Journal of Fluid Mechanics*, 611:215–236, 9 2008.
- [253] A. Wray and M. Y. Hussaini. Numerical experiments in boundary-layer stability. *Proceedings of the Royal Society of London. A. Mathematical and Physical Sciences*, 392:373–389, 4 1984.
- [254] Ugo Piomelli, Thomas A. Zang, Charles G. Speziale, and M. Yousuff Hussaini. On the large-eddy simulation of transitional wall-bounded flows. *Physics of Fluids A: Fluid Dynamics*, 2:257–265, 9 1990.

- [255] Satish Muthu and Shanti Bhushan. Comparison between temporal and spatial direct numerical simulations for bypass transition flows. *Journal of Turbulence*, 21:311–354, 6 2020.
- [256] P. Moin, T.-H. Shih, D. Driver, and N. N. Mansour. Direct numerical simulation of a three-dimensional turbulent boundary layer. *Physics of Fluids A: Fluid Dynamics*, 2:1846, 6 1990.
- [257] Gary N Coleman, John Kim, and Anh-Tuan Le. A numerical study of three-dimensional wall-bounded flows. *International Journal of Heat and Fluid Flow*, 16:333–342, 1996.
- [258] G. N. Coleman, J. Kim, and P. R. Spalart. A numerical study of strained three-dimensional wall-bounded turbulence. *Journal of Fluid Mechanics*, 416:75–116, 2000.
- [259] Shuisheng He, Adrián Lozano-Durán, Jundi He, and Minjeong Cho. Transition of a temporally developing three-dimensional turbulent boundary layer. *Physical Review Fluids*, 8:064606, 6 2023.
- [260] R. Vinuesa, A. Bobke, R. Örlü, and P. Schlatter. On determining characteristic length scales in pressure-gradient turbulent boundary layers. *Physics of Fluids*, 28:55101, 5 2016.
- [261] Benjamin Segun Oluwadare and Shuisheng He. Experimental Study of Turbulence Response in a Slowly Accelerating Turbulent Channel Flow. *Journal of Fluids Engineering*, 145, 8 2023.
- [262] Ivan Marusic and Jason P. Monty. Attached Eddy Model of Wall Turbulence. *Annual Review of Fluid Mechanics*, 51:49–74, 2019.
- [263] M. Guala, M. Metzger, and B. J. McKeon. Interactions within the turbulent boundary layer at high Reynolds number. *Journal of Fluid Mechanics*, 666:573–604, 1 2011.
- [264] Ronald J. Adrian. Hairpin vortex organization in wall turbulence. *Physics of Fluids*, 19:041301, 4 2007.
- [265] Cheng Cheng, Wei Shyy, and Lin Fu. Streamwise inclination angle of wall-attached eddies in turbulent channel flows. *Journal of Fluid Mechanics*, 946:A49, 9 2022.

- [266] Ali Uzun and Mujeeb R. Malik. High-Fidelity Simulation of Turbulent Flow Past Gaussian Bump. *AIAA Journal*, 60:2130–2149, 4 2022.
- [267] V Baskaran, A J Smits, and P N Joubert. A turbulent flow over a curved hill Part 1. Growth of an internal boundary layer. *Journal of Fluid Mechanics*, 182: 47–83, 1987.
- [268] Nobuyuki Otsu. A Threshold Selection Method from Gray-Level Histograms. *IEEE Transactions on Systems, Man, and Cybernetics*, 9:62–66, 1 1979.
- [269] Sattaya Yimprasert, Mathias Kvik, P. Henrik Alfredsson, and Masaharu Matsubara. Flow visualization and skin friction determination in transitional channel flow. *Experiments in Fluids*, 62:1–16, 2 2021.